



# **Investigation of semi-solid metal processing route**

Thesis submitted for Master of Engineering

By

**MIAN WAJID ALI SHAH**

School of Mechanical & Manufacturing Engineering

Dublin City University

April 2006

Supervisors

Dr Dermot Brabazon and Dr Lisa Looney

# Contents

<b>Nomenclature</b> .....	xi
<b>Preface</b> .....	xiv
<b>Acknowledgements</b> .....	xv
<b>Dedication</b> .....	xvi
<b>Abstract</b> .....	xvii

## 1. Introduction

1.1 Introduction of Semi-Solid Metal Processing .....	1
1.1.1 Application of SSP .....	2
1.1.2 Advantages of SSM Processing.....	4
1.2 Mechanical properties of SSM.....	5
1.3 Factors affecting Thixoforming operation.....	7
1.4 Rheology.....	10
1.4.1 Rheology of SSM .....	10
1.5 Viscosity of Newtonian & Non-Newtonian Fluids .....	11
1.6 Factor affecting viscosity .....	15

1.6.1	Effect of temperature .....	15
1.6.2	Effect of pressure .....	16
1.6.3	Effect of shear rate .....	16
1.7	Non-Newtonian Fluids .....	16
1.7.1	Time independent Non-Newtonian fluids .....	17
1.7.2	Time dependent Non-Newtonian fluids .....	17
1.8	Viscometer .....	19
1.8.1	Concentric cylinder viscometer .....	20
1.8.2	Cone & plate viscometer .....	21
1.8.3	Parallel plate viscometer .....	22
1.8.4	Falling sphere viscometer .....	23
1.9	Capillary viscometer .....	24
1.9.1	Glass capillary viscometer .....	27
1.9.2	End effects .....	28
1.9.3	Kinetic energy correction .....	30
1.9.4	Slip effect .....	30
1.10	Previous work on semi-solid Rheological modeling.....	31
1.11	Summary .....	56

## **2. Design analysis and construction**

2.1	Introduction .....	54
2.2	System Design .....	58

2.2.1	Table design.....	58
2.2.2	Injection chamber and capillary design .....	59
2.2.3	Capillary mould with surrounding furnaces .....	59
2.2.4	Piston motion mechanism .....	61
2.2.5	Fluid pressure measurement calculations .....	62
2.2.6	Temperature measurement .....	65
2.3	System control .....	65
2.4	Experimental procedure .....	68
2.4.1	Material preparation .....	68
2.4.2	Experimental setup .....	70
2.5	Summary .....	72

### **3. Model Setup**

3.1	Finite element analysis .....	73
3.1.1	Grid Geometry creation .....	73
3.1.2	Meshing of geometry .....	74
3.1.3	Mesh examination for quality.....	76
3.1.4	Zone and boundary specification.....	76
3.2	Fluent .....	76
3.2.1	Reading file in fluent .....	72
3.2.2	Grid checking for quality and smoothness .....	77

3.2.3	Scaling Grid .....	78
3.2.4	Solver formulation .....	78
3.2.5	Multiphase modeling .....	80
3.2.6	Mixture Model .....	80
3.2.7	Viscous modeling .....	82
3.2.8	Energy & radiation modeling .....	82
3.2.9	Material modeling .....	82
3.2.10	Phase modeling .....	83
3.2.11	Operating and boundary condition .....	83
3.2.12	Model initializing solution .....	82
3.3	Summary .....	84

## **4. Results .....**

4.1	Numerical calculations and results .....	86
4.2	Material properties for modeling and simulation experiments and results .....	93

## **5. Discussion and conclusions .....**

5.1	Discussion on numerical results .....	105
5.2	Viscosity variation with solid fraction and plunger velocity .....	106
5.3	Velocity variation with solid fraction and plunger velocity .....	108

5.4 Pressure variation with solid fraction and plunger velocity .....109

5.5 Static pressure variation with increasing velocity and  
solid fraction ..... 110

5.6 Conclusions .....111

**References** ..... 112

**Appendixes** .....122

## List of Tables

1.1 Comparison mechanical properties of SSF A356 alloy to conventional processes.....	6
1.2 Viscosity of substances at room and specified temperature .....	14
1.3 Table showing value of $m$ , according to several authors .....	31
1.4 Properties of A356 alloy used by Paradise et al for the capillary experiment ...	37
1.5 Physical properties and different parameter values for L. Orgeas experiments..	43
4.1 Steady state viscosities of alloy A356 at $0.33 f_s$ used by Dermot et al .....	87
4.2 Steady state viscosities of alloy A356 at $0.4 f_s$ used by Dermot et al .....	87
4.3 Velocity values for different shear rates with a flow index of $n = 0.3$ .....	89
4.4 Velocity values for different shear rates with a flow index of $n = 0.1$ .....	90
4.5 Velocity values for different shear rates with a flow index of $n = -0.1$ .....	90
4.6 Values for different shear rates with a flow index of $n = -0.3$ .....	90
4.7 Velocity values for different shear rates with a flow index of $n = 1$ .....	91
4.8 $\Delta P$ values at different shear rates, viscosities of the semi-solid and $n = 0.3$ ..	92
4.9 $\Delta P$ values at different shear rates, viscosities of the semi-solid and $n = 0.1$ ..	92
4.10 $\Delta P$ values at different shear rates, viscosities of the semi-solid and $n = -0.1$ .	92
4.11 $\Delta P$ values at different shear rates, viscosities of the semi-solid and $n = -0.3$ ..	93
4.12 $\Delta P$ values at different shear rates, viscosities of the semi-solid and $n = 1$ ...	93
4.13 Physical properties of materials for simulation in present work .....	94
4.14 Solid fraction and billet temperatures for a plunger speeds of 0.075 m/s, 0.5 m/s and 1m/s for simulation in present work .....	95

## List of Figures

1.1	Micrographs of (a) dendritic and (b) globular Al-Si alloy.....	2
1.2	Pictures of thixoformed parts (a) suspension support and (b) diesel engine pump housing.....	3
1.3	Different processes (a) Rheocasting, (b) thixocasting, and (c) thixomolding .	12
1.4	Different type of fluid behaviour .....	13
1.5	Graph showing the effect of viscosity change for a given shear rate .....	18
1.6	Graph showing Shear stress vs. Shear rate for time dependent fluids .....	18
1.7	Schematic of Concentric Cylinder Viscometer .....	21
1.8	Schematic of cone and plate viscometer.....	22
1.9	Geometry of parallel plate viscometer .....	23
1.10	Geometry of falling sphere viscometer .....	24
1.11	Schematic diagram of Glass capillary viscometer .....	28
1.12	Modified capillary viscometer used for Bernhard et al .....	33
1.13	Die geometry used for experiments and simulation by Paradies et al .....	35
1.14	Capillary viscometer used for Nohn et al work .....	39
1.15	Rig geometries used in the work of L. Orgeas et al .....	41
1.16	(a) Vertical and (b) horizontal capillary viscometers used by Afrath et al ...	45
1.17	Schematic View of parallel plate viscometer used by Figueredo et al .....	48
2.1	Drawing layout of capillary viscometer .....	58
2.2	Graphical user interface for the temperature logging from the injection Chamber and the semi-solid material .....	67



2.3	Graphical user interface developed to record the load cell readings .....	67
2.4	Graphical user interface for the Unimotor servomotor controller program ...	68
3.1	Vertices representation for grid geometry .....	74
3.2	Connected vertices to form geometry for simulation .....	74
3.3	Grid generated in GAMBIT for conical section of the capillary viscometer.	75
3.4	Fluent program structure .....	77
3.5	Schematic diagram of Segregated Solution Method .....	79
4.a	Al-Si phase diagram .....	88
4.1	Dynamic pressure of A356 at $0.33 f_s$ , 871 K and 0.075 m/s .....	96
4.2	Velocity of A356 at $0.33 f_s$ , 871 K and 0.075 m/s .....	96
4.3	Viscosity of A356 at $0.33 f_s$ , 871 K and 0.075 m/s .....	96
4.4	Dynamic pressure of A356 at $0.40 f_s$ , 863 K and 0.075 m/s .....	97
4.5	Velocity of A356 at $0.40 f_s$ , 863 K and 0.075 m/s.....	97
4.6	Viscosity of A356 at $0.40 f_s$ , 863 K and 0.075 m/s .....	97
4.7	Dynamic pressure of A356 at $0.50 f_s$ , 848 K and 0.075 m/s .....	98
4.8	Velocity of A356 at $0.50 f_s$ , 848 K and 0.075 m/s .....	98
4.9	Viscosity of A356 at $0.50 f_s$ , 848 K and 0.075 m/s .....	98
4.10	Dynamic pressure of A356 at $0.33 f_s$ , 871 K and 0.5 m/s .....	99
4.11	Velocity of A356 at $0.33 f_s$ , 871 K and 0.5 m/s .....	99
4.12	Viscosity of A356 at $0.33 f_s$ , 871 K and 0.5 m/s .....	99
4.13	Dynamic pressure of A356 at $0.40 f_s$ , 863 K and 0.5 m/s .....	100
4.14	Velocity of A356 at $0.40 f_s$ , 863 K and 0.5 m/s.....	100

4.15	Viscosity of A356 at $0.40 f_s$ , 863 K and 0.5 m/s .....	100
4.16	Dynamic pressure of A356 at $0.50 f_s$ , 848 K and 0.5 m/s .....	101
4.17	Velocity of A356 at $0.50 f_s$ , 848 K and 0.5 m/s .....	101
4.18	Viscosity of A356 at $0.50 f_s$ , 848 K and 0.5 m/s .....	101
4.19	Dynamic pressure of A356 at $0.33 f_s$ , 871 K and 1 m/s .....	102
4.20	Velocity of A356 at $0.33 f_s$ , 871 K and 1 m/s .....	102
4.21	Viscosity of A356 at $0.33 f_s$ , 871 K and 0.5 m/s .....	102
4.22	Dynamic pressure of A356 at $0.40 f_s$ , 863 K and 1 m/s .....	103
4.23	Velocity of A356 at $0.40 f_s$ , 863 K and 1 m/s.....	103
4.24	Viscosity of A356 at $0.40 f_s$ , 863 K and 1 m/s .....	103
4.25	Dynamic pressure of A356 at $0.50 f_s$ , 848 K and 1 m/s .....	104
4.26	Velocity of A356 at $0.50 f_s$ , 848 K and 1 m/s .....	104
4.27	Viscosity of A356 at $0.50 f_s$ , 848 K and 1 m/s .....	104

## Nomenclature

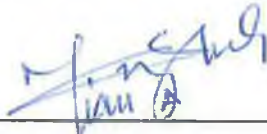
$\eta$	=	Viscosity or apparent viscosity of material, Pa.s
$\tau$	=	Shear stress, Pa.
$\dot{\gamma}$	=	$\frac{dv_z}{dr}$ = Shear rate, $s^{-1}$ .
$\nu$	=	Kinematic viscosity, $m^2/kg.sec$
$\rho$	=	Density of material, $kg/m^3$
$K$	=	Consistency index, $Pa.s^n$
$N$	=	Flow index (dimensionless)
$\tau_0$	=	Yield stress, Pa
$A$	=	Constant for Arrhenius Equation.
$E$	=	Activation energy, (J/mol)
$R_a$	=	Universal gas constant (8.314 J/mol K)
$T$	=	Absolute temperature, K
$r_a$	=	Inner cylinder radius of concentric cylinder viscometer, m
$r_b$	=	Outer cylinder radius of concentric cylinder viscometer, m
$r$	=	Radius at which shear is measured for concentric cylinder viscometer, m
$\omega$	=	Angular speed of concentric cylinder viscometer, rad/sec
$T_a$	=	Torque,
$L$	=	Height of inner cylinder of concentric cylinder viscometer, m
$R$	=	Radius from the centre to the end cone and plate in cone and plate and parallel plate viscometers respectively, m
$\theta$	=	Cone angle
$r_p$	=	Radius of rotating plate in parallel plate viscometer, m
$h$	=	Gap between the parallel plates, m
$r_s$	=	Radius of sphere in falling sphere viscometer, m

$U_t$	=	Terminal velocity of falling body, $m/s$
$\rho_2$	=	Density of sphere, $kg/m^3$
$\rho_1$	=	Density of fluid, $kg/m^3$
$\Delta P$	=	$(P_o - P_L)$ , Change in pressure in capillary viscometer, $Pa$
$P_o$	=	Pressure recorded with first pressure sensor in paradies work, $Pa$
$P_L$	=	Pressure recorded with second pressure sensor in paradies work, $Pa$
$L_c$	=	Length of the capillary tube, $m$
$R_c$	=	Radius of capillary tube, $m$
$Q$	=	Flow rate, $m^3/s$
$V_{aver}$	=	Average velocity in capillary tube, $m/s$
$D$	=	Diameter of capillary tube, $m$
$\dot{\gamma}_w$	=	Shear rate at the wall of capillary tube, $1/s$
$\tau_w$	=	Shear stress at the wall of capillary tube, $Pa$
$t$	=	Flow measure time, $sec$
$C$	=	Constant for glass capillary viscometer.
$L_e$	=	Equivalent length with end correction in capillary viscometer, $m$
$m$	=	Numerical factor, dimensionless
$V_{ram}$	=	Velocity of the ram, $m/s$
$A_{shot\ sleeve}$	=	Area of shot sleeve, $m^2$
$A_{tube}$	=	Area of capillary tube, $m^2$
$V_{tube}$	=	Flow velocity in tube, $m/s$
$f_s$	=	Solid fraction
$\mu_o$	=	Temperature dependent viscosity, $Pa.s$
$\dot{\gamma}_0$	=	Maximum shear rate, $1/s$
$\alpha$	=	2.5 (Parameter Constant for Orgeas et al.)
$B$	=	22 (Parameter Constant for Orgeas et al.)
$\beta$	=	2.34 (Parameter Constant for Orgeas et al.)
$H$	=	Height of capillary tube, $m$
$W$	=	Width of capillary tube used in Afrath work, $m$

$\eta_{rep}$	=	Representative viscosity, <i>Pa.s</i>
$\dot{\gamma}_{rep}$	=	Representative shear rate, <i>1/s</i>
$\sigma^P$	=	Plastic stress, <i>Pa.</i>
$\epsilon^P$	=	Plastic strain, <i>m</i>
$C_0$	=	Composition of alloy, %
$C_L$	=	Composition of liquid phase, %
$\delta$	=	Solid fraction sensitivity parameter (10 from work of Braccini et al)
$t_s$	=	Shearing time, <i>sec</i>
$T_a$	=	Cooling temperature, °C
$m$	=	Power law index (Dimensionless)
$L_I$	=	Length of injection chamber for present work, <i>m</i>
$r_I$	=	Radius of injection chamber for present work, <i>m</i>
$V_I$	=	Plunger velocity in injection chamber, <i>m/sec</i>
$V_c$	=	Velocity in capillary tube, <i>m/s</i>
$A_I$	=	Area of injection chamber, <i>m<sup>2</sup></i>
$A_c$	=	Area of capillary tube, <i>m<sup>2</sup></i>

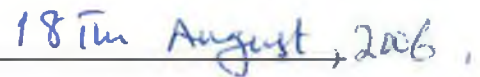
## Preface

I hereby certify that this material, which I now submit for assessment on the programme of study leading to the award of Masters of Engineering is entirely my own work and not been taken form the work of others save and to the extent that such work has been referenced and acknowledged within the text of my work.



---

MIAN WAJID ALI SHAH



---

DATE

## Acknowledgement

First of all, my sincere thanks go to my supervisor Dr Dermot Brabazon for his supervision during this work. He has overseen and done whatever it takes to make it possible. His useful advice, help, encouragement and time spent in this project is appreciated which made my work more easy and understandable.

I would also like to thank these special people especially Chris Crouch, Alan Meehan, Martin Johnson, Keith Hickey, Liam Domican, Cian Merne, Jim Barry and all the mechanical lab staff for their technical support and help during this project, to get this project off the ground and it is gratefully appreciated.

I would also like to pay my special thanks to some of my friends here in DCU for their help and support during my studies in DCU especially Dr Sumsun Naher, Mesbah Sumniah , Qasim Murtaza, Dr Murshid, Ahmad and all my friends who helped me in any aspect during my stay in DCU.

Finally I would like to thanks my parents, brothers and sisters for both moral and financial support throughout my studies

## **Dedication**

I would like to dedicate my thesis to my parents, brother, sisters and all the members of my family. I would like to offer them my special thanks with a grateful heart for their moral, financial and personal support. They stood by me in thick and thin and gave me the encouragement and helped me out in ways no one else could in the time when I was about to give way.



## Abstract

Two main objectives were complete during this work. One was the design and construction of a high temperature capillary viscometer and the second was the modelling of semi-solid metal flow with a view to aiding the design and providing data for comparison purposes. The high temperature capillary viscometer has been constructed and has been used for preliminary testing. This device will be used to measure the viscosity of semi-solid metals under high temperature and shear rate conditions, similar to those found in industry. The capillary viscometer is a single point system that can be used to calculate the viscosity by measuring the flow rate and pressure difference between the two end of the capillary tube as the viscosity directly proportional to the pressure drop and inversely proportional to the flow rate. Design criteria included a requirement for a highly controllable temperature up to 800 °C, injection shear rates above 10,000 s<sup>-1</sup>, and controllable injection profiles. A 2D, two phase theoretical unsteady state model using a computational fluid dynamics (CFD) software FLUENT was developed. This was used to evaluate the viscosity of semi-solid metals passing through the designed capillary viscometer at injection speeds of 0.075, 0.5, and 1 m/s. The effects of fractions solid ( $f_s$ ) of the metal from 0.25 to 0.50 were also investigated. Strong correlations between these parameters and the resulting viscosity were noted for the power law viscosity equations which were used to develop the Fluent models.

# Chapter 1

## Introduction

### 1.1 Introduction to semi-solid metal processing

Semi-solid metal processing (SSP), also called Thixoforming, is relatively a new technology for manufacturing of engineering components. Its success depends on the achievement of a suitable microstructure prior to deformation and on the knowledge of the rheological properties of the material. The rheological data is necessary in order to describe and control the flow of the semi-solid material [1]. An important factor affecting the rheology in SSP is the the alloy must have a solid metal spheroidal structure rather than dendritic in the liquid matrix [2].

Prof. Merton Fleming and his co-worker first explored SSP in the late 1960's and early 1970's, while working in Massachusetts Institute of Technologies (MIT's) Solidification Processing Laboratory [3]. In 1969, Steve Metz, a graduate student, was studying hot tearing in cast steel; specifically he was measuring the stress the component could sustain while it was partially solidified, through a fraction solid ( $f_s$ ) of 0.8 and higher. It was concluded that viscosity is a critical parameter in the interdendritic liquid. In 1971, David Spenser, another graduate student took the task of evaluating the viscosity of the metals (Sn-15%Pb) while partially solidified [4 and 5]. He used a Couette rheometer for shearing the dendritic structure. A surprising result that Spenser found was that the semi-solid metal remained fluid for a longer time during solidification when it had been shear from the liquid state as the temperature dropped into the semi-solid range. This later turned out to be due to a change in the metal microstructure from dendritic to spheroidal. This development opened the gateway to processing metals in the semi-solid state [6-8]. It took nearly twenty years for the thixoforming process to mature from an academic curiosity to that of a commonly used production process. Since 1992, it has grown into a well known industrial technology [9, 10]. SSP is currently in competition with traditional

manufacturing processes. It is usually used for components that require lower densities but higher mechanical properties necessary in the aerospace and automobile industries.

SSP is getting used world wide, especially in the manufacturing of lightweight parts and advance components for fuel saving and the production of near net shape pore-free components having both thin and thick sections. Research in America, Europe and Asia has been conducted in order to understand and solve the problem of feedstock availability, quality, reproducibility, material testing, process security, control and market acceptance. Research has also been conducted on the rheology, recycling, process parameters, die temperature profile, heat treatments, and components properties [11-13].

Fig: 1.1 shows the microstructure of conventionally cast and thixoformed Al-SiC alloy.

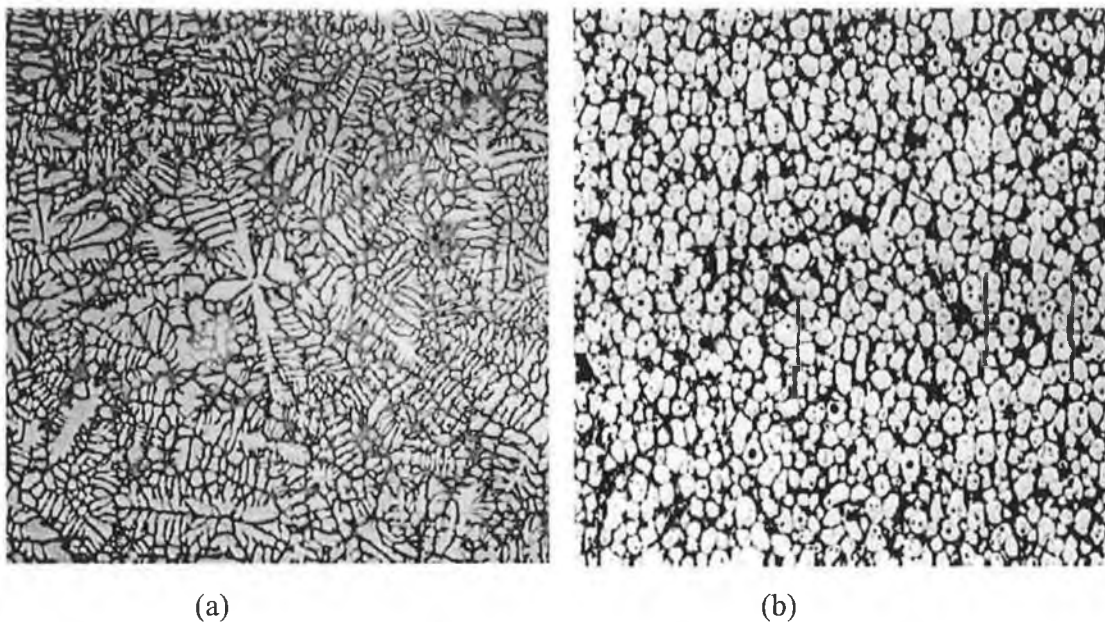


Figure 1.1 Micrographs of (a) dendritic conventional casting and (b) a globular thixoformed Al-Si alloy [81].

### 1.1.1 Application of SSP

The growth of the SSM production in Europe and America is remarkable over the last two years. SSM seems to be competitive when the intended part associates with intricate design, combining thin and thick section, to reduce and eliminate machining, and for high integrity parts. Many products from the SSM are widely used. The most important

application of SSP is the series production of part for the automotive sectors. In automobile industry there is an increasing tendency of using lightweight and higher quality parts, because we are now confronted with the need of less fuel consumption and precaution against stringent exhaust gas regulation. Car air-conditioning parts such as compressor that can withstand high temperature can be successfully produced by SSP. It is also applicable in manufacturing of small components such as Golf Putter, Actuator Arm, luxury Ergonomic Pen, Automotive Pulley etc. SSP contributed a significant weight reduction in the manufacturing of automobile components such as drum disk, steering knuckle, steering arms, engine brackets, front and rear suspension arm, oil pump, fuel rail etc. The products such as rocker arm, engine mounts, brake cylinders, clutch cylinders, belt covers, wheels, pistons, body frame and motor housing are also the dominant manufactured parts. Aluminium alloy A356 F is used for low-pressure fuel rails, as they need ductility in case of crash. A356-T5 has been chosen for thin walled structural nodes because of its ductility and medium yield strength. A356-T6 is being used for thixocast suspension parts, which required strength and elongation beyond the possibilities of T5. Aluminium alloy A357-T5 is employed for wheel and high pressure and hydraulic components [13-18]. Figure 1.2 shows some of the applications of semi-solid processing in the manufacturing industries.

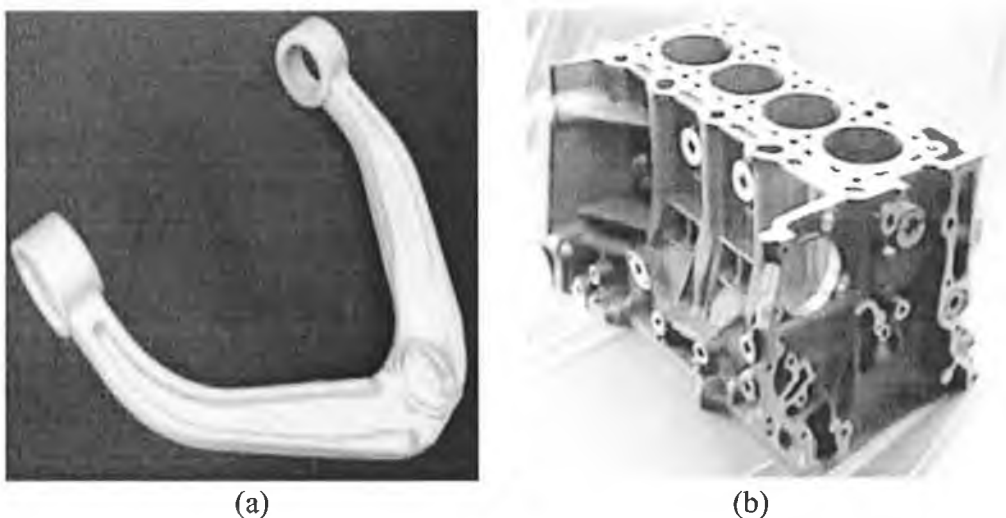


Figure 1.2 Thixoformed automobile (a) suspension arm and (b) cylinder block [18, 99]

### 1.1.2 Advantages of SSM processing

One of the advantages of the thixoforming process over conventional process is that it extends die life, the cost of which plays a very large part in the total production cost. Compared to liquid alloys, semi-solid metals (SSM) require lower heat content, so the degradation of the die due to the thermal cycling and wear can be reduced and also faster casting cycle times are possible due to the lower heat content to be extracted. Thinner section and more intricate parts can be formed SSP. Due to lower forming load requirements, smaller presses can replace the larger one [19]. With faster production cycle and smaller thermal stresses, die productivity and durability are high. In SS slurries, shrinkage during solidification is smaller, thus allowing net shape casting with final parts being close to the nominal dimensions and reduces the amount of wastage. The pressure drop in the piece due to shrinkage is much smaller than regular casting; hydrogen porosity is less likely to occur. In the SS metal, the compactness of the casting piece is higher, leading to improved mechanical properties of the parts [10]. Energy efficiency is increased, as SS slurries give the possibilities complex and near net shape geometries in one forming step, so it avoids the unnecessary steps, less forming energy is required for the forming process, and because of the lower forming temperature, low casting forces are required. Lighter parts can be produced by SSF to replace heavier steel components produced by conventional methods [22]. Part safety is increased due to the better mechanical properties and foundry safety is increased due to the absence of the molten metals [21]. Despite these advantages, there is some limitation and drawbacks of SSP.

Temperature plays a very important role in the SSM processing because the solid fraction and viscosity depend upon temperature. Temperature control is therefore very important. It is necessary to control ram speed during the filling of the die. Low speed results in incomplete filling of the die while higher speeds result in turbulence and gas entrapping, so ram speed should be appropriate for the process. Special equipment and skills may be required that cost more than those for conventional casting [19]. Due to the cost of the large scale SSP equipment, there are only a few suppliers and manufactures. Raw material is also relatively expensive. Oxides can be trapped in the casting of parts especially those of steel. Oxide skin should be prevented or removed from the billet before the casting process. This requires special equipments such as the use of the over

flow to carry out the oxide layers, or an inert gas atmosphere can be used during the process [21]. Also there can be a change in the liquid and solid phase fraction, which can effect the composition, or bonding of the solid particles can occur (agglomeration) [19, 23 and 24].

## **1.2 Mechanical properties of SSM**

Mechanical properties generally include the reaction of a material to mechanical loadings. In the majority of the cases, it is the mechanical properties with which the engineer is principally concerned in material selection. These mechanical properties are the strength of the material i.e. tensile, compressive and shear strength, hardness, ductility, toughness, impact resistance and fatigue resistance [25]. To determine the mechanical properties of the material various standardized tests have been developed. The materials are subjected to these laboratory tests under controlled conditions, so that their reaction to change in the condition can be determined. Engineers must be very careful because the data should be applied to the condition similar to the testing conditions [26]. The variety of material available to engineer is vast and optimum use of them must be made if a product is to compete in the market place. A good knowledge of material is therefore essential not only for the product design but also for consideration of how the product will be manufactured.

SSM has good mechanical properties. It shows good tensile strength, high yield strength, hardness and elongation, superior than most of the conventional processes [27]. In any of the manufacturing process, the properties attained are determined by the variables that govern the process like die temperature, piston velocity, billet temperature, shot chamber temperature, rate of heat up, die lubricant and time of transfer. Mechanical properties of SSM also greatly depend upon the impurities, grain size, porosity, heat treatment, and microstructure. For example, impurities like Fe, Si can greatly affect the mechanical properties. An increase in Fe content decreases elongation, toughness, ultimate tensile strength, and can increase micro-porosity (because of easy debonding) while an increase in Si contents up to 4% increases feed ability, but further increases in Si contents towards

the eutectic composition decrease fluidity (due to increased area of eutectic grain at higher Si contents) [21]. By decreasing the grain size, mechanical properties generally increase, because of the increased resistance to slip and increased grain boundaries. Grain size can be reduced with high cooling rates, marginally with Si contents up to 3%, by isothermal holding and addition of grain refinements. Strength, and especially elongation, increase also with smaller and more finely distributed porosity [21]. Table 1.1 shows some of the mechanical properties of semi-solid forming process compared to conventional casting processes.

Casting process	Tensile strength (MPa)	Yield strength (MPa)	Elongation (%)	Hardness (HB)
Sand cast	140	90	2	60
Sand cast (T6)	250	220	1	105
Permanent Mould Cast	180	90	3	60
Permanent Mould Cast (T6)	300	240	2	100
Squeeze casting (T6)	283	207	10	
Closed Die Forging (T6)	340	280	90	
Stir casting	236	135	15	
Stir casting (T6)	290-320	220-240	13-19	
Thixoformed	224	112	14	60
Thixoformed (T6)	329	270	15	

Table No: 1.1 Comparison of mechanical properties of SSF A356 alloy to conventional processes [21].

Experiments on alloy 357-T6 in SSTT (semi solid thermal transformation) with electromagnetic stirring show a yield strength of 300 MPa, an ultimate tensile strength of 341 MPa and elongation of 10.8% as compared to the conventional sand cast 357 T6 (296 MPa, 345 MPa, 2% respectively). It was observed that for the same number of cycles to failure for 357-T6 (annealed at 538 °C for 3 hours and aged at 177 °C for 6 hours), the failure fatigue stress is greater than those of the conventional cast A356-T6 alloy [28, [29]. Commercial A356 and A357 semi-solid billet fabricated by both magneto hydrodynamics (MHD) and grain-refined (GR) methods were used to investigate yield strength. It was found that yield stress decreases sharply at a temperature of 570 °C for A356 and at 573 °C for A357 respectively. GR alloy has a greater yield strength as compared to MHD in a solid fraction range of 0.5-1.0 due to the entrapped liquid with in the primary spheroidised solid particles [30]. In another experiment the fatigue strength of Al-Si-Mg-T6 casting at  $10^7$  cycles of semi solid casting compared with that of squeeze and gravity casting showed that the fatigue strength compares well against the conventionally cast methods. Either oxides or pores which contribute directly to fatigue strength were found to be smaller in SSP than in squeeze casting in the same machines [31 and 32].

### **1.3 Factor affecting thixoforming operation**

There are some factors, which have a significant influence on the thixoforming operation (Thixoforming is manufacturing of billet of the desired microstructure and the subsequent reheating and forming of the billet in the semi-solid state) [3]. Temperature has the most influence to determine the relative solid and liquid friction. At low solid fraction the semi solid mixture behaves as a non-linear slurry and as the fraction of solid increases, it changes from a suspension to a network of connected solid particles. Therefore as the solid fraction increases so does the viscosity. Even under unshearing conditions, inter-particle bonding increases as a function of time and as a result gives rise to an increased viscosity of the melt after shearing is started. Relation between the apparent viscosity and



temperature of the semi-solid slurry can be obtained with a rotational viscometer [20 and 33].

Apart from the solid fraction, the viscosity also depends upon the shear rate and shear time. Viscosity generally decreases with an increase in the shear rate or upon the introduction of a shear rate or shear stresses. Stirring can be active or passive. Mechanical and electromagnetic stirring is termed active stirring because of their direct nature of the inducing shear. Passive stirring, on the other hand, shears a solidifying melt by forcing it through a narrow tube or channel under close temperature control within the semi-solid range [21 and 34]. The decrease in the apparent viscosity at a constant shear rate can be considered to occur in two stages resulting in an exponential decrease. In the first stage, there is a rapid decrease due to the breaking of inter-aggregate bonding, which release the liquid entrapped with in the agglomerates, and secondly, the decrease in the viscosity occurs due to spheroidization particle. The second stage is a relative slow process, result in the decrease in the size of the agglomerates and causing the particles to become spherical and uniform size. It also results in the decrease effective volume fraction of the primary phase [19]. The spheroids of the solid can more easily move over one another providing a non-restricted microstructure and a fluent semi-solid metal. Agglomeration and re-agglomeration processes occur normally in stirred semi-solid slurry. They are both competitive processes and dynamic equilibrium is establish between agglomeration and dis-agglomeration. Dendritic fragmentation and solid ripening produce the reduction in the viscosity, and it is observed that after a certain time period, the viscosity reaches a steady state. Then only a small reduction is observed in the viscosity, causes by ripening after this period [21].

Apart from these factors, Thixoforming operation also depends upon history of the material prior to processing. Under steady state shearing, the microstructure evolves towards a steady configuration, while the effective viscosity decreases. During a rapid transient in shear, the microstructure does not have enough time to change and there fore the effective viscosity increases [10].

Viscosity also depends upon the particle morphology. The particle morphology before a change in shear rate or temperature will dictate that what kind of morphology will be present after the change. More equiaxed rounded particles delay the transition to a new

morphology. The flow behaviour greatly depends upon the particle morphologies as well as size of the particles. A fine spheroid microstructure having a little entrapped eutectic with in the primary phase. Solidification and cooling rate also play a very important role in order to predict the particle morphology. Rapid solidification rate of an alloy can lead to coring. It may also result in the hot shortness where weak grain boundaries results in detrimental mechanical properties. To homogenise the microstructure, heating is due to high temperature and then allow the atom collision [21]. For a higher cooling rates, a high apparent viscosity for a given fraction of solid has been observed attributed to the hydrodynamic effect of the smaller particles, but most commonly to their more irregular geometry. Microstructure properties and viscosity are also dependent upon the composition of the alloy [12].

Die design, temperature, and lubricant should also be considered in a thixoforming process. They are usually different from those used in conventional high-pressure die-casting in order to take into account the different initiative features of the thixocasting process. Gate size of the die should be similar to the injection diameter in order to produce high quality thixocasting [21 and 27]. If feeding through the gate is required, then die thickness should also be as large as possible. Die temperature needs to be strictly controlled in order to prevent the premature freezing during the forming operation. But the temperature of the die generally depends upon the shape of the part to be produced. Die temperature should be kept as low as possible in order to prevent the sticking of the materials [35]. Die filling parameters should also be taken into account. Thixotropic material requires the viscosity to be specified as a function of shear rate history and temperature. Filling velocity and ram speed need to be controlled. Ram speed should be at a certain level to enable the solid stream to enter the mould without turbulence. Too low a velocity can cause the pre-mature freezing and incomplete die filling; while for a high velocity can result in porosity due to turbulence. However for each piston speed, the correct viscosity value is different and temperature adjustment on holding time may be needed. With in a certain range, the desired viscosity range for an optimal filling of the component may be adjusted by the smart geometry of the gating system. The final pressure and dwell time also need to be considering feed shrinkage during solidification in order to prevent porosity [21 and 36].

Jetting could be avoided by having large solid fraction but large fraction solid tends to increase the liquid segregation. The forming rate should be kept as high as possible in general, as long as the turbulence does not occur to avoid the segregation of the solid and liquid phases. Large tensile components at the free surface should also be avoided as these can cause cracking [21 and 33].

## **1.4 Rheology**

Rheology can be defined as “the study of deformation and flow of matter” under an applied force. It is a Greek word which means “the study of flow”. The definition was accepted when the American Society of Rheology was founded in 1929. In late 1920s, two scientists (Professor Marcus Reiner and Professor Eugene Bingham) laid the foundation of rheology. The first published papers were for the materials like asphalt, lubricants, paints, plastics and rubber to describe the properties and behaviour of these materials. Rheology has become a wider and expanded subject nowadays. It is involved in the development and processing of plastic, paint, metals, food, polymers, biological fluids and suspensions. It is also involved in filtration, forming materials, reaction involving mineral slurries, cosmetics, refining in the petroleum industry, coating, thickening and de-watering of mineral slurries. Two components are used generally to describe the consistency of different products, i.e. viscosity which is the resistance to flow and elasticity which refers to the way material returns to its original state after removing the applied force [37-39].

### **1.4.1 Rheology of semi-solid metals**

Material characteristic depends on several factors like the size, shape and distribution of the solid particles in the material, solid fraction, shear rate, processing history and the viscosity of the material. During the solidification of the conventionally cast alloys, a stage is reached in which a dendritic microstructure is formed. The dendrite network has poor ductility and feed ability, and can result in the hot tearing. For the alloys being processed in the semi-solid state, these dendrite structures must be changed into globular

microstructure, in order to reduce its resistance to shear, and help them to flow, as the globular microstructure will help the grains to slide and roll over each other [40 and 41]. The dendrites that are usually formed during the solidification of the alloy melt and can be easily broken up either by mechanical stirring or by electromagnetic stirring. Semi-solid casting and forming processes depend upon the thixotropic behaviour of the semi-solid alloy. These processes required a semi-solid feed stock that has a globular solid particles surrounded by liquids. For the process, the equiaxed dendritic structure of the material must be changed to the globular microstructure. "Rheocasting" is the process stirring of the slurry during solidification to produce the required globular microstructure. Upon production the material is injected into the die. Thixoforging is the process of feeding the chips of fine microstructure to a machine where the chips are partially melted and obtain a suitable structure for semi-solid forming [3]. Figures 1.3 shows the flow chart of processes of Rheocasting, Thixocasting, and Thixoforging respectively [3, 42 and 43].

## **1.5 Viscosity of Newtonian and non-Newtonian fluids**

Fluids in which the shear stress is directly proportional to the shear rate are called Newtonian fluids. In a plot of shear stress versus stress-rate, a straight line represents a Newtonian fluid response whose slope is the viscosity, see figure 1.4. For Newtonian fluids the viscosity of the fluid is constant regardless of the shear stress or shear rate [44 and 45]. Most gases and liquids (water, benzene, and ethyl alcohol etc) are Newtonian fluids [37].

A Newtonian behaviour is exhibited by fluids in which the dissipation of the viscous energy is due to the collision of comparatively small molecular species. All gases and most of the liquids and solutions of low molecular weight come into this category.

Exceptional cases are colloidal suspensions and polymeric solutions where the molecular species are relatively large [45]. General properties of Newtonian fluids are [44, 46]

- stress at any point depends upon the instantaneous velocity gradient at the point.

- stress is a linear function of the velocity gradient.
- stress is isotropic when there is no motion.

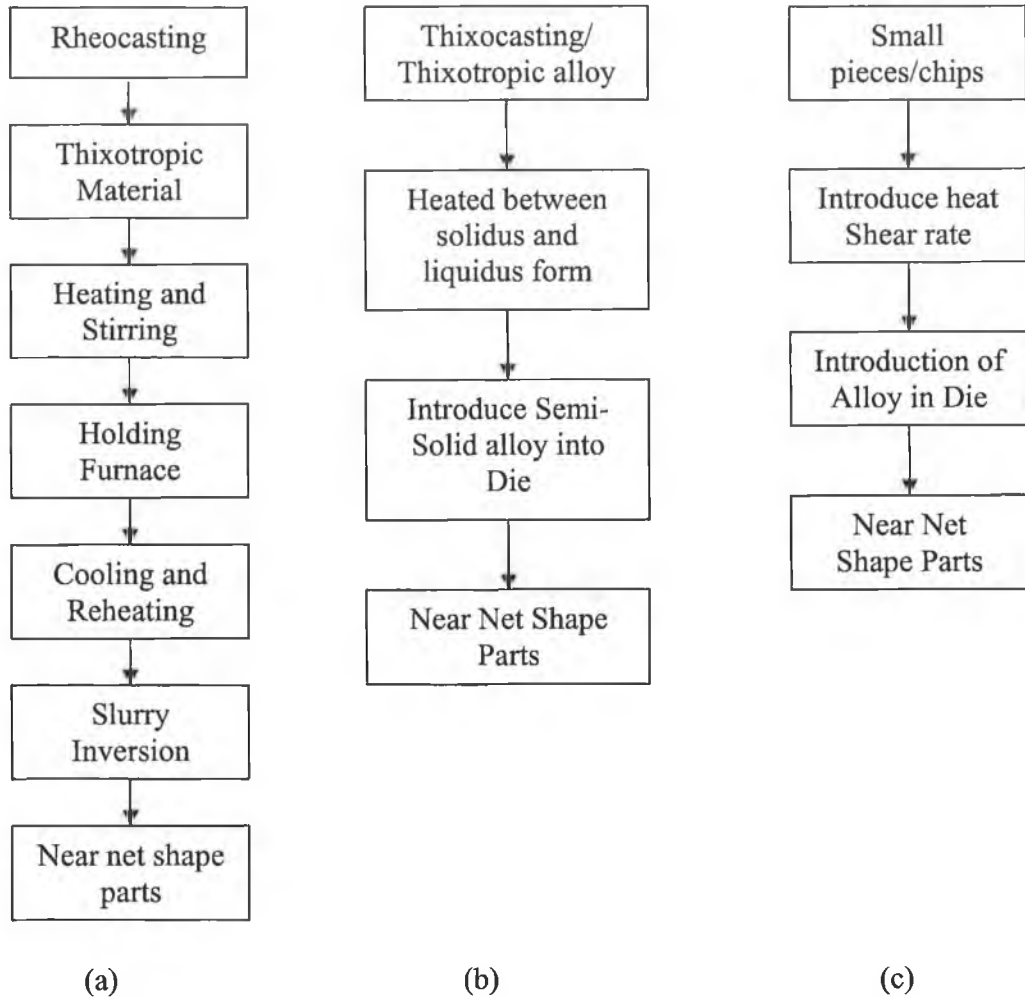


Figure 1.3 Flow chart of the (a) Rheocasting, (b) Thixocasting, And (c) Thixoforging processes [7].

Viscosity is the quantity that describes a fluid resistance to flow and is defined as the internal friction of a fluid. The dynamic viscosity of the Newtonian fluids is given by

$$\eta = \frac{\tau}{\dot{\gamma}} \quad (1).$$

$\eta$  is viscosity of material,  $\dot{\gamma}$  is the shear rate and  $\tau$  is the shear stress , Kinematic viscosity,  $\nu$ , is defined as the ratio of viscosity  $\eta$  of a substance to its density,  $\rho$ , and is given by

$$\nu = \eta / \rho \quad (2)$$

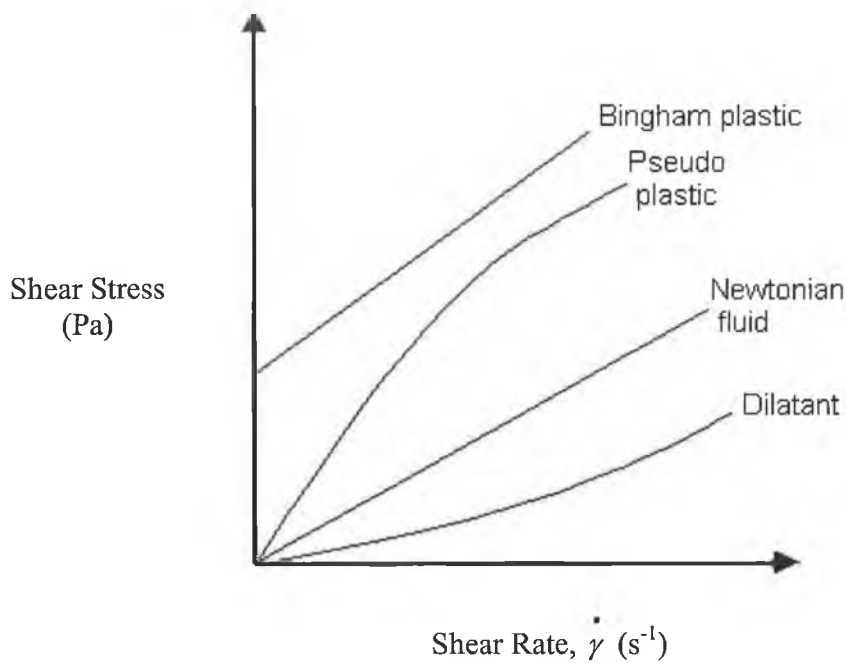


Figure 1.4 Different types of fluid behaviour [37].

Viscosity is a rheological property of material which presents itself when the velocity gradient between different layers of the material is observed. It helps in understanding the hydrodynamics and kinetics of reaction in metal casting, to estimate a solid fraction, predict the important transport coefficients like diffusibility, thermal conductivity and surface tension of the material. The study of viscosity is an important problem in SSM for the structure analysis and processes. During the viscous flow the mechanical energy is transferred to heat energy.

Non-Newtonian fluids are the fluids for which the viscosity is not constant. In these fluids viscosity varies with time and depends upon the shear rate or shear stress at which it is measured [44 and 47]. The viscosities of some substances are given in table 1.2.

Substance	Viscosity, $\eta$ ( mPa.s)
Air	$10^{-2}$
Benzene	0.65
Molten sodium chloride (1173 K)	1.01
Water	1.0
Ethyl alcohol	1.20
Mercury ( 293K)	1.55
Molten lead (673 K)	2.33
Ethylene glycol ( 673 K)	20
Olive oil	100
Caster oil	600
100% Glycerine ( 293 K)	1500
Honey	$10^4$
Bitumen	$10^{11}$
Molten glass	$10^{15}$

Table: 1.2 Viscosity of substances at room temperature, some which are measured at other temperatures are indicated [48, 49].

For non-Newtonian fluids the equation of the stress is given by

$$\tau = K \dot{\gamma}^n \quad (3).$$

This called as the power law equation [44]. It is used for fluids exhibiting no plastic behaviour. When a material exhibits plastic behaviour, a yield stress term can be added to this. This then give the well known Herschel-Bulkley equation.

$$\tau = \tau_0 + K \dot{\gamma}^n \quad (4).$$

$$\eta = \frac{\tau - \tau_0}{\dot{\gamma}} = K \dot{\gamma}^{n-1} \quad (5).$$

K is called consistency index and n is the power law index. The fluid behaviour is represented by the term K and n. For greater values of K, fluid is more viscous. Newtonian fluid can be viewed as a special case of Equation 3 when exponential n is equal to 1.0 and the term K becomes the viscosity. The term n is actually an indication of non-Newtonian behaviour [44]. The pseudoplasticity of the material is evident for values of n less than one whereas shear thickening behaviour occurs for values of n greater than one [49]. Examples of this type of fluids are mud, polymer solution, natural gums and blood.

Another type of fluid in which no yield stress is observed but for which the viscosity increases with the increase in the shear rate or velocity gradient. They are called dilatant fluids or shear thickening. For the dilatant fluids, the power law exponent is greater than one. Due to the fact that the viscosity is not constant for pseudoplastic and dilatant fluids, the viscosities of these fluids is often referred to as apparent viscosity. Time dependent fluids also have a viscosity that varies with time, which is therefore also referred to as apparent viscosity. The behaviour of these fluids is shown in fig: 1.4 [58-63].

## 1.6 Factors effecting viscosity

Many different factors affect the viscosity of fluids. The effect of the main three, temperature, pressure, and shear rate, are described below [39 and 50].

### 1.6.1 Effect of temperature

Temperature plays a very important role in processing of semi-solid metal and alloys.

With increasing temperature the viscosity of the fluid decreases. Temperature provides the activation energy to the molecules of the fluid that causes motion in them. Motion occurs when the fluid molecules slide past each other and the ease of flow depend upon the molecular chain and the force of attraction between the molecules. Viscosity and



temperature of the Newtonian fluid can be related, based on the Arrhenius equation, with the following equation.

$$\eta = A e^{E/RaT} \quad (6)$$

Where  $\eta$  is the coefficient of viscosity,  $E$  is the activation energy,  $A$  is constant,  $R_a$  is the universal gas constant and  $T$  is the absolute temperature.

### 1.6.2 Effect of pressure

Increasing pressure will increase the viscosity of the liquid because the distance between the molecules of the substance is reduced. Viscosity greatly depend upon the free volume which is defined as “the difference between the actual volume and a volume in which such close packaging of molecules occurs that no motion can take place”. The greater the free volume, the more easily will be the motion and hence the lower will be the viscosity.

### 1.6.3 Effect of shear rate

For semi-solid materials, increasing shearing and associated deformation of the material, results in a decrease in the viscosity of the material. With the greater shear rate, for these non-Newtonian, pseudoplastic fluids, the microstructure becomes globular during shearing which helps increase the fluidity of the material and therefore reduce the viscosity [51-53]

## 1.7 Non-Newtonian fluids

Non-Newtonian fluids are those fluids whose flow curve (shear stress versus shear rate) is non-linear or does not pass through the origin, that is where the apparent viscosity, shear stress divided by the shear strain, is not constant at a given temperature and pressure but is dependent upon the flow conditions such as flow geometry, shear stress, shear rate etc and sometimes even on the kinematics history of the fluid element under consideration. For non-Newtonian material, the viscosity of the material either increases or decreases as the strain rate or the rate of flow increases. Some non-Newtonian materials are solutions, melts of high polymers, solid suspensions, emulsions, and foams. In addition polymers of

high molecular weight or chain length such as gel concentrated suspensions of long fibre exhibit elastic as well as non-Newtonian viscous behaviours [54-57].

#### 1.7.1 Time-independent non-Newtonian fluids

This category includes fluids for which the shear stress vs. shear rate curve is not linear and is time independent. They can be sub-divided into fluids, which resist a small shear stress indefinitely, but can easily flow under the action of large shear stresses that surpasses yield stress. These are generally called Bingham fluid or viscoplastic fluids. In these fluids the viscosity is infinite at low stress, and with the increase of the stress to a high value there is decrease in the viscosity with increasing velocity gradients. Examples of these fluids are toothpaste, jellies and some slurries [37].

#### 1.7.2 Time-dependent non-Newtonian fluids

Many real fluids cannot be described by a simple equation which we can apply to time independent fluids. There are some fluids in which the apparent viscosity not only depends on the shear rate but also on the shear time. These can be subdivided into two groups, according as to whether the shear stress decreases or increases with time when the fluid is sheared at a constant rate.

The fluids, in which the viscosity can be decreases with time, are called thixotropic fluids [37]. If a thixotropic material is sheared for a certain period of time, at a constant rate, the structure will be progressively broken down and the apparent viscosity will decrease with time. The rate of shearing depends upon the number of linkages available for the break down. Thixotropy is often a reversible process and after period of no shear, the material structure and viscosity builds up again gradually. It should not be confused with the false-body. True thixotropic material break down completely under the action of high stresses and behave like the true liquids even when the stresses are being removed, until the time as the structure has reformed. False-body materials, on the other hand are those, who do not lose their solid properties entirely and can still exhibit a yield value even though this might be diminished [63]

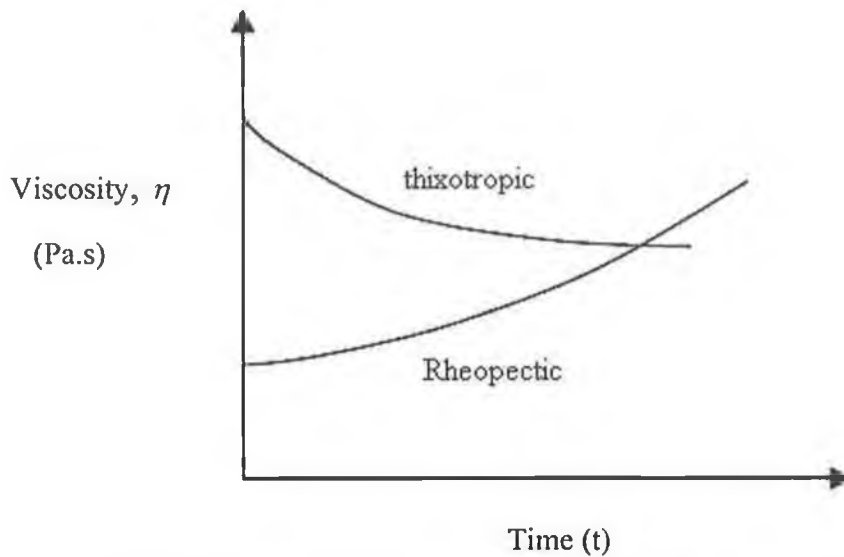


Figure 1.5 Effect of viscosity change for a given shear rate [83]

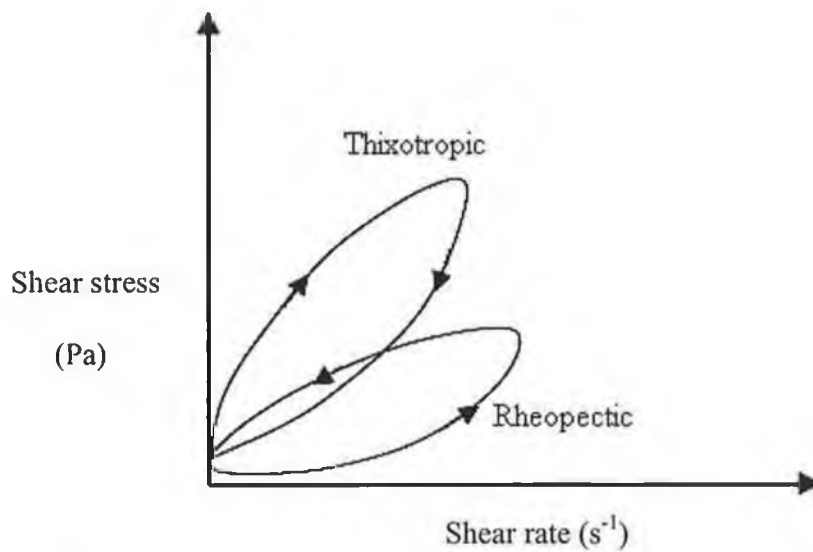


Figure 1.6 Shear stress vs. Shear rate for time dependent fluids [83]

For some fluids, the viscosity can increase with time; these fluids are called rheopectic, the longer the fluid goes under shearing, the higher will be the viscosity. It is a rare kind of material which shows rheopectic behaviours. These materials stiffen upon shaking [39]. Viscosity increase is due to the structure formation in the fluids. Freundlich and Julius Berger [63], by using the 42 per cent gypsum paste in water, mixing it for some

time and found that mixture re-solidify after forty minutes. It was clear in that case that a moderate amount of shear facilitates built up structure, but the large amount of shear destroys it. If we consider the flow of this material in a capillary tube, at a moderate injection pressure, the flow is rapid at first and then decreases as the structure build up. At a high pressure difference, flow is always rapid and does not allow the structure to build up. A lot of work has been done to find out the time dependent viscosity of the materials and the exact process parameters for semi-solid metal processing [63-67]. Fig: 1.5 shows both the rheopectic and thixotropic behaviour of material.

## **1.8 Viscometers**

Mathematical models are commonly used to describe the properties of the materials. Rheology is however a practical science and contemplation alone will not solve all the problems. Some practical aspects need to be considered to solve the problem involved in measurement of the rheological properties of the material. These are the essential properties which are involved in the movement of matter. The strain rate is defined from the fluid flow in a given instrument geometry and the corresponding stresses are the measure of the resistance to flow. The type of equipment suited to generate these flows and determine the rheological data in constitutive equation are called the rheometer or viscometer and the study is called viscometry. These instruments are usually simple and well defined and designed so that there is a controlled shear rate in a single direction. Before describing any instrument specifically, we may need to consider the basic principles it may be used for. The basic principles which all rheometers follow are to provide flow kinematics, preferably one dimensional, in order to determine the shear rate strain accurately, easily and independent of fluid type.

There are different devices used to measure the rheological behaviour of fluids like capillary flow viscometer, rotating and oscillating coaxial cylinder viscometer, rotating and oscillating disk viscometer, rotating and oscillating concentric sphere viscometer, cone and plate viscometer, double cone viscometer, conicylindrical viscometer, oscillating plate viscometer, falling sphere viscometer, parallel plate viscometer [68-70].

Some of them are discussed as in the sections below. Rheometers may be divided in two main categories. The first is associated with the relative motion of between two opposing surfaces of the apparatus, the motion may be tangential in which case the shear is applied (concentric cylinder viscometer), or normal, in which case the material is extended or compressed. In the other type of the viscometer, sample of the fluid is contained within the walls of the tube with open ends; relative movement takes place in the axial part of the sample and that in contact with the wall (capillary viscometer).

### 1.8.1 Concentric cylinder viscometer

This is a rotational type viscometer that can operate continuously at a given shear rate to perform the steady state measurement. It is used to determine and detect the time dependency. It is the most widely used instrument for rheological measurements. Shear rate and shear stress data is required to determine the absolute viscosity. This type of viscometer can be used for almost all the fluids with high or low shear rates.

This type consists of two concentric cylinders of which the inner one rotates. The gap between the two cylinders which is called annulus where we place the fluid under test. The torque on the stationary cylinder and the velocity on the other cylinder are measured to determine the shear rate and shear stress which is needed for the viscosity calculations. Calculating the torque, it is easy to calculate the shear stress at any point with a radius between the two cylinders. By increasing or decreasing the rotating speed of the inner cylinder, the shear rate can be altered. Fig: 1.7 shows a concentric type cylindrical viscometer.

The general equation used to determine the shear rate is given by

$$\dot{\gamma} = \left( \frac{2\omega}{r^2} \right) \left( \frac{r_a^2 r_b^2}{r_b^2 - r_a^2} \right) \approx \frac{r_a \omega}{r_b - r_a} \quad (7)$$

Assuming that  $\dot{\gamma}$  is independent of  $r$  in the narrow gap. Where  $r_a$  and  $r_b$  are the inner and outer cylinder radii respectively,  $r$  is the radius at which the shear rate is measured,  $\omega$  is the angular speed. The shear stress ( $\tau$ ) at the wall of the inner cylinder is given by

$$\tau = \frac{T_a}{2\pi r_a^2 L} \quad (8)$$

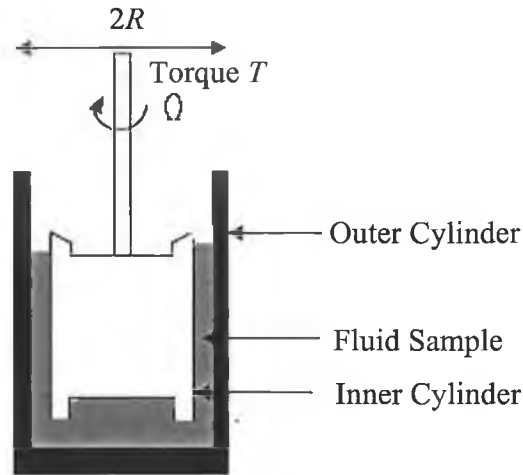


Figure 1.7 Schematic of Concentric Cylinder Viscometer

Where  $T_a$  is the torque,  $r_a$  is the radius of the inner cylinder and  $L$  is the height of the inner cylinder [69 and 71].

### 1.8.2 Cone and plate viscometer

This device is used to measure the shear viscosity of time-independent non-Newtonian fluids. This type gives the uniform rate and direct measurement of the first normal stress drive. Working equation for the shear rate and shear strain can be derived in spherical coordinates. Fig: 1.8 shows the cone and plate viscometer. The fluid is held between a cone and a plate, the plate rotates at an angular frequency " $\omega$ " ( $\text{rads}^{-1}$ ) while the cone remains stationary, torque  $T_a$  on the cone is measured using a transducer. If the cone angle  $\theta$  is small ( $<4^\circ$ ) then shear rate of the liquid is uniform and given by [45 and 69].

The equation for the shear rate is given by

$$\dot{\gamma} = \omega / \tan \theta \quad (9)$$

Shear stress is given as

$$\tau = 3T_a / 2\pi R^3 \quad (10)$$

By putting value in equation 1, we can find the viscosity of the fluid.  $R$  is the radius from the centre to the end of the cone.

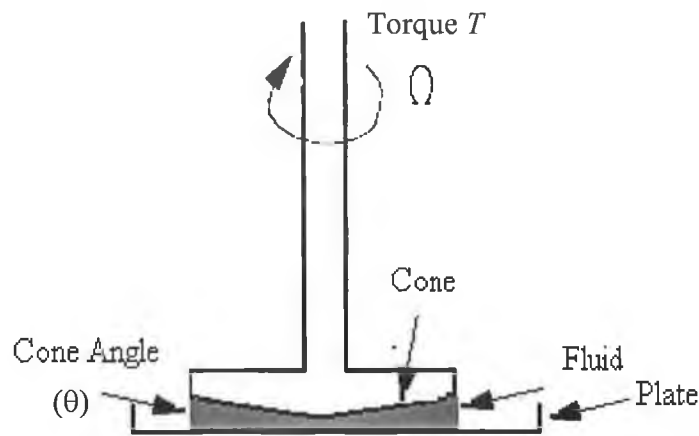


Figure 1.8 Schematic of cone and plate viscometer

### 1.8.3 Parallel plate viscometer

Parallel plate viscometer operate the same way as the cone and plate, except the shear rate is no longer uniform and analysis for the non-Newtonian fluids are more difficult. Fig: 1.9 shows the parallel plate viscometer which consist of a disk rotating in a cylindrical cavity. As both the plates are circular, shear rate will vary at different diameter. However the maximum value can be find out with outer edge of the plate.

For parallel plate viscometer the shear rate is given by [69 and 72].

$$\dot{\gamma} = \frac{r_p \omega}{h} \quad (11)$$

$r_p$  is the radius of the rotating plate and  $h$  is the gap between the plates.

The shear stress is given by

$$\tau = 3T / 2 \pi R^3 \quad (12)$$

This is the same equation as that for the cone and plate viscometer.

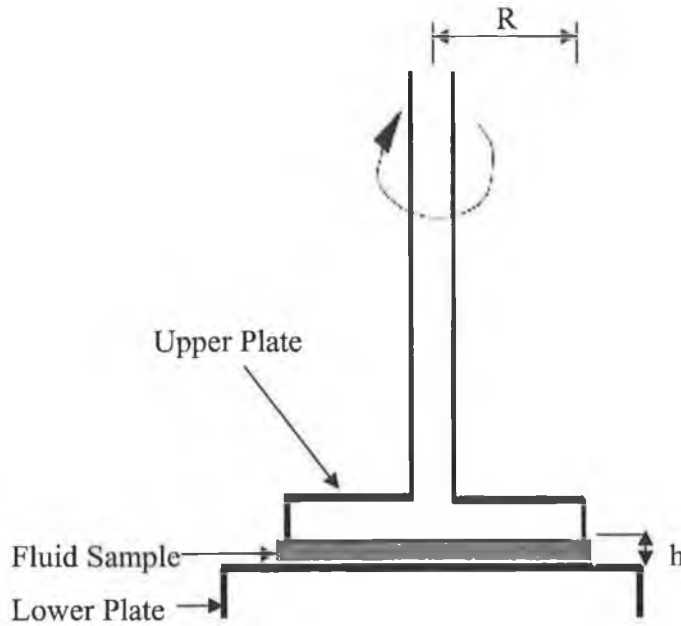


Figure 1.9 Geometry of parallel plate viscometer

#### 1.8.4 Falling sphere viscometer

It is one of the earliest viscometers used to determine the absolute shear viscosity of Newtonian fluids. It is the most simple method. This method is used for fluids with viscosities in the range of  $10^{-3}$  to  $10^5$  Pa. s. Due to the simplicity of design, it is suited to high pressure and high temperature viscosity studies. A sphere is allowed to fall in a viscous liquid through a known distance and its velocity is determined. The restraining force due to the resistance of the falling sphere is given by [69 and 70]. Fig. 1.10 shows the geometry of a falling sphere viscometer.

Equation for the restraining force is given by

$$F = 6 \pi r_s U_t \quad (13)$$

Where  $r_s$  is the radius of the sphere, and  $U_t$  is the terminal velocity of the falling body.

If the sphere has a density  $\rho_2$ , and the density of the fluid is  $\rho_1$ , then by balancing equation 10, with the net force of gravity and buoyancy exerted on a solid sphere is given by



$$\eta = \frac{2gr_s^2(\rho_2 - \rho_1)}{9U_t} \quad (14)$$

Equation 14 shows the relationship between the viscosity of the fluid and terminal velocity of the falling sphere.

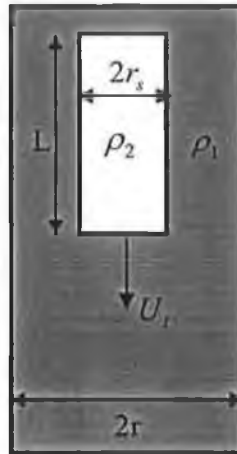


Figure 1.10 Geometry of falling sphere viscometer

## 1.9 Capillary viscometer

Capillary viscometers are generally used because of their inherent features such as simplicity, accuracy, similarities to processes like extrusion die, and that fact that there is no free surface. It has certain advantages like to perform the test under production conditions, fast and reliable results, assist product development formulation, therefore new and better product are available faster. It is normally used in the coating industries to optimise the coating processes in laboratory to reduce the test runs on machines and to avoid low quality goods. It is also used in paper industry, petroleum industry and for basic rheological research [45]. The main use of this viscometer is probably for pharmaceutical solutions, which are normally injected in a needle. It is also used for lubricants or transmission fluids in mechanical equipments. A typical type of capillary viscometer is generally used for measuring the viscosity of an oil of about 200 mPa.s. In

such a viscometer, the sample to be measured is contained in a reservoir and is forced through the capillary or slit of known geometry by means of an external pressure.

However most capillary viscometers require both the measurement of the pressure drop and flow rate in order to determine the viscosity of the fluid. In order to determine the viscosity for a non-Newtonian fluid for a range of different shear rates, it is necessary to drive either the pressure head or change the dimensions of the capillary tube [44 and 80]. In order to determine the viscosity of the fluid, there are many parameters which should be taken into account. Viscosity of the fluid is directly proportional to the density of the fluid, gravitational acceleration, effective hydrostatic head of the liquid, diameter of the tube, and drain time. It is also inversely proportional to the volume of flow during the time and length of the capillary tube [10]. When the pressure drives the fluid in the capillary tube, then the velocity is maximum in the centre, while the velocity gradient or shear rates are maximum at the wall and zero at the centre of flow. For the shear thinning process, the apparent shear rate is less than the true shear rate with the converse applying at the centre of the tube. The flow in the capillary or tube is non-homogeneous and capillary viscometers are restricted to measure unsteady shear functions [48].

Capillary viscometers prove, therefore very useful but there are some drawbacks in their use. Some errors can be introduced during the flow through a capillary tube. These can be the influence of end effects, pressure dependence of viscosity, thixotropy, viscous heating, compressibility and effective fluid slip relative to the wall of the tube and kinetic energy effects etc [73].

A large proportion of fundamental viscosity determination are made using the capillary viscometer, the theory of which is based on the Hagen-Poiseuille law. The equation for use with this equipment is given by

$$\eta = \frac{\Delta P \pi R_c^4}{8L_c Q} \quad (15)$$

$\Delta P$  is the pressure drop along the length of the capillary in Pa,  $R_s$  is the radius of the tube in m,  $L_c$  is the length in m, while  $Q$  is the flow rate,  $m^3/s$ , through the tube. This is the equation for a fluid where the flow is laminar, there is no slip at the wall of the tube, and

the rate of shear depends upon the shear stress at that point. Most fluids with pronounced non-Newtonian behaviour have such high viscosities that their flow is laminar in most of the industrial cases [44].

For pseudo plastic fluid [44], the shear rate and shear stress at the wall is given by

$$\dot{\gamma}_w = \left[ \frac{3n+1}{4n} \right] \left[ \frac{8V_{aver}}{D} \right] \quad (16)$$

$$\dot{\gamma}_w = \frac{4V_{aver}}{R_c} \left( \frac{3}{4} + \frac{1}{4n} \right) \quad (17)$$

$$\dot{\gamma}_w = \frac{4Q}{\pi R_c^3} \left( \frac{3}{4} + \frac{1}{4n} \right) \quad (18)$$

$$\dot{\gamma}_w = \frac{4Q}{\pi R_c^3} \left[ \frac{3}{4} + \frac{1}{4} \left( \frac{d \ln Q}{d \ln \tau_w} \right) \right] \quad (19)$$

$$\tau_w = \frac{\Delta P R_c}{2L} \quad (20)$$

Where  $V_{aver}$  is the average velocity, m/s,  $R_c$  is the radius of the capillary tube, m,  $\tau_w$  is the shear stress at the wall, Pa,  $\dot{\gamma}_w$  is the shear rate at the wall, 1/s. The parameters  $n$  and  $K$  are the flow index (dimensionless) and consistency index, Pa.s<sup>n</sup> respectively. Where  $n = \frac{d \log \tau_w}{d \log \frac{8V}{D}}$  is the slope of the measured  $\log \tau_w - \log \left( \frac{8V}{D} \right)$ . Once the value of  $n$  is

calculated, we can use the equation to find the value of  $K$  from given equation as

$$\log(\Delta P) = n \log(Q) + n \log \left[ \frac{4}{\pi R_c^3} \left( \frac{3}{4} + \frac{1}{4n} \right) \right] + \log(K) - \log \left( \frac{R_c}{2L_c} \right) \quad (21)$$

Then the viscosity is simply calculated as

$$\eta = \frac{\tau_w}{\dot{\gamma}_w} \quad (22)$$

Putting values in Equation 22 from equation 18 and 20, we have

$$\eta = \left( \frac{4n}{3n+1} \right) \left( \frac{\Delta P D^2}{32 L_c V} \right) \quad (23)$$

$$\eta = \left( \frac{4n}{3n+1} \right) \left( \frac{\Delta P D^4}{128 L_c Q} \right) \quad (24)$$

Where the assumptions to derive the above equations cannot be accepted, corrections need to be made to take account of them. A example of a typical glass capillary viscometer is shown in figure 1.11. A defined flow rate can be a achieve with the help of a pump for a constant flow, which in this case consists of a mercury filled stainless steel cylinder, in which a stainless steel piston is forced at a constant rate by a rigidly coupled worm shafts. Various flow rates can be obtained in the capillary by changing the speed of the driving unit and gear combination. The glass capillary is mounted horizontally between the stainless steel entrances and exit chambers [46].

### 1.9.1 Glass capillary viscometer

The simplest and most commonly used viscometer is called an Ostwald viscometer. This viscometer consist of a U shape in which the fluid to be analyse is poured, see figure 1.11. The whole arrangement is placed in thermo stated water bath to reach the measurement temperature. The viscosity of the liquid is measured by sucking the fluid with the help of a vacuum pump on one arm of the tube and then measuring the time it takes to flow back through a capillary of fixed length and radius. The time it takes to travel through the capillary is related to viscosity by the following equation.

$$t = C \eta / \rho \quad (25)$$

$\rho$  is called the density of the liquid,  $t$  is the measure flow time, and  $C$  is a constant which depends upon the precise size and dimension of the U-tube. The higher the viscosity of the fluid, the longer the time it will take to flow through the tube [69]. It is mainly used for the viscosity of Newtonian fluids [74].

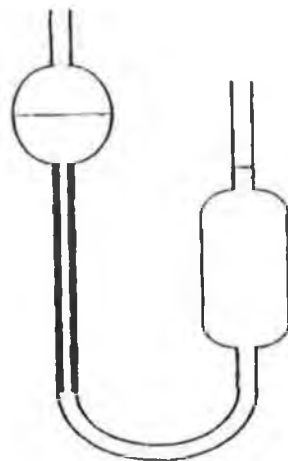


Figure 1.11 Glass capillary viscometer [69]

### 1.9.2 End Effects

One of the largest errors that may arise in capillary viscometer measurements is due to what is known as the end effect. Near the entrance and exit region of the tube, the velocity profile is not constant along the tube, but it is in a state of transitions between the flow configuration inside and outside the tube. The pressure gradient is not constant over these regions. If the flow is from a large reservoir in which the velocity is low, it must be accelerated in the tube entrance region to the final tube velocity. This results in an increased pressure gradient across the region due to the change in momentum and the energy loss as eddies. For viscoelastic fluids there is an additional pressure drop at the entrance due to the elastic or normal stress effect [69]. To reduce this effect, the ratio  $\frac{L_c}{R_c}$  must be kept as large as possible making it difficult to thermo-regulate the fluid sample [68]. However if the tube is long enough, the pressure drop due to the end effect is a negligible fraction of the total pressure drop. Appropriate tube dimensions are generally

used to effectively eliminate the end effect error. The dimension requirements are most often quoted as those for which the length to diameter ratio is equal to or greater than 100. End effects can however be corrected by determining an equivalent extra length  $L_e$  of the tube which has to be added to the actual length if the total measured “ $\Delta P$ ” was that for an entirely developed region. Consider the pressure gradient due to friction in a fully developed flow in a tube of length  $L_c$ , plus the extra pressure drop due to entrance effect; this is accounted for by including the extra length [68].

$$\frac{\Delta P}{(L_c + L_e)} = \frac{2\tau_w}{R_c} \quad (26)$$

Hence, if several tubes of different  $\frac{L_c}{R_c}$  ratio are used and  $\Delta P$  is plotted against  $\frac{L_c}{R_c}$  for the same value of shear rate in the tube, the plot should be linear, in addition, if the flow has become fully developed within tube, and the intercept at  $\Delta P = 0$  determines  $L_e$ . The intercept on the  $\Delta P$  axis at  $\frac{L_c}{R_c} = 0$  is the pressure drop  $\Delta P$  due to the combined end

effects. Since a different value of  $L_e$  for each value of  $\tau_w$ ,  $\frac{L_c}{R_c}$  can be correlated. This

correction some time called the coquette correction and is usually written in the form

$$L_e = n_1 R \quad (27)$$

But the value of  $n_1$  is variously evaluated. Rayleigh gives 0.824, Scheader, 0.805, and Bond, 0.566. Also to calculate the end effect, a capillary with different diameter, but the same length to diameter ratio should be used [75].

For a capillary of diameter  $D$ , length  $L$ , and pressure drop  $\Delta P$ , the shear rate at the wall is given by [76]

$$\tau_w = \frac{\Delta P D}{4(L_c + L_e D)} \quad (28)$$

$L_e$  is the equivalent associated with end corrections.

### 1.9.3 Kinetic Energy Correction

The liquid entering the capillary is accelerated at the expense of the measured pressure drop; this kinetic energy of the liquid is entirely dissipated as heat at the exit chamber [70]. The amount of this conversion of static pressure to kinetic energy may be expressed as a part of the measured pressure drop by subtracting of this term (kinetic energy correction),  $m\rho Q/8\pi L$  from Eq: 15

$$\eta = \frac{\Delta P \pi R^4}{8LQ} - \frac{m\rho Q}{8\pi L} \quad (29)$$

$m$  is the numerical factor, dimensionless coefficient of order 1 that depends on the flow pattern at the end of the capillary and especially the shape of the capillary ends. The value of  $m$  has been variously evaluated by different authors, see table 1.3

The kinetic energy effect is about 1% according to the British and American specifications and 2% for the German specification [77]. The kinetic energy effect can play a significant role in the determination of the viscosity, and accurate determination will lead to the accurate viscosity and process.

The design and construction of the capillary will be in such a way that it illuminates the jet formulation occurring at the exit. An equal attention to both the inlet and outlet of the capillary should be taken into account to minimise the kinetic energy effect and it can be possible with different experimental procedures with different capillary length and different designing at the inlet and end of the capillary tube.

### 1.9.4 Slip effect

There is a possibility of wall slip in a capillary viscometer. Different authors after studying the capillary viscometer concluded that for different diameters of the capillary will give different result for the same  $\Delta P$  values. Experiments performed on the capillary viscometer shows that the wall slip velocity is directly proportional to the shear stress at the wall and inversely proportional to the diameter of the capillary tube and gives good results.

Author	Value of m
Reynolds	0.50
Hagenbach	0.79
Coutte and Wilberforce	1.00
Boussinesq	1.12
Riemann	1.124
Swindells	1.12 – 1.17
Knobbs	1.14
Jacobson	1.25 – 1.55

Table: 1.3 Value of “m”, according to several authors [70]

Thondavadi and Lemlich after performing experiments on foam for a 3m long capillary and with different diameters varying from 1-5 cm concluded that the slip velocity also depends upon the material of the capillary tube. They found no slip for a capillary tube made up of steel. The slip velocity is also found to be due to the nature of the surface of the wall, where a thin film of material can stick to the surface and thickness of this is of significance [78 - 79].

### 1.10 Previous work on semi-solid metal Rheological modelling

A number of attempts have been made to model steady state rheological flow of semi-solid metals [59-61, 64, 84]. Thixotropic behaviour i.e. the time dependence of rheological behaviour for semi-solid flow has been modelled by a number of workers [62, 65-67]. One phase models [10, 25, 51-52] and two phase models for partially solidified material have been investigated previously [85-90]. Work has been conducted on various alloys to determine the changes in viscosity due to the variation in time, shear rate, solid morphology and solid fraction [91, 92].



Data from rheological experiments can help determine what processing parameters should be used such as suitable microstructure, shear thinning response, time dependency, controlled ram speed and solid fraction are the important parameters need to be considered and find out for investigation of the process.

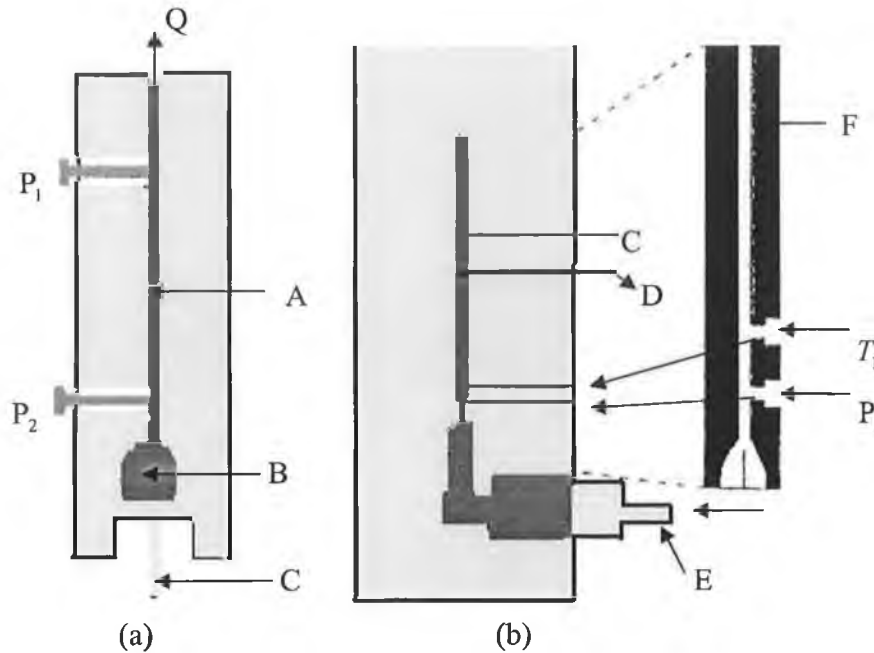
Many attempts have been made to determine the shear rate effect of the viscosity with different techniques like parallel plate viscometers, rotating cylinder viscometer, rotating spindles, Couette rheometer, compression test methods used for low shear rate viscosity measurement and capillary tube viscometer for high shear rate viscosity measurements. The sections below cover some of the most relevant previous work.

#### 1.10.1 Bernhard model for investigation of rheology of semi-solid material.

Bernhard et al [93] presented their model with a design, construction and simulation of a modified capillary viscometer. This viscometer can be used for high shear rate and high temperature. For semi-solid metal processing and to measure the viscosity of semi-solid materials. The capillary viscometer that can be adapted to time controlled die casting process with a die machine H 630SC, was used for these experiments. The capillary viscometer was designed in such a manner that a few assumptions could be made in the simulation and construction were that the process was considered to be an isothermal process that is no heat transfer occurring in the process, keeping the capillary temperature close to the billet temperature, the capillary inlet is raised to a temperature to come close to the temperature of the billet in a furnace. Capillaries with different length and material with different diameters were used to record the difference in their records and adiabatic condition in the capillary was exercised.

The construction of the capillary viscometer involved two dies, i.e. the stationary and movable dies. A plunger mechanism was used to push the semi-solid material into the capillary viscometer; two different pressure sensors were used to record the pressure of the liquid at two different appropriate positions to see the pressure difference between these points and a temperature measuring devices that can measure the temperature of the semi-solid metal across the chamber. Figures 1.12 a, and b shows the construction of the capillary viscometer used by Bernhard et al. Before starting the actual experiment, the inlet of the capillary was heated to 500 °C to bring it closer to the temperature of the

billet to prevent pre-mature freezing. The billet was reheated in the vertical induction heating system to a temperature of  $578^{\circ}\text{C}$  before setting it into the die. Different plunger speeds were used to obtain



A, F: Capillary Tubes      E, C: Plunger  
 B & D: Measured material     $P_1, P_2$ : Pressure Sensors  
 Q: Flow Rate                       $T_1$ : Temperature Sensor

Figure 1.12 (a) and (b) show the modified capillary viscometer used in the work of Bernhard et al [93].

different shear rates for different experiments. Apparent viscosity was measured with the change in pressure and plunger velocity during the experiments. MAGMA soft package with numerical filling simulation techniques was used to simulate the flow and experimental results were compared with the simulation results. From some of the experimental results which show that the apparent viscosity decreases with increasing the shear rate with different plunger speed. The change in pressure showed by the two pressure sensors shows an increase in the pressure, possible reason may be the increase in the back flow pressure that's is the resistance to the flow in the narrow capillary tube, and the plunger speed decrease with the increase in the pressure in the capillary tube.

From the experiments they can be concluded that even in a small change in the experimental setup like boundary conditions, temperature of the billet or plunger velocity can affect the whole system and their results. Good experimental results can be obtained if there is a small variation between the temperature of the billet and inlet of the capillary inlet temperature. Variation in the billet temperature should be constant and homogenous though out the billet. Capillary inlet must be changed with the new inner profile to obtain the condition of no slip in the capillary tube. Good results can be obtained with improved simulation modeling to investigate the flow behaviour of the fluid and time calculation should be decrease.

#### 1.10.2 Paradise model for semi-solid metal using industrial capillary viscometer.

Paradies et al [36] performed experiments to develop a new model to provide a benchmark to predict the shear rate history dependent flow response of thixotropic alloys. A capillary type industrial viscometer was used to determine the effect of liquid fraction, piston velocity and die temperature on pressure during the die filling with a rheocast A356 alloy with a prior spheroidal micro structure and to compare Newtonian non-Newtonian and thixotropic viscosity model.

The geometry used for the experiment consists of piston, shot sleeve, a small diameter tube and a reservoir. Two pressure sensor and a thermocouple (T) of type K was used to measure the pressure and temperature in the capillary tube. The first pressure ( $P_0$ ) sensor was placed at a distance of 10 mm from the end of the shot sleeve. Sccond pressure sensor ( $P_L$ ) at the end of the tube i.e. final pressure in the tube considered as the atmospheric pressure. The diameter of the shot sleeve is 78 mm with a length of 206 mm, while the capillary is 350 mm long and 10 mm in diameter. Figure 1.13 shows the capillary viscometer used to measure the viscosity of semi-solid A356 for Paradies work.

The model developed was for a liquid fraction of 20% to 40%. The experiments performed for a laminar flow of an incompressible, steady state, isothermal Newtonian fluid and power law fluid to solve the exact momentum equation with the assumption of no slip at the wall and ignoring the losses at the entrance and exit boundary conditions were used.

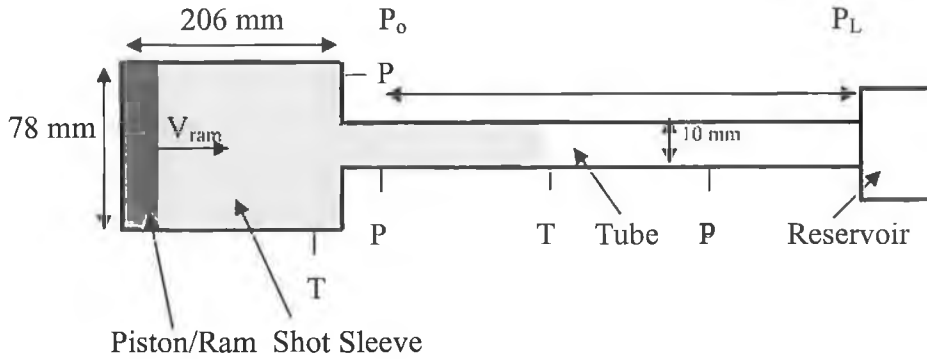


Figure 1.13: Die geometry used for experiments and simulation by Paradies et al [36]

The boundary conditions used were the constant piston velocity, heat transfer rate in shot sleeve and the tube, atmospheric pressure in the reservoir and constant exterior temperature of the die using ProCast<sup>TM</sup> software with finite element analysis solving fluid flow and heat transfer equations, with an axisymmetric flow in the tube was assumed. For simulation, die and billet temperature were assumed to be homogenous and were set at the process temperature. Power law viscosity model is defined by the following equation

$$\tau_{rz} = K \left[ \frac{dv_z}{dr} \right]^{n-1} \frac{dv_z}{dr} \quad (30)$$

$\tau_{rz}$  is the shear rate,  $\frac{dv_z}{dr}$  is the shear rate,  $r$  and  $z$  shows the radial and axial coordinate

respectively.  $K \left[ \frac{dv_z}{dr} \right]^{n-1}$  is the term used for the apparent viscosity in case of Newtonian

fluids and equal to unity.  $K$  and  $n$  are constant used for shear rate thickening and thinning.

Shear stress equation can be given as

$$\tau_{rz} = \frac{P_o - P_L}{2L} \times r_c \quad (31)$$

Where  $P_o - P_L$  shows the change in pressure between the two points,  $L_c$  is the total length of the capillary, and  $r$  is the distance at which the shear rate is apply from the wall

in the capillary. Velocity in the axial direction can be find out with the following equation by putting the value of  $\tau_{rz}$  in equation (30) from equation (31) and after integration is given by

$$v_z = \left( \frac{nR}{n+1} \right) \left[ \frac{P_o - P_L}{2KL_c} \right]^{\frac{1}{n}} \left[ 1 - \left( \frac{r_c}{R_c} \right)^{\frac{n+1}{n}} \right] \quad (32)$$

Where  $R_c$  is the radius of the tube By integrating the velocity over the entire cross-section and dividing by the cross-sectional area, average velocity for the power law in the tube can be find out by the equation

$$V_{ram} \frac{A_{shotsleeve}}{A_{tube}} = V_{tube} = \frac{\int_0^{2\pi} \int_0^{R_c} v_z r_c dr_c d\theta}{\int_0^{2\pi} \int_0^{R_c} r dr_c d\theta} = \frac{nR_c}{3n+1} \left[ \frac{(P_o - P_L)R_c}{2KL} \right]^{\frac{1}{n}} \quad (33)$$

The Hagen-Poiseuille can be obtained for putting  $K = \mu$ ,  $n = 1$  in equation (32). If the value of  $n$  and  $K$  are known, the apparent viscosity can be calculated form equation (33) for a given change of pressure.

Heat transfer at the surface of the wall was found to be negligibly small during the experiment with a constant ram velocity but increase significantly at the end of the experiment when the velocity of ram is zero showing a possible increase in contact between the surface and material. It shows that the surface is adiabatic for a short period of time for a lubricated die when the alloy flows through the tube. Results from the experiments also showed that the constant ram velocity assumption for simulation seem to be ended prior to the complete filling of the tube causes the increase in pressure while the pressure was constant at the end of the experiment till the velocity start decreasing. Decrease in the velocity can also be caused by the deformation occurring in the shot sleeve to fill it while filling the tube as the radius of the billet is smaller than the radius of the shot sleeve. The shot sleeve must be filled up completely before the material start flowing in the tube. This shows that the steady state assumption of the flow to find the

velocity boundary condition needed to be change and the time dependent model should be develop for the flow of semi-solid material.

The result shows that the apparent viscosity at pressure of 0.2 bars was lower than the apparent viscosity in the literature. Lower pressure than the expected may be a cause of the slip between the semi-solid and wall of the tube as lubricant is used on the wall of the tube showing that no slip wall condition was not adequate to model the pressure variation in the flow of the semi-solid material. Segregation evidence in some of the experiments after metallographic study was found. There was an inconsistency in the decrease of measures pressure with the ram velocity. Pressure at the end when the velocity decreases is greater than expected by simulation (should decrease proportionally with  $V^n$  for a power law fluid) by using a power law coefficient of 0.5. Doubling the velocity will increase the pressure by 40%, but it was not reflected in the experiments and only an increase of 10% in the maximum pressure was achieved. Such kind of models of apparent viscosity fit for the liquid of fraction above 40% and below this limit current correlation is not satisfactory. The experiments show that for a lubricated die, the heat transfer is nearly adiabatic between the die and semi solid meat. The initial simulation was failed to model the important experimental parameters like the pressure with decreasing velocities and the pressure at the realistic velocity.

Additional experiments are required for a slipping coefficient with different diameter of the tube to predict the experimentally determined pressure; additional experiments for increased velocities are required in order to find the increase segregation and to find the velocity boundary condition at the die wall and the time dependent viscosity. Table No: 1.4 shows the properties of the material used during the experiment.

Alloy A356 at 577 °C	
Heat Capacity	$3.05 \times 10^3 \text{ k Jm}^{-3}\text{K}^{-1}$
Density	$2.685 \times 10^3 \text{ kgm}^{-3}$
Thermal conductivity	$145 \text{ Wm}^{-1}\text{K}^{-1}$

Table No: 1.4 Properties of A356 alloy for the experiment by paradise et al [36].

### 1.10.3 Nohn Model

Nohn et al. [94] developed another model to investigate the flow in the capillary tube viscometer of semi-solid metal. They develop both the simulation and experimental models to find out the viscosity and the material properties of the alloy A356 in the semi-solid state through a servo hydraulic forming press machine. In the model it was assumed that material properties strongly depend upon the filling velocity, shear rate and temperature and are important factors for simulation input. While pressure exerted during the process was found out during the experiments and used to find the material properties by extruding the semi-solid A356 alloy. The MAGMA soft package was used for the simulation of various parts development. MAGMA soft uses the basic continuity, energy and momentum equations with a single phase approach. Ostwald-de Waele model was used to determine the viscosity of the semi-solid alloy with temperature dependent coefficient  $m$  and shear rate index  $n$  for the shear rate thinning materials.

$$\eta = \left( T \cdot \dot{\gamma} \right) = \rho \cdot m \cdot \dot{\gamma}^{n-1} \quad (34)$$

$$\dot{\gamma} = \sqrt{\frac{1}{2} S_2} = \sqrt{\frac{1}{2} \delta_{ij} \delta_{ji}} \quad (35)$$

$$\delta_{ij} = \left[ \frac{\delta v_i}{\delta x_j} + \frac{\delta v_j}{\delta x_i} \right] \quad (36)$$

Where  $S_2$  is the second invariant of deformation tensor  $\delta_{ij}$ . Steady state behaviour was neglected because of the small shot time. During their experiments they found that shear rate, temperature and solid fraction curve  $f_s$  are important parameters for the viscosity variation during the cooling and solidification during the filling of capillary. The solid fraction curve tried to find out with detail experiments for alloy A356 by measuring the heat energy contents used during the reheating of the billet to semi-solid state.

Servo hydraulic forming press was used to perform the experiments to find the viscosity of A356 alloy. The geometry consist of a plunger, shot chamber, heating elements around the shot chamber and capillary, small capillary of 10 mm diameter and a collecting basin

at the end of the assembly. The billet was 76 mm in diameter. The reheated billet was pressed with the help of a plunger through a capillary and into the collecting basin at the end of the process. A pressure sensor connecting to the top of the plunger was used to measure the pressure served in the process. Figure 1.14 shows construction of viscometer used for Nohn work.

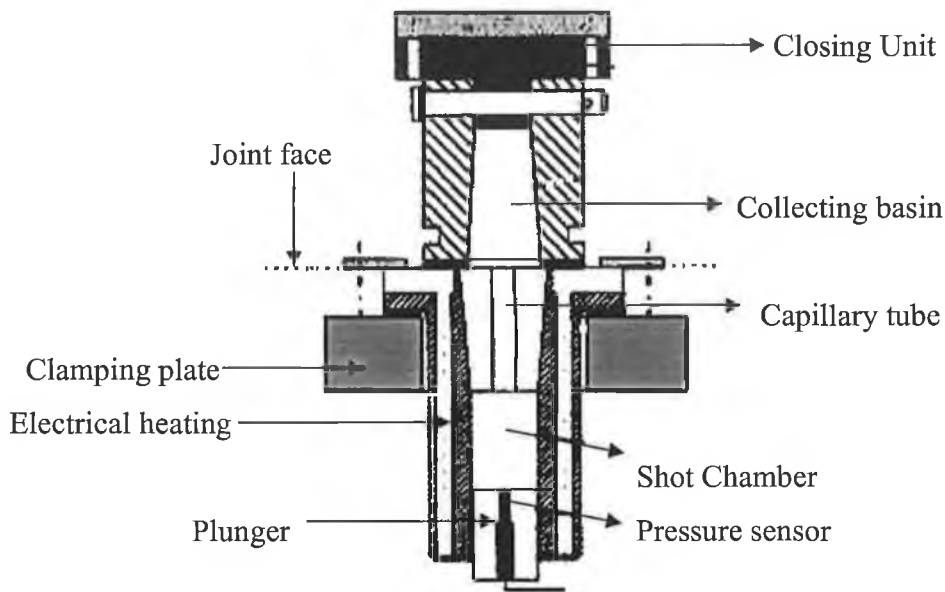


Figure 1.14 shows the capillary viscometer used for Nohn et al work [94]

Analysis of the flow in the tube was carried out by mean of the momentum balance on the cylindrical shell for the laminar fluid flow, which is given by

$$2\pi r L \tau_{rz} \Big|_r^{r+\Delta r} = 2\pi r \Delta r_c (p + \rho g z) \Big|_0^L \quad (37)$$

Velocity in the centre of the tube is maximum and minimum and the wall of the tube, therefore average velocity can be calculated at a half of maximum for the half cylindrical shell. Viscous stress increase with the wall of the tube linearly with radius independent of material rheology. This enable to use the famous Hagen-Poiseuille equation for the viscosity calculation and the volumetric flow Q.



$$\tau_{rz} = \left( \frac{P_L - P_O}{2L_c} + \rho g \right) r_c \quad (38)$$

$$\tau = \eta \frac{dv_z}{dr} \quad (39)$$

$$Q = \pi R_c^2 \bar{v}_z = \frac{\pi R_c^4}{8\eta L_c} (P_O - P_L) \quad (40)$$

$$D_{app} = \frac{4Q}{\pi R_c^3} \quad (41)$$

Equation 40 and 41 can be used to determine the apparent viscosity and shear rate as Newtonian equation were used to find non-Newtonian properties. The experiments were performed with a constant plunger velocity for four different inductive reheated billets. Experiments consist of three steps. Shot sleeve has a larger diameter than the billet prepared for these experiments, deformation of the billet will first occur in the shot sleeve, followed by an increase in the linear pressure while filling the capillary and ended up with the filling of basin a when stationary state is reached. Viscosity as a function of shear rate and temperature was taken at every point during the experiment with strong shear thinning behaviour. Simulation results are helpful to find out the viscosity data field for each velocity at different temperature as the filling velocity strongly depend upon viscosity. From the experiment it was concluded that if the material properties are used as fitting parameter, then we can achieve good agreement between the experiment and simulations. Good shear rate agreement between the experiment and simulation, but the injection pressure curve could not be calculated, indicated that time response must be included in the simulation. Also indicate that in single phase model, the movement of solid particles and liquid fraction can underestimate the pressure results.

#### 1.10.4 Orgeas Model

Orgeas et al. [95] performed simulation of the semi-solid material with PLCO model with one phase flow i.e. homogenous flow for two phases with and without the parabolic shaft inserted in the capillary tube. Figure 1.15 shows the geometry used for this work.

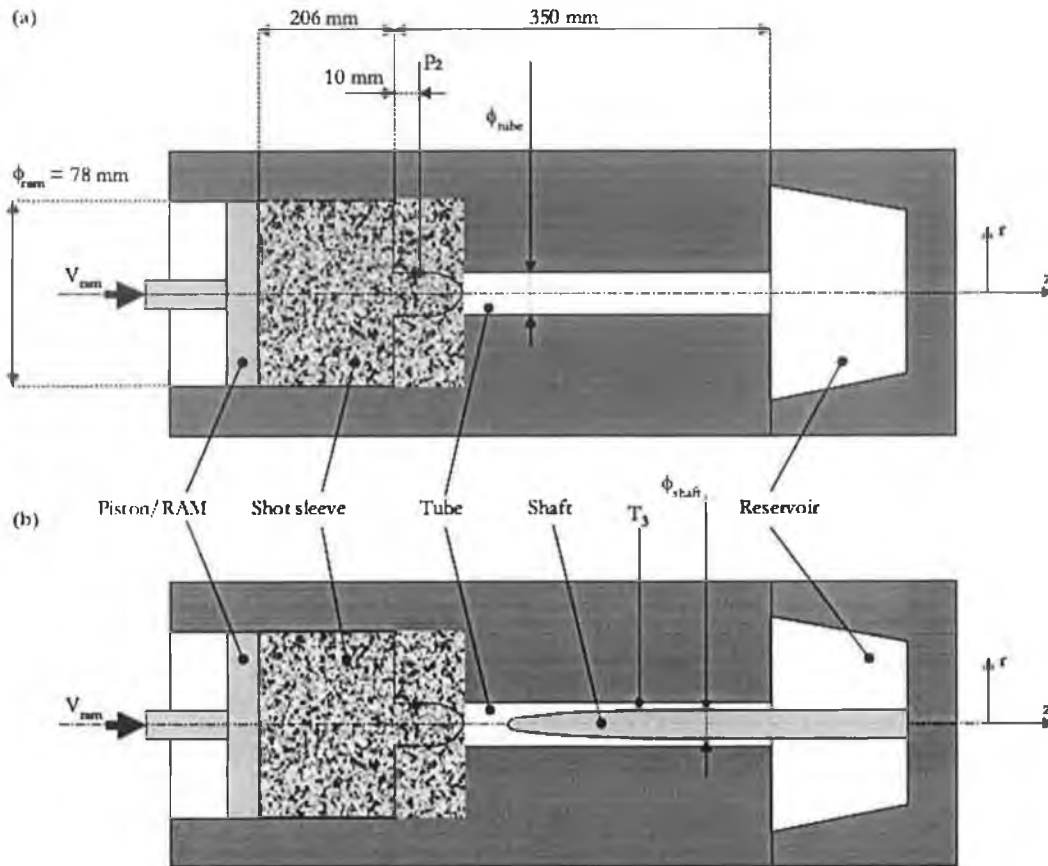


Figure: 1.15 (a) and (b) shows the rig geometries used in the work of L. Orgeas et al [95]

Different process parameters and boundary conditions were used to simulate the flow. This model can be used theoretically for solid fraction range of 0-1. Assumption made for the model was the incompressible flow of purely viscous isotropic nature material, with commercial finite element code ProCast™. The differential equation for mass balance, momentum balance and energy balance can be solved for each element. Viscosity of the semi-solid can be found with the help of the following power law modified equation.

$$\mu = \mu_o \left( \frac{\dot{\gamma}}{\dot{\gamma}_c} \right)^{n-1} \quad \text{if } \dot{\gamma} \geq \dot{\gamma}_c \quad (42)$$

$$\mu = \mu_o \left( \frac{\dot{\gamma}_0}{\dot{\gamma}_c} \right)^{n-1} \quad \text{if } \dot{\gamma} < \dot{\gamma}_c \quad (43)$$

Where  $\mu_0$  temperature dependent viscosity at a shear rate  $\dot{\gamma}_C$ ,  $n$  is the shear thinning sensitivity coefficient,  $\dot{\gamma}_0$  (largest shear rate) is the shear rate cut-off use to improve the convergence of the finite element system, and depending mainly on the geometry and mechanical boundary conditions. Viscosity strongly depends upon the temperature of the billet and solid fraction, is interrelated with solid fraction ( $f_s$ ) and  $n$  given in the equation as

$$\mu_0 = \mu_{liquid} \exp(B f_s) \quad (44)$$

$$n = \frac{1 - n_{min}}{2} \left[ 1 - \tanh\left(\frac{2\alpha(f_s - f_{s,0})}{1 - n_{min}}\right) \right] + n_{min} \quad (45)$$

$$\dot{\gamma}_0 = x \left( \frac{\phi_{shotsleeve}}{\phi_{tube}} \right)^\beta \frac{v_{ram,0}}{\phi_{tube}} \quad (46)$$

Where B is the parameter depending on the microstructure of SSM, and dictates the dependence of viscosity on the solid fraction, h is the heat transfer coefficient depends upon the position, local pressure and volume fraction of solid and  $x, \beta$  can be obtained from the simulation calculations. The shaft experiment was performed to determine the constitutive parameter B in Eq: 44.

The pressure  $p_2$  decrease with the decrease of B. From the set of experiment performed either with or without shaft, it can be concluded that process is not isothermal even for a short injection time (<1sec). Therefore thermal effects are important to be considered for SSM flow. From the results show that the deformation is fast and heterogeneous. For rheological behaviour of SSM flow, mechanical behaviour the boundary condition is important i.e. the free slip considered due to the liquid metal on SS interface acting as a perfect lubricant should be modelled accurately, but for laboratory consideration, the no slip velocity for isothermal process is valuable. The cut-off value  $\dot{\gamma}_0$  should be position dependent of the particle along the stream lines, i.e. any variation in the viscosity should

be taken into account along with the stream lines. Table No: 1.5 shows the thermo physical and rheological properties of alloy A356 for the experiments.

Density, $\rho$ at T = 560 and 615 °C	2580 kgm <sup>-3</sup> and 2380 kgm <sup>-3</sup>
Specific latent heat of fusion, L	389000 Jkg <sup>-1</sup>
Specific heat, $C_p$	900 Jkg <sup>-1</sup> K <sup>-1</sup>
Thermal conductivity, k	150 W m <sup>-1</sup> K <sup>-1</sup>
Dynamic viscosity of liquid Al,	1 x 10 <sup>-3</sup> Pa.s
Minimum shear rate sensitivity, $n_{\min}$	0.25
Critical fraction of solid, $f_{s,0}$	0.35
Parameter, $\alpha$	2.5
Parameter, B	22
Parameter, $\beta$	2.34
Parameter, $x$	

Table No: 1.5 Physical properties of alloy A356 and parameters used by L. Orgeas et al.

#### 1.10.5 Afrath Model

Afrath et al. [96] Develop a new experimental set for processing the semi-solid metal through a capillary viscometer with a high pressure die casting machine to determine the shear rate variation along with the pressure variation. Both the vertical and horizontal type mechanism of slot capillary was used. The capillary was of rectangular nature with different width and height. Figure 1.16 a & b shows the geometry of capillary viscometer both in rectangular and vertical positions. The alloy used for the experiment were Sn-15%Pb and aluminium alloy with the conditions close enough to real semi-solid metal forming process for the experiments. The experiments involves both the high temperature and low temperature model alloys. This model was an attempt to obtain the rheological data for thixoforming operation to develop a two phase numerical simulation model.

A capillary of rectangular cross-section was used to extrude the semi-solid metal slurry through it. A simple equation for flow rate is given by

$$Q = V_{aver} . H . W \quad (47)$$

Where  $Q$ ,  $V_{aver}$ ,  $H$  and  $W$  is flow rate, average velocity, height and width of the capillary tube. Apparent shear rate at the wall of the capillary can be found with equation

$$\gamma_{ap} = \frac{6Q}{W.H^2} \quad (48)$$

$\gamma_{ap}$  is the apparent shear rate. For non-Newtonian metal flow the representative shear rate and viscosity is given by

$$\gamma_{rep} = \gamma_{ap} \frac{\pi}{4} \quad (49)$$

$$\eta_{rep} = \frac{\tau_w}{\gamma_{rep}} \quad (50)$$

An H 630 SC high pressure die-casting machine with two piezoelectric type pressure sensors (ranges 0-200 MPa) installed along the length to evaluate the viscosities of semi solid alloys of Sn15%Pb and aluminium. The assembly consists of plunger used to push the semi-solid metal in two the ingate. Two movable dies and a fix die halves with two pressure sensor and thermocouples to find the pressure and temperature at two different points. The change in pressure was used to find the viscosity of semi-solid metal. The pressure drop and the flow rate are inversely proportional to each other shown in the equations. For isothermal conditions during the experiments for alloy Sn15%Pb alloy, the vertical capillary viscometer was heated to a temperature of 350 °C . As the temperature of the vertical capillary is limited to 350 °C , it cannot be used for a range greater than this limit for rheological measurement of semi-solid material. For the pressure time curve, a quasi-stationary flow is assumed, despite the downward drift signaled by the first pressure sensor near the ingate. Three inches diameter billet with a length of 160 mm heated in convection furnace were used for these isothermal experiments. The solid fraction set was taken from the phase fraction diagram based on Scheil equation. For the

first set of experiment, a temperature of  $186^{\circ}\text{C}$  with a solid fraction of 0.6 with a slurry flow velocity of 2-7 m/sec, show variation in shear rate between 1800 and 9200  $\text{s}^{-1}$

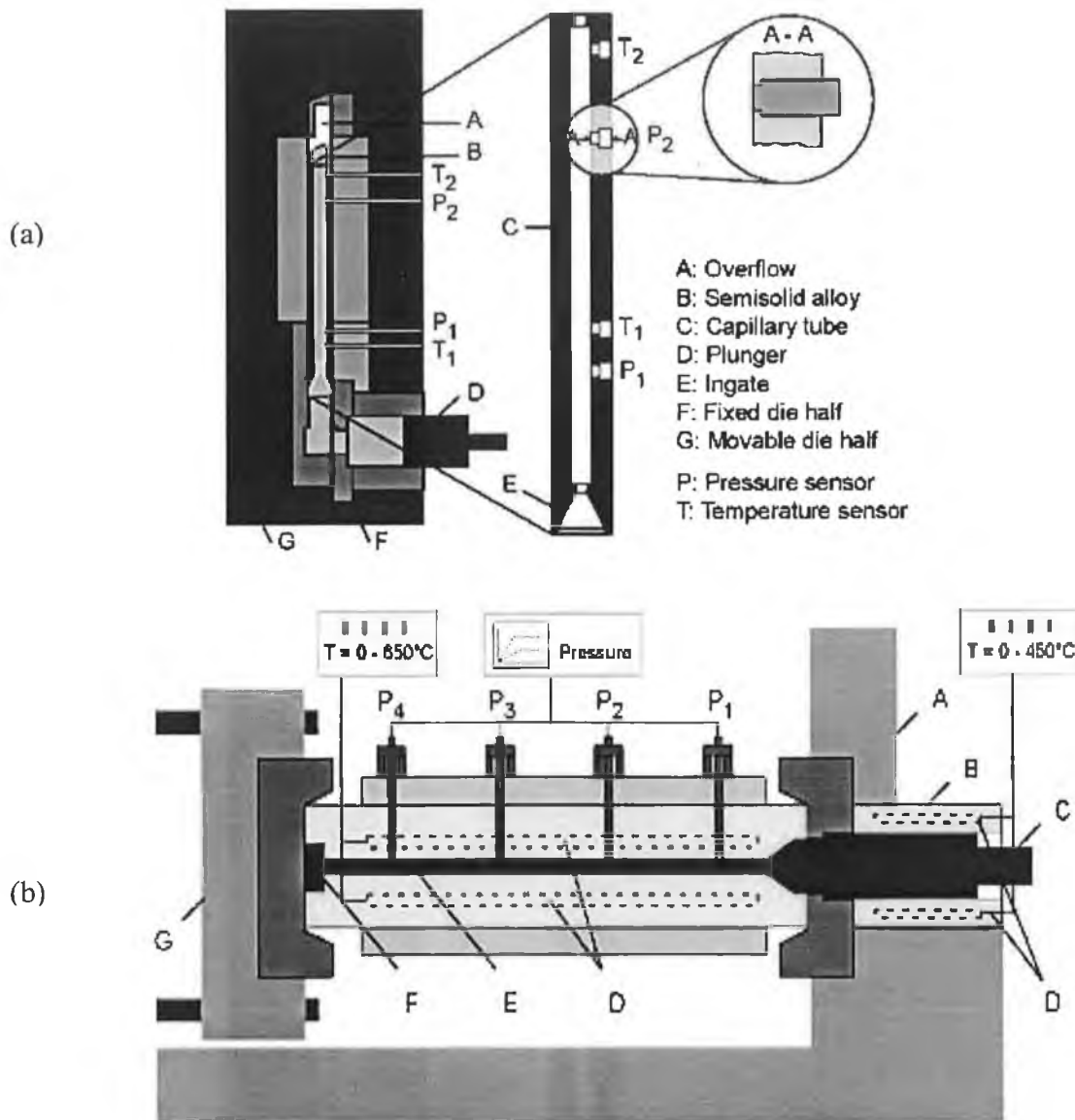


Figure 1.16 (a) Vertical and (b) horizontal capillary viscometers used by Afrath et al [96].

A high temperature horizontal capillary viscometer is designed for high melting alloy like aluminium and magnesium to measure the rheological properties at high temperature up to  $650^{\circ}\text{C}$ . A heating system was provided that surrounded the viscometer to keep it at a

certain temperature to stop any kind of solidification inside the system during the experiment and ensure the continuous flow with a short set up time. The shot sleeve temperature was kept at 450 °C while the capillary temperature was kept at 650 °C with the help of heating cartridges. Four highly sensitivity force sensor for load transmission are connected to pressure sensors due to high sensitivity were provided for pressure sensing mounted on the water cooled rack on the top of the assembly because of the limited maximum temperature.. The semi-solid is introduced in the shot chamber pushed in through plunger in capillary tube, after filling the tube, some of the metal over flows. The pressure sensor will measure any pressure drop or non-linearity in the system.

Experiments were performed with A356 alloy with a 3 inches diameter and 160 mm long billet with a solid fraction of 0.4 and 0.35 at 854 K and 858 K respectively at a velocity of 1.4 to 3.55 ms<sup>-1</sup>, corresponding to a variance in shear rate between 1300 and 3200 s<sup>-1</sup>.

These experiments can show the flow characteristic of semi-solid material at different experimental conditions. Flow characteristic of magnesium alloy AZ91 with solid fraction 0.5 in the semi-solid state was completely different from AlSiMg0.3 alloy, showing no specific characteristic or flow path after removing the solidified sample from the capillary tube.

#### 1.10.6 Figueredo Model

Figueredo et al. [97] designed and built a parallel plate viscometer using different geometries to measure the viscosity of semi-solid material at high shear rate at transient conditions. Figure 1.15 shows the geometry of parallel plate viscometer used in this work. Aluminium alloy A357 was used for different experiments with a billet diameter of 75 mm and length of 100 mm in a step wise manner. A high density graphite crucible with inner diameter of 83 mm was used to heat 200 mg of semi-solid slurry with induction coil controlled with close loop temperature controller for ten minutes with a power source of 20 kW in a vacuum chamber. On the inner side of the crucible, a thermocouple protected with quartz sheeting is attached to measure and control the temperature for the process. Chamber pressure was kept at 10<sup>-1</sup> torr to minimize the oxidation. The parallel plate disk used for the experiment was 30 mm diameter made of high density graphite material. The lower plate was fixed while the upper plate can be

moved up and down selecting the range for the experiments. Both the gap and the angular velocity was changed and adjusted sourcing the change in the viscosity of material as viscosity depends upon the angular velocity and gap between the plates. Lower plate surface was made rough to minimize the slippage. The maximum angular velocity the D.C motor can produce is 2500 rev/min for the experiment which can be controlled with a controller with variable rate speeds. A torque sensor is applied to measure the value of torque placed between the D.C motor and rotating plates. Angular velocity is measure with the help of a tachometer provided at the top of the assembly. Data measure from temperature variation, torque, plate separation and angular velocity can be measure with data acquisition system.

For parallel plate, the shear rate can be calculated as

$$\dot{\gamma} = \frac{\omega R}{h} \quad (51)$$

$\dot{\gamma}$ ,  $\omega$ ,  $R$ ,  $h$  are the shear rate, angular velocity, radius and plate spacing between the plates respectively. For the geometry the shear stress for the non-Newtonian fluid is given by

$$\tau_R = \frac{M}{2\pi R^3} \left[ 3 + \frac{d \ln M}{d \ln \dot{\gamma}_R} \right] \quad (52)$$

$$\tau_R = \eta \dot{\gamma}_R \quad (53)$$

$$\eta_{app} = \tau_R = \frac{M}{2\pi R^3 \dot{\gamma}_R} \left[ 3 + \frac{d \ln T}{d \ln \dot{\gamma}_R} \right] \quad (54)$$

Where  $T$  is the torque required to rotate the upper plate. Two different types of experiments were performed with different experimental setup. A cylindrical shape billet of 250 cm<sup>3</sup> was introduced in a crucible. The rotating plate was kept just above the surface of the billet, crucible is evacuated and temperature is raised to a semi-solid state



region until volume fraction of 0.5 after 45 sec is observed. the plate is then immersed in the semi-solid liquid to an extent minimizing the gap between the plate to 12 mm and run for a few rpm. After 5 min when the billet become homogenous, shearing is then start at a rate of  $400 \text{ s}^{-1}$  for 100 sec, followed by an increase in the shear rate by decreasing the gap between the plate from 12 mm to 4 mm for 20sec to 30 sec. Results shows that by stepwise increase in the shear rate (either by decreasing the gap or increasing angular velocity) stepwise decrease in the viscosity. Resulted sudden increase of the shear rate produces a sudden decrease in the viscosity followed by a gradual increase corresponding. to restoration of the structure under the new shear rate. Equation 52 and 54 cannot be used with the first experimental method.

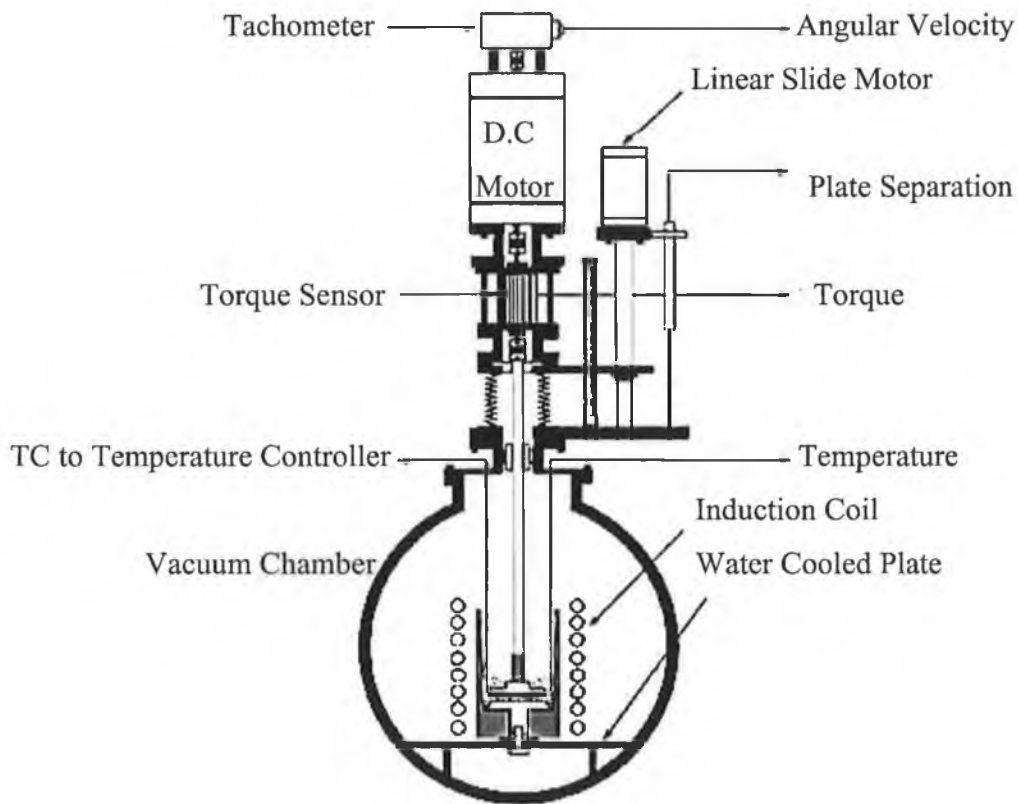


Figure: 1.17 Schematic View of parallel plate viscometer used by Figueredo at el [97].

In the second type, a disk of  $75 \text{ cm}^3$  was loaded in the crucible keeping the rotating plate above the surface as in the first experiment, evacuating and heating is performed to

desirable homogenous and sample temperature (semi-solid state) for 15 min. rotating plate is then lower down to touch the surface of the material and start rotating with a constant rotating speed for 100 sec to obtain a constant torque. The decreasing the gap between the plate to 6 mm and either increasing or decreasing the angular velocity shows a variation in viscosity is observed. Viscosity values were also calculated from the above equation. Some correction needed to be added to the equation which can be smaller with a larger diameter crucible to the plates.

Experimental results shows that the viscosity of the slurry mainly depends on the volume of fraction, shear rate and holding temperature. Shear thinning behaviour was observed for both experiments for different solid fraction and shear rate. Shear thickening behaviour could not be observed during any experiment. The results disagree with the previous experiment performed on the alloy Sn-Pb for the same solid fraction and shear rate. More detail experiment need to be done for transition time as low as 200 ms and for larger shear rate amplitude.

#### 1.10.7 Braccini Model

Braccini et al. [98] investigated the rheological behaviour both experimentally and theoretically of semi-solid alloy Al-8wt %Cu with a couette type rheometer. Solid fraction and solid morphology both are the important parameters for the rheology of the material in the mushy zone. Hot tearing problems can be decreases with grain refinements.

Two alloys of Al-8wt %Cu, refined and unrefined grain structure was used in the experiments within temperature range of 550°C and 587°C with a fraction solid of 0.70.

The couette rheometer consists of two cylinders, i.e. an inner cylinder (stationary) and an outer cylinder (rotating). The outer cylinder acts as a container for the alloy located in between the two cylinders in the liquid state and brings to semi-solid state of desired temperature within the container with a cooling rate of 20 K min<sup>-1</sup>, held at that temperature for 3 min. the alloy is then subjected to a shear rate. Two thermocouples are attached to the inner and outer cylinder to measure the temperature changes in the experiment. Torque transducer measure the torque through the semi-solid alloy attached to the inner cylinder. Grooves of 1 mm length x 0.5 mm height were machine to avoid the

slippage at the interface. Stain steel cylinders surfaces were oxidized and coated with AQUAGEL™ to prevent corrosion. Tangential velocity for Newtonian fluid can be written in Navier-stroke equation can be written as

$$v_{\theta}(r) = \frac{\omega}{R_e^2 - R_i^2} \left( R_e^2 r - \frac{R_e^2 R_i^2}{r} \right) \quad (55)$$

$\omega, R_e, R_i$  are the outer cylinder velocity, radii's of the outer and inner cylinder respectively. Expression for the shear rate and shear stress for constant torque can be given as

$$\dot{\gamma}(r) = r \frac{d}{dr} \left( \frac{1}{r} v_{\theta}(r) \right) = \frac{2R_e^2 R_i^2}{R_e^2 - R_i^2} \frac{\omega}{r^2} \quad (56)$$

$$\tau(r) = \frac{T}{2\pi h r^2} \quad (57)$$

Where  $h$  is the height of the longitudinal grooves. For the given apparatus the shear rate is measured at the inner cylinder wall so the shear rate is given by ( $r = R_i$ )

$$\dot{\gamma} = \frac{2R_e^2}{R_e^2 - R_i^2} \Omega \quad (58)$$

$$\tau = \frac{T}{2\pi h R_i^2} \quad (59)$$

Plastic stress and plastic strain can be calculated by neglecting the elastic effects

$$\sigma^P = \sqrt{3}\tau \quad (60)$$

$$\dot{\varepsilon}^P = \frac{1}{\sqrt{3}} \dot{\gamma} \quad (61)$$

Compression test on the solid phase were performed with bars of Al-4.5wt%Cu alloy sample to determine the strain rate sensitivity and activation energy of viscoplastic law. Experiment were performed both for constant share rate and shear rate jump up to study

transient stage between the elastic deformation and viscoplastic plateau. Microstructure evaluation, if thermodynamic equilibrium is assumed during mechanical testing in the partially solidified state can be given as

$$f_s = \frac{C_L - C_0}{(1 - k_0)C_L} \quad (62)$$

Where  $f_s$ ,  $C_0$ ,  $C_L$  are the solid fraction, global composition of the alloy and composition of the liquid phase.  $k_0$  is the partition coefficient. For no solid diffusion case, equation is given by

$$f_s = 1 - \left( \frac{C_L}{C_0} \right)^{\frac{1}{k_0 - 1}} \quad (63)$$

Partially re-melting experiments were also performed to evaluate the microstructure with a temperature of 550 °C which is the 2 K above the eutectic temperature of Al-Cu, re-solidification performed at 20 K min<sup>-1</sup> and immersed in the lead bath for 5 to 60 min and removed and quenched in cold water.

Scheil Equation 22 can be used at the beginning and then increase toward the value by lever rule of equation 21. In the unrefined structure due to the entrapped liquid in the dendritic arm structure in the solid grains, both the effective solid fraction and entrapped liquid should be considered for the analysis of the rheological properties.

Mechanical behaviour of the refined structure and unrefined structure with both mechanical compression and partially solidified state was observed. For the compression of the unrefined structure of Al-4.5%Cu the stress after the transient reaches a saturation stationary value and follow the following law

$$\sigma_s \propto \left[ \varepsilon \exp\left(\frac{A}{RT}\right) \right]^m \quad (64)$$

Where  $Q$ ,  $m$  is the activation energy and strain rate respectively ( $Q=154\text{kJmol}^{-1}$ ,  $m=0.26$ ) shows a good agreement with the previous experiment for the same alloy.

For the grain refined structure experiment in the couette rheometer, shows a gradual increase in the stress value before the gradual decrease for large strains. The maximum stress depends upon the shear rate sensitivity and solid fraction and follow the empirical law proposed by Joly and Mehrabian given by

$$\sigma^P_{\max} \propto \exp(\delta f_s) \quad (65)$$

Where  $\delta$  is specific to microstructure called solid fraction sensitivity parameter ( $\delta=10$  for the experiment.) In the unrefined grain structure, stress-strain curve shows a much decrease lower steady state value after the peak value. This decrease in the steady state value for the unrefined alloy is neither a function of strain rate and temperature.  $\delta = 8.7$  can be found out by plotting the maximum stress versus the effective solid fraction for these experiments.  $\delta$  value can be a bit low a compared with the refined state. Because of the dendritic arm structure of the unrefined alloy, the shear path develop near the inner cylinder where the shear stress is maximum and early damage of the dendritic structure occurs, and the early damage of the material leads to the smaller peak stress. Both the refined and unrefined couette rheometer experiments measured stresses are equal in both alloys but different deformation mechanism. In the unrefined structure, the peak stress is the result of the breakdown of the structure which is a irreversible phenomenon while in the defined state both the deformation and formation mechanism occur due to the solid-solid interaction showing a reversible phenomenon. The solid fraction vs. maximum stress provides a useful way to understand the rheological behavior of the solidifying alloys.

#### 1.10.8 Kaprans Model

Kaprans et al. [101] used a CFD software FLOW-3D, Version 7.1 to investigate thixotropic behaviour during the flow of the material and to analyze the experimental results. Alloy A357 used for the experiments for rapid compression test with different solid fraction close to the conditions used for the thixocasting process and the information obtain from these experiments can be used to model the flow of partially solidified material.

Designed experimental chamber consist of billet (length = 42mm, diameter = 36mm) prepared by different routes (magneto hydrodynamics, re-crystallization and partial melting, spray forming) injection speeds, different solid fraction and soaking times is heated on the top of sindanyo pedestal by induction. Two thermocouples near the surface and centre of the slug is used to monitor and control the temperature of the slug. The force used during the compression of the slug can be measured with the load cell incorporated into the upper part of the chamber allowing a data collection at a rate of 2 kHz. The compression velocity is varied from 200 mm/sec to 2000 mm/sec during the experiments carried out in low thermal conductivity for isothermal conditions.

Load cell record an increase in load when the sindanyo insert first touch the slug followed by a decrease in the load during the rapid compression. The results show a variation for billet with different soaking time, production route. Peak and minimum loads can be calculated at different displacement and times. By using a simple analytical treatment for compression, it is clear that the viscosity fall rapidly with increase in the shear rate showing shear thinning behaviour. Spheroidicity of the particles can be calculated by

$$\text{Form factor} = \frac{4\pi A}{p^2} \quad (66)$$

Where  $A$  and  $p$  is the area and perimeter of the particle. Experiment showing an increase in the form factor with an increase in the soaking time and temperature resulting decrease in the viscosity. Experimental results also showing that the form factor greater than 0.8 can be achieved for the feedstock produced with the re-crystallization and partial melting (RAP). Initial break down load and low flow is desirable for slug to support itself but rapid shearing with results in low viscosity when entering the gating system.

#### 1.10.9 Brabazon Model

Brabazon et al. [12] built and developed a high temperature Searle type viscometer. Alloys Al-04%Si and A356 with a solid fraction of 35 and 33 respectively were used to evaluate the temporal viscosity at a shear rate varying from 3.1-124.8 s<sup>-1</sup> for a time period of 60 minutes followed by a rest time 60 min of no shear. Experiments shows that the viscosity depends upon factor indicated in Eq: 67

$$\eta = f(\dot{\gamma}, t_s, T_a, \dot{T}, C_o, h) \quad (67)$$

Where  $\eta, \dot{\gamma}, t_s, T_a, C_o, h$  are the viscosity, shear rate, shearing time, cooling temperature, composition of the alloy and history effect (solid morphology, size and distribution) respectively. High cooling rate and solute content results in increased viscosity due to the dendritic micro-structure. Experiments were carried out to study isothermal steady state viscosity, temperature dependent viscosity, thixotropic and isostructure viscosity with variation in shear rate, shear time and shearing temperature keeping the cooling rate constant.

Design of the Searle type viscometer consists of four resistance heating cables to heat the caster, one around the reservoir and three in the length wise fashion of the narrow section. Thermocouple of type K used to measure and control the temperature with a temperature controller keeping temperature variation as low as  $1^\circ\text{C}$ . Rotor with a diameter 34 mm axially grooved (to avoid slipping between the material and rotor wall) and to enforce wall adhesion in the narrow section of 40 mm diameter and 242 mm long narrow section of the crucible cup to obtain constant shear rate. Gap size of 3 mm was chosen for the rotor/crucible. For the geometry where the shear rate and apparent viscosity of pseudoplastic and Newtonian fluid is same is given by

$$\dot{\gamma} = 6.3 \Omega \quad (68)$$

Tests were carried out to record the apparent viscosity at a continuous cooling rate after filling the rheometer crucible with molten alloy  $5^\circ\text{C}$  above the liquidus temperature at constant shear rate of  $3.1 \text{ s}^{-1}$  for apparent viscosity vs. average shearing zone fraction solid and shear rate vs. apparent viscosity at various times period was recorded. Results showing that coherency point of  $f_s = 0.23$ , at which the appreciable viscosity increase is noted for both alloys but limited to a  $f_s = 0.5$  because of torque sensor limitation. At this point there is a sharp rise in viscosity of A 356 alloy at  $f_s = 0.45$  because of the close packing of the solid particles. Viscosities show large variation at different times at constant shear rate. Higher cooling rate results in a dendritic structure and increase

viscosities. Large particle size may result in high viscosity and may change the coherency point for the alloys. Similar microstructure and coherency point for both the alloys both low cooling rate is resulted.

Steady state apparent viscosities at various shear rate does not show too much difference in the results for the two alloys with Al-4%Si  $f_s = 0.36$ , and A356 alloy  $f_s = 0.33$ .

Different co-efficient were used for the Ostwald-De Waele power law model.

$$\tau = C \dot{\gamma}^n \quad (69)$$

Where  $C$  is the power law constant and  $n$  shear rate exponent. While the power law relationship can be given as

$$\eta = C \dot{\gamma}^m \quad (70)$$

Where  $m$  is the power law index equal to  $n - 1$ . Different values for  $m$  is used for different solid fraction and shear rate.

Results shows that increase shear period can result in a more spheroidal microstructure and therefore decrease the viscosity of alloy and most of the viscosity variation occurs during the first five minute of shearing for all the high shear rates. But the results of viscosity evolution with time difference for each of the alloy at lower shear rate of  $3.1 \text{ s}^{-1}$ . Low shear rate shows highest isostructural viscosities while high shear rate show relatively low viscosities related to the microstructure agglomeration. Thixotropic test for alloy Al-4%Si  $f_s = 0.36$  with up and down ramp time of 3.6 s and different rest time shows that increase rest time will increase shear stress and the viscosity alloy. Time period for the alloy being kept in the semi-solid state must be taken into account for thixotropy tests.



## **1.11 Summary**

Many different experimental and modelling methods have been employed to investigate the rheology of semi-solid metals. Comparatively little research however has been conducted to investigate the high shear rate rheology of these fluids. This work aims to redress that balance by providing a new high shear rate, high temperature capillary viscometer for semi-solid metals and to develop a finite volume model which can be used to compare with the experimental results obtained from this device. The next chapter, Chapter 2, presents results of the design analysis and the resulting viscometer developed in this work. Chapter 3 presents the set-up of the model developed in this work. Chapter 4 presents the results of the modelling work and Chapter 5 present the discussion and conclusions.

## Chapter 2

# Design Analysis and Construction

### 2.1 Introduction

A standard capillary viscometer was not commercially available for this project. A high temperature (up to 650 °C) capillary viscometer was therefore designed and commissioned. This project involved the design of all components and the selection of proper material for this capillary viscometer. The design of the system had to be broken in to individual components. These included initially producing several different plausible solutions. Each solution was analysed from several different view points for applicability.

The aim of the project was to design, construct and commission this high temperature capillary viscometer in order to evaluate the viscosity of semi-solid metals under the high shear rates that are being used industrially. A major design objective therefore was to provide variable operational ranges of injection chamber temperature, capillary temperature, and injection shear rate profile and accurate control of these parameters in order to fully evaluate their effects. Design factors will include the requirement of cast material at various temperatures in order to analyse the crystalline structure of the forming metal, design rate of flow, melt pressure, viscosity and need of the rig to easy move and stable under operation. The operation of the rig is designed for all of the critical variables that need adjustment during experiments could be tuned to the specific requirement of the operator. Following considerations were taken into account for the design and construction of the capillary viscometer.

- System construction materials must withstand high temperatures encountered
- Size and thickness of the construction materials needs to be analysed
- Injection speed profiles need to be controllable with a maximum speed of at least 3 m/s.

- Controllable injection chamber and capillary temperature.
- Appropriate insulation for the injection chamber and tube.
- Easy to remove the investigated sample fluids which have solidified.

## 2.2 System Design

A schematic layout of the capillary viscometer showing the main parts such as the injection chamber, the capillary, and the plunger drive system is shown in figure 2.1 and detail pictures are given in appendixes C, D and E for the detail layout and picture of parts individually).

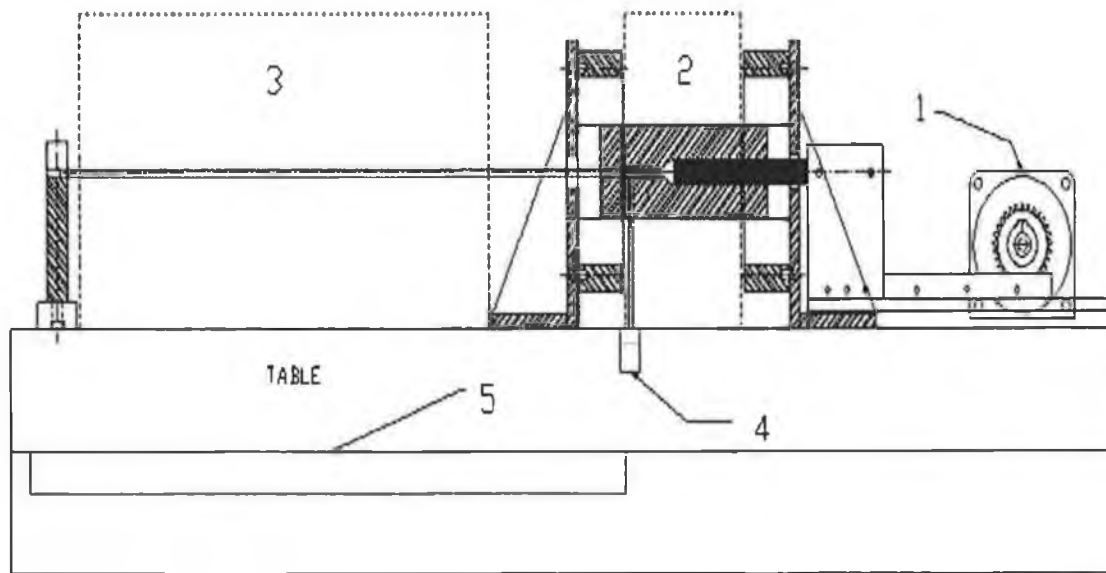


Figure: 2.1 Capillary viscometer schematic, 1: motor, 2: injection chamber and furnace, 3: capillary and furnace, 4: load cell and 5: quench tank.

### 2.2.1 Table design

The frame of the table was designed to be strong and withstand the expected applied force from the motor. A thin steel sheet (4 mm thick) was used to cover the tabletop. A number of cross beams were welded to the underside of this table especially around the motor mounting. To make the entire table mobile lockable casters were mounted to the

bottom of the table in each corner. The table carries the mounting brackets for a stainless steel water tank beneath the table. This tank was positioned to be able to quickly quench tested samples. A slot was cut in the steel tabletop sheet so that a cut capillary could pass through and into the quenching water tank. The motor and motor mechanism (rail, plunger assembly, rack and rack support), load cells and the stainless fibre board filled box furnaces around both the injection chamber and the capillary were mounted onto the table [appendixes D and E].

### 2.2.2 Injection chamber and capillary design

Material used for the injection chamber was Ovar Supreme. This is a common die material for aluminium injection moulding. The external diameter was 90 mm and the internal diameter of the loading section was 25.05 mm. There were three holes provided at the top of the chamber to allow the insertion of thermocouples evenly spaced between the mounts, in order to measure the temperature of the metal. Another hole was provided on the underside of the chamber to allow for the placement of a 6 mm diameter loading pin which connected the channel wall loading to a load cell placed beneath the table. This enabled measurement of the fluid pressure. Stainless steel tubing of 6mm internal diameter and 8 mm external diameter was used for the capillary. More general information on metal injection moulding die design can be found in Appendix C, D and E].

### 2.2.3 Capillary mould with surrounding furnaces

The capillary mould is made of steel and is attached to the injection chamber; it is surrounded by the fibre board for the sake of insulation and heater band providing heat to keep the system isothermal. The other end of the capillary is open to the atmosphere and supported on the mould support, which means that the pressure difference will be between the pressure measured by the load cells and the atmospheric pressure. The capillary is 6 mm in diameter and 740 mm long [129]. Three thermocouple equally spaced are located in the capillary with surrounding furnace to measure and maintain temperature with the help of the heating elements and insulation material around the

capillary. The rest of the arrangement is the same as that for the injection chamber with surrounding furnace [appendixes C, D and E].

### Insulation

Insulation of the injection chamber and mould cavity was required for safety, stopping heat radiation and heat transfer. Ceramic fibre board was cut into the required shape required and used for this purpose due to the high specific heat capacity, low thermal conductivity and low density.

### Stainless steel cover

Stainless steel covers were used to enclose the insulation fibre board both around the mould and the injection chamber. Stainless steel was used for the purpose because of its good surface finish, high anti-corrosion capabilities and that it withstands high temperatures. The stainless steel covers for the injection chamber and insulation material were welded with four sided strips to insure system rigidity. This was important as any misalignment might cause the plunger to dig into the internal bore of the chamber. In addition, from the design layout it can be seen that chamber is lying inside the insulation material on the mounting brackets such that the injection chamber is completely separated from the rest of the steel structure [125][appendixes D and E]

### Heating elements

The heating elements were placed at either end of the chamber. It was used to keep the temperature constant in the mould chamber so that the system is kept isothermal. Four Thermofast heating element of 230V and 2000 W capacity are used. They were able to reach a temperature above 800 °C and were supported at either end of the mould cavity with fibre board. These elements are not in a direct contact with the chamber, so no further insulation was required as the thermal insulation inside the steel cover is sufficient. Stainless steel covers were added with the thermal barrier at the interior and act as a operating guard over the critical areas [127, 128] and [appendixes C and E].

#### 2.2.4 Piston Motion Mechanism

The piston motion mechanism consists of the servomotor and controller, rack and pinion, plunger and plunger holding assembly, motor support brackets and aluminium plate.

##### Servomotors and controllers

A USB connection wire was connected between the PC and the servomotor controller. This allowed programmes to be downloaded to the servomotor for the motor control. These programmes were written and downloaded using the Control Techniques software supplied with the servomotor system. The servomotor, via the gearing mechanism employed, can develop a torque of 75.6 Nm and can reach to the maximum speed of 14.43 m/sec. Servomotors are famous for their high speed, high torque characteristic, high torque to inertia ratio, excellent velocity control, and quiet operation [108, 109, 119 & 20]. Speed and position control were maintained in this system via encoder feedback. The control system is PID based and execution of the PLC controller programme can be initiated either via controller connected push buttons or via PC signal to the controller [appendixes C and D]

##### Rack and Pinion

The rack and pinion mechanism is used for all kind of machine tools, like hydraulic machine, drill presses, automobile steering. The motor, rack and pinions were mounted horizontal on the table in this work. The rack, which was cut to 325 mm length and 30 mm width, was mounted on a linear slide mechanism. The pinion translating the motor rotation to the linear motion of the rack was 70 mm in diameter at the point of meshing [appendixes C, D and E].

##### Plunger and plunger assembly

The injection ram was designed to inject the semi-solid metal into the injection chamber. Semi-solid metal could require a large force to drive it through capillary viscometer. Material used for the plunger was high quality steel (see appendix for detail). The plunger needed to be guided as accurately as possible in the injection chamber and high dimensional accuracy was needed between the plunger and injection chamber as forces

are great and the injection speed is high. The plunger was machined to 24.90 mm diameter and the chamber inner diameter to 25.05 mm. Before each experiment is performed, it is important that the alignment of the injection ram and injection chamber is ensured. This was performed by placing the plunger into the chamber before tightening of the fixture screws. The plunger holding assembly was designed to allow free movement of the end not in the chamber to allow self-aligning of the plunger during injection [appendixes C, D and F].

Motor support bracket and steel plate

Motor and all motion mechanism were mounted on an aluminium plate to align them with the injection chamber. The thickness of the plate is 16 mm while the length and width are 650 x 650 mm [appendixes E]

### 2.2.5 Fluid pressure measurement calculations

Large loads are expected in the mould and injection chamber due to the large reduction in volume. Surface friction between the two different surfaces would be affected by parameters like surface roughness, surface coatings, and material types creating the friction. Frictional force can be calculated on the wall surface using the product of coefficient of friction for stainless steel and the surface area of the cavity. If we assumed the coefficient of friction as  $0.3\mu$  and the surface area of the cavity is given by

$$\text{Area} = 2 \pi r h = 0.011 \text{ m}^2 \quad 2.1 \quad (\text{Appendix B})$$

$$\text{then the frictional force} = \mu PA = 0.014 \text{ N} \quad 2.2 \quad (\text{Appendix B})$$

The coefficient of friction can also be further reduced with the use of a high temperature lubricating agent such as boron nitride. This value was therefore not used in further calculations. Mould design mainly consisted of sizing the length and diameter of the mould cavity. Assuming the volume of the slug placed into the injection chamber flows all the way through and fills the capillary then:

Volume of slug to be injected = Volume of capillary

$$\pi r_1^2 L_1 = \pi r_c^2 L_2 \quad (2.3) \quad (\text{Appendix B})$$

Where  $r_i$  and  $r_c$  are the radius of injection chamber and capillary tube and  $L_i$  and  $L_c$  are the length of aluminium slug and mould respectively. For the quality and consistency in the process, the length of the mould cavity was set to 740 mm which is smaller in comparison to the expected volume for this diameter. This was done, in order to meet the test requirements, so that a volume of aluminium would pass through the capillary. Another reason for the length is in order to avoid the kinetic energy effect, see chapter one. The length is long enough to fulfil the condition which is  $L/D > 100$  to minimize the end effect in capillary tube [118, 119].

The maximum velocity  $V_i$  with which the plunger can travel is 14.43 m/sec. An approximate velocity that the fluid sample will go through the mould can be calculated using the following relationship.

$$V_i A_i = V_{tube} A_c \quad (2.4) \quad (\text{Appendix A})$$

Where  $A_1$  and  $A_2$  represent the inlet and outlet areas, while  $V_i$  and  $V_{tube}$  represent the velocity at the inlet and outlet respectively. Bernoulli's equation was used to calculate the pressure of the material through the mould. The following assumptions were made about the material and the process as follows.

1. No friction losses within the flow.
2. Unsteady state and incompressible flow.
3. No heat transfer through the material
4. No rotational work on material.

Calculated pressure on the billet was 4.42 MPa by using the Bernoulli's equation:

$$P_1 + \frac{1}{2} \rho V_1^2 + \rho g h_1 = P_2 + \frac{1}{2} \rho V_c^2 + \rho g h_2 \quad (2.5) \quad (\text{Appendix A})$$

Where  $P_1$  and  $P_2$  are the pressure at inlet (injection chamber) and outlet (capillary tube/mould), and  $V_i$  and  $V_c$  are the velocities at inlet and outlet respectively.  $\rho g h_1$  and  $\rho g h_2$  are equal because there is no pressure head and no height differences, as the capillary viscometer was placed horizontally on the table. The pressure in the capillary for a specified pressure of 4.42 MPa in the injection chamber would be 4.01 MPa



(appendix A). During the casting process, this was expected to be the maximum pressure at maximum speed [36, 121-124].

#### Fluid pressure measurement load cell choice

Various techniques were assessed for reading the pressure near the injection chamber due to heat. The most obvious device to use would be a pressure sensor. The pressure sensor is used to calculate the compression loads by molten metals. Two individual load cells that are designed for this specific task are oriented.

- Positioned underneath the chamber in the centre of the channel between the compression chamber and mould seat.
- Rear part of the table at the end of mould cavity.

The load cell used was a sub-miniature compression load cell, which can be used where space is at the premium. Its size made it easy to incorporate with the developed rig. It can easily operate within a temperature range of -53 °C to 121°C. The cost of pressure sensor that could withstand high temperature was very high, so a system with a pressure sensor and quartz is used to measure the pressure. The quartz rod is used as a thermal separation barrier for the load cell; it is a brittle material and a perfect transmitter for the compressive loads. The quartz rod situated on the load cell will transmit the pressure from the inner diameter of the capillary and the molten metal passed by to the load cell which will be mounted beneath the top surface of the table in specially designed ceramic holder provided to add insulation from heat and keep it safe from damages. The ceramic load cell holder is 100 mm in diameter having 4 holes (M10x20 drilled and tapped) spacing 90° to each other to hold it to the load cell support brackets. A narrow cavity of diameter 8 mm is providing to locate the connecting wires and power supply (see appendix). The load cell supporting bracket is made of steel and holds the ceramic piece. The load cell bracket are both attached to the underneath table. The load cell is connected to the computer with Lab view programming which will show the deflection in case of any force rise. This reading is scaled by the program in the LabVIEW to show the pressure applied by the molten metal at that point in the capillary and was recorded against time [130] and [appendixes A, D and E].

### 2.2.6 Temperature measurement

Thermocouples are used to measure the temperature of the flowing metal in the injection chamber. Three individual thermocouples are included in the design of the injection chamber and another three in the mould cavity section. The holes for the thermocouple are mounted on the top of the chamber evenly spaced between the mounts. A specific thermocouple of type K bimetallic junction is used in this project. The maximum temperature with which this thermocouple can withstand is 1100 °C for continuous contact and 1350 °C for short period contact. This kind of thermocouple is made up of nickel and chromium coated with aluminium oxide. This thermocouple works on the principle that a current is forced to flow when it is subjected to a change in temperature, this current is directly proportional to change in temperature between the measurement and reference junction, and depends on the metal within the thermocouple. It has a quick response with high temperature resistance. The signal cables which can be used with this kind of thermocouple has a temperature range of -25 °C to 200 °C which will suits the working temperature around the rig [appendixes C, D and E].

## 2.3 System Control

LabVIEW was used for controlling the motion of motor by input signals to the controller and recording output data from the load cells and thermocouples. LabVIEW is a graphical programming language that uses icon instead of using instruction as line of text. It uses data flow programming, where the flow of data determines execution. It provides powerful graphical representation for signals, measurement analysis and data presentation with enough flexibility of programming language without the complexity of the traditional development tool. It is specially designed to get the data or measurement needed from the physical sensor easily and quickly. LabVIEW contains more than 400 built in function design to extract, analyze and process signals using the information from the input data. It also offers tools for control, simulation and design. It can perform wave form measurement, array based measurement and single point measurement. LabVIEW is also called as virtual instrument because their appearance and operation imitate physical

instrument. Its working involves the acquiring of information, analyze information and presentation. It is capable of interacting and acquiring information for all electric devices from any source. It can be used to built in channel orientation system for scaling input data, high speed wave for generation, fast and accurate analogue, timer input, event counting and high speed digital wave output generation.

It consists of front panel, shows the controller (knobs, dial, push buttons) and indicators (graphs), used as the input and output terminals repetitively. Block diagram is the graphical representation in which we can add codes to control front panel objects. The front panel object appears as terminal (terminal are the entry and exit ports that exchange the information between the front panel and the block diagram) on the block diagram. We cannot delete any terminal in the block diagram unless deleted in the front panel.

Automation is an important part of engineering design. Speed, repeatability, accuracy, sensor, payload, degree of freedom and type of motion are all the important parameters of automated system, which a designer must consider. LabVIEW is used to control the motion of the motor and heat which will be the output, acquiring data from the two load cell and six thermocouples as input signals in term of voltage. Load cell, thermocouples and motor are all connected to the computer controlled with the LabVIEW program [131].

In this work LabView was used to record the temperatures of the injection chamber and the material to be injected. The GUI screen for this application in shown in figure 2.2. The load from the load cell was also recorded on the PC at a high acquisition speed using LabView. The GUI screen for this application in shown in figure 2.3. The motion of the plunger was controlled via proprietary software that came with the servo-motor. The screenshot of the graphical user interface for this software is shown in figure 2.4. Individual macros were written to perform specified injection speed profiles with this interface. These short programs were then downloaded to the controller where they could be called to run independently of the PC. This enabled more robust control of the servomotor for reliable control and enhanced safety of the rig.

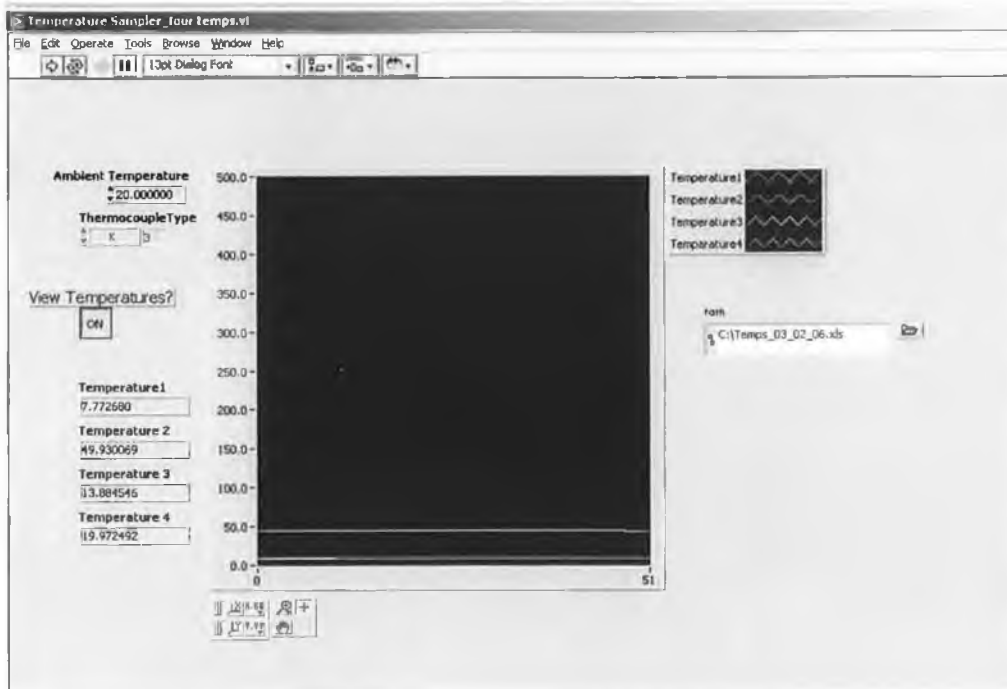


Figure 2.2 Graphical user interface for the temperature logging from the injection chamber and the semi-solid material.

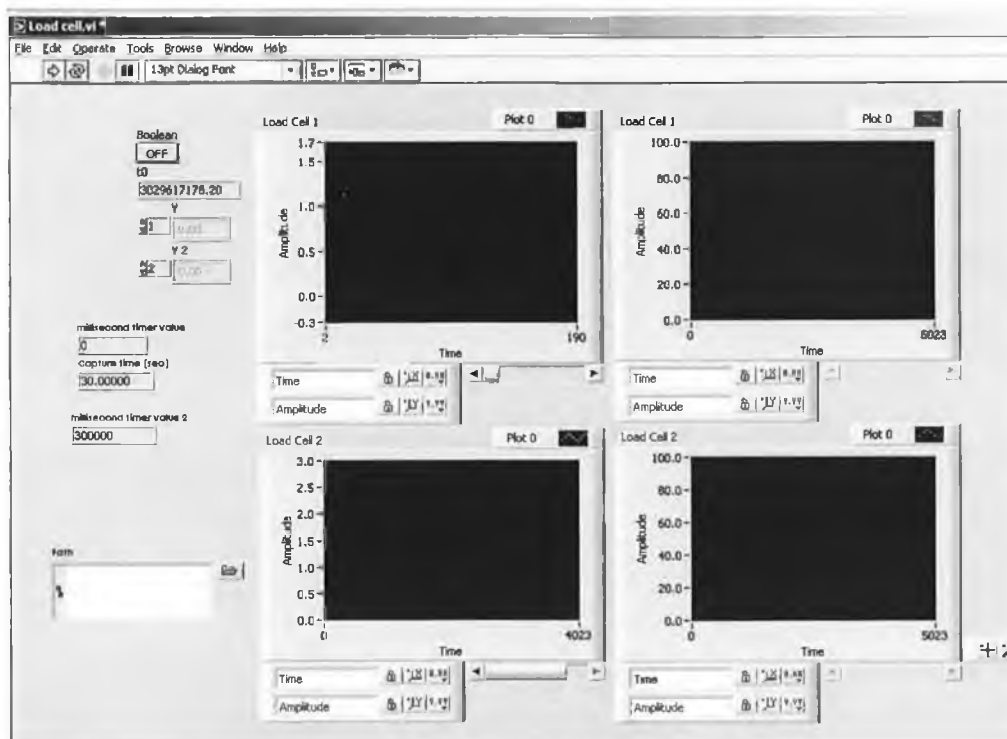


Figure 2.3 Graphical user interface developed to record the load cell readings.

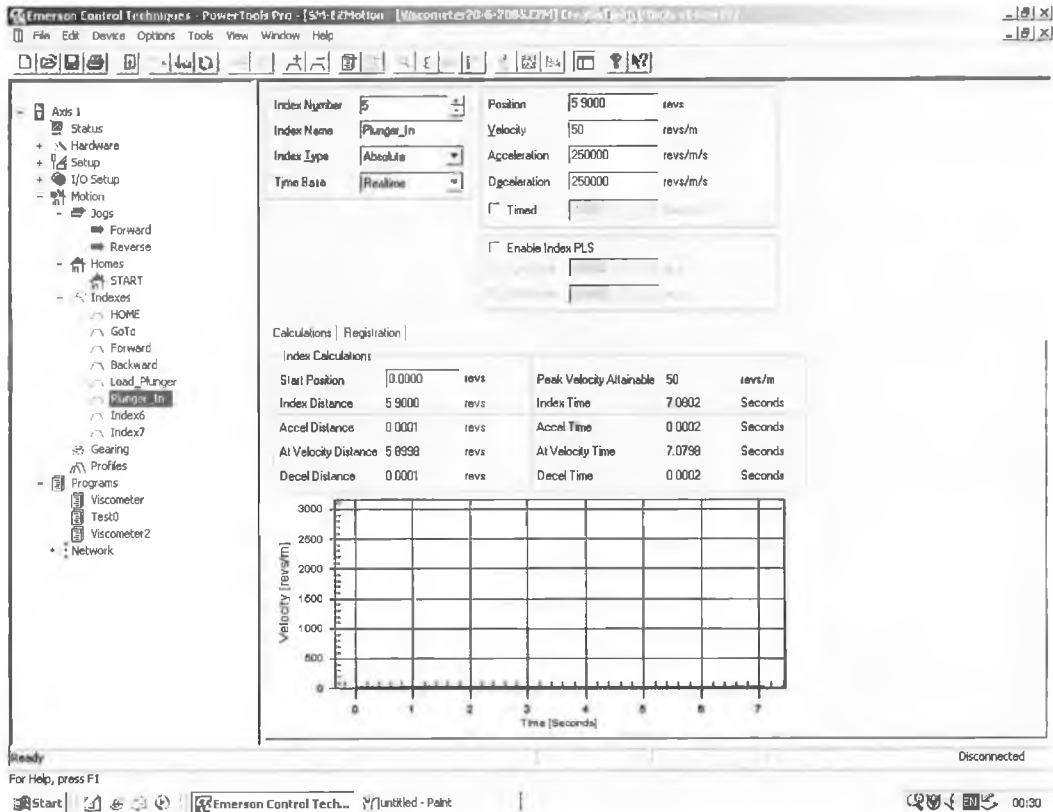


Figure 2.4 Graphical user interface for the Unimotor servomotor controller programme.

## 2.4 Experimental procedure

### 2.4.1 Material preparation

One of the disadvantages of semi-solid metal processing is the cost effectiveness for the preparation of the billet and it is almost 50 % of the total cost of the component restricting the use of semi-solid metal processing to limited potential applications. Cost of the billet preparation must be reduced to minimize the cost of the parts and improve the adaptation of the process on a commercial scale.

A new cheap, easy and less time consuming method has been developed to prepare the billet for the semi-solid metal process with spheroidal microstructure. This simple and natural method is called direct thermal method (DTM). The method is used to make the billet of alloy A356 for processing through the capillary viscometer. In this method the

low temperature alloy is poured into a cylindrical mould with low thermal mass and high thermal conductivity allowing the metal to cool rapidly to the semi-solid state and have low heat losses to atmosphere. This makes the process in an isothermal holding condition in the mould for some time as there would be no heat losses to the atmosphere. The mould is then dropped into a water quenching held at for rapid cooling to prevent any change in the microstructure after the material preparation. In this type of billet preparation for our experiments, the copper tube with an inner diameter of 24.8 mm is used as a cylindrical mould with a wall thickness of 1 mm.

The furnace is allowed to rise to a temperature of  $700^{\circ}\text{C}$  and stabilize the temperature for 15 minutes along with the crucible that will allow drying any moisture present in crucible preventing any air entrapment. The crucible is then taken out and aluminium alloy A356 is then placed in the crucible and put back in the furnace to heat at  $700^{\circ}\text{C}$  for a period of 45-60 minutes allowing the material to liquefy completely. The copper tube should be heated to  $40^{\circ}\text{C}$  allow to dry all the moisture inside tube and allow to cold before liquid metal is poured into the tube. A thermocouple of type K is used to record the temperature when crucible with alloy is taken out of the furnace. The thermocouple is place in the material and the temperature is noted till the desired pouring temperature reach for pouring in the copper mould. It takes 40 seconds till the temperature recorded by the thermocouple reached to  $660^{\circ}\text{C}$ , pouring of the material in the copper tube is performed. For laminar flow of metal in the copper tube, ensure that liquid metal hits the wall of the copper tube, and this will help to allow sufficient time for the air to escape resulting in less porosity. Allow the material to solidify in the copper tube for 60 seconds and then quench it into the water tank to stop any microstructure changes in the material. The quenching water and ambient temperature were recorded before the experiment.

This process is done for different heating temperature, different holding time in the crucible, different pouring temperature and different holding time in the copper cylindrical tube. Experiments were also performed for the same temperature, holding time and pouring temperature for a naturally cooled A356 alloys. The results obtained for the first case was mostly spheroidal microstructure while in the later case show the dendritic microstructure behaviour [132] and [Appendix F]

## 2.4.2 Experimental setup

Before starting the experimental, a number of things need to be checked are

- Check the motor and the controller to see that they are working properly and the motor is in the running mode, and switch off the motor if it is not used.
- Check that controller program is working.
- Plunger is aligned perfectly with the injection chamber and free to move in the injection chamber.
- Plunger should be tightened up with the plunger holding assembly before running the experiment.
- Plunger should be in the proper new position and every time after making changes on the plunger position should be adjusted and downloaded in program and check that plunger load position, plunger in position and plunger home position at the start of the experiment and program is working properly for it. Any desirable changes like changes in the speed, position made to the program should be download to the program.
- Die chamber is cleaned and sprayed with Boron Nitride solution and fixed in between the two supports with mounting screws.
- Injection chamber support should be well tightened and adjust the position of the injection with the help of the four screws provided underneath the table to move it up and down.
- After every experiment performed there is possibility of wear and tear in the insulation material, should be checked and change if possible otherwise to make the adjustment. Fibre board is a soft material and cannot afford too much load or pressure as results it can be compressed and make plunger very tight in the injection chamber.
- Heater bands should be checked for working for both the injection chamber and capillary tube and any wire from heater bands power supply should not be touching the surrounding metal.
- Thermocouples are in the right position and check for working in the Lab VIEW programming.

- Load cell is in right position and checked before the experiment for working with Lab View.
- Two steel rod for detecting flowing metal pressure is in the right positions, right length and free to move in hole without any harm in the chamber and touching the surface of the load cell.
- Capillary tube is of the right length and fit well in between die chamber and capillary support.
- Goggles, gloves and all the protective clothing should be ready and used all the time.
- Water tank filled with normal tap water

Turn on the power supply for the PC, motor, controller and heater bands. First of all set the position of the plunger and plunger assembly by defining the plunger load, plunger in and plunger home position in the program. This program is then downloaded to the motor. This enables robust remote control of the motor. Turn on the heater bands to start heating injection chamber and capillary surrounding. Follow the step wise increase procedure, set up the temperature on the temperature controller containing relays that will automatically on and off when set temperature is reached. Set the temperature initially to  $200^{\circ}\text{C}$  and wait for the temperature to rise to specified temperature and keep checking it recorded temperature of all the thermocouples with the Lab View program. When the temperature reached  $200^{\circ}\text{C}$  mark, the temperature was increased to  $400^{\circ}\text{C}$  and then to  $598^{\circ}\text{C}$  in a step wise manner (at  $598^{\circ}\text{C}$  fraction solid of alloy A356 would be 0.33) [12]. When the temperature reaches  $598^{\circ}\text{C}$ , it was allowed time to stabilise.

Place billet inside injection chamber with the help of tongs and push it all the way through to reach the end position of 125 mm long hole of injection chamber. Leave the billet in injection chamber for half an hour and keep checking the temperature of the billet with thermocouple. When the temperature of billet becomes stable the program should be started on computer to bring plunger to loading position. Position of plunger should be in such a way that it touches the back of the billet to close the gap between the plunger and billet to prevent any air entrapment. Start the LabVIEW program for load



cells and push the plunger into the injection chamber by selecting the plunger-in position via the LabVIEW GUI. This process of the metal flow will take approximately 2 to 7 seconds' time to finish the process but on the lab view program we will specify a time of 30 seconds data collection time. When plunger is in position, leave it for 30 seconds in injection chamber to make sure that capillary tube is properly filled and the alloy sufficient time for the metal to flow to end of capillary tube before start bringing it back to the home position. Now bring the plunger back to its original home position and stop the program for the load cell and save the results to specified folder.

Open the end support of the capillary tube and take the capillary tube out using all the precautions and through it in water tank for quenching to retain the same micro-structure at the end of the experiment. When the capillary tube became cold, took it out of water tank and cut it into sections for metallographic examination.

## **2.5 Summary**

This chapter presents the design of the capillary viscometer which was designed, built and commissioned during this work. The programmes developed to record the temperatures and pressures of the semi-solid metal are presented. The method and program used to control the plunger motion is also presented. Material preparation and the experimental method for operation of the capillary viscometer is presented at the end of this chapter. With the system designed, built and the operation procedure set in place the rig was ready to obtain experimental results. The first of these are presented in appendix J.

# Chapter 3

## Model set-up

### 3.1 Finite Element Analysis

Semi-solid material flow is generally composed of natural behaviour (thermal conductivity, elasticity, viscosity) and disturbance (temperature, pressure, force and moments of the system). The Finite element method was used to solve the flow of semi-solid through capillary viscometer by simulating the flow with same physical characteristic used industrially. Solving the flow of semi-solid A356 with finite element analysis involved geometry creation and meshing, set up for modelling and material properties, boundary condition and initialization with results [Appendix G].

#### 3.1.1 Grid geometry generation

GAMBIT is the package used to create and modify grid for this project. Points or vertices were created and were used to model the geometry. Vertices in X-Y co-ordinate system were created in their required position by taking the reference point or the distance from the relative point in the XY co-ordinate system selected for entity and different entity names were used as Gambit allows us to create an entity with a label name. In figure 3.1, shows the vertices created for grid.  $(X_o, Y_o)$  is the reference point. Join together the vertices either by connecting vertices command by picking the required vertices that need to be joined together as shown in figure 3.2. In figure 3.2, AB shows the inlet of the injection chamber which is 25 mm in diameter; ABCD shows the injection chamber of length 125 mm. CDEF shows the semi-cone angle section of capillary viscometer, EFGH shows the capillary tube, GH is the outlet of capillary while JK is the axis of capillary viscometer. Faces created and given different name for calculation purposes later on by joining together vertices for the specified face by lines or curves and

then later, all the lines and curves are grouped in single shape to react like a single geometry [Appendix G].

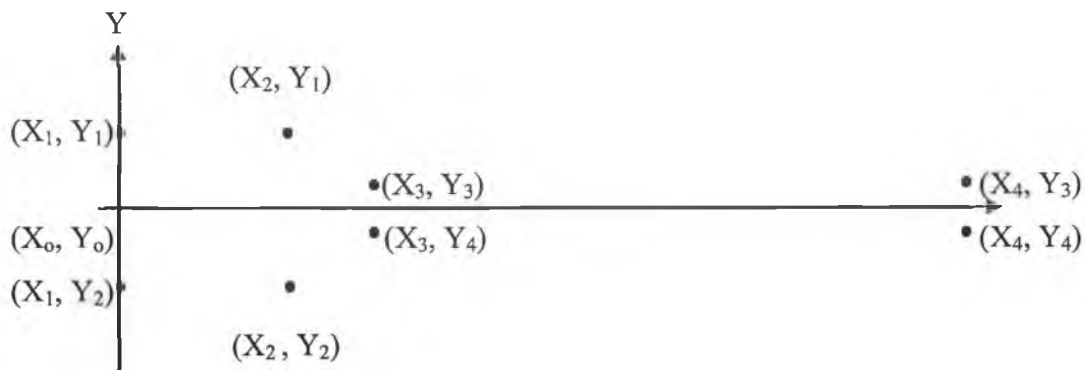


Figure 3.1 Indication of the vertices in millimetre distance representation created for the grid geometry;  $(X_0, Y_0) = (0,0)$  = reference point;  $(X_1, Y_1) = (0, 12.5)$ ;  $(X_2, Y_2) = (125, -12.5)$ ;  $(X_3, Y_3) = (141.45, 3)$ ;  $(X_4, Y_4) = (881.45, -3)$

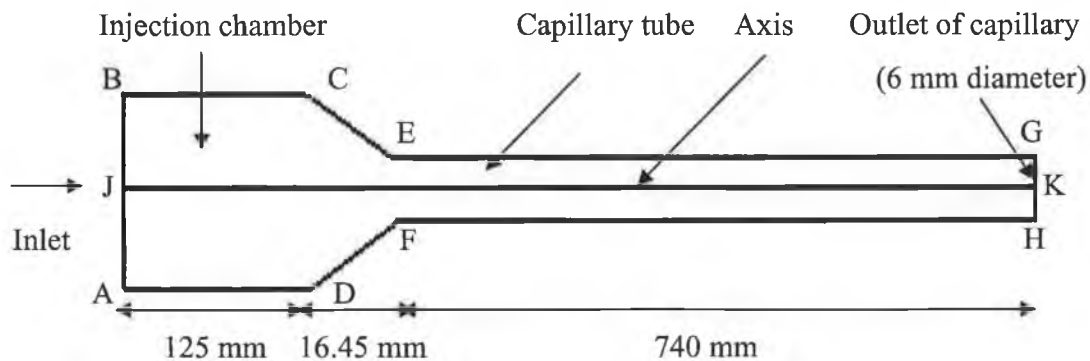


Figure: 3.2 shows connected vertices to form geometry for simulation

### 3.1.2 Meshing of Geometry

Meshing was used to create and discretize the solution domain into finite elements, called nodes, cell, or elements. In semi-solid flow the function like pressure, velocities and viscosities of the flowing fluid could vary with the flow in specified time in every domain and elements, therefore it was necessary to solve the problem for each cell and solution

for all the elements would be a solution for domain. . Fine meshing was necessary for result accuracy with more elements but more the element more will be the required computational time and memory. Due to constraining memory and time, it is necessary to limit the number of elements. The technique used for meshing our geometry was line meshing by dividing lines into part separately and uniformly distributed with different number of elements by specifying interval size and spacing of nodes. Mesh was created on faces. Meshing of each face was done according to the flow and calculations at that face. AB was divided into 50 nodes, BC and AD, were divided into 125 nodes, CE and DF with 40 nodes, EG and FH with 740 nodes, and EF and GH with 50 nodes. CDEF which is the semi-cone angle section is divided in more part as compared to the other parts because most of the changes could occur in this part. Outlet of the capillary is also divided into greater number of nodes as we need good calculation at exit of capillary tube. Quadrilateral meshing was used in the problem because our geometry has unparallel and irregular shapes involved. It is more accurate and gives us good results.. Details of material properties, boundary conditions and initialization are discussed in detail in the following topics in chapter [Appendix G].

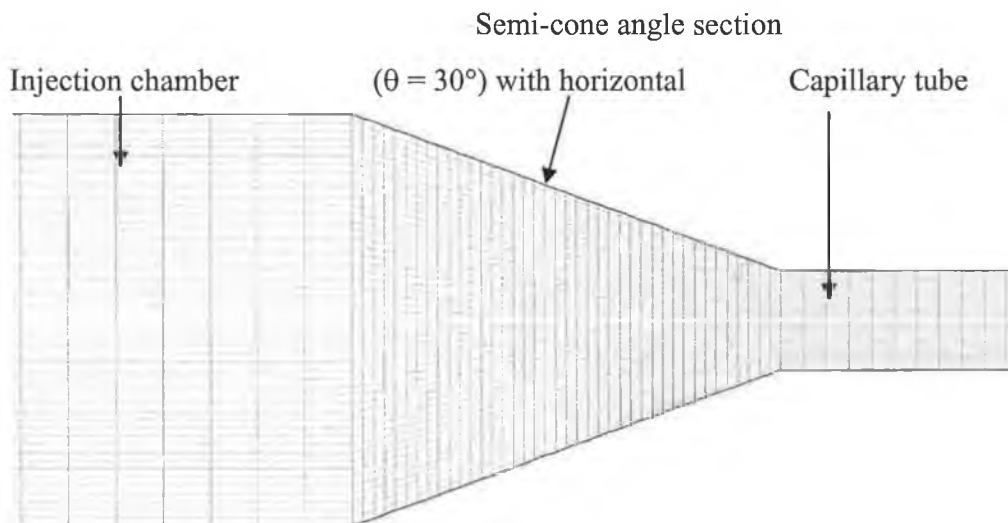


Figure 3.3 Grid generated in GAMBIT for conical section of the capillary viscometer

### 3.1.3 Mesh examination for Quality

Mesh was examined to check the quality of the examined mesh for the negative volume, aspect ratio and skewness because properties like aspect ratio and skewness can greatly affect the accuracy of the results and robustness of solution. Examine mesh with quality type option menu and 2D element was selected for quality examination of the mesh. All the faces were examined for quality by selecting the upper and lower limit by dragging the slide bar up and down and were examined for all the worse elements. Different limits were applied and different part of the mesh was examined to see if quality could be improved. The aspect ratio was kept high to increase the size of the element for more accurate calculation in semi-cone angle section, capillary tube and exit of capillary. The aspect ratio was taken as 1 as the aspect ratio greater than 1.6 could create problems and fluid might lose calculation properties and will not be more accurate. The increased aspect ratio also results in less skewness (distortion in the elements) because of the decrease in the element size will minimize the angle of skewness at the edge element as greater the angle of skewness, more will be distortion, less accurate results and destabilize the solution [Appendix G].

### 3.1.4 Zones and boundary specification

Geometry was created by face generation and each face was given its entity name. Selecting zones from operational tools, all these faces were defined as boundaries and the boundary types. Face AB was specified as inlet velocity for the fluid, GH as the outlet pressure on the fluid, JK was taken as the axis of the flow while faces BC, AD, CF, DF EG and FH was specified as the wall of geometry. In the specified quantum type menu, all faces were selected in the entity type and material for flow though these faces were selected as fluid.

## 3.2 Fluent

Computational fluid dynamic (CFD) software Fluent was used to model the flow of semi-solid material. The basic program structure for fluent is given in figure: 3.4

After generating the mesh in Gambit, the grid was read into solver Fluent for operation like modeling, material physical properties, operation and boundary conditions and analysis of the results [Appendix G].

### 3.2.1 Reading files into Fluent

The grid was generated and design with all required dimensions and meshing in Gambit which is the pre-processor for fluent for geometry generation and mesh modelling. As the grid was read by fluent, reported the progress of convergence. Fluent reported that 17500 quadrilateral cells have been read along with the boundary faces and different zones identifiers.

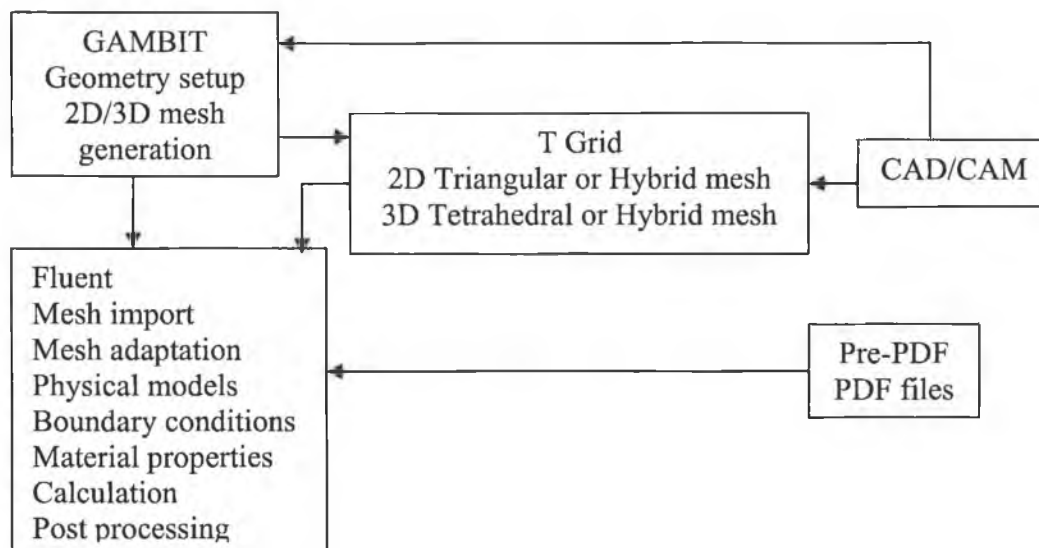


Figure 3.4 Fluent Program structure

### 3.2.2 Grid checking for quality and smoothness.

After reading the grid in fluent, it is good to detect any grid trouble before starting with problem setup to avoid the problem due to incorrect mesh connectivity. It gave information about X and Y values from the grid, volume statistics, grid topology and periodic boundary information, verification of simplex counters, and (for axisymmetric cases) node position verification with respect to the  $x$  axis. No negative Volume was found, therefore no error in the grid was reported, because Fluent cannot start any

calculation with a negative volume value. In order to simulate flow in the developed experimental apparatus the Domain Extents were set as follows:

$X = 881.45 \text{ mm}$

$Y = 25 \text{ mm}$

Total volume ( $\text{m}^3$ ):  $3.509672\text{e-}03$

The X dimension was the total length of the capillary and injection section of the die chamber. The Y dimension was the diameter of the injection chamber used in this work. It also gave us information about the number of nodes, number of faces, thread pointers, cells per face, face cells, bridge faces, right-handed cells, face handedness, element type, consistency, boundary types, face pairs, periodic boundaries and node count, solve cell and solve face count, face children, cell children and storage. After checking the grid, smooth option is selected from file main menu, smooth and swap option was selected for the best quality of the grid to make the element smooth with skewness factor 0.3 selected for the minimum value of skewness.

### 3.2.3 Scaling grid

The grid for this project was generated in millimetres; however we can change our grid system at any time. The scale factor selected for both X and Y was 0.001. The domain was set with  $X_0$  and  $Y_0 = 0$ , while the  $X_{\max}$  and  $Y_{\max}$  were set to 881.45 mm and 12.5 mm respectively.

### 3.2.4 Solver Formulation

The solver panel allows selecting the solution method for the calculations. We have a choice to select numerical methods in fluent. For modelling the problem, we selected segregated solver. The segregated solver (Figure 4) was used to provide accurate results for a broad range of flow and control volume technique was used for the flow. Incompressible flow was assumed for the model therefore segregated solver was selected because it is more appropriate for the incompressible, low velocities flow, and it requires low memory spaces as compared to the coupled solver. Segregated solver provides us more physical models which are not available with coupled solvers like volume of fluid model, multiphase mixture model, and Eulerian multiphase model and was useful to use

as mixture multiphase model was used for the semi-solid material. In segregated solver, the governing equations (momentum, continuity, mass flow rate, energy, species, and turbulence and scalar equations) were solved sequentially in our model (Segregated solver solve for a single variable like pressure, velocity and temperature by considering all cells at the same time). We selected the segregated solver for modelling multiphase flow (solid and liquid phases). As there were more than one unknown values like pressure, viscosity, velocity and temperature and appears in all equation and the explicit formulation cannot be used with the segregated solver. therefore the implicit formulation was selected. Several iterations of the solution loops were needed to be performed before a converged solution to be obtained (segregated solver uses the equations which are non linear and coupled). The steps need to be performed for each iteration given in the figure 3.5.

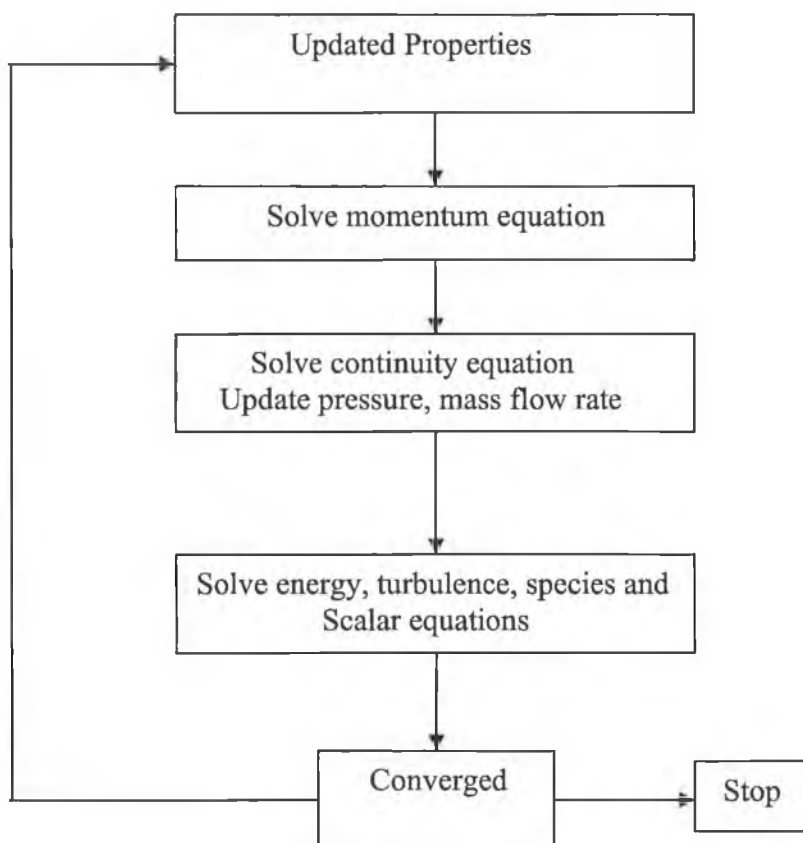


Figure 3.5 Segregated Solution Method



For the dimensionality of the problem we selected the 2D, indicates that the problem was a two dimensional problem and we can use the two dimensional option of fluent. The 2D space option was selected because for geometry it was assumed that axis are symmetric and no rotational work. 2D also required less computational memory, reduced number of elements and for fast calculations. Time dependent solver i.e. the unsteady state condition was used for the flow as the velocity would change with time and position in the capillary viscometer and also to simulate the flow with time and position in the capillary viscometer. For velocity formulation absolute velocity with second order unsteady state formulation was used to give us more accurate results [Appendix G].

### 3.2.5 Multiphase modelling

Semi-solid modelling was done using multiphase modelling. Multiphase flow can be defined by gas- liquid or liquid-liquid flow, gas-solid flow, liquid-solid flow or three phase flow. The regimes which could best describe our problem were the liquid-solid flow of the material. Both Mixture model and Eulerian model could be used but for modelling of semi-solid material through capillary viscometer, we selected Mixture model as the Mixture model can be used to solve a simpler problem and less computational efforts, more computationally stable and require less memory than Eulerian model [appendix G].

### 3.2.6 Mixture Model

Mixture model was used to design two phases that is liquid which is the primary phase and solid particle which is the secondary phase. This model was selected because it allowed the phases to interpenetrate and control volume will therefore be between 0 and 1, depending upon the space occupied by two phases. It was assumed that the flow is homogenous, we selected the homogenous mixture model assuming that there would be no slip velocity and the phases would move with the same velocity in capillary viscometer with very strong coupling between the phases. Mixture model would solve continuity, momentum and energy equation for mixture, volume fraction equation for secondary phase and algebraic equation for the relative velocities. Continuity equation for the mixture model is given by

$$\frac{\partial}{\partial t}(\rho_m) + \nabla \cdot (\rho_m \vec{v}_m) = \dot{m} \quad (3.1)$$

$$\vec{v}_m = \frac{\sum_{k=1}^n \alpha_k \rho_k \vec{v}_k}{\rho_m} \quad (3.2)$$

$$\rho_m = \sum_{k=1}^n \alpha_k \rho_k \quad (3.3)$$

Where  $\vec{v}_m$ ,  $\rho_m$  are the mass average velocity and density of the mixture,  $\dot{m}$  is the mass transfer due to cavitation and  $\alpha_k$  is the volume fraction of the phase k.

Momentum equation is given by

$$\frac{\partial}{\partial t}(\rho_m \vec{v}_m) + \nabla \cdot (\rho_m \vec{v}_m) = -\nabla P + \nabla \cdot [\mu_m (\nabla \vec{v}_m + \nabla \vec{v}_m^T)] + \rho_m \vec{g} + \vec{F} + \nabla \cdot \sum_{k=1}^n \alpha_k \rho_k \vec{v}_{dr,k} \quad (3.4)$$

$$\mu_m = \sum_{k=1}^n \alpha_k \mu_k \quad (3.5)$$

$$\vec{v}_{dr,k} = \vec{v}_k - \vec{v}_m \quad (3.6)$$

Where n,  $\vec{F}$ ,  $\mu_m$ ,  $\vec{v}_{dr,k}$  is the number of phases, body force, viscosity of mixture and drift velocity for the secondary phase respectively.

#### Limitation of mixture model

There are a few limitations while using a multi-phase mixture model such as it can only be used with a segregated solver, with only one compressible phase, solidification and melting, mixing of species and reacting flow cannot be modelled. Mixture model cannot be used for inviscid flow and second order time stepping formulation is not allowed.

### 3.2.7 Viscous modelling

Defining the problem like inviscid, laminar and turbulent flow, the viscous panel will allow us to define different parameters. As we are taking the flow to be a laminar flow because of semi-solid metal material having greater value for viscosity and the geometry design for the process that will make it laminar flow and illuminate any turbulence. Considering the flow as incompressible and isothermal, viscous heating option is turned off for our problem, as the viscous heating option greatly works with compressible flow and with the coupled solver.

### 3.2.8 Energy/Radiation modelling

Parameter relating energy and heat transfer modelled for problem was selected by putting all inputs for energy and heat transfer. System was assumed to be well isolated with isolate material, considering there will be no radiation or heat transfer in the flow region as system was assumed to be isothermal.

### 3.2.9 Material modelling

Material modelling helps us to define and create proper material with appropriate properties. Semi-solid aluminium was not present in the list given, we needed to create a new material from the global data base and to modify the properties for material or we could also modify the properties of an existing material and was given the name as semi-solid A356 aluminium alloy and was saved to system. Material under consideration defined in the material type; selecting fluid type from the available two types i.e. fluid and solid. Material properties were changed according semi-solid flow and system suitability. From the data base, liquid-solid material for fluid was modified. In Physical properties of the material we defined some of the material properties like density, specific heat, thermal conductivity and viscosity and all input value for the properties relating the problem [Table 4.13]. Flow was assumed to be incompressible flow i.e. density of material does not change, considering the density to be constant and not a function of temperature. Selecting constant and put the density for aluminium A356 alloy for the certain temperature and pressure. Thermal conductivity of the material was kept constant by considering that enough insulation provided to keep the material isothermal, and

heater bands were also provided, surrounding the die injection chamber in case of any heat losses, keeping it at a certain temperature. The specific heat capacity of the fluid and the surrounding chamber and capillary were set as a constant value at the operating temperature and condition [Table 4.13]. Power law non-Newtonian viscosity model was defined for the viscosity of the material. The equation for the viscosity with power law non-Newtonian model is given by

$$\eta = K \dot{\gamma}^{n-1} e^{T/t} \quad (3.7)$$

$T$  is the reference temperature ( $^{\circ} \text{C}$  or  $273 \text{ K}$ ) while  $t$  is the temperature of the flowing fluid. Minimum viscosity ( $\eta_{min}$ ) and maximum viscosity ( $\eta_{max}$ ) for the semi-solid flow of alloy A356 was selected as 0.01 and 100 Pa.s respectively.

### 3.2.10 Phase modelling

In phase modelling we defined two phases (liquid and solid phase) for semi-solid material flow and properties of phases were defined and modified for each phase and interaction between them. The liquid phase was defined as the primary phase while the solid particles were defined as secondary phase for the alloy A356. Diameter of the secondary phase particles was taken as  $10^{-5} \text{ m}$ . The name and properties of primary and secondary phase were specified.

### 3.2.11 Operating and boundary conditions

The gauge pressure was set to zero as Fluent takes the gauge pressure as an operating pressure and atmospheric pressure was taken as the operating pressure. Relationship between the absolute pressure, gauge pressure and atmospheric pressure is given by

$$P_{\text{absolute}} = P_{\text{gauge}} + P_{\text{oper}} \quad (3.8)$$

Gravitational acceleration was set at  $9.81 \text{ ms}^{-2}$ . Boundary conditions were set for the capillary viscometer. Zones and boundaries already specified in Gambit needed to be defined the boundary conditions for each zone and their respected values. Semi-solid A356 alloy was defined as the flowing fluid through capillary viscometer. For the zone inlet velocity, the velocity inlet was set to 0.075 m/s, 0.5 m/s and 1 m/s respectively for

each set of experiments and temperature of the fluid (semi-solid) for the inlet boundary conditions while pressure outlet was specified as the outlet boundary condition as pressure at the outlet of the capillary viscometer (atmospheric pressure). Wall of the capillary viscometer was specified for specified wall thickness (32.5 mm) and temperature with isothermal condition. Selecting stationary wall condition for wall, as it was assumed that grid will remain stationary with the flow with no slip conditions.

### 3.2.12 Model initializing solution

Model solution allows us to solve the equation related to the model. Fluent automatically solved all those equations that have been defined in the model. We specified the inlet velocity to initialize the flow of semi-solid material as it is the only known parameter. Different inlet velocities as given in table 4.14 were used to initialize the solution. Volume fraction of solid for the secondary phase was specified at the particular temperature for the initialize solution [Table 4.14]. For the Residual to be printed, plotted and to be monitored at different intervals of time or iterations, print and plot options were selected. The number of iteration defined for the solution was taken as 10000 iterations for convergence. Time statistic of pressure, velocity, viscosity and number of iterations was also set for solution to plot the results and the data for each variable by selecting the time date statistic for the flow. Numbers of time step was taken as 100 while time step size was taken as (0.001). Each iteration was used to monitor the convergence of the solution. Solution was converged after 1550 iterations and the semi-solid flowed through the end of the capillary viscometer. Once the solution was converged, we could easily find the flow time of the material through the capillary viscometer. Results for the viscosity, velocity and pressure variation during the flow of semi-solid material in the capillary viscometer were obtained and were saved to the specified files

## 3.3 Summary

In this chapter, GAMBIT was used to create and modify the grid for this project and to model the geometry for capillary viscometer. Computation fluid dynamics software

Fluent was used to model the flow of semi-solid A356 with the specified material properties and boundary condition for flow through capillary viscometer. Data was captured and results were obtained for the pressure, velocity and viscosity variation of semi-solid flow with different material inlet conditions and the results are presented in the next chapter 4.

# Chapter 4

## Results

### 4.1 Numerical calculation and results

Numerical calculations were carried out to relate the rotational speed of the motor to the linear speed of the plunger, and to the velocity in the capillary tube to the shear rate in the capillary. Tables 4.3-4.7 were generated in order to allow the setting of the motor speed for the specific desired shear rate. Further user of this device can select a shear rate and set of motor speed appropriately by using these tables. It allowed us selection of the motor speed limitation for the experiments as motor has a maximum speed on 3000 rpm, so our system is limited to this motor speed [appendix C]. Tables 4.8-4.12 were generated in order to allow calculations of the limits of the load cell allowed to measure the pressure in the capillary viscometer. These also allowed the determination of the load cell measurement range required. The load cell of 250 Newton load can be only used with a maximum pressure of 8.84 MPa (Appendix A). Our system is limited to work at that pressure and beyond that pressure our system would not measure the pressure. In tables 4.8-4.12, the highlighted values show that our system will not be applicable for those shear rates for their mentioned viscosities.

This information was used to find different values of shear rate for the purpose of comparison with previous work. The values were also used for designing of capillary viscometer and to select the process parameters for semi-solid metal processing. Different value of shear rate were taken from previous work with rotational type viscometers and converted into equivalent linear speeds for the capillary viscometer [21]. Table 4.1 shows viscosity of semi-solid A356 alloy with a solid fraction of some of the shear rate range used previously and used as a reference for this work  $f_s = 0.33$  with a power law index on  $n = -0.3$  at different shear rates conditions while Table 4.2 shows the viscosity at a solid fraction of  $f_s = 0.4$  for alloy A356 using the same value of power law

index with different shearing conditions [21]. These two value for solid fraction  $f_s=0.33$  and 0.4 is used for the both the simulation and experimental work in this project

Material alloy	Fraction solid, $f_s$	Shear rate range (1/s)	viscosity $\eta$ (Pa .s)	Power law Index $n$
A356	0.33	3.1	60	-0.3
A356	0.33	6.3	10.8	-0.3
A356	0.33	23.7	3.2	-0.3
A356	0.33	54.9	1.2	-0.3
A356	0.33	106	0.42	-0.3

Table: 4.1 Steady state viscosities of alloy A356 at 0.33  $f_s$  [21]

Material alloy	Fraction solid, $f_s$	Shear rate range (1/s)	viscosity $\eta$ (Pa .s)	Power law Index $n$
A356	0.4	4	75	-0.3
A356	0.4	8.5	28	-0.3
A356	0.4	12.5	5.9	-0.3
A356	0.4	75	2.2	-0.3
A356	0.4	100	1.3	-0.3
A356	0.4	108	0.7	-0.3

Table: 4.2 Steady state viscosities of alloy A356 at 0.40  $f_s$  [21]

Equation 4.1 was used to calculate the linear velocity in the capillary viscometer for the specific shear rate used previously for rotational type capillary viscometer. The shear rate at the wall of the capillary is given by:

$$\dot{\gamma}_w = \frac{4Q}{\pi R_c^3} \left( \frac{3}{4} + \frac{1}{4n} \right) \quad (4.1)$$



$$Q = A_1 \times V_1 \quad (4.2)$$

$$A_1 = \pi R_c^2 \quad (4.3)$$

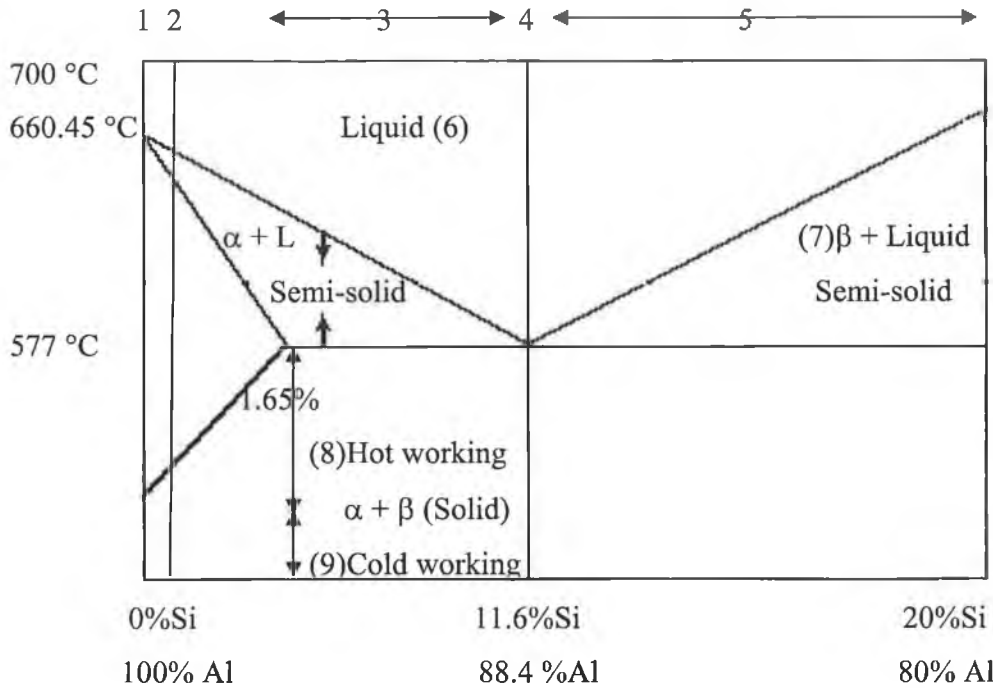


Fig: 4a Schematic of Al-Si phase diagram indicating (1) pure Metals, (2) solid solution, (3) hypoeutectic alloy, (4) eutectic alloys, (5) hypereutectic alloys, (6) liquid alloys, (7) semi-solid metals, (8) hot working temperature range, (9) cold working temperature range.

$Q$  is the flow rate,  $\text{m}^3/\text{sec}$ ,  $A_1$  is the area in  $\text{m}^2$  and  $V_1$  is the velocity  $\text{m/s}$  in the capillary tube,  $R_c$  is the radius in  $\text{m}$  of the capillary tube, and  $n$  is the flow index (dimensionless).

$$\dot{\gamma}_w = \frac{4A_1V_1}{\pi R_c^3} \left( \frac{3}{4} + \frac{1}{4n} \right)$$

Different values of shear rates and flow index in equation 4.1 were used to calculate velocity in the tube.. By applying equation

$$A_1V_1 = A_2V_2 \quad (4.4)$$

$A_1$  and  $A_2$  are area of the tube and die-chamber respectively. Putting values of  $V_1$ ,  $A_1$  and  $A_2$  in equation 4.4,  $V_2$  can be found which is the velocity of semi-solid in die-chamber

$$V_2 = 2\pi R_2 N \quad (4.5)$$

$R_2$  is the radius of gear and  $N$  is the speed in rev/min. The motor used in the designed experimental work has a gear ratio of 1:7.

The value of  $n$  has a great effect on the velocities and shear rates as shown in equation 4.1 and shows the thixotropic behaviour of the material. Different shear rates were investigated with different values of  $n$  used in equation 4.1 to find effect on velocity of the material with different values of flow index  $n$ . Results are shown in the tables below how the velocity variation occurs with the increasing or decreasing value of  $n$ . Table 4.3 and 4.4 shows different value of velocities both linear and rotational at different shear rate for  $n = 0.3$  and  $n = 0.1$  respectively.

The value of  $n$  was also investigated at negative levels. Table 4.5 and 4.6 shows the values of velocities in the injection chamber, and capillary tube and motor speed in rev/min for values of  $n$  taken as  $-0.1$  and  $-0.3$  respectively. For Newtonian fluid  $n$  is taken as 1 and velocity is calculated at different shear rates in the capillary tube. Values of  $n$  less than 1 are indicative of pseudoplastic fluids. Table 4.7 shows the values of velocity in different section of capillary viscometer for  $n$  equal to 1.

Shear rate (1/s)	Capillary velocity (m/sec)	Injection chamber velocity (m/sec)	Rotational speed, after gearing (rev/min)	Motor speed, PLC setting (rev/min)
3.1	0.001468	0.0000845	0.0646	0.4522
6.3	0.002984	0.0001718	0.1313	0.9193
23.7	0.0112	0.0006466	0.494	3.4583
54.9	0.026	0.001497	1.144	8.0112
82.7	0.03917	0.0022564	1.7239	12.067
112.8	0.05343	0.003077	2.3514	16.4601
500	0.2368	0.01364	10.4231	72.9617
1000	0.47364	0.027284	20.8464	145.9235
10000	4.47364	0.27284	208.4621	1459.235

Table: 4.3 Velocity values for different shear rates with a flow index of  $n = 0.3$

Shear rate 1/s	Capillary velocity (m/sec)	Injection chamber velocity (m/sec)	Rotational speed, after gearing (rev/min)	Motor speed, PLC setting (rev/min)
3.1	0.000715	0.0000412	0.0314	0.2203
6.3	0.001453	0.00008369	0.063944	0.44761
23.7	0.005469	0.000315	0.2406	1.6848
54.9	0.01266	0.0007297	0.55755	3.9028
82.7	0.019084	0.001099	0.83988	5.8792
112.8	0.02603	0.001499	1.14554	8.018817
500	0.11538	0.006646	5.0779	35.5454
1000	0.23076	0.01329	10.15408	71.07853
10000	2.30769	0.13292	101.5584	710.853

Table: 4.4 Velocity values for different shear rates with a flow index of  $n = 0.1$

Shear rate 1/s	Capillary velocity (m/sec)	Injection chamber velocity (m/sec)	Rotational speed, after gearing (rev/min)	Motor speed, PLC setting (rev/min)
3.1	0.001328	0.00007652	0.0584	0.40928
6.3	0.0027	0.00015552	0.11882	0.83176
23.7	0.0101	0.000585	0.447	3.129
54.9	0.02352	0.001355	1.03546	7.2482
82.7	0.03544	0.002041	1.5597	10.9158
112.8	0.04834	0.0027845	2.1275	14.8925
500	0.21428	0.012342	9.43042	66.0129
1000	0.42857	0.02468	18.8608	132.025
10000	4.2857	0.2468	188.608	1320.26

Table: 4.5 Velocity values for different shear rates with a flow index of  $n = -0.1$

Shear rate 1/s	Capillary velocity (m/sec)	Injection chamber velocity (m/sec)	Rotational speed, after gearing (rev/min)	Motor speed, PLC setting (rev/min)
3.1	0.0279	0.001607	1.2278	8.5949
6.3	0.05767	0.003265	2.4953	17.4672
23.7	0.2133	0.01228	9.387	65.7099
54.9	0.4941	0.02846	21.7448	152.214
82.7	0.7443	0.042872	32.7559	229.291
112.8	1.01521	0.05847	44.678	312.7462
500	4.5	0.2592	198.038	1386.27
1000	9	0.5184	396.081	2772.57
10000	90	5.18405	3960.81	27725.73

Table: 4.6 Velocity values for different shear rates with a flow index of  $n = -0.3$

Shear rate 1/s	Capillary velocity (m/sec)	Injection chamber velocity (m/sec)	Rotational speed, after gearing (rev/min)	Motor speed, PLC setting (rev/min)
3.1	0.002325	0.00013392	0.1023	0.7162
6.3	0.004725	0.0002721	0.2078	1.45
23.7	0.017775	0.001023	0.78	5.4757
54.9	0.041175	0.002371	1.812	12.684
82.7	0.06202	0.003572	2.7296	19.1
112.8	0.0846	0.004872	3.7231	26.06
500	0.375	0.0216	16.5	115.522
1000	0.75	0.0432	33.0064	231.04
10000	7.5	0.432	330.06	2310.45

Table: 4.7 Velocity values for different shear rates with a flow index of  $n = 1$

The pressure differential across the capillary,  $\Delta P$ , is directly related to the fluid viscosity. The following equation shows the relationship between the viscosity and change in pressure of material.

$$\eta = \frac{\Delta P \pi R^4}{8LQ} \quad (4.6)$$

$R$  is the radius of capillary tube in m,  $L$  is the length of capillary in m, and  $Q$  is the flow rate  $m^3/sec$ . The values of  $R$  and  $L$  were constant from the design. Different shear rate in equation 4.1 shows different capillary and motor velocities leading to different flow rate in capillary. Putting values from table 4.3-table 4.7 for velocities in equation 4.6, we generated tables 4.8-4.12 at different shear rates and viscosities at different values of  $n$ . Table 4.8 to 4.12 shows the resulting of change in pressure  $\Delta P$  at values of  $n = 0.3, 0.1, -0.1, -0.3, 1$  and viscosity values taken as 0.01, 0.1, 1, 10, and 100. Values for  $Q$  and  $A$  were obtained from equation 4.2 and 4.3 respectively and then put in equation 4.6. In equation 4.6, we have two unknowns, that viscosity  $\eta$  and  $\Delta P$ . Keeping value  $\eta$  constant in equation 4.6, different value of  $\Delta P$  can be obtained with changing value of flow index  $n$ .

Shear rate, (1/s)	$\Delta P$ (Pa) at $\eta = 0.01$ (Pa.s)	$\Delta P$ (Pa) at $\eta = 0.1$ (Pa.s)	$\Delta P$ (Pa) at $\eta = 1$ (Pa.s)	$\Delta P$ (Pa) at $\eta = 10$ (Pa.s)	$\Delta P$ (Pa) at $\eta = 100$ (Pa.s)
3.1	9.70896	97.0896	970.836	9708.36	97083.6
6.3	19.734	197.34	1973.4	19734.1	197341
23.7	74.069	740.69	7406.929	74069.29	740692.9
54.9	171.94	1719.4	17194.6	171946.9	1719465
82.7	259.044	2590.44	25904.4	259044	2590440
112.8	353.35	3533.502	35335.02	353350.2	3533502
500	1566.03	15660.3	156603	1566030	15660300
1000	3132.35	31323.5	313233	3132330	31323300
10000	31323.5	313235	3132330	31323300	313233000

Table 4.8  $\Delta P$  values at specified shear rates, viscosities of the semi-solid and  $n = 0.3$

Shear rate, (1/s)	$\Delta P$ (Pa) at $\eta = 0.01$ (Pa.s)	$\Delta P$ (Pa) at $\eta = 0.1$ (Pa.s)	$\Delta P$ (Pa) at $\eta = 1$ (Pa.s)	$\Delta P$ (Pa) at $\eta = 10$ (Pa.s)	$\Delta P$ (Pa) at $\eta = 100$ (Pa.s)
3.1	4.73104	47.3104	473.104	4731.04	47310.4
6.3	9.609168	96.09168	960.91	9609.1	96091.68
23.7	36.168	361.68	3616.8	36168	361680
54.9	83.724	837.24	8372.4	83724.7	837247
82.7	126.208	1262.08	12620.8	126208	1262080
112.8	172.144	1721.44	17214.4	172144	1721449
500	763.046	7630.46	76304.6	763046	7630460
1000	1526.152	15261.52	152615.2	1526152	15261520
10000	15261.52	152615.2	1526152	15261520	152615200

Table 4.9  $\Delta P$  values at different shear rates, viscosities of the semi-solid and  $n = 0.1$

Shear rate, (1/s)	$\Delta P$ (Pa) at $\eta = 0.01$ (Pa.s)	$\Delta P$ (Pa) at $\eta = 0.1$ (Pa.s)	$\Delta P$ (Pa) at $\eta = 1$ (Pa.s)	$\Delta P$ (Pa) at $\eta = 10$ (Pa.s)	$\Delta P$ (Pa) at $\eta = 100$ (Pa.s)
3.1	8.7825	87.825	878.25	8782.5	87825
6.3	17.85599	178.55	1785.5	17855.99	178559.9
23.7	66.79433	667.94	6679.433	66794.33	667943.3
54.9	155.545	1555.45	15554.5	155545	1555450
82.7	234.376	2343.7	23437.6	234376	2343760
112.8	319.688	3196.88	31968.8	319688	3196880
500	1417.1	14171	141710	1417100	14170380
1000	2834.27	28342.7	283427	2834270	28342740
10000	28342.7	283427	2834270	28342740	283427400

Table 4.10  $\Delta P$  values at different shear rates, viscosities of the semi-solid and  $n = -0.1$

Shear rate, (1/s)	$\Delta P$ ( Pa) at $\eta = 0.01$ (Pa.s)	$\Delta P$ (Pa) at $\eta = 0.1$ (Pa.s)	$\Delta P$ (Pa) at $\eta = 1$ (Pa.s)	$\Delta P$ (Pa) at $\eta = 10$ (Pa.s)	$\Delta P$ (Pa) at $\eta = 100$ (Pa.s)
3.1	18.45119	184.5119	1845.119	18451.19	1845119
6.3	381.3907	3813.907	38139.07	381390.7	3813907
23.7	1410.623	14106.23	141062.3	1410623	14106230
54.9	3267.646	32676.46	326764.6	3267646	32676460
82.7	4922.301	49223.01	492230.1	4922301	49223010
112.8	6713.918	67139.18	671391.8	6713918	67139180
500	29759.98	297599.8	2975998	29759980	297599800
1000	59519.91	595199.7	5951997	59519970	595199700
10000	595199.7	5951997	59519970	595199700	595199700

Table 4.11  $\Delta P$  values at different shear rates, viscosities of the semi-solid and  $n = 0.3$

Shear rate, (1/s)	$\Delta P$ ( Pa) at $\eta = 0.01$ (Pa.s)	$\Delta P$ (Pa) at $\eta = 0.1$ (Pa.s)	$\Delta P$ (Pa) at $\eta = 1$ (Pa.s)	$\Delta P$ (Pa) at $\eta = 10$ (Pa.s)	$\Delta P$ (Pa) at $\eta = 100$ (Pa.s)
3.1	15.3775	153.76	1537.5	15375	153750
6.3	31.2479	312.47	3124.7	31247	312479
23.7	117.551	1175.55	11755	117550	1175510
54.9	272.3	2723	27230	272300	2723038
82.7	410.158	4101.5	41015.8	410158	4101580
112.8	559.48	5594.8	55948	559480	5594870
500	2479.99	24799	247999	2479998	2479990
1000	4959.99	49599	495999	4959990	49599900
10000	49599.99	495990	4959900	49599900	495999000

Table 4.12  $\Delta P$  values at different shear rates, viscosities of the semi-solid and  $n = 1$

## 4.2 Material properties for modelling and simulation experiments and results

A non-Newtonian power law with laminar, axisymmetric, isothermal, incompressible flow and with no slip at the boundary wall is assumed for these simulations. Material properties were kept constant for all the simulations. The thixotropic behaviour of semi-solid aluminium was studied through simulations with different boundary conditions.

Initial simulation results were compared with previous results from a rotational type viscometer [21]. This allowed initial linear speed calculations to determine the velocities

required to push the slurry from the load position to the entrance of the capillary without inducing turbulence. Pressure and velocity profiles were obtained and variations during transient flow was studied after different holding times and shear stresses. The main interest in the simulations was to obtain transient response flow data during semisolid metal processing. In Fluent three sets of simulation results were obtained from model set-up parameters with an inlet velocity of  $0.075 \text{ ms}^{-1}$ ,  $0.5 \text{ ms}^{-1}$  and  $1 \text{ ms}^{-1}$  and at different temperature (solid fractions). During the simulation, dynamic pressure, velocity and viscosities were continuously recorded so that they could be assessed with the different plunger velocity and solid fraction set conditions. Table No: 4.13 shows the material property data of aluminium alloy A356 for different experiments and Table No: 4.14 shows fluid velocity and solid fractions used during the experiments [21, 36, and 93]. Transient flow results were recorded at a time interval of 2 seconds for inlet velocity of  $0.075 \text{ m/s}$ , 0.28 sec for an inlet plunger speed of  $0.5 \text{ m/sec}$  and 0.1 sec for an inlet plunger velocity of  $1 \text{ m/sec}$ . Transient results are more important in this process than steady state as actual processing occurs in a very short time period. Variation of pressure, viscosity and velocity with respect to distance in the capillary viscometer were recorded. Velocity, pressure and viscosity curves were recorded at different motor speed, temperature and different solid fraction from the start to end point in capillary viscometer.

Property	Value
Density, $\text{kg-m}^3$	2685
Thermal conductivity $\text{W-m}^{-1}\text{-K}^{-1}$	150
Heat capacity	950
Power law index, $n$	-0.3
Consistency index, K	100

Table: 4.13 Physical properties of A356 aluminium alloy material for the simulation [21,36,93].

Case No:	Plunger velocity, m/s	Solid fraction, $f_s$	Temperature of the billet, K
1.	0.075, 0.5 and 1	0.25	878
2.	0.075, 0.5 and 1	0.30	874
3.	0.075, 0.5 and 1	0.33	871
4.	0.075, 0.5 and 1	0.40	863
5.	0.075, 0.5 and 1	0.50	848

Table: 4.14 Solid fraction, billet temperature and plunger speed for simulation [21].

All these parameters play very important roles in semi-solid metal processing. Figures 4.1 to 4.3 show the dynamic pressure, velocity and viscosity variation of the semi-solid flowing through the injection chamber, semi-cone angle section and capillary tube section for a fraction solid of 0.33, temperature of 871 K and motor inlet velocity of 0.075 m/sec respectively. Figures 4.4 to 4.6 show variation of pressure, velocity and viscosity at fraction solid of 0.40, temperature of 863 K and 0.075 m/sec inlet velocity. Flow results at the same input velocity for temperatures of 848 K at solid fraction of 0.50) are shown in figures 4.7 to 4.9 respectively. These figures show a general trend of increased viscosity with increasing solid fraction [appendix H]

Similarly, flow results at the higher injection speeds of 0.5 m/s were obtained and shown in figures 4.10-4.18 for the solid fraction of 0.33, 0.40 and 0.50. For the inlet velocity of 0.5 m/sec large shearing is observed mostly in cone section of viscometer where most of velocity variation occurred and can be seen in figure 4.12, 4.15 and 4.18. Dynamic pressure and velocity showed some increase while viscosity of the semi-solid showed some decrease as velocity was increased from 0.075- 0.5 m/sec.

The inlet velocity of 1 m/sec was chosen as this is close to that used in practice during semi-solid metal processing to study the flow pattern at this higher velocity. Flow results at this higher injection speed of 1 m/s can be seen in figures 4.19-4.27. At this injection speed, a more noticeable increase in the velocity and dynamic pressure in the viscometer were apparent with a corresponding increase in the viscosity of the semi-solid.



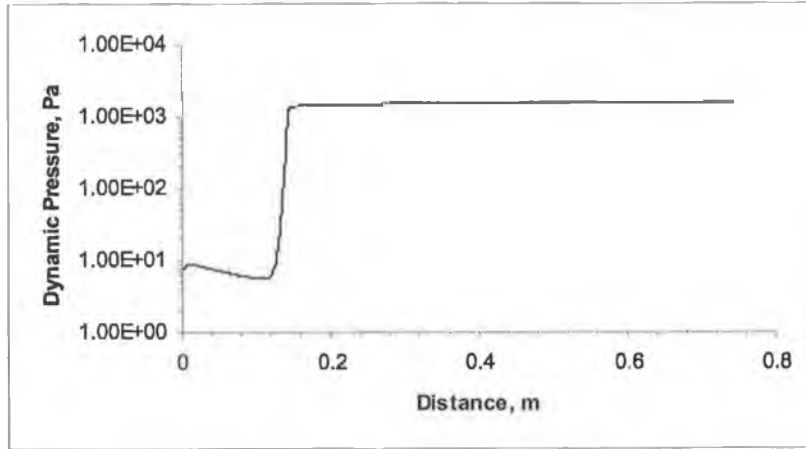


Figure: 4.1 Dynamic pressure at  $0.33 f_s$ , 871 K and 0.075 m/s plunger velocity

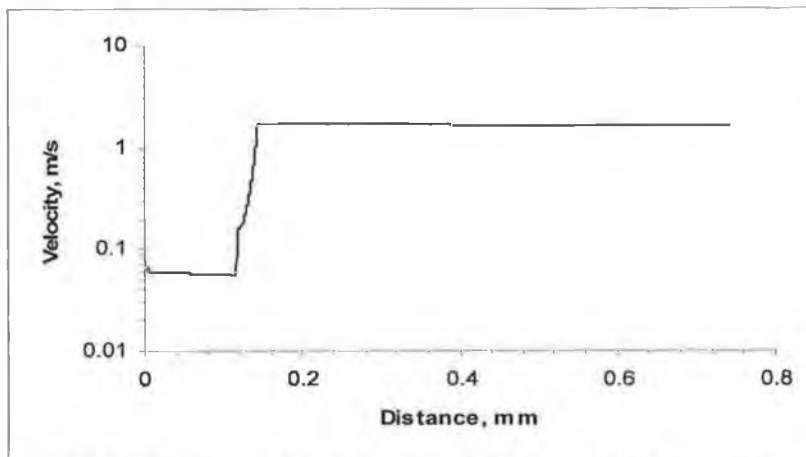


Figure: 4.2 Velocity at  $0.33 f_s$ , 871 K and 0.075 m/s plunger velocity

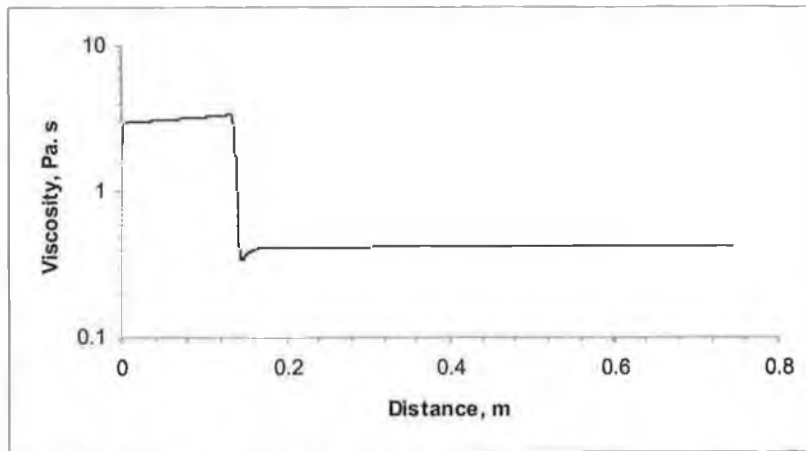


Figure: 4.3 Viscosity at  $0.33 f_s$ , 871 K and 0.075 m/s plunger velocity

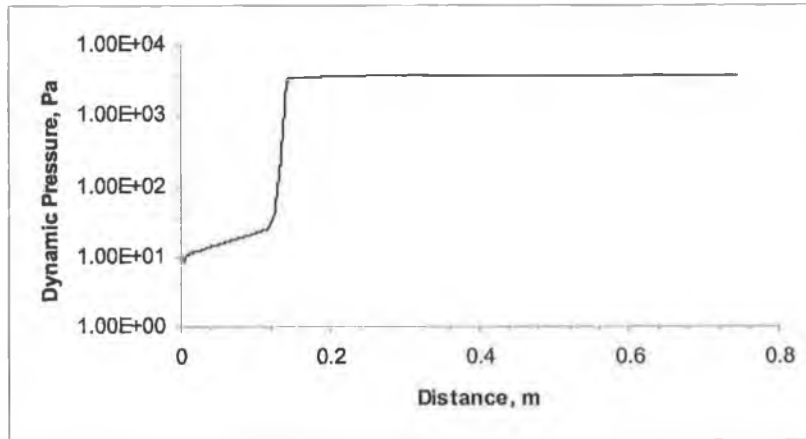


Figure: 4.4 Dynamic pressure at  $0.40 f_s$ , 863 K and 0.075 m/s plunger velocity

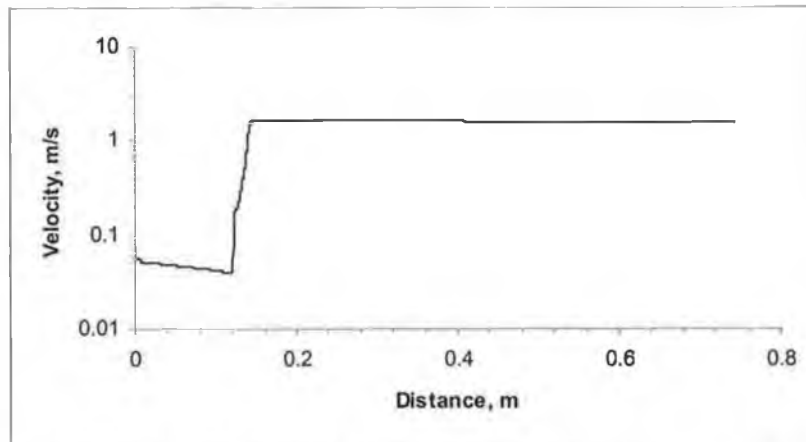


Figure: 4.5 Velocity at  $0.40 f_s$ , 863 K and 0.075 m/s plunger velocity

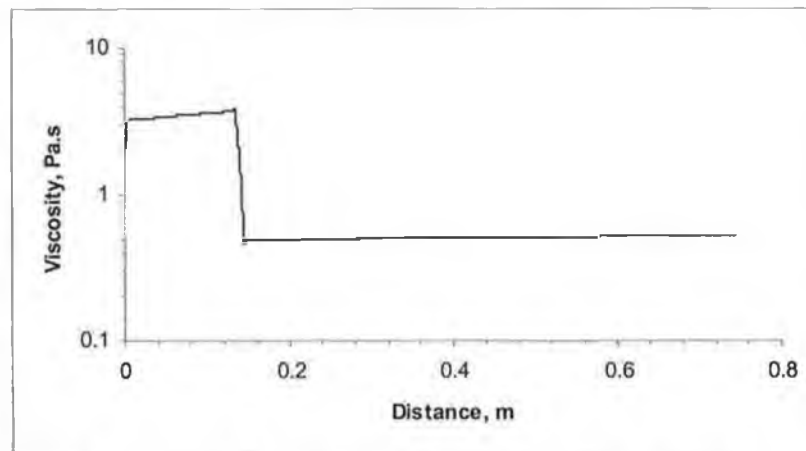


Figure: 4.6 viscosity at  $0.40 f_s$ , 863 K and 0.075 m/s plunger velocity

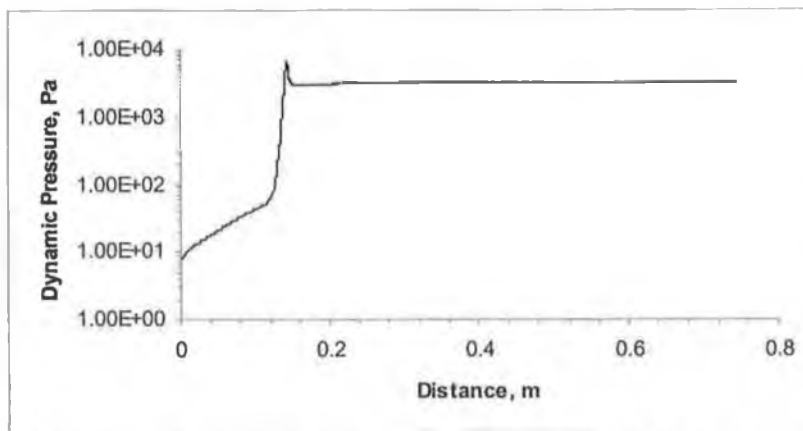


Figure: 4.7 Dynamic pressure at  $0.50 f_s$ , 848 K and 0.075 m/s plunger velocity

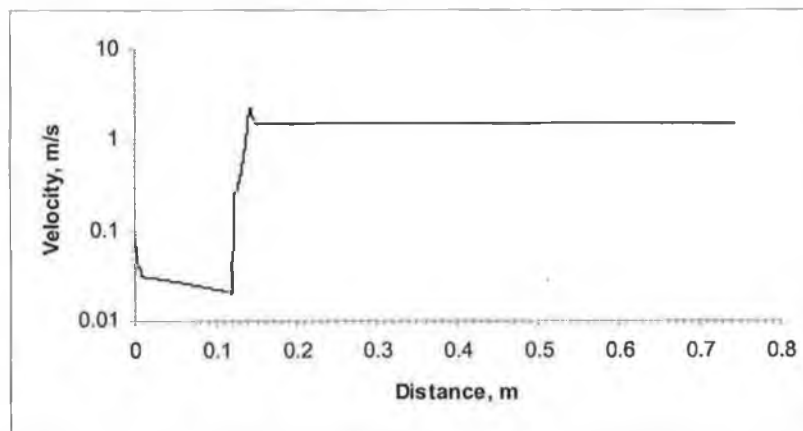


Figure: 4.8 Velocity at  $0.50 f_s$ , 848 K and 0.075 m/s plunger velocity

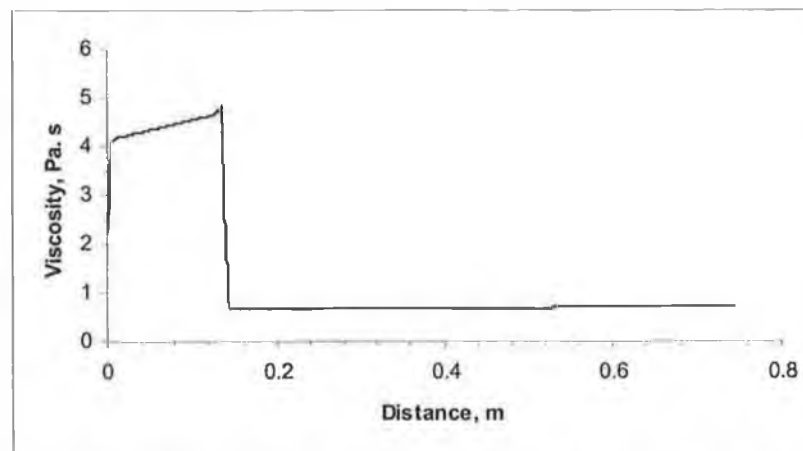


Figure: 4.9 Viscosity at  $0.50 f_s$ , 848 K and 0.075 m/s plunger velocity

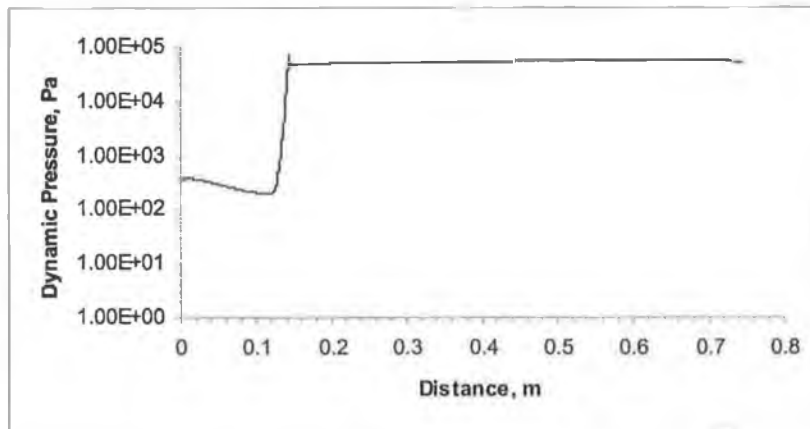


Figure: 4.10 Dynamic pressure of A356 at  $0.33 f_s$ , 871 K and 0.5 m/s plunger velocity

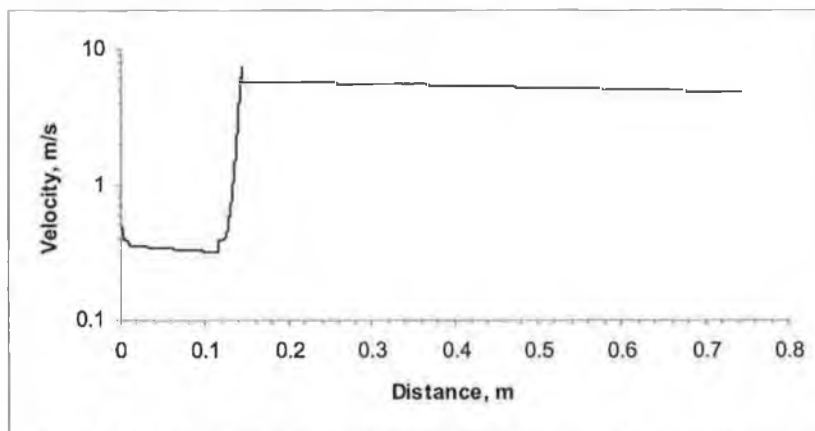


Figure: 4.11 Velocity of A356 at  $0.33 f_s$ , 871 K and 0.5 m/s plunger velocity

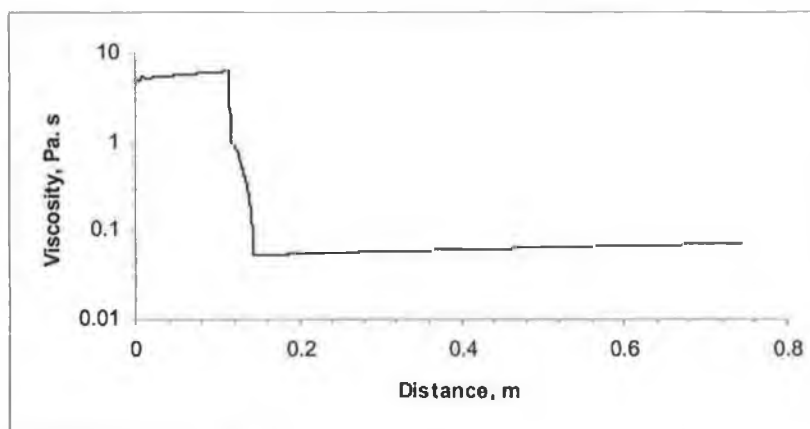


Figure: 4.12 Viscosity of A356 at  $0.33 f_s$ , 871 K and 0.5 m/s plunger velocity

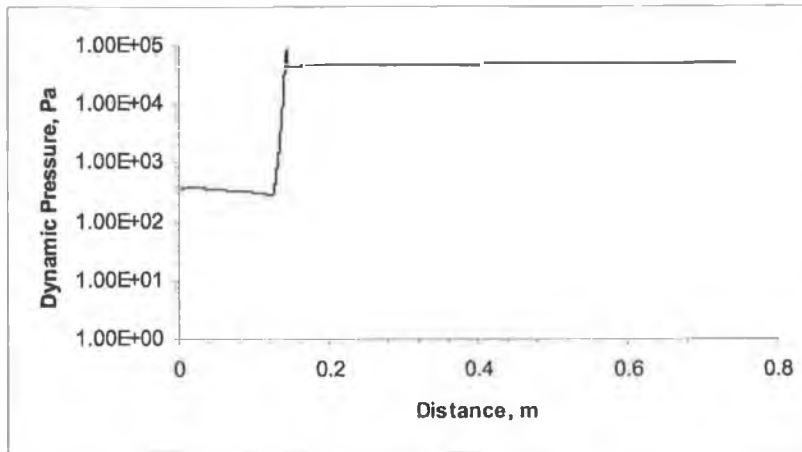


Figure: 4.13 Dynamic pressure of A356 at  $0.4 f_s$ , 863 K and 0.5 m/s plunger velocity

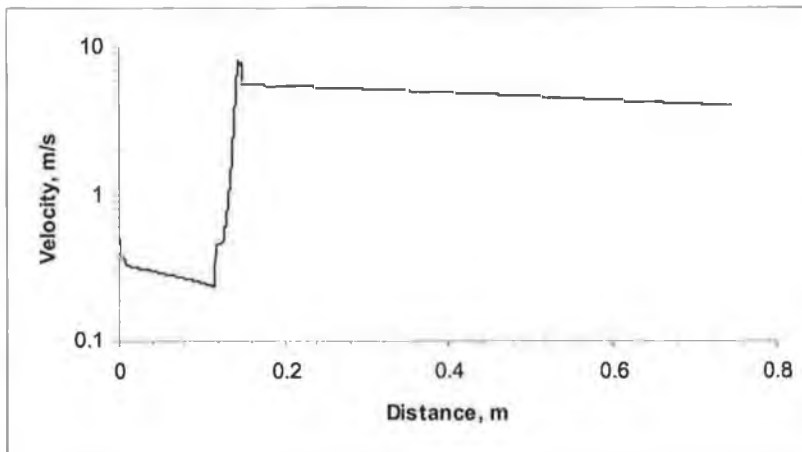


Figure: 4.14 Velocity of A356 at  $0.4 f_s$ , 863 K and 0.5 m/s plunger velocity

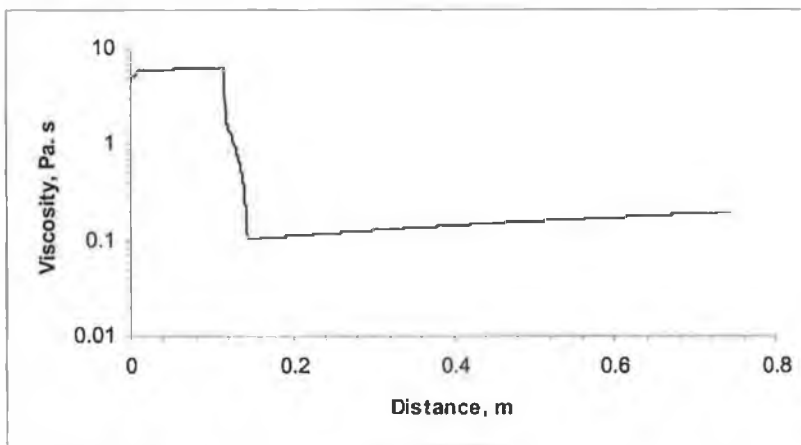


Figure: 4.15 Viscosity of A356 at  $0.4 f_s$ , 863 K and 0.5 m/s plunger velocity

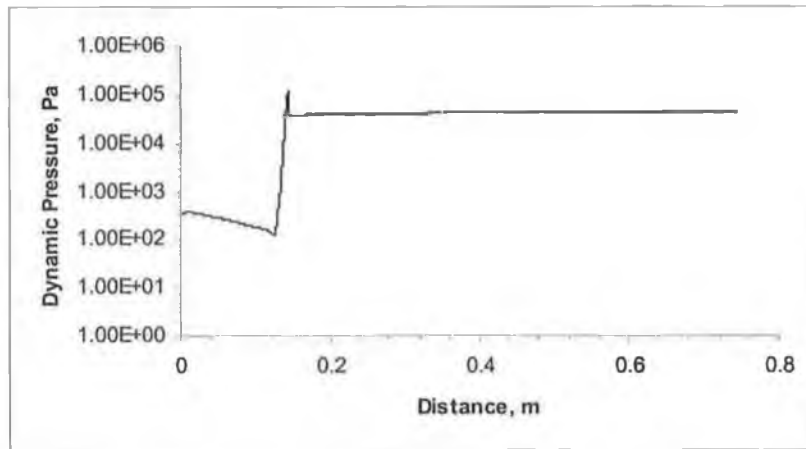


Figure: 4.16 Dynamic pressure of A356 at  $0.5 f_s$ , 848 K and 0.5 m/s plunger velocity

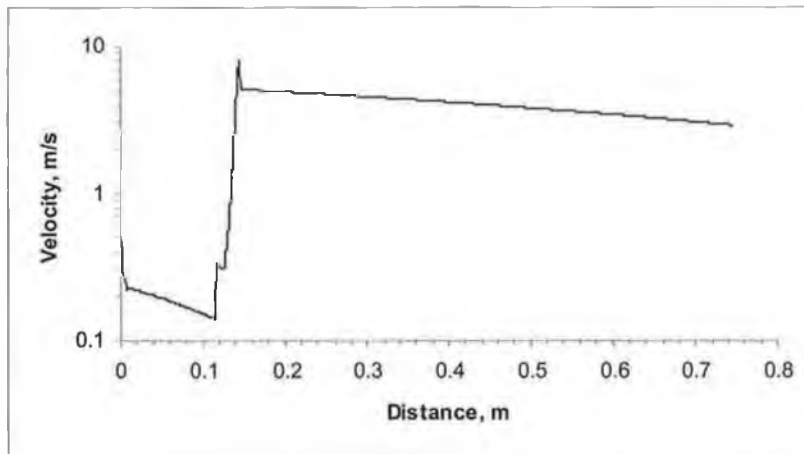


Figure: 4.17 Velocity of A356 at  $0.5 f_s$ , 848 K and 0.5 m/s plunger velocity

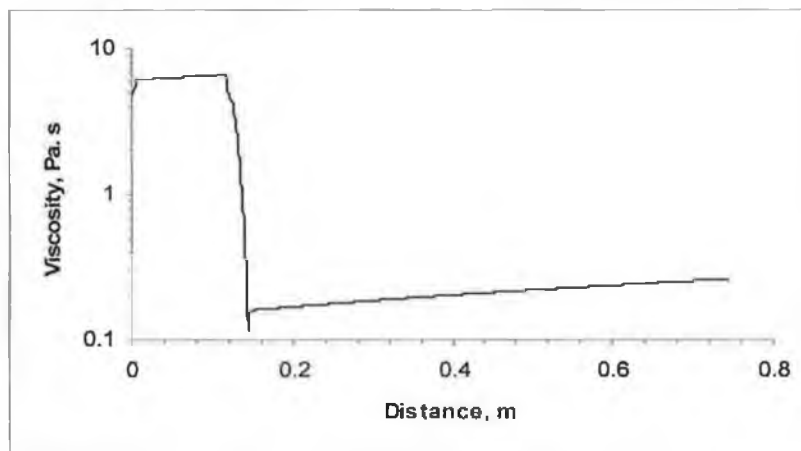


Figure: 4.18 Viscosity of A356 at  $0.50 f_s$ , 848 K and 0.5 m/s plunger

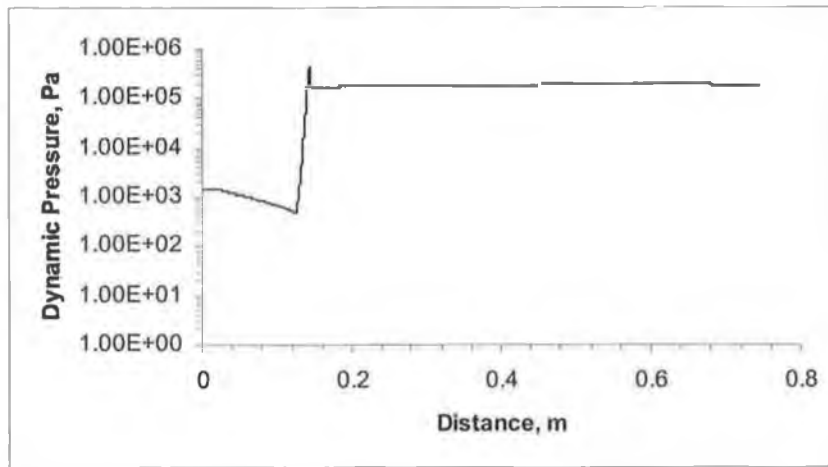


Figure: 4.19 Dynamic pressure of A356 at  $0.33 f_s$ , 871 K and 1 m/s plunger velocity

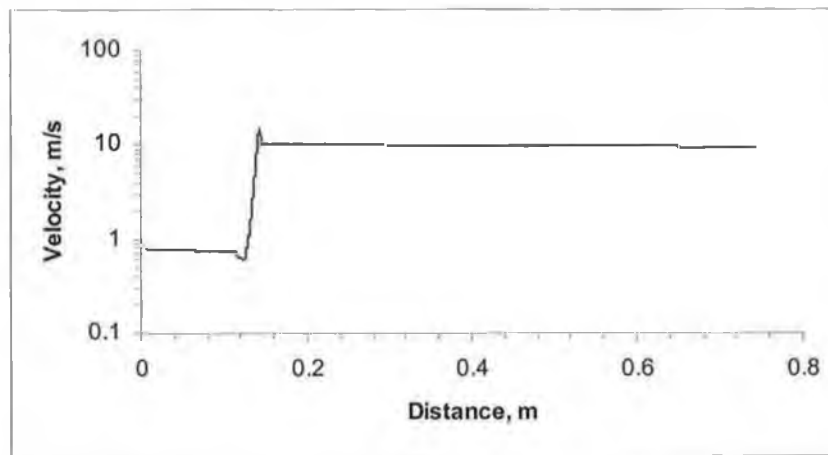


Figure: 4.20 Velocity of A356 at  $0.33 f_s$ , 871 K and 1 m/s plunger velocity

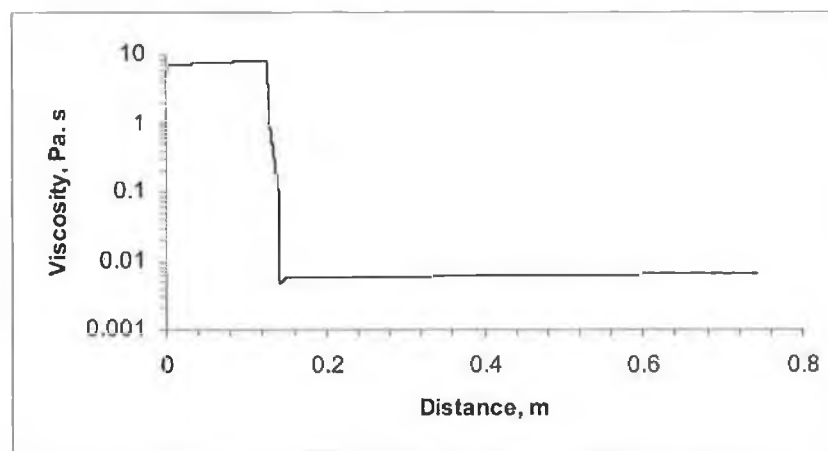


Figure: 4.21 Viscosity of A356 at  $0.33 f_s$ , 871 K and 1 m/s plunger velocity

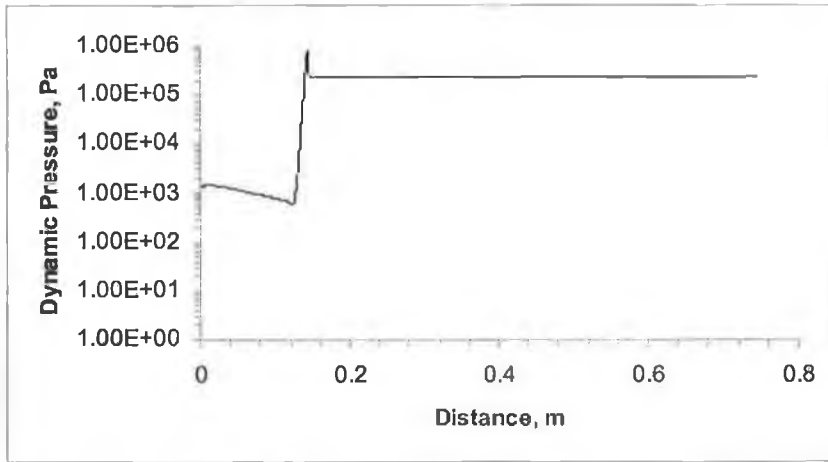


Figure: 4.22 Dynamic pressure of A356 at  $0.40 f_s$ , 863 K and 1 m/s plunger velocity

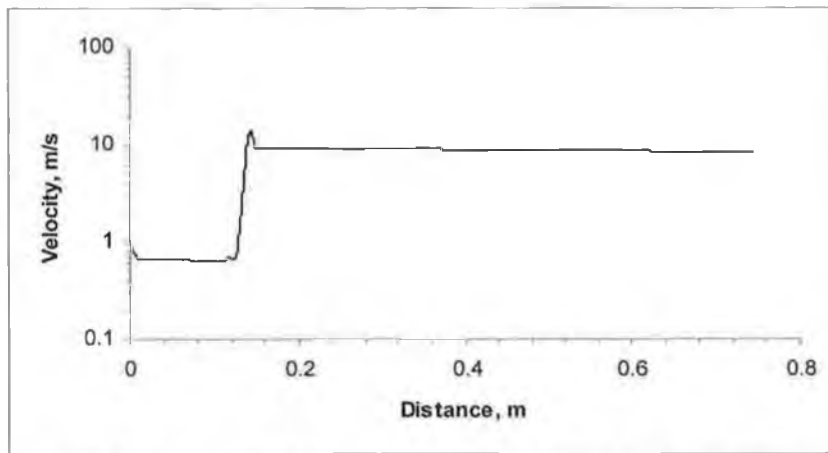


Figure: 4.23 Velocity of A356 at  $0.40 f_s$ , 863 K and 1 m/s plunger velocity

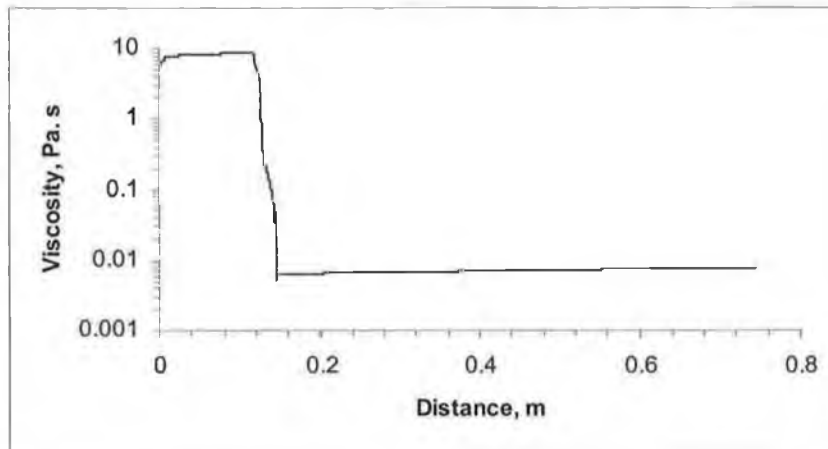


Figure No: 4.24 Viscosity of A356 at  $0.40 f_s$ , 863 K and 1 m/s plunger velocity



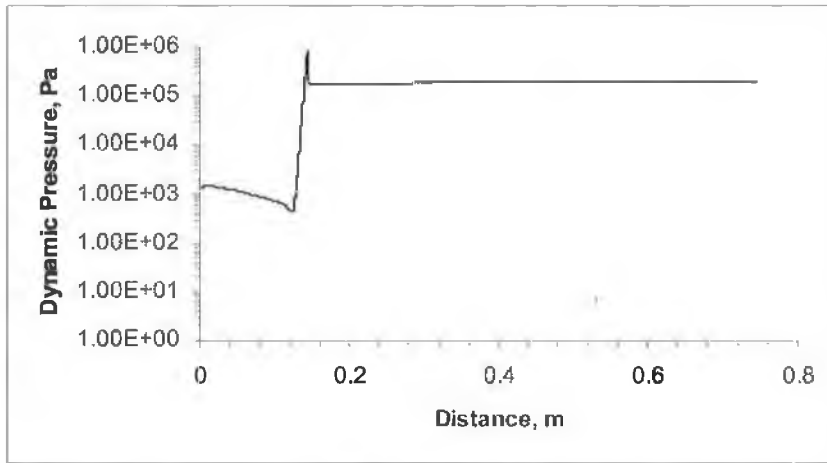


Figure: 4.25 Dynamic pressure of A356 at  $0.50 f_s$ , 848 K and 1 m/s plunger velocity

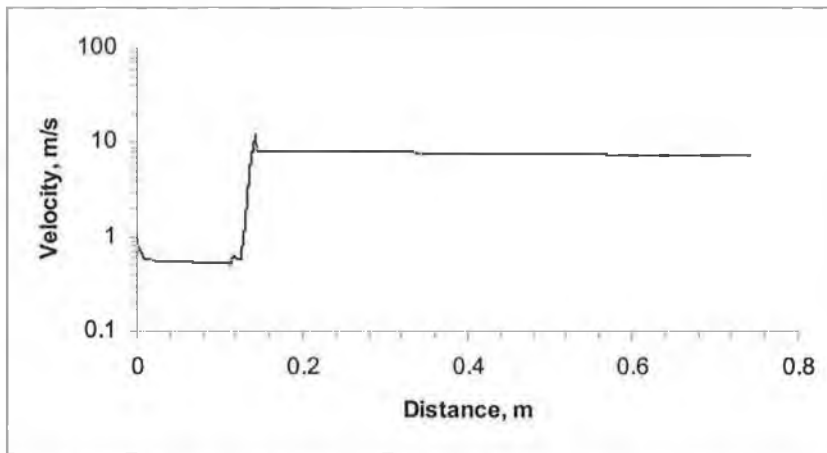


Figure: 4.26 Velocity of A356 at  $0.5 f_s$ , 848 K and 1 m/s plunger velocity

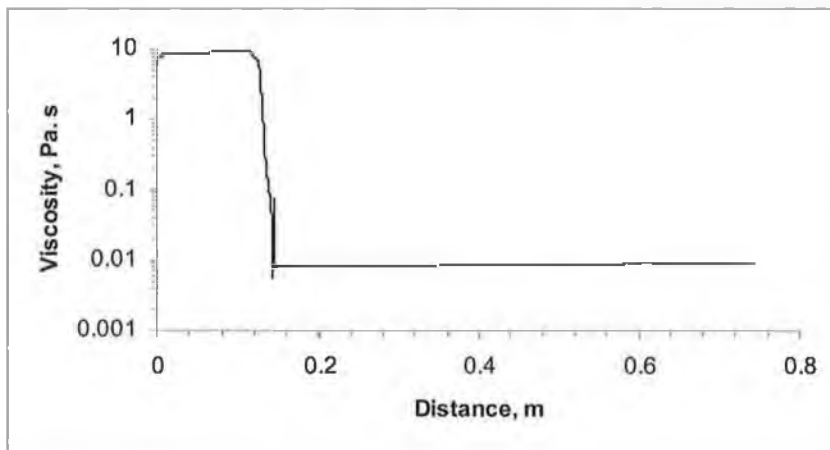


Figure: 4.27 Viscosity of A356 at  $0.50 f_s$ , 848 K and 1 m/s plunger velocity

# Chapter 5

## Discussion and Conclusions

### 5.1 Discussion on Numerical results

Different values of shear rate were used to calculate the velocity in capillary tube and injection chamber at different values of  $n$ , shown in tables 4.3 – 4.7. These values of  $n$  were used to examine the appropriate value for simulation and experimental work. This analysis also indicates the velocity of semi-solid metal in the capillary tube, injection chamber and motor rotation speed. From the results it is clear that shearing in capillary tube greatly depend upon the inlet velocity i.e. the velocity at which the plunger push the metal inside the injection chamber and value of  $n$ . shearing in the capillary tube increases with the increase in injection velocity [Tables 4.3-4.7]. It can be seen in table 4.3 that when the motor speed increases from (0.4522)-(0.9193) rpm, that cause an increase in the capillary tube velocity results in shear rate increased from (3.1) – (6.3 s<sup>-1</sup>).

Shear rate in capillary viscometer also depends upon the value of flow index  $n$ . Decreasing the value of flow index  $n$ , would increase the shearing and even with less plunger speed, more shearing would occur in the capillary tube. When value of  $n$  is decreased from (0.3) – (0.1), it causes more shearing with less injection speed. From table 4.3 for motor speed of 0.4522 rpm, shear rate is 3.1 s<sup>-1</sup> with flow index value of  $n = 0.3$ , but when the value of is decreased to  $n = 0.1$ , same shear rate of 3.1 s<sup>-1</sup> is obtained with a motor speed of 0.2203 rpm [Table 4.3 and 4.4]. If the shear rate is kept constant and the value of  $n$  changed, different values of motor speed can be obtained.

The negative value of flow index  $n$  also has a great effect on the shearing. If the negative value of  $n$  is increased, it will increase the required injection speed to produce same shear rate [Table 4.5 and 4.6]. When negative value of  $n$  is increased from (-0.1) - (-0.3), motor speed increased from 0.40928 - 8.5949 rpm for producing

the same shear rate of  $3.1 \text{ s}^{-1}$  which is almost sixteen times greater than the one for  $n = -0.1$  [Table 4.5 and 4.6] [Appendix I for graphs].

Equation 4.6 was used to calculate  $\Delta P$  as it plays an important role to find the viscosity of material. From equation 4.6, it is clear that with the increase in the value of  $\Delta P$ , the viscosity of the material increases and with the decrease of  $\Delta P$ , viscosity decreases. Table 4.8-4.12 shows values of  $\Delta P$  at different shear rates, value of flow index  $n$  and viscosities. The results show that with the increase of shear rate or decrease in viscosity will result in an increase  $\Delta P$ . But it again depends on the value of flow index  $n$ . From table 4.8 & 4.9, it can be seen that when value of flow index  $n$  decreases from 0.3-0.1, the value of  $\Delta P$  decreases from 97.083-47.310 k Pa, with the same shear rate of  $3.1 \text{ s}^{-1}$  and viscosity value of  $\eta = 100 \text{ Pa.s}$  [Table 4.8 and 4.9]. The negative value flow index  $n$  was increased form (-0.1) - (-0.3),  $\Delta P$  value increased from 87.82 k Pa - 1.84 M Pa for the same shear rate value of  $3.1 \text{ s}^{-1}$  and  $\eta = 100 \text{ Pa.s}$  [Table 4.10 and 4.11] [Appendix I for graphs].

From the above discussion it can be concluded that value of decreasing positive value of flow index  $n$  will decrease the value of  $\Delta P$  and equation 4.6 will shows lower viscosities values, while the increase in the negative value flow index  $n$  will results in an increased value of  $\Delta P$ , and equation 4.6 will show higher viscosity value of material. Therefore the value of  $n$  can plays an important role in the processing of semi-solid metal through capillary viscometer. Different simulation works should be performed and compared that with the experimental work to find out the appropriate value of  $n$  for the semi-solid processing.

## **5.2 Viscosity variation with solid fraction and plunger velocity**

Simulation was performed in Fluent (computational fluid dynamics) to study the variation of the viscosity for a plunger speed of 0.075 m/s, 0.5 and 1 m/s with different solid fraction. Thixotropic behaviour of semi-solid processing in the capillary viscometer greatly depends upon the value of power law index  $n$  and consistency index  $K$ . Therefore, to study the effect of solid fraction and plunger velocity on viscosity, both these value of  $n$  and  $K$  were kept constant. The simulation results from the Fluent shows decrease in the viscosity of material (shear

thinning) for almost all the simulations with different solid fraction and velocity i.e. the apparent viscosity decreased with the increase in the shear rate (increase in plunger velocity) [Fig: 4.3, 4.6, 4.9, 4.12, 4.15]. Deformation could occur in the semi-solid due increased velocity. Decrease in viscosity depends on injection velocity for the same solid fraction for the transient state but when the shear stress becomes constant for extended shear periods, the viscosity also becomes constant, (i.e. no more microstructure changes occur) resulting in the steady state viscosity of the semi-solid material.

Viscosity also shows a variation with the temperature changes. Solid fraction greatly depends on the temperature. As the temperature increase, the viscosity decreases. In figure 4.3, for a velocity of 0.075 m/s and fraction solid 0.3, the viscosity is increased from 2.1 Pa.s - 3.15 Pa.s in the loading section of the chamber, as the velocity decreases [Figure 4.3]. This can be due to the resistance to the flow of the metal and can be associated with the back flow pressure of the material which keeps increasing until the metal reaches the semi-cone angle part which starts after 25 mm diameter section of length of 125 mm from the inlet position of the capillary viscometer. This resistance which cause a decrease in velocity and an associated increase in the viscosity is low enough at low velocity and solid fraction but shows some increase with the velocity and solid fraction of the material. This resistance is more for a fraction solid of 0.5 as the viscosity increased to almost 4.97 Pa.s for the same plunger velocity of 0.075 m/s [Figure 4.9]. This initial increased in the viscosity also increases with the increase of injection velocity. When injection speed is increased to 0.5 m/sec and 1 m/sec, this initial resistance to the flow increases causing the viscosity increase of the semi-solid material for the same solid fraction 0.33, 0.4, 0.5 [Figure 4.12, 4.15, 4.18, 4.21, 4.24, 4.27], . As the metal reaches the half cone angle section, viscosity decreased due to the increase in the velocity which in turn was caused by the decrease in diameter of the chamber cross section. That is the section where most material deformation occurs and the largest decrease in viscosity and increase in velocity was noted.

The viscosity decreases in semi-cone angle part of the capillary viscometer due to increase in the velocity. This decrease is again depends on the injection velocity and solid fraction. This decrease in viscosity is high for high injection chamber velocity for the same solid fraction. For a solid fraction 0.50, the viscosity dropped to 0.8 Pa.s for an injection speed of 0.075 m/s and 0.15 for 0.5 m/s [Figure 4.9 and 4.18]

### 5.3 Velocity variation with plunger velocity and solid fraction

Plunger velocity plays an important role in the filling of the mould properly. At higher plunger velocities, resulting in the air entrap causes the porosity in the material while the low plunger velocity can result the incomplete filling of the mould. Solidification can also occur due to the low velocity as the tip of the flowing material comes in contact with air for a longer period [36, 93 and 95]. As the process is isothermal and no heat lost was taken into account due to the heater bands provided around the capillary mould and die, no solidification was expected to occur and the metal flow through the capillary viscometer to the very end without any solidification or stoppage even at low plunger speed of 0.075 m/s. The SSM starts from rest and pushed with the help of plunger resulting in the sudden acceleration. The velocity of the material is greater at the centre and low at the surface of the wall because of the greater wall fraction at the wall as compared to the centre [36 and 95]. Plunger velocity of 0.075 m/s, 0.5 m/s and 1 m/s was used for the simulation and the results are presented in the figure 4.2, 4.11 and 4.20 for 0.33  $f_s$ . These results show a variation in velocity at different solid fraction, plunger velocities and temperature along with the geometry of the viscometer. The transient state response of semi-solid material was studied.

At a low solid fraction (0.33) and low velocity of 0.075 m/s [also appendix H for low solid fraction of 0.25 and 0.30], the velocity showed little variation in 25 mm diameter section of capillary viscometer [Figure 4.2]. For low solid fraction, this decrease in the velocity is low as compare to the high solid fraction [Figure 4.2, 4.4 and 4.5]. For higher injection velocities, this decrease could be greater and could be associated with back flow pressure of the material for the same solid fraction of 0.33 [Figure 4.2, 4.11 and 4.20]. Velocity increased when reached semi-cone angle part of the viscometer due to the change in the cross-section area of the flow till it reaches the tube of diameter 6 mm and again depend on the initial injection velocity, This increase in the velocity of SSM depends upon the plunger velocity and solid fraction. At a low plunger velocity, this increment is low and will be much lower for the increase solid fraction, while for a high plunger velocity results in high velocity of the SS material [Figure 4.2, 4.11 and 4.20].

The material at low solid fraction and plunger velocity does not show too much variation in the capillary tube of 6 mm. The velocity shows a decrease in capillary tube and low plunger velocity, this decrement is low, while high enough for higher velocity of 0.5 m/s & 1 m/s and high solid fraction of 0.5 [Figure 4.17 and 4.26]. At high solid fraction, the SS material act strangely and shows too much variation when it passes through he capillary tube in the transient state conditions. And the velocity profile is like a zigzag line showing the velocity is greatly unstable at high solid fraction [Figure 4.17 and 4.26].

#### **5.4 Dynamic pressure variation with velocity and solid fraction**

Simulation results for different solid fraction shows a variation in their dynamic pressure at different velocities. A constant velocity of the plunger would insure that there is equally pressure applied on the billet to push the metal in the injection chamber. The dynamic pressure of fluid is the pressure due to the velocity of the flowing fluid. The transient stat response was studied for the initial plunger velocity of 0.075, 0.5m/s and 1 m/s and with different solid fraction. Dynamic pressure determines the function of the filling rate of the semi-solid material in the injection chamber. From the simulation results obtained dynamics pressure increased greatly with increased plunger velocity and velocity of the flowing liquid [Figure 4.1, 4.1 and 4 4.19]. In the injection chamber the first process would be the upsetting and breaking of the solid-solid and solid liquid bonds to allow the material to flow. The dynamic pressure does not show much variation for low fraction solid at low velocity in the injection chamber [Figure 4.1] but for high velocity and solid fraction it show some deviation and decreases before entering the semi-cone angle area [Figure 4.7, 4.16 and 4.25]. For a low solid fraction of 0.33 at a plunger velocity of 0.075 m/s, the dynamic pressure was recorded as 2 k Pa [Figure 4.1] while for the same solid fraction at plunger velocity of 0.5 m/s it was recorded as 90 k Pa [Figure 4.7] showing that the dynamic pressure increases as the velocity of the flowing fluid increases. For the transient state at solid fraction of 0.33 at 0.075 m/s the pressure variation was constant, showing no variation in the conical section or the capillary tube, but the pressure drops a bit as compared to that in the 0.30 fraction solid

[appendix H.4 and H.8]. This showed that the dynamic pressure decreased with the increase in the solid fraction of the material. Pressure on the wall increases as the solid fraction and velocity of the material increases, as pressure increase can cause more deformation in the material resulting in lower semi-solid metal viscosity. At a higher velocity of 0.5 m/s and a solid fraction of 0.30, a decrease in the dynamic pressure of the material was found after it reached the capillary tube, showing a resistance to the flow [appendixes H]. Under steady state conditions, this process becomes more fluent and the variation in the dynamic pressure is low as compared to the transient state.

### **5.5 Static pressure variation with increasing velocity and solid fraction**

The static pressure is also called as the thermodynamic pressure of the fluid when it flows. It is defined as the pressure of the fluid that could move along with the fluid thus being static relative to the moving fluid. Static pressure of the fluid at the wall of the capillary viscometer depends upon the solid fraction of the material. Static pressure seemed to be increasing with increasing solid fraction. For a transient state of the fluid, the static pressure was very high in the beginning of the process but decrease as the process moved towards the steady state. The static pressure reached to zero gauge pressure at the end of the process, which is defined as the outlet boundary condition for the process (atmospheric pressure was recorded as the zero gauge pressure). Any variation in the pressure below or above the atmospheric pressure was recorded as the gauge pressure. The static pressure difference was used for the viscosity calculation of the material. The static pressure difference between the first and second load cell was designed to be measured and used in the calculations. The fluid static pressure starts decreasing after it reached the semi-cone angle because of the increased velocity and reduced to atmospheric pressure at the capillary outlet.

## 5.6 Conclusions

The capillary viscometer can be used to determine the viscosity of the semi-solid material at various temperatures, pressures and shear rates. Examination of different plunger velocities shows that higher velocities would result in the lower viscosities of the semi-solid metal with thixotropic behaviour. Higher velocities also decrease the process time and solidification effects can be neglected.

Results presented in the previous chapters indicate the large effect that the shear rate can have on the flow regime. It is important to understand this variation to have a good idea of the system and to understand the regime better if adequate account of associated viscosity changes is to be taken into account during a controlled die casting injection cycle.

From the simulation results it can be concluded that the velocity of the material before entering the semi-cone angle section depends both on the solid fraction and velocity of the plunger. Higher solid fractions will cause the decreased velocity of the material in the 25 mm diameter section. The values obtained from these simulations aided the designing of the experimental rig. The construction of this viscometer will be very useful for comparison against results already obtained from simulation and other workers and to generate more results which will help to develop a more accurate model of SSM flow over varying shear rate ranges. Values of  $n$  and  $K$  required more simulation and experiment to find the right values for use in simulation. Lower values of  $n$  result in a lower viscosity reading while larger values of  $K$  result in lower viscosity values.

The value of  $n$  plays a particularly important role in flow simulation of semi-solid material. It affects calculation of shear rate, velocity of motor and change in pressure. For motor velocity, when value of  $n$  is decreased, it decreases the motor velocity and shear rate and viscosity increases. The value of  $n$  also plays an important role in calculation of change in pressure. When value of  $n$  decreases, it decreases the change in pressure of the fluid, resulting in lower viscosities and high shear rates.



## References

1. M. Ferrante, E. de Freitas, M. Bonilha and V. Sinka, Rheological properties and microstructure evolution of semi solid aluminium alloys inoculated with Mischmetal and Titanium, 5<sup>th</sup> Int. Conf. on semi solid processing of alloy and composites, 1998, 35-42
2. P. Kapranos, P.J Ward, H.V Atkinson and D.H Kirkwood. Near net shaping by semi solid metal processing, Material and Design, volume 21, issue 4, 387-394.
3. M.C. Fleming, Semi-solid forming: the process and path forward, Metallurgical Science and Technology, Vol. 18(2)(2000), Page 3-4.
4. D.B. Spencer, M.C. Flemings and R. Mehrabian. Rheological behaviour of Sn-15%Pb in the crystallization range, Metallurgical Trans. 3, 1972. 1925-1932.
5. P.A. Joly and R. Mehrabian, The rheology of a partially solid alloy, Journal of Material Science, 11, 1976, 1393-1418.
6. P.A. Joly, Rheological properties and structure of semi-solid tin-lead alloy, PhD thesis, Dept of Material Science and Engineering, MIT, 1974.
7. D. Apelian, A roadmap for semi solid processing, 6<sup>th</sup> Int. Conf. on semi solid processing of alloys and composites, 2000, 47-54.
8. D.B. Spencer, PhD thesis, MIT, Cambridge, MA, 1971.
9. M. Garat, S. Blais, C. Pluchon and W.R Loue, Aluminium semi solid processing from the billet to the finished part, 5th Int. Conf. on semi solid processing of alloy and composites, 1998, xvii.
10. A. Alexandrou and G.R. Burgos, Mathematical and computational modelling in die-filling in semi-solid metal processing, Journal of Material Processing Technology, 1996, 59-72.
11. T.R. Noll, C.H. Kiehne and B. Friedrich, Recycling of semi-solid processing residues, 6<sup>th</sup> Int. Conf. on semi solid processing of alloys and composites, 2000, 35-40.
12. D. Brabazon, D.J. Browne and A.J. Carr, Experimental Investigation of the transient and steady state rheological behaviour of Al-Si alloys in the mushy state, Material Science and Engineering, A356, 2003, 69-80

13. M. Garat, L. Maenner, Ch. Sztur, State of the art of thixocasting, 6<sup>th</sup> Int. Conf. on semi solid processing of alloys and composites, 2000, 187-194
14. G. Chiarmetta, Thixoforming and weight reduction- industrial application of SeSoF, 5th Int. Conf. on semi solid processing of alloy and composites, 1998, 87-95
15. G. Chiarmetta, S.P.A Stampal , WHY THIXO? 6<sup>th</sup> Int. Conf. on semi solid processing of alloys and composites, 2000, 15-21.
16. W.L. Winterbottom, Semi-solid forming application, high volume automotive products, Metallurgical Science and Technology, Vol 18 (2), 2000, 5-10.
17. K. Young and P. Eisen, Semi-solid metal technological alternatives for different applications, Metallurgical Science and Technology, Vol 18 (2), 2000, 11-15.
18. P. Giordano and D. Chiarmetta, New rhoecasting, A valid alternative to tradition technology for the production of automotive parts, 8<sup>th</sup> Int. Conf. on semi solid processing of alloys and composites, 2004.
19. C.J. Quaak, Rheology of partially solidified aluminium alloy, PhD thesis.
20. A. M. Alper, Phase diagram: Principle and Techniques of phase diagram, Academic press, Material Science and Technology, Vol 1: 1970.
21. D. Brabazon, Processing and Properties of Rheocast Alloys, PhD thesis National University of Ireland, 2001.
22. C.S. Rice and P.F. Mendez, Slurry based semi-solid die casting, Advance Material and Processes, 159, 10, 2001.
23. Z. Fan, Semi-solid metal processing, International Materials Reviews, Vol 47, 2002, 1-39.
24. J.L. Jorstad, High integrity die-casting process variation, International conference on structural Aluminium casting, Nov 2003.
25. M. Gordon, Mastering Manufacturing, Macmillan, 1993.
26. H.C. Kazanas, Basic manufacturing processes, McGraw-hill, 1981.
27. K.C. Sharma, J.H. Ferreira, G. Govender, O.Damm, Effect of process variable on A356 SSM Casting, 6<sup>th</sup> Int. Conf. on SS processing of alloys and composites 2000, 253-258.
28. S.C. Bergsma, M.E. Kassner, E. Evangelista, and E. Cerri, The Optimize tensile and fatigue properties electro magnetically stirred and thermally

- transformed semi solid 357 and modified 319 aluminium alloy, metallurgical science and technology, Vol. 18 (2), 2000, 21-26.
29. M. Rosso, P. Giordano, G.L. Chiarmetta, study of the influence heat treatment cycles of thixoformed automotive parts, 6<sup>th</sup> Int. Conf. on SS processing of alloys and composites, 2000, 325-330.
  30. Q.Y. Pan and D. Apelian, yield stress of aluminium alloy in the semi solid state, semi solid material processing centre metal processing institute, WPI, Worcester, MA 01609 USA. 6-399).
  31. M. Badiali, C.J. Davidson, J.R. Griffiths and A. Zanada, Fatigue properties of semi solid cast Al-7Si-0.3Mg-T6 alloy, CSIRO Manufacturing Science and Technology, Kenmore, Australia, 6-349.
  32. H. Jiang, L. Yalin, W. Huang and L. Xiaoli, Micro-structural evolution and mechanical properties of Al-4Cu-Mg alloy, Material characteristic, 51, 2003, 1-10.
  33. S.P. Midson, L.E. Thornhill and K.P. Young, Influence of key Process parameters on the quality of semi solid metal cast Aluminium Components, Int. Conf. on SS processing of alloys and composites 1998, 181-188.
  34. M. Suery, A. Zavaliangos, Key problem in the rheology of semi solid alloys, 6<sup>th</sup> Int. Conf. on SS processing of alloys and composites 2000, 129-135.
  35. C.G Kang and D.W Kang, Forging process analysis of SS Aluminium materials, 4<sup>th</sup> Int. Conf. on SS processing of alloys and composites 1996, 142-147.
  36. C.J Paradies, M. Rappaz and T. Imwinkelried and J.P. Gabthuler, Simulation of the pressure die casting of a thixotropic aluminium alloy, 4<sup>th</sup> Int. Conf. on semi-solid processing of alloy and composites, 1996, 115-119.
  37. Novel De Nevers, Fluid Mechanics For Chemical Engineers, Second Edition, Page 458-467
  38. Fredrick R. Eirich, Rheology "Theory and Application", Volume 3, page 1-31.
  39. H. A Barnes, An introduction to Rheology, Oxford; Amsterdam: Elsevier, 1989.
  40. G.H. Nickodemus, C.M.Wang, M.L. Tims, J.J Fisher and J.J Cardarella, Rheology of Material for Semi-Solid Metalworking Applications, 5th Int. Conf. on semi solid processing of alloy and composites, 1998, 29-34.

41. P. Kapranos, DH Kirkwood, H.V Atkinson, Development of Hypereutectic Aluminium Alloys for Thixoforming Based on the A390 Composition, 6th Int. Conf. on semi solid processing of alloy and composites, 341-346.
42. I. Presse, and K. Young, Die-casting System For Semi-Solid Liquid and Semi-Solid Metal Casting Applications, 6<sup>th</sup> Int. Conf. on semi solid processing of alloys and composites, 2000, 41-45.
43. T. Basner, Rheocasting of semi-solid A357 aluminium alloy, SAE Technical Paper Series, 2000, 1-7.
44. Li Ma, Denny C. Davis, Leonard G. Obaldo, Gustavo V.Barbosa- Canovas, Engineering properties of food and other biological materials, a laboratory manual Washington State University, Washington. Page 99-114.
45. P. J. Fryer, D. L. Pyle and C. D. Rielly, Chemical engineering for the food industry London, Blackie Academic and Professional, 1997, 195-219.
46. D. Morton, Process fluid mechanics, London; Englewood Cliffs: Prentice-Hall, 1980.
47. S.I. Bakhtiyarov and R.A. OverFelt, Measurement Of Liquid Metal Viscosity by Rotating Techniques, Alta Material, Vol: 47, page 4311-4319, 1999.
48. R.P.Chhabra and J.F.Richardson, Non-Newtonian flow in the process industry, fundamentals and engineering applications, Oxford: Butterworth-Heinemann, 1999, page 4-40.
49. M.C. Flemings, Behaviour of metals in the semi-solid state, Metallurgical Transactions, A22, 1991, 957-981.
50. M.C. Flemings, Metallurgical Transactions, 22 A, 1991, 957.
51. M. Modigell, J. Koke, Rheological modelling on semi-solid metal alloy and simulation of thixocasting process, Material processing technology, Vol 111, 1999, 53-58.
52. A. Wahlen, Modelling the thixotropic flow behaviour of the semi-solid aluminium alloys, 6<sup>th</sup> Int. Conf. on SS processing of alloys and composites, 2000,565-570.
53. J. F. Steffe, Rheological methods in food process engineering, second edition, Freeman Press, USA.
54. A.H. Skelland, Non-Newtonian flow and heat transfer, New York: Wiley, 1967.

55. G. Böhme, *Non-Newtonian fluid mechanics*, Oxford; Amsterdam: North-Holland, 1987.
56. R.J. Wilkens, J.D. Miller and J.R. Plummer, New techniques for measuring and modelling cavern dimensions in a Bingham plastic fluids, *Chemical Engineering Science*, 60, 2005, 2269-2275.
57. B. Aydin, F. Larachia, Trickle bed hydrodynamics and flow regime transition at elevated temperature for Newtonian and Non-Newtonian liquids, *Chemical Engineering Science*, 60, 2005, 6686-6700.
58. A.R.A McLelland, N.G. Henderson and H.V Atkinson, *Material science and engineering*, A 232, 1997, 110-118
59. A.M Mullis, Determining optical semi-solid forming process parameter by simulation techniques, 5<sup>th</sup> Int. Conf. on SS processing of alloys and composites, 2000, 325-334.
60. C. Rouff, V. Favier, R. Bigot, 7<sup>th</sup> Int. Conf. on SS processing of alloys and composites, 2002, 423-428.
61. P.J Ward, H.V. Atkinson, D.H. Kirkwood, *Mathematical modelling in metal processing and manufacturing*, COM, Ottawa, Canada, 2000
62. Z. Fan, J.Y. Chen, Modelling of rheological behaviour of semi-solid metal slurries part 2, Steady state behaviour, *journal of material science and technology*, volume 18, march 2002, page 243-249.
63. W. L. Wilkinson, *Non-Newtonian fluids: fluid mechanics, mixing and heat transfer*, International series of monographs on chemical engineering, Vol.1, London : Pergamon, 1960.
64. Z. Fan, J.Y. Chen, Modelling of rheological behaviour of semi-solid metal slurries part 3, Transient state behaviour, *journal of material science and technology*, volume 18, march 2002, page 243-249.
65. M. Madam and F. Ajersch, Rheological model of semi-solid A356-SiC composite alloys. Part I: Dissociation of agglomerate structures during shear, *material science and engineering*, Vol. 212, July 1996, 157-170(14).
66. M. Modigell, J. Koke, Time dependent rheological properties of semi-solid metal alloys, *International Journal of the Mechanics of Time-Dependent Materials* 3(1), S.15-30, 1999 ISSN 1385-2000.
67. P. Kumar, Constitutive, Modelling and characterization of flow behaviour of semi-solid metal alloy slurry, *Acta Metall. Mater.* 42, 3, 595-602.

68. J. H Prentice, Measurements in the Rheology of foodstuffs, London: Elsevier Applied Science, c1984, page 51-61.
69. J.G. Webster, The Measurement, Instrumentation and Sensors, CRC handbook, CRC and IEEE press, page 30.1-30.20.
70. Linford, A, Flow measurement and meters, 2nd edition, London : Spon, 1961
71. D.J. Donald, Shear rate and viscosity correction for a Casson fluid in cylindrical Couette geometries, Journal of Colloid and Interface Science, 267, 2003, 204-210.
72. A.F. Borghesani, Flow dynamics and transport phenomena, page 89-100.
73. N.P. Cheremisinoff, Encyclopedia of fluid mechanics, Vol.7: Rheology and non-Newtonian flows, Gulf Publishers, 1988, page 20-51.
74. D.J. McClements, Food, emulsions: principles, practice, and techniques, Boca Raton : CRC Press, 1999, page 250-258.
75. M. Mooney, Journal of Rheology, Vol 2, page 210 (1993)
76. U. Yilmazer and Dilhan M. kalyon , Slip effect in Capillary And Parallel Disk Torsional Flow of Highly Filled Suspension, Department of Chemistry and Chemical Engineering, Steven Institute of Technology, Castle point, Hoboken, New Jersey 07030.
77. W. A. Caw, R. G. Wylie, Capillary Viscometer of negligible Kinetic energy effect, British Journal of Applied Physics, Vol 12, March 1961.
78. B. Herzhaft, Rheology of Aqueous Foam, a literature review of some experimental work, Oil and Gas Science and Technology, Vol 54 (1999), No 5, pp 587-596.
79. U. Yilmazer and D.H. Kalyon, Slip effect in capillary and parallel disk Torsional flow of highly filled suspension, Journal of Rheology, 33 (8), 1989, 1197-1212.
80. J.P. Tordella, Capillary flow of molten polyethylene, A photographic study of melt fracture, Journal of Rheology 1, 1957, 203-212.
81. P. Kapranos, A. Taylor, J. Grice, Thixoforming, As good as gold, 8<sup>th</sup> Int. Conf. on SS processing of alloys and composites, 2004.
82. G. Chiarmetta, Thixoforming and weight reduction, Industrial application of SeSoF, 5<sup>th</sup> Int. Conf. on SS processing of alloys and composites, 1998, 87-96.
83. He Mingzhao, Slurry rheology of lime stone and its effect of ultra-fine grinding, Licentiate thesis, university of technology, Lulea, Sweden, 2005.

84. A.R.A McLelland, N.G. Henderson and H.V Atkinson, *Material science and engineering*, A 232, 1997, 110-118
85. M. Suery, C.L. Martin, L. Salvo, Overview of the rheological behaviour of globular and dendritic structure, 4<sup>th</sup> Int. Conf. on SS processing of alloys and composites, 1996, 21-29.
86. A. Zavaliangos, Physical mechanism of flow at high volume fraction solid, 4<sup>th</sup> Int. Conf. on SS processing of alloys and composites, 1996, 40-46.
87. T.Y. Nguyen and D. Favier, Theoretical and Experimental study of isothermal behaviour of alloy in the semi solid state, *International Journal of plasticity*, Vol 13, 1994, 237-259.
88. G.R. Borgos, A.N. Alexandrou, V. Entov, Two phase flow of semi solid material, 5<sup>th</sup> Int. Conf. on SS processing of alloys and composites, 1998, 217-224.
89. M. Modigell, J. Koke, J. Petera, Two phase model for metal alloys in the semi-solid state, 5<sup>th</sup> Int. Conf. on SS processing of alloys and composites, 1998, 317-326.
90. T.Y. Nguyen, D. Favier, Viscoplasticity behaviour of porous metallic material, with liquid and experimental identification on a Sn-Pb alloy, *International Journal of plasticity*, Vol 10, 1994, 663-693.
91. Arvind Kumar, Pradip Dutta, Modelling of transport phenomenon in continuous casting of non-dendritic billets, *International Journal of heat and mass transfer*, 48, 2005, 3474-3488.
92. B.P. Gautham, P.C. Kapur, Rheological model for short duration response of semi-solid metals, *Material science and engineering*, A393, 2005, 223-228.
93. D. Bernhard, H. Muller-Spath and P.R.Sahm, 5<sup>th</sup> Int. Conf. on SS processing of alloys and composites, 1998, 51-55.
94. B. Nohn and D. Hartmann, Use of simulation tools for optimization of the thixoforming process, 6<sup>th</sup> Int. Conf. on SS processing of alloys and composites, 2000, 795-800.
95. L. Orgeas, C.J. Paradies, M. Rappaz, T. Imwinkelried and J.P Gabathuler, Modelling of semi-solid process using a modified temperature-dependent power-law model, *Modelling and simulation in materials science and engineering*, 11, 2003, 553-574.

96. C. Afrath, J. Aguilar and A. Buehrig-polaczek, Rheological measurement of semi-solid alloys under high shear rate conditions, 8<sup>th</sup> Int. Conf. on SS processing of alloys and composites, 2004.
97. A.M. de Figueredo, A. Kato and M.C. Flemings, Viscosity of semi-solid A357 alloy in the transient high shear rate regime, Metallurgical science and technology, Vol 18 (2), 2000.
98. M. Braccini, C.L. Martin, A. Tourabi and M. Suery, Low shear rate behaviour at high solid fraction of partially solidified Al-8 wt% Cu alloys, Material science and engineering, A 337, 2000, 1-11.
99. K. Kueroki, T. Suenga and K. Tanikawa, Establishment of manufacturing technology for high strength aluminium cylinder block in diesel engine applying a rheocasting process, 8<sup>th</sup> Int. Conf. on SS processing of alloys and composites, 1996, 30-34.
100. D.J. Donald, shear rate and viscosity correction for a Casson fluid in cylindrical Couette geometries, Journal of Colloid and Interface Science, 267, 2003, 204-210.
101. P. Kapranos, T.Y. Liu, H.V. Atkinson and D.H. Kirkwood, Investigation into rapid compression of semi-solid alloy slugs, Journal of Material Processing Technology, 111, 2001, 31-36.
102. Joseph Edward Shigley, Engineering Design, Second Edition, page 1-29.
103. Lyndon Edwards & Mark Endean, Manufacturing with Material, Milton Keynes, England: Open University, Materials Dept; London; Boston; Bu, 1990. Page 11-68. (Materials in action series).
104. Rod Black, Design and Manufacturing, An Integrated Approach, Macmillan Press limited, 1996, page 1-29.
105. Polak, Peter. - Engineering design elements / P. Polak. - London: McGraw-Hill, 1991, page 1-10.
106. Dieter, George Ellwood. - Engineering design: a materials and processing approach / George E. Dieter. - 3rd ed. London: McGraw-Hill, 2000, page 1-80.
107. Ertas, Atila, The engineering design process - 2nd ed. - New York: John Wiley & Sons, 1996, page 1-55.



108. Mott, Robert L. - Machine elements in mechanical design- 4th ed. - Upper Saddle River, N.J.; [Great Britain]: Pearson Prentice Hall, 2004, PAGE 822-824.
109. Control Techniques, Servomotor and Controller, Help files and Manuals.
110. E. Paul DeGarmo & J. Temple Black, Material and Processing in Manufacturing, Seventh Edition, Macmillan Publishing Company, 1998, page 355-363
111. Kalpakjian, Serope, Manufacturing processes for engineering materials, Addison-Wesley Publishing Company- Reprinted with corrections, July 1985, page 268-372
112. Kazanas, H. C. - Basic manufacturing processes, McGraw-Hill, 1981, page 130-136
113. Foseco foundryman's handbook / revised and edited by John R. Brown, 10th ed. - Oxford; Boston, MA: Butterworth-Heinemann, 1994, page 1-30
114. Ceramics and glasses, engineering material handbook, volume 4, ASM International. 1991, page 228-230 & 820
115. Ray, Martyn S, The technology and applications of engineering materials, Prentice/Hall International, 1987, page 268-274
116. ASM Handbook, Material Selection and Design, Vol 20, Material Information Society, ASM International, page 427-660
117. Larry Horath, Fundamental of Material Science for Technologists, Properties, Testing and Laboratory Exercise, Prentice Hall, Page 216-224
118. W. A. Caw and R. G. Wylie, Capillary Viscometer with Negligible Kinetic Effect, British Journal of Applied Physics, Vol 12, March 1961, page 94-98
119. Ronald Darby, Viscoelastic fluids: an introduction to their properties and behavior, Chemical processing and engineering, Vol 9, New York: M. Dekker, 1976, page 282-297
120. Bhasin A. Kumar, Moore J. John, 5<sup>th</sup> International Conf of Semi-Solid Alloy and Composites, June 1998, page xvii-xxxi
121. D. Bernhard, H. Muller Spath and P. R. Sahm, Investigation of Rheology of Semi-Solids Materials by using a modified capillary viscometer and numerical simulation, 5<sup>th</sup> International Conf of Semi-Solid Alloy and Composites, June 1998, page 51-55

122. Robert L. Norton, Machine Design, An Integrated Approach, Prentice Hall, Page 708-710
123. Maria A. Barrufet and Agustinus Setiadarma, Experimental viscosities of heavy oil mixture up to 450 K and high pressure using a mercury capillary viscometer, Journal of Petroleum Science and Engineering Vol 40, 2003, page 17-26
124. Y. T. Nguyen and T. D. Vu, Solving the inverse problem of capillary viscometer by tikhonov regularization, journal of non-Newtonian fluid mechanics, Vol 87, 1999, page 103-116
125. [www.prismengineering.ie](http://www.prismengineering.ie)
126. [www.labequip.com](http://www.labequip.com)
127. [www.rdpe.com](http://www.rdpe.com)
128. [www.elemex.ie](http://www.elemex.ie)
129. [www.elitefurnaces.com](http://www.elitefurnaces.com)
130. [www.impactirl.ie](http://www.impactirl.ie)
131. [www.ni.com](http://www.ni.com)
132. Thomas Tobin, Project thesis, Investigation of semi-solid processing route II, Dublin city university, Dublin, Ireland, 2005

## **Appendix:A Estimation of expected force on load cell, expected velocity in capillary, expected pressure at start of capillary and maximum pressure that load cell can read**

### **Calculation of expected force on load cell**

For instance, from initial examination of the design brief large loads were expected in the injection chamber, mainly due to the large reduction in volume.

Specified maximum output motor torque: 75.6 Nm

Diameter of the gear:  $36 \times 10^{-3}$ m

Diameter of the capillary & load pin (quartz rod):  $6 \times 10^{-3}$ m

$$\Rightarrow \text{The linear force from the motor } F = \frac{Nm}{m} = \frac{75.6}{36 \times 10^{-3}} = 2.1kN$$

$$\Rightarrow \text{The pressure on the billet } P = \frac{F}{A} = \frac{2100}{\Pi(12.5 \times 10^{-3})^2} = 4.27MPa$$

$\therefore$  The load on the 6 mm capillary & injection pin

$$4.27MPa = \frac{Load}{A} = \frac{Load}{\Pi(3 \times 10^{-3})^2} = 120.73N$$

### **Calculation of expected velocity in capillary**

Maximum velocity and pressure that can be produced and exerted by semi-solid aluminium passing through the mould cavity had to be established so that suitable clamping forces and seating for the mould could be designed. We have used a velocity of 1m/sec in our calculations as it is used industrially, so using this value and the area of each cavity the velocity of the material going through the mould could be calculated.

$$V_1 A_1 = V_2 A_2$$

$$(1m/s)(\pi (12.5 \times 10^{-3})^2) = (V_2) (\pi (3 \times 10^{-3})^2)$$

$$V_2 = 17.36m/s$$

### Calculation of expected pressure at start of capillary

Bernoulli's equation can be used to find the pressure in mould cavity. From appendix A, calculated pressure on the billet is 4.42MPa. Using Bernoulli's equation the pressure in the mould cavity can be calculated. There is no head of the pressure, so

$$\rho gh_1 = \rho gh_2$$

$$P_1 + \frac{1}{2} \rho V_1^2 + \rho gh_1 = P_2 + \frac{1}{2} \rho V_2^2 + \rho gh_2$$

$$4.27 \text{ MPa} + \frac{1}{2} (2685)(1)^2 = P_2 + \frac{1}{2} (2685)(17.36)^2$$

$$P_2 = 3.866 \text{ MPa}$$

Where  $\rho$  the density of aluminium alloy and  $g$  is the constant.

This is the maximum pressure, which could act on the mould during the casting process at maximum speed of 1 m/sec. Pressure values for other velocities could have been calculated; however the accuracy of these results would not have been comparable to the readings of the load cell. The diameter of the exiting aluminium would be greater than that of the mould and no value of this diameter could be found from research. A direct relationship was made between pressure and velocity but this formula could not be used either. This was due to constant value  $C$  changing with each change in velocity, effectively leaving more than one unknown in the equation.

### Calculation of maximum pressure load cell can measure

Pressure on the load cell can be calculated as  $P = F/A$  (G.1)

$A = \text{Area of the load cell pin} = A = \pi R^2$  (G.2)

$R = \text{Radius of the load cell pin} = 3 \text{ mm} = 3 \times 10^{-3} \text{ m}$

$P = 250/\pi (3 \times 10^{-3})^2$  (Load cell capacity = 250 N)

$P = 8.8419 \text{ MPa}$

Load cell can measure a pressure of 8.8419 MPa.

## **Appendix: B Calculation of frictional force from injection chamber wall and equivalent extrusion length**

### **Calculation of frictional force from injection chamber**

Calculations for the frictional force acting on the wall of the mould cavity were calculated using the product of the coefficient of friction for stainless steel and surface area of the cavity.

Coefficient of friction for stainless steel: 0.3

Surface area of the cavity:  $2\pi r h = (2) (3.14) (3 \times 10^{-3}) (600 \times 10^{-3})$

$$A = 0.011 \text{ m}^2$$

The frictional force =  $0.3\mu \times 0.011\text{m}^2 = 0.0034 \text{ N}$

### **Calculation of equivalent extrusion length**

Designing the length and diameter of the mould cavity

Volume of the slug to be injected = Volume of the mould cavity

$$\pi r_1^2 L_1 = \pi r_2^2 L_2$$

$$\pi (12.5 \times 10^{-3})^2 (70 \times 10^{-3}) = \pi (3 \times 10^{-3})^2 (L_2)$$

$$L_2 = 1.2 \text{ m}$$

Where:

$r_1$  is the radius of the injection chamber.

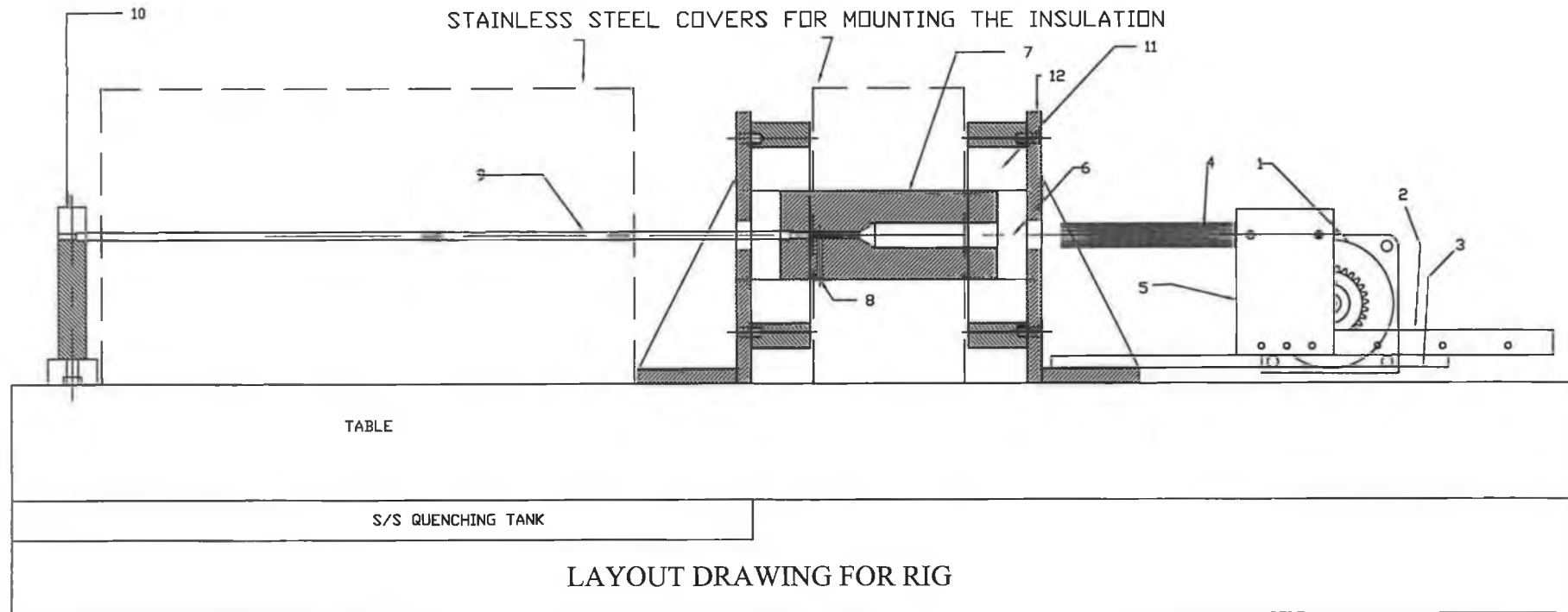
$r_2$  is the radius of the capillary tube and die cavity.

$L_1$  is the length of the aluminium slug.

$L_2$  is the length of the mould.

## Appendix: C Capillary viscometer part specification

Part no	Part Name	Part Description
1.	UNIMOTOR UM 142	7:1 Alpha Torque increasing gear box $V_{\max} = 3000\text{rpm}$ or 14.32 m/sec Temperature capability = 850 °C Maximum Torque = 75.6 Nm
2.	Pinion	Inner dia = 70 mm Outer dia = 78 mm
3.	Rack and rack support	Rack = 500L x 25 W x 25 H
4.	Rail	650 mm x 80mm x12 mm
5.	Plunger and Plunger holding assembly	Plunger Material : Over Supreme 100L x 34.5D (plunger holder) 180L x 24.9D mm (injection chamber) Assembly Material : steel 100L x 50W x 148H (mm)
6.	Injection Ram	
7.	Injection chamber	Material : Over supreme Inlet tube: 125L x 25D (mm) Conical portion: 16.5L x 6mm outer dia Capillary tube: 744L x 6D (mm)
8.	Ceramic tube and load cell	Pressure reading area
9.	Capillary tube mould	Stainless steel
10.	Mould support	Stainless steel
11.	Insulation mounting covers	Stainless steel
12.	Injection chamber support	Stainless steel
13.	Quenching tank	800L x 644W x151H (mm)
14.	Thermocouple	K type bimetallic junction Capacity = 1100 °C



1- UNIMOTOR UM 142,  
7:1 Alpha Torque Increasing Gear Box.  
V<sub>max</sub> = 300 rpm, 14.32m/s.  
Temperature Capability = 850 oC.  
Maximum Torque = 75.6 N-m.  
Motor gear box assembly is controlled  
with Uni-drive SP 2401 Controller.

2- RACK & RACK SUPPORT,  
Rack = 500 L X 25 W X 25 H.  
Pinion.  
Inner Diameter = 70 mm.  
Outer Diameter = 78 mm.

3- RAIL & SLIDE.  
Rail = 650L X 80W X 12T.

4- PLUNGER.  
Material: Ovar Supreme.  
100L X 34.5D.  
180L X 24.9D.

5- PLUNGER HOLDING ASSEMBLY.  
Material: Steel.  
100L X 50W X 148H.

6- INJECTION RAM.

7- INJECTION CHAMBER.  
Material: Ovar Supreme.  
Inlet Tube: 125L X 25D (mm).  
Conical Portion: 16.50L X 6mm  
Outer Diameter.  
Capillary tube: 70L X 6D (mm).

8- CERAMIC SEPARATION AREA.

9- INJECTION CHAMBER SUPPORT.

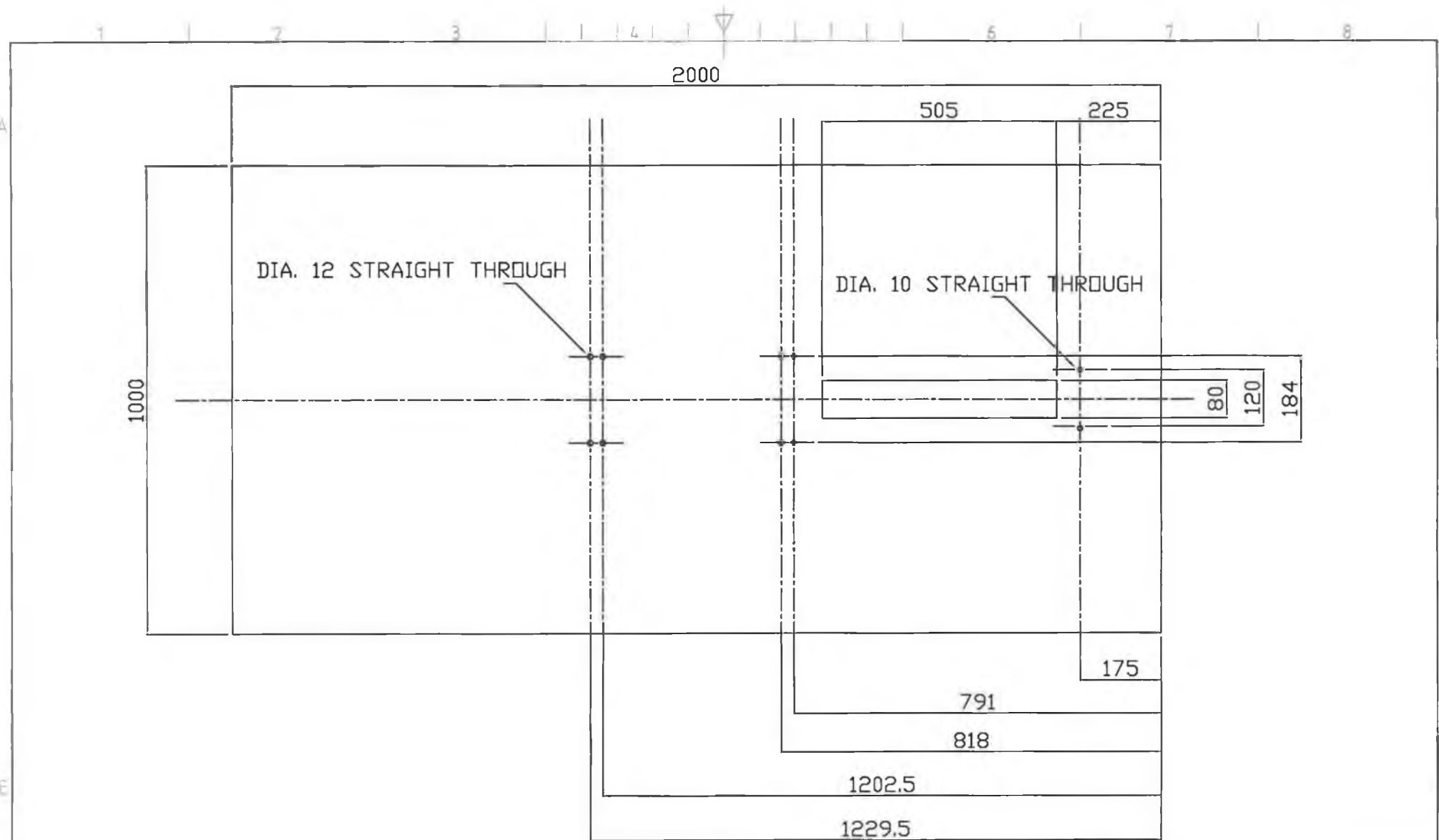
10- PRESURE READING AREA.

11- STAINLESS STEEL COVERS FOR MOUNTING  
INSULATION

12- MOULD SUPPORT.

13- QUNCHING TANK.  
800L X 644W X 151H (mm).

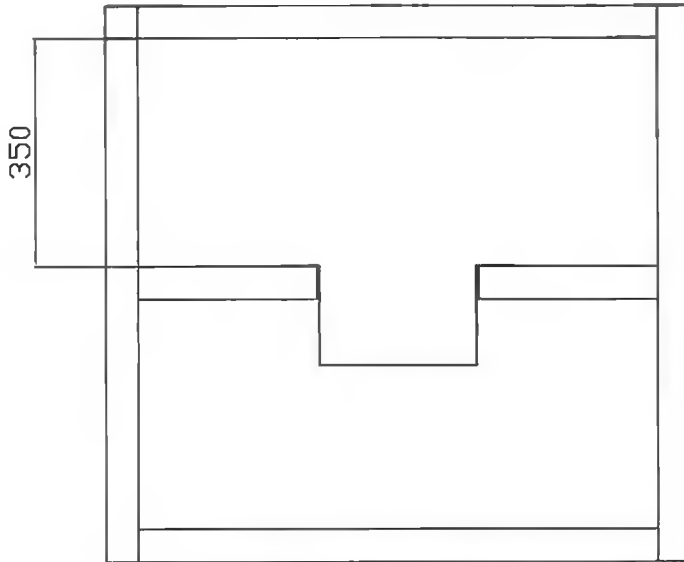
Layout of capillary  
viscometer



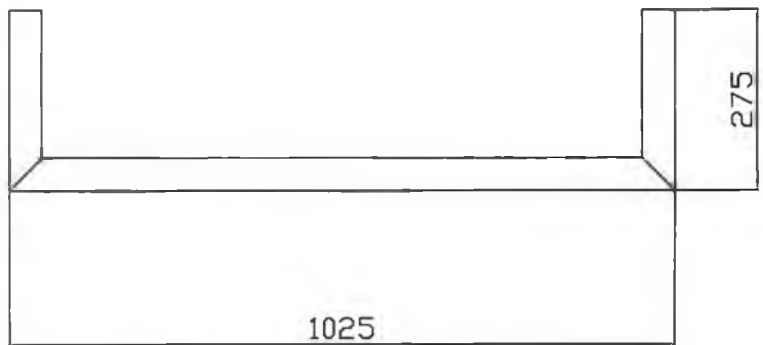
PROJECT	PRESSURE INJECTION OF SEMI-MOLTEN ALUMINUM INTO THIN WALLED MOLD.			
DRAWING 1	PLAN LAYOUT			
DRAWN	E.D.C	DATE	23/08/03	SCALE NTS
Page: 127			TITLE: TABLE TOP LAYOUT	
			REV.	1



TOP OF TABLE

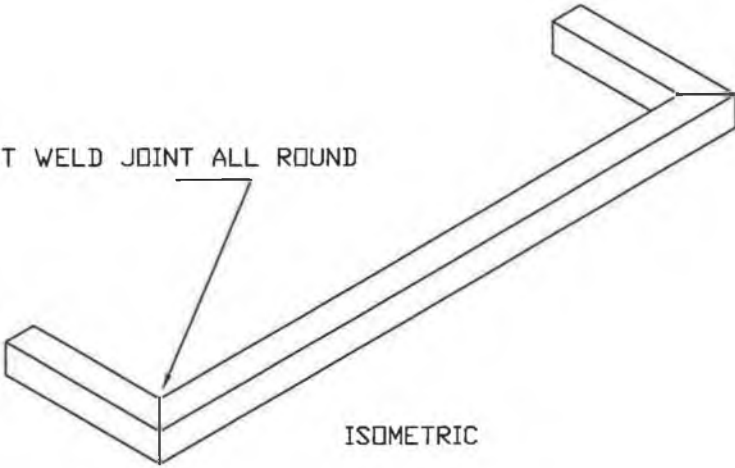


END VIEW OF TABLE



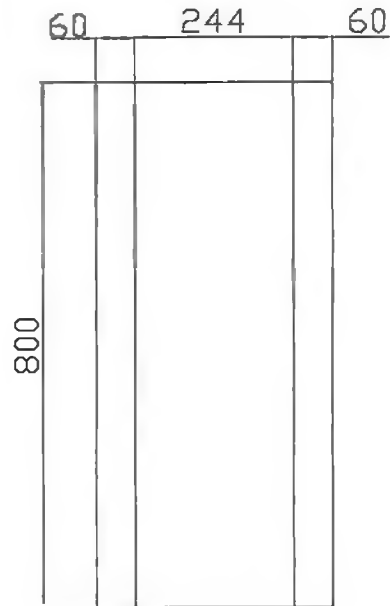
BRACKET TO BE MADE UP & WELDED TO EACH SIDE

BUTT WELD JOINT ALL ROUND

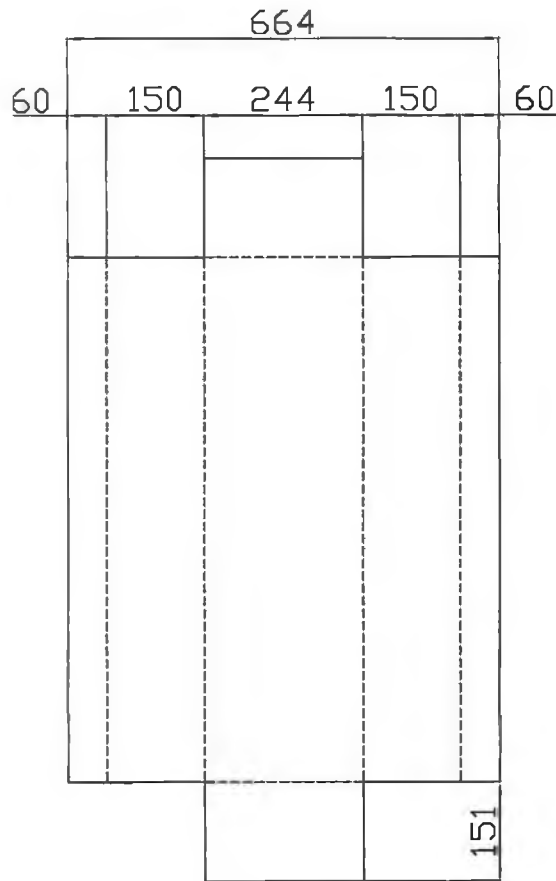


ISOMETRIC

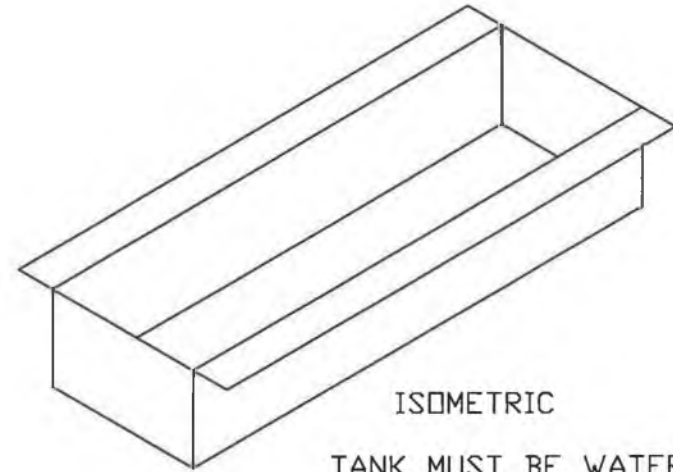
PROJECT	PRESSURE INJECTION OF SEMI-MOLTEN ALUMINUM INTO THIN WALLED MOLD.		
DRAWING 7	POSITION & ASSEMBLY FOR BRACKET		
DRAWN	E.D.C	DATE	20/08/03
Page: 128		TITLE: TANK BRACKET	SCALE NTS
		QUANTITY: 2	REV. 3



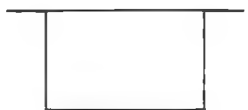
PLAN



DEVELOPMENT



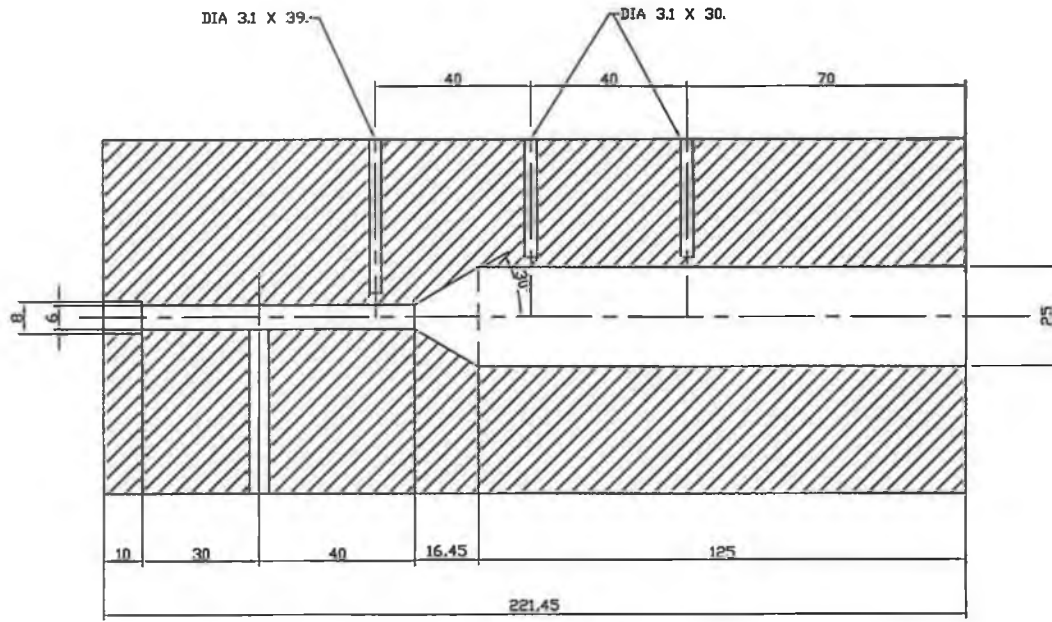
ISOMETRIC  
TANK MUST BE WATER TIGHT



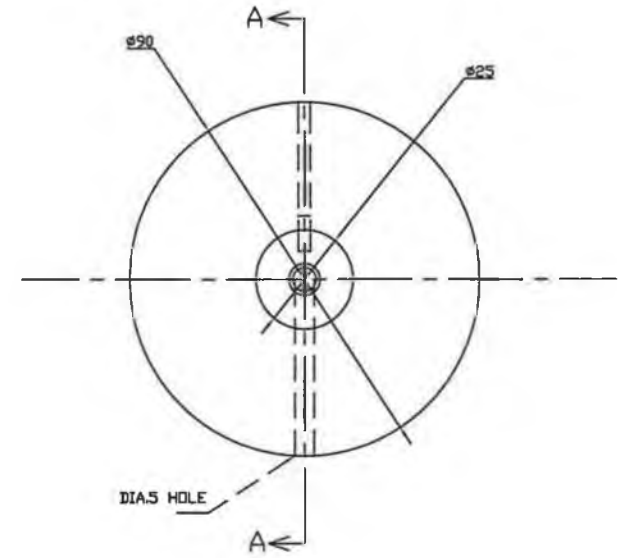
ELEVATION

BEND ON THE DASHED LINES

PROJECT	PRESSURE INJECTION OF SEMI-MOLTEN ALUMINUM INTO THIN WALLED MOLD.			
DRAWING 15	PLAN/ ELEVATION/ DEVELOPMENT			
DRAWN	E.D.C	DATE	13/08/03	SCALE NTS
Page: 129			TITLE: S/S TANK	
			REV.	1

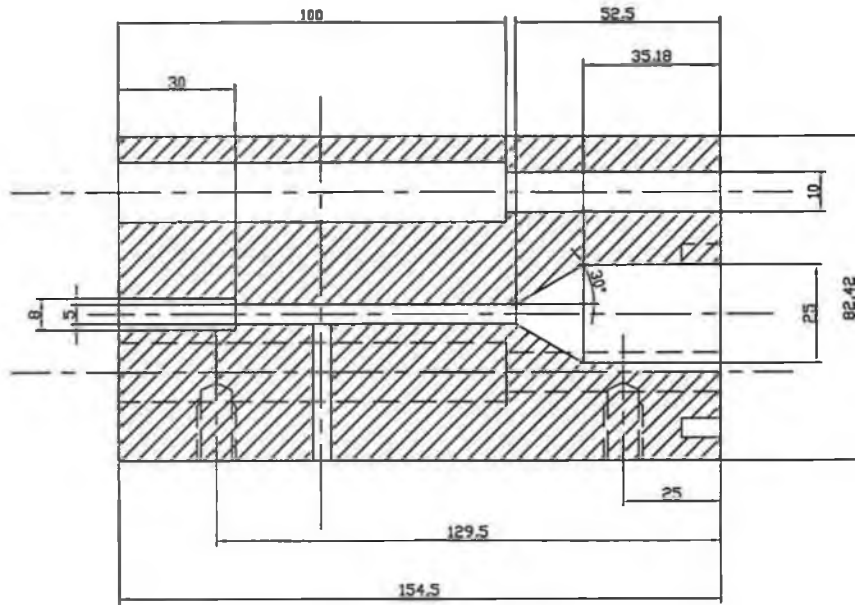


SECTION AA

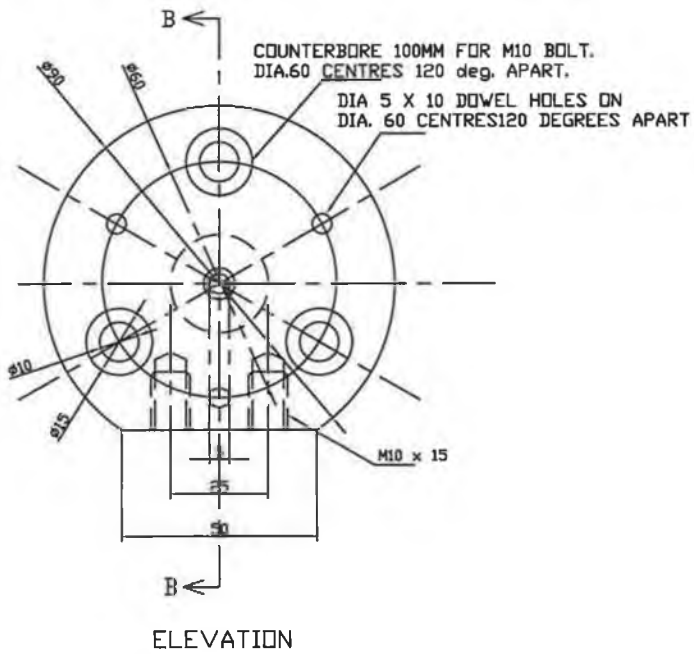


ELEVATION

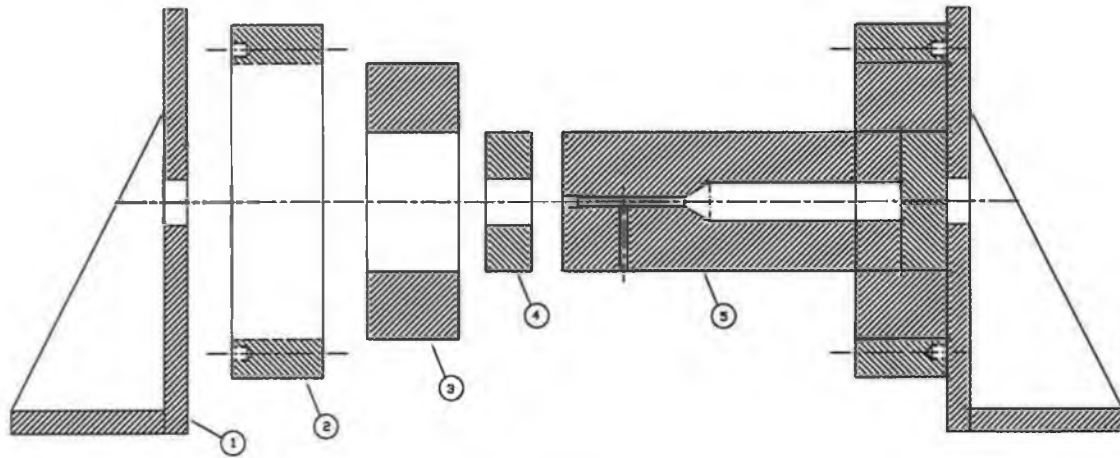
PROJECT	PRESSURE INJECTION OF SEMI-MOLTEN ALUMINUM INTO THIN WALLED MOLD.				
DRAWING 4	REDUCTION CHAMBER (DIA.25-6).				
DRAWN	E.D.C		DATE	16/08/03	SCALE NTS
Page: 130			TITLE: INJECTION CHAMBER		
			QUANTITY: 1	REV.	6



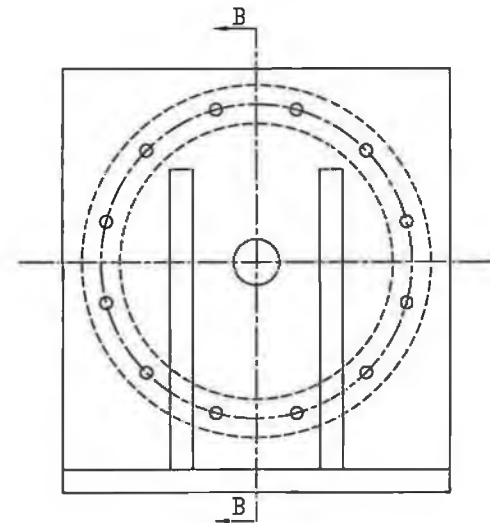
SECTION BB



PROJECT	PRESSURE INJECTION OF SEMI-MOLTEN ALUMINUM INTO THIN WALLED MOLD.				
DRAWING NO	REDUCTION CHAMBER (DIA.25-5).				
DRAWN	E.O.C	DATE	17/06/03	SCALE NTS	
Page: 131		TITLE: CONCEPT INJECTION RAM			
				REV.	3



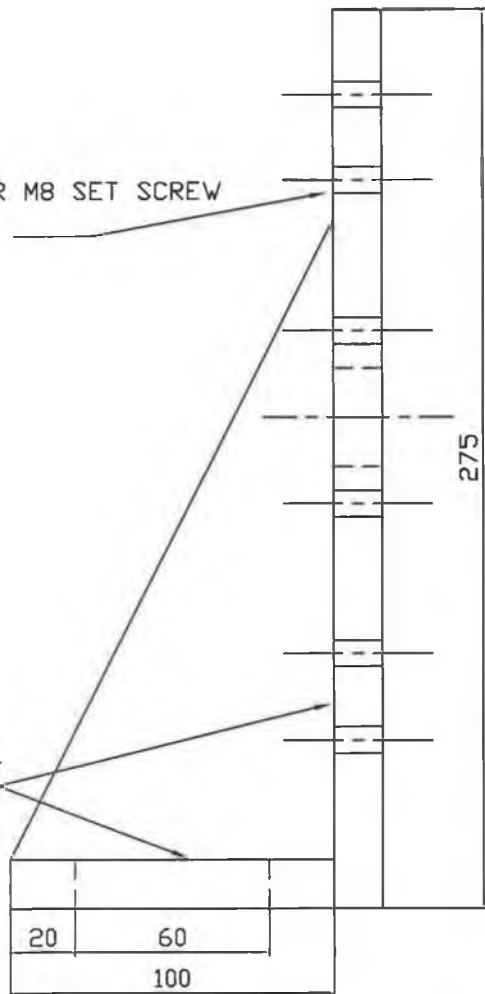
SECTION BB



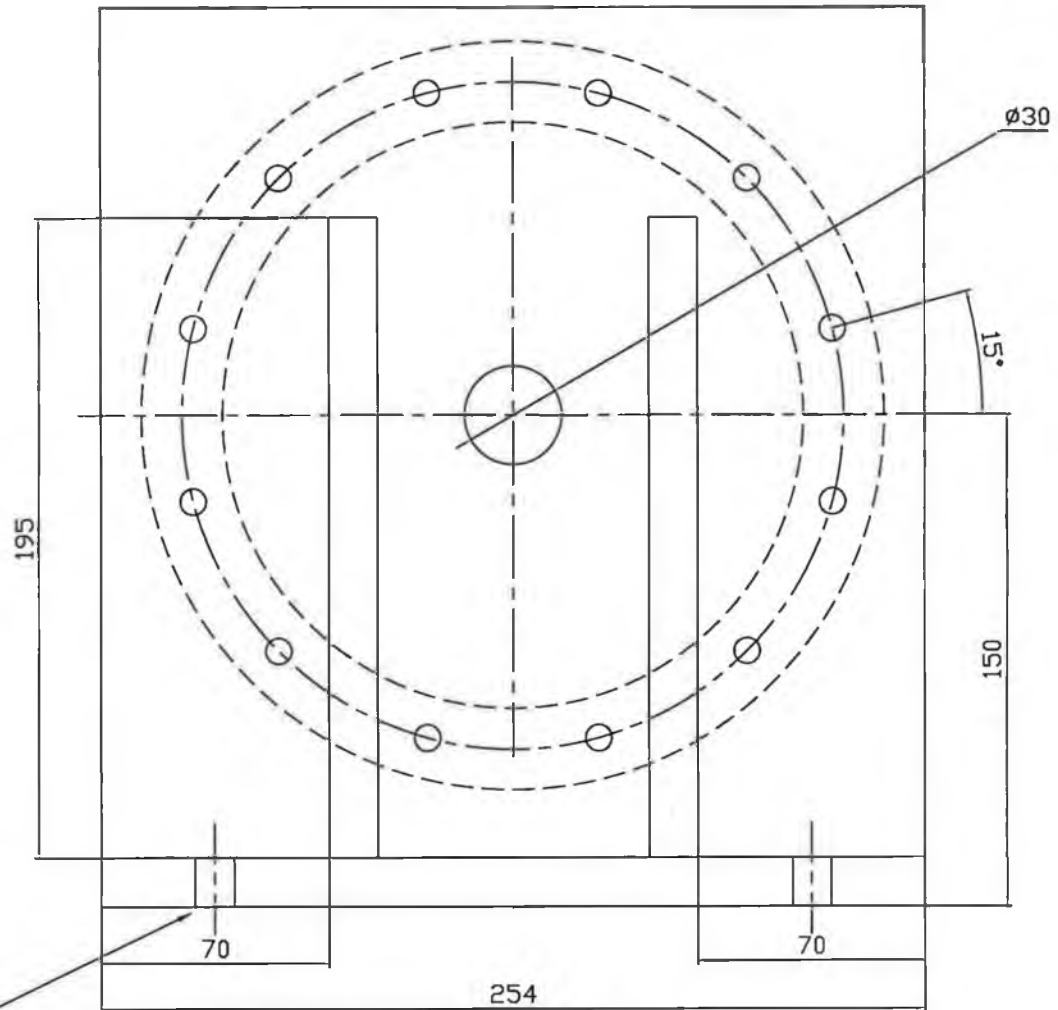
PROJECT	PRESSURE INJECTION OF SEMI-MOLTEN ALUMINUM INTO THIN WALLED MOLD.			
DRAWING 16	SECTIONAL ELEVATION / END VIEW			
DRAWN	E.D.C	DATE	20/08/03	SCALE NTS
Page: 132	TITLE: SECTION THROUGH			
	REV. 2	INJECTION CHAMBER ASSEMBLY		

CLEARANCE HOLE FOR M8 SET SCREW  
ON DIA. 204 PCD.

FILLET WELD JOINT



ELEVATION



END VIEW

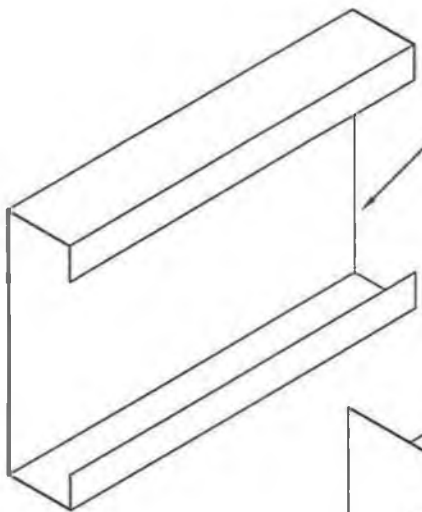
CLEARANCE SLOTS FOR  
M12 BOLTS

PROJECT	PRESSURE INJECTION OF SEMI-MOLTEN ALUMINUM INTO THIN WALLED MOLD.			
DRAWING 2	SUPPORTS FOR INJ. CHAMBER			
DRAWN	E.D.C	DATE	20/08/03	SCALE NTS
Page: 133			TITLE: SUPPORT BRACKET	
			QUANTITY: 2	REV. 4

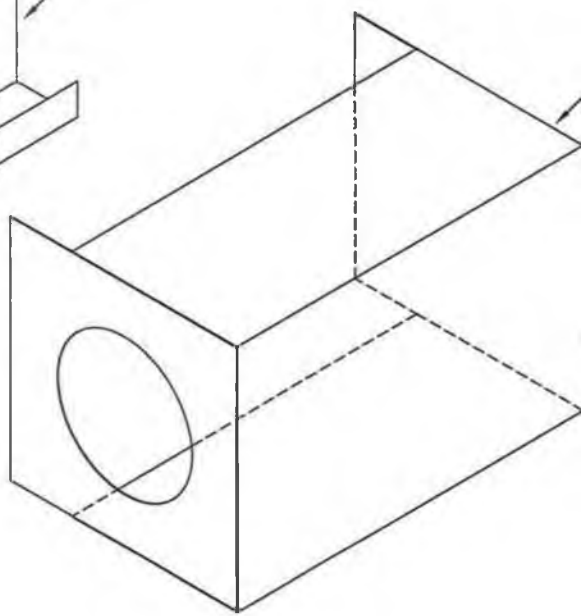


1 2 3 4

A



PART 1



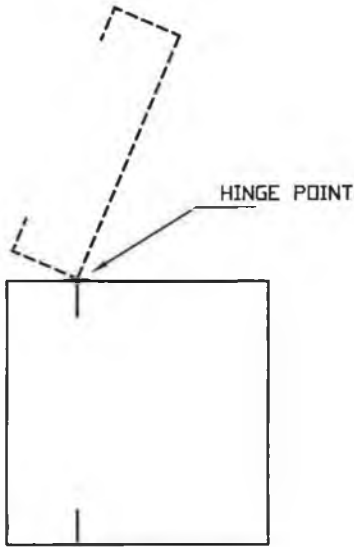
EXPLODED ISOMETRIC

E

F

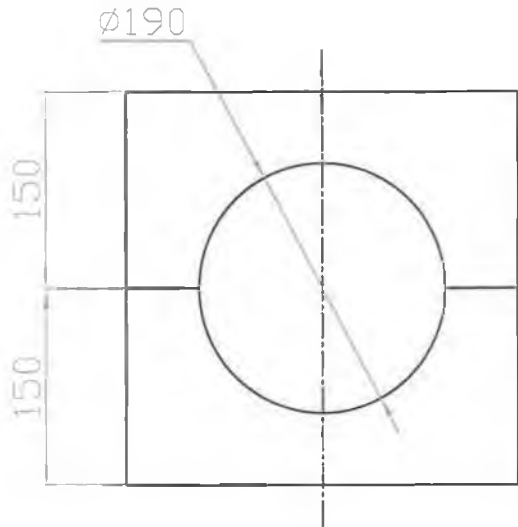
1 2 3 4

PART 2

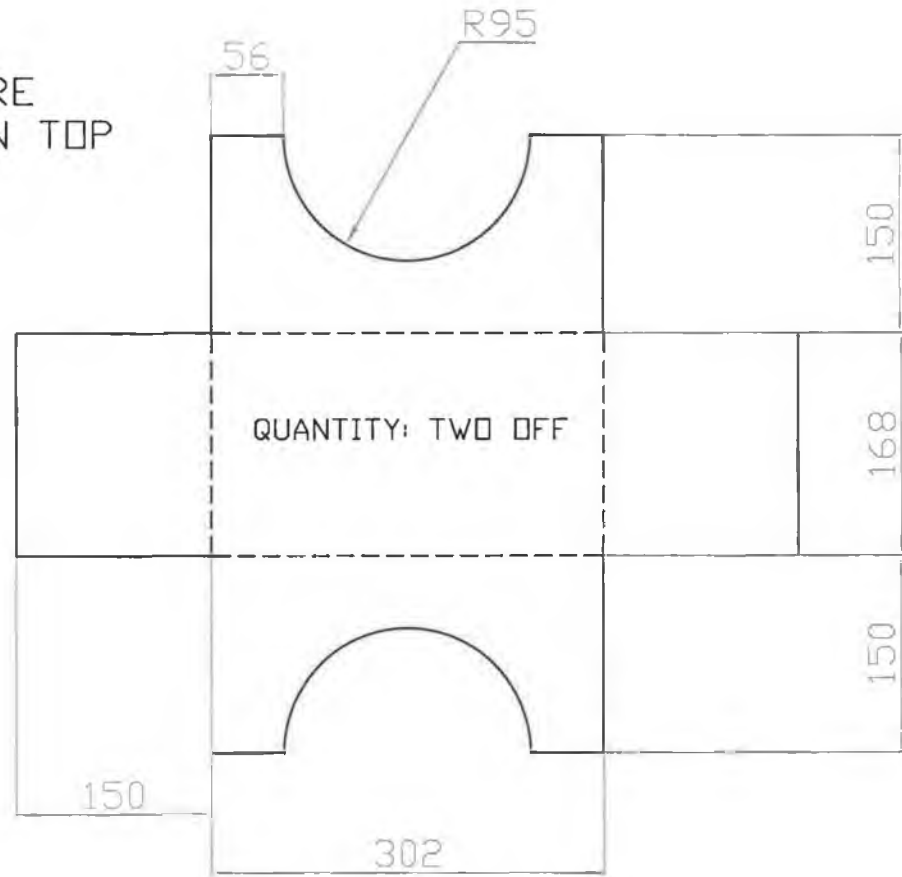
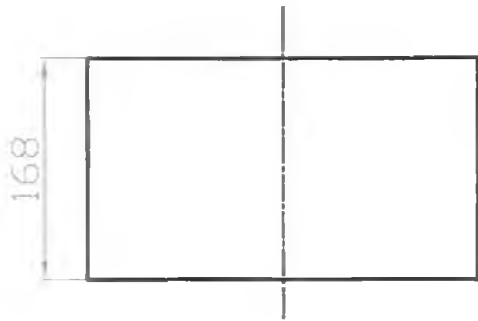


END VIEW OF ASSEMBLY

PROJECT	PRESSURE INJECTION OF SEMI-MOLTEN ALUMINUM INTO THIN WALLED MOLD.			
DRAWING 13	ISOMETRIC VIEW OF MOLD COVER			
DRAWN	E.O.C	DATE	13/08/03	SCALE NTS
Page: 134		TITLE: ISOMETRIC ASSEMBLY		REV. 2



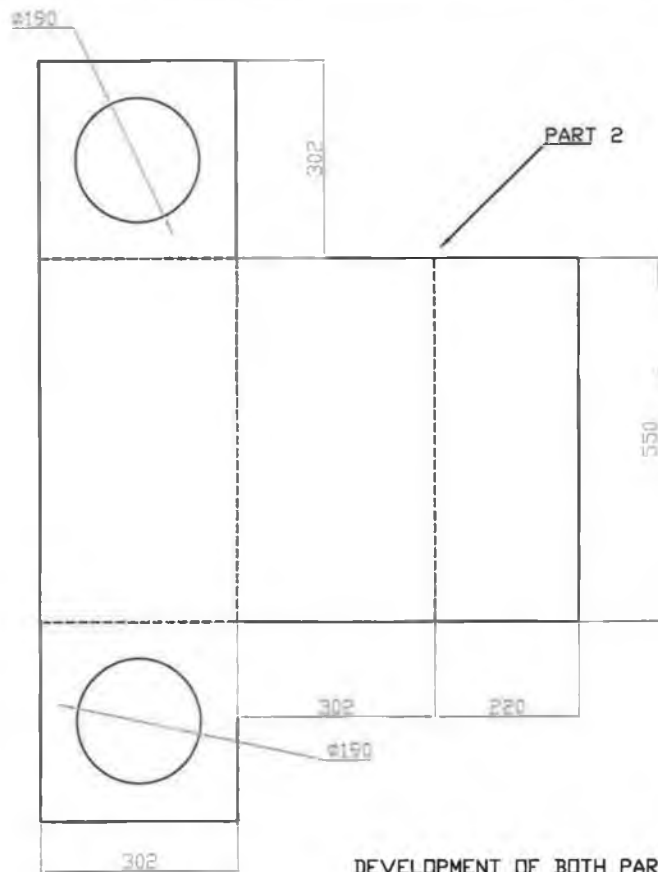
NO JOINT HERE  
JUST LAID ON TOP



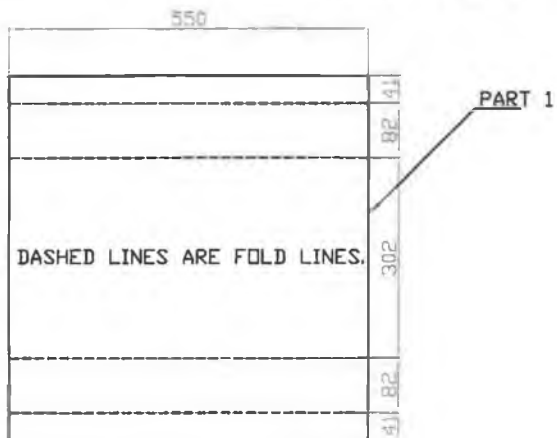
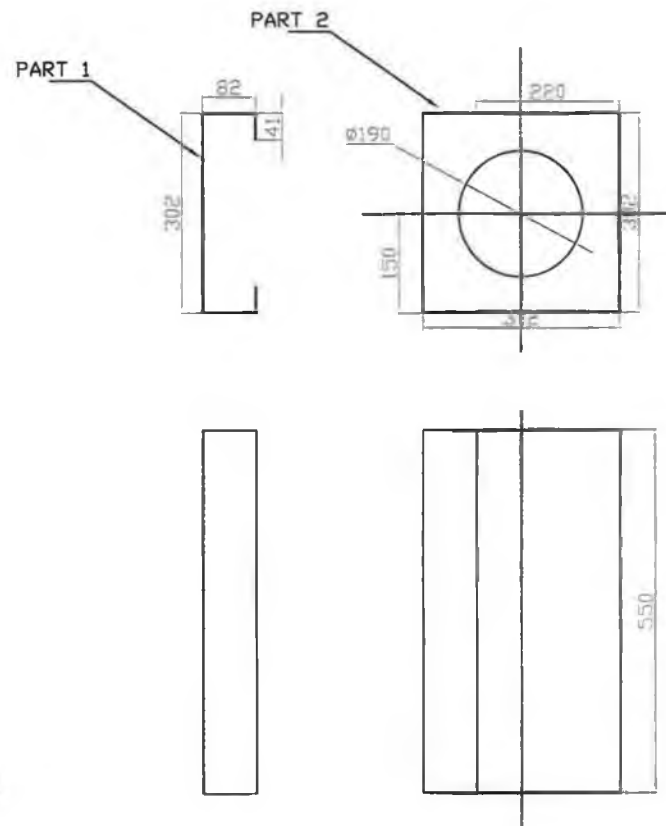
DEVELOPMENT FOR BOTH TOP & BOTTOM IS IDENTICAL.

DASHED LINES ARE FOLD LINES.

PROJECT	PRESSURE INJECTION OF SEMI-MOLTEN ALUMINUM INTO THIN WALLED MOLD.			
DRAWING 14	PLAN /ELEVATION/ DEVELOPMENT			
DRAWN	E.O.C	DATE	13/08/03	SCALE NTS
page: 135		TITLE: INJ. CHAMBER COVER		
QUANTITY: TWO			REV.	2

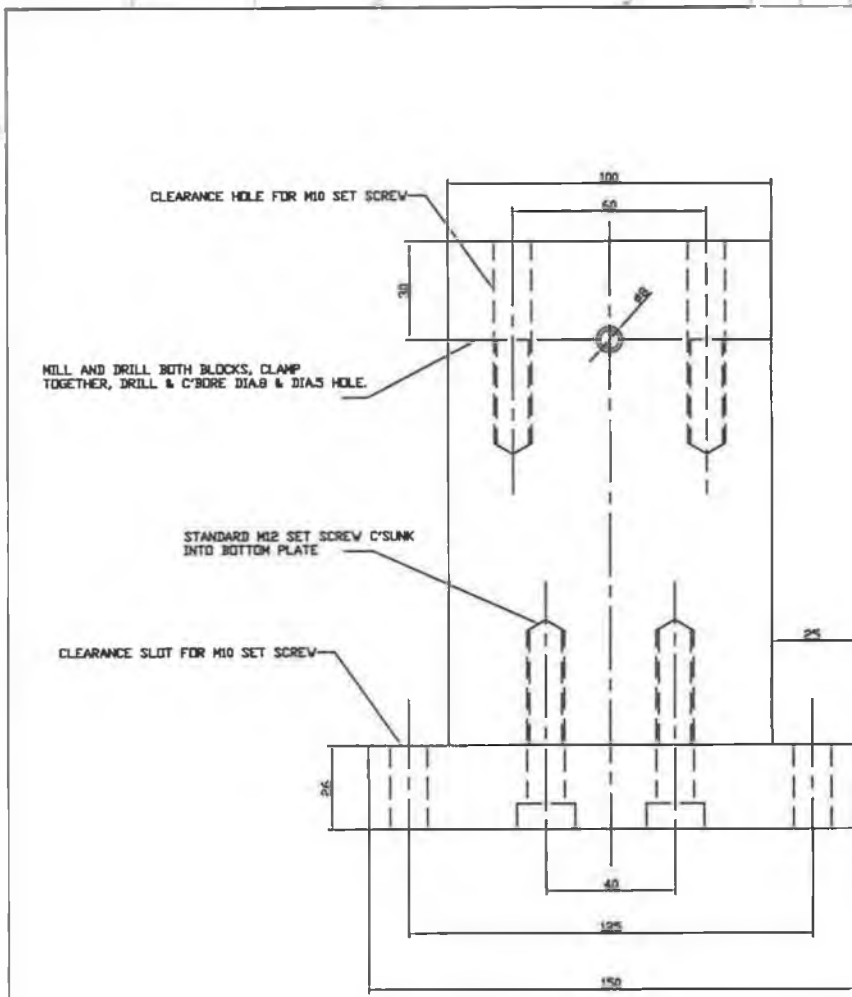


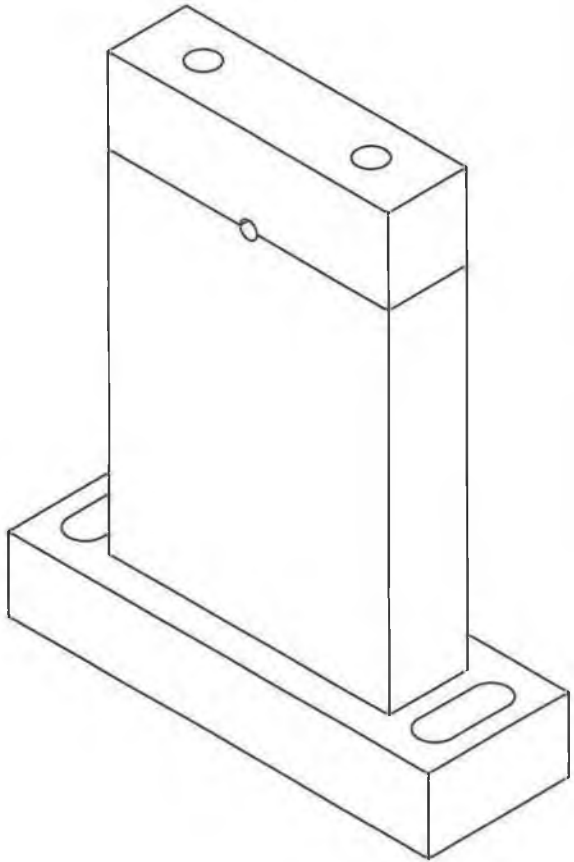
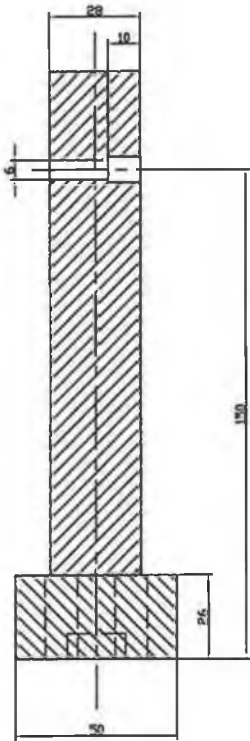
DEVELOPMENT OF BOTH PARTS OF MOULD HOUSES.



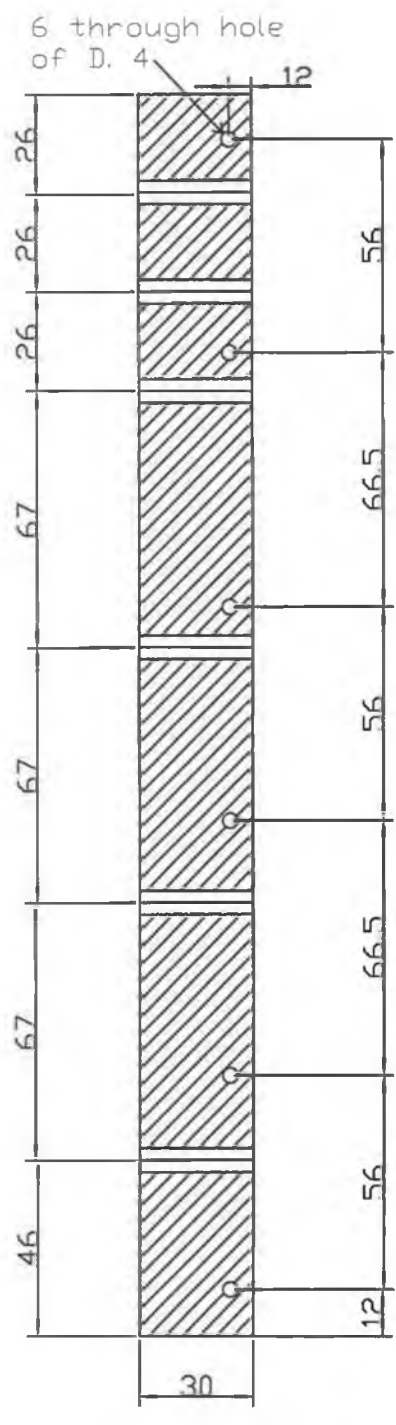
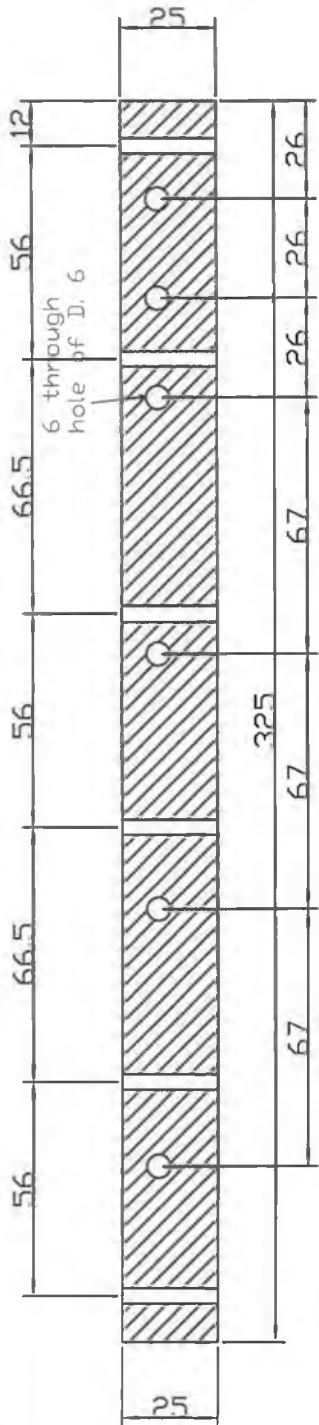
DASHED LINES ARE FOLD LINES.

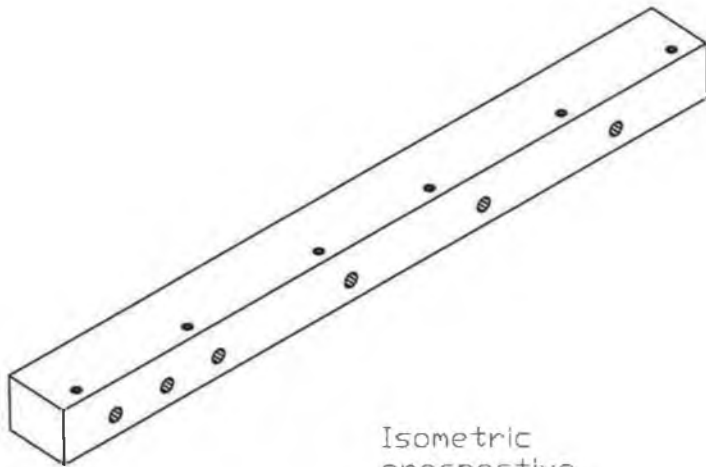
PROJECT	PRESSURE INJECTION OF SEMI-MOLTEN ALUMINUM INTO THIN WALLED MOLD.			
DRAWING 12	PLAN/	ELEVATION/	DEVELOPMENT	
DRAWN	E.O.C	DATE	13/08/03	SCALE NTS
Page: 136			TITLE: S/S MOLD COVER	
			REV.	2



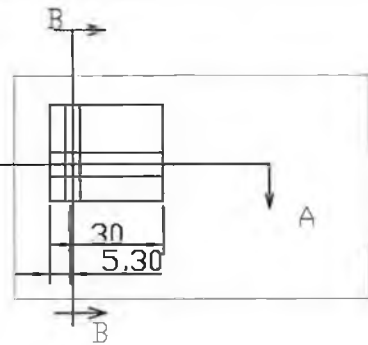


PROJECT	PRESSURE INJECTION OF SEMI-MOLTEN ALUMINUM INTO THIN WALLED MOLD.				
DRAWING 1	FINAL DESIGN FOR MOLD CLAMP.				
DRAWN	E.O.C		DATE	16/07/03	SCALE NTS
Page: 137			TITLE: MOLD SUPPORT CLAMP		
			QUANTITY: 1	REV.	3





Isometric  
prespective

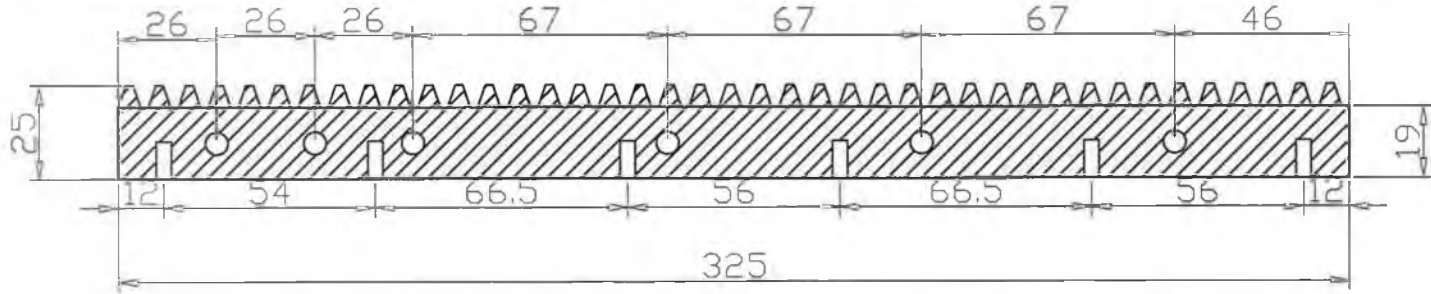


Front elevation

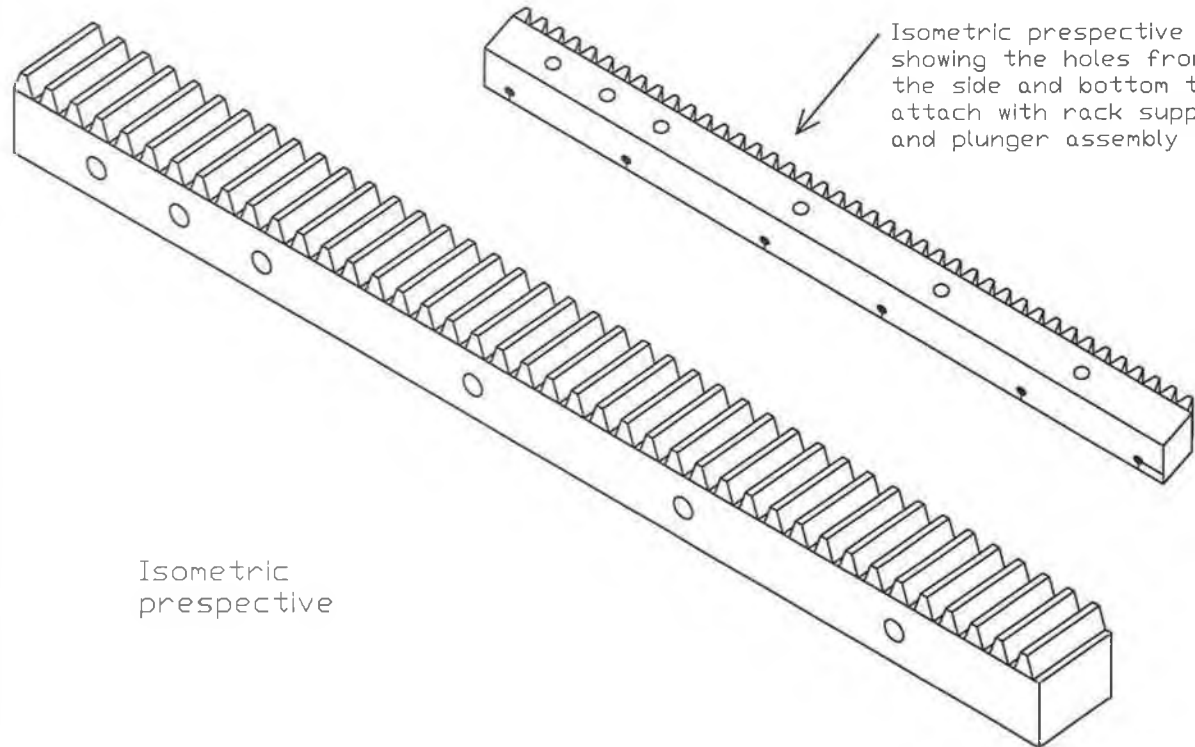
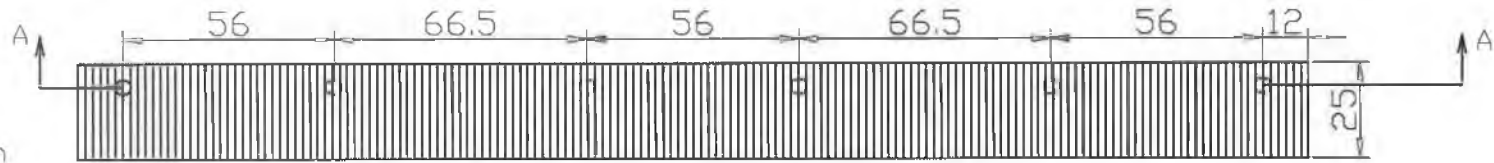
Project	Pressure injection of semi-molten Aluminum into thin walled mold			
Drawing	Scale: Not to scale			
Material : steel	Date:	Project	Project	
Page: 138	Title: Rail		Quantity: 1	



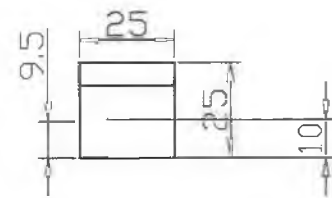
Section A-A



Top elevation

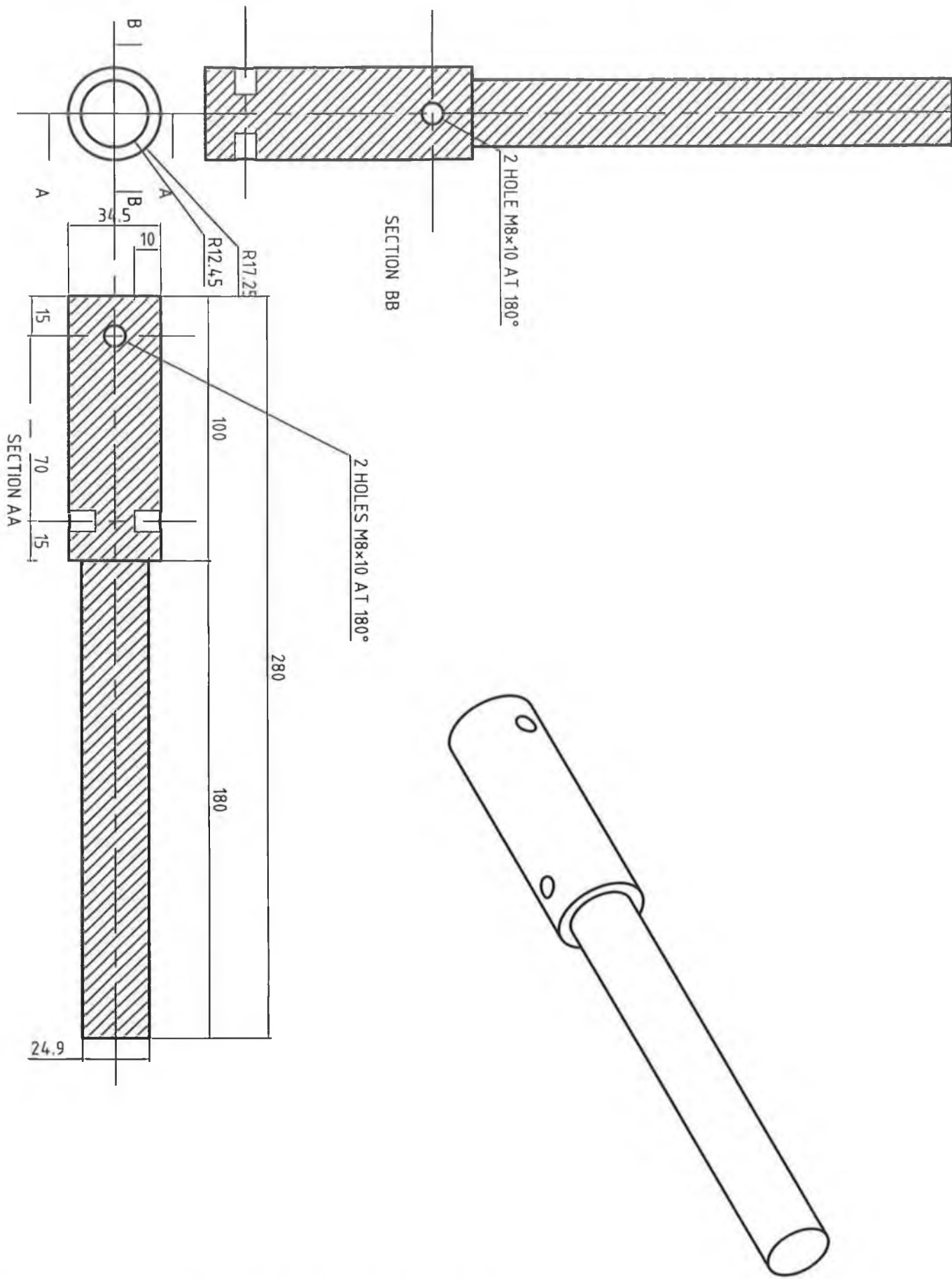


Isometric prespective



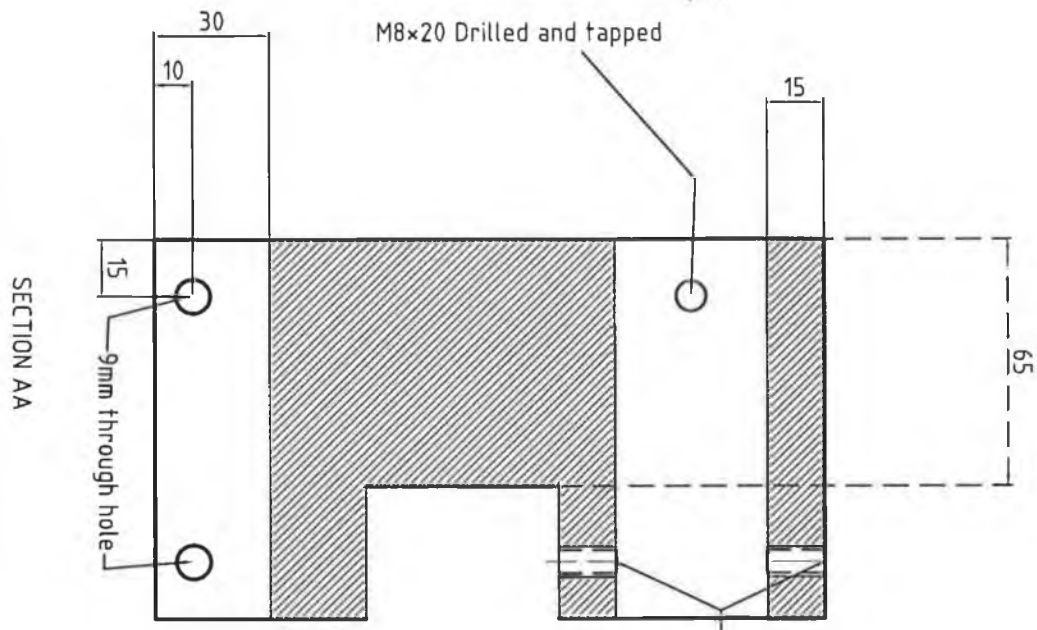
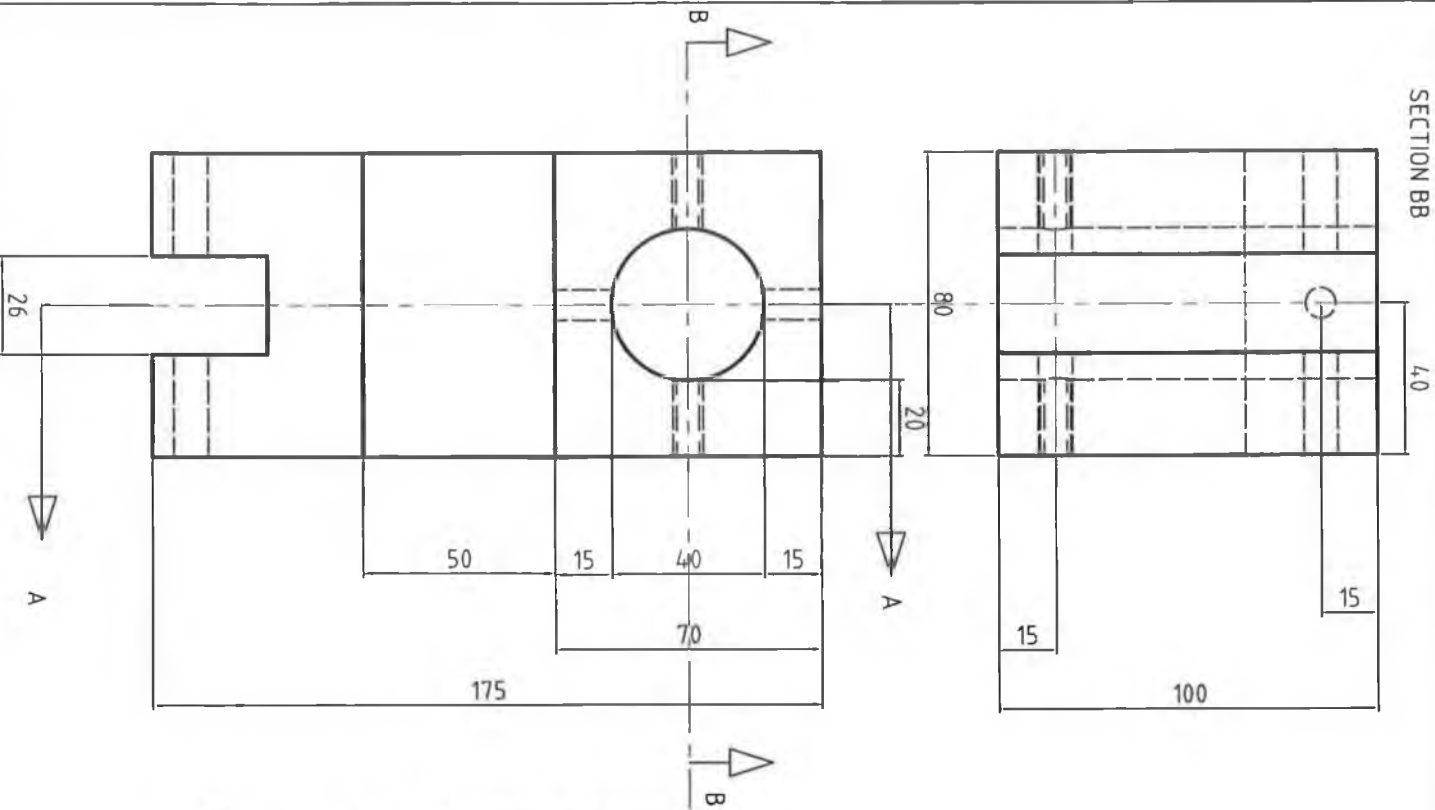
Front elevation

Project	Pressure injection of semi-molten Aluminum into thin walled mold		
Drawing	Scale: Not to scale		
Material : steel	Date:	Project	Project
Page: 139	Title: Rail		
	Quantity: 1		

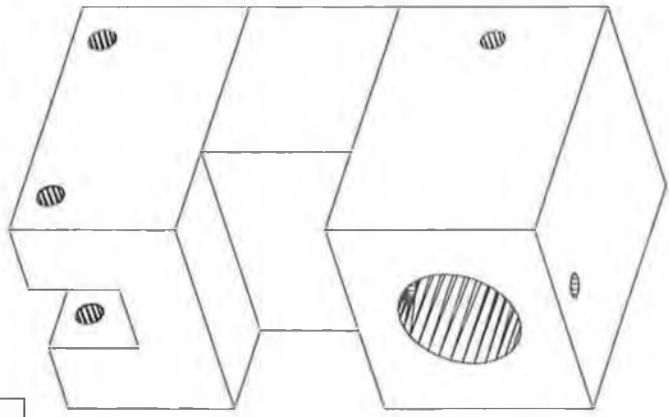


Project	Pressure injection of semi-molten Aluminum into thin walled mold		
rawing :	PLUNGER	Appendix	
Material :	steel	Date:	Project
Page: 140	Title: PLUNGER		
	Quntity 1:		

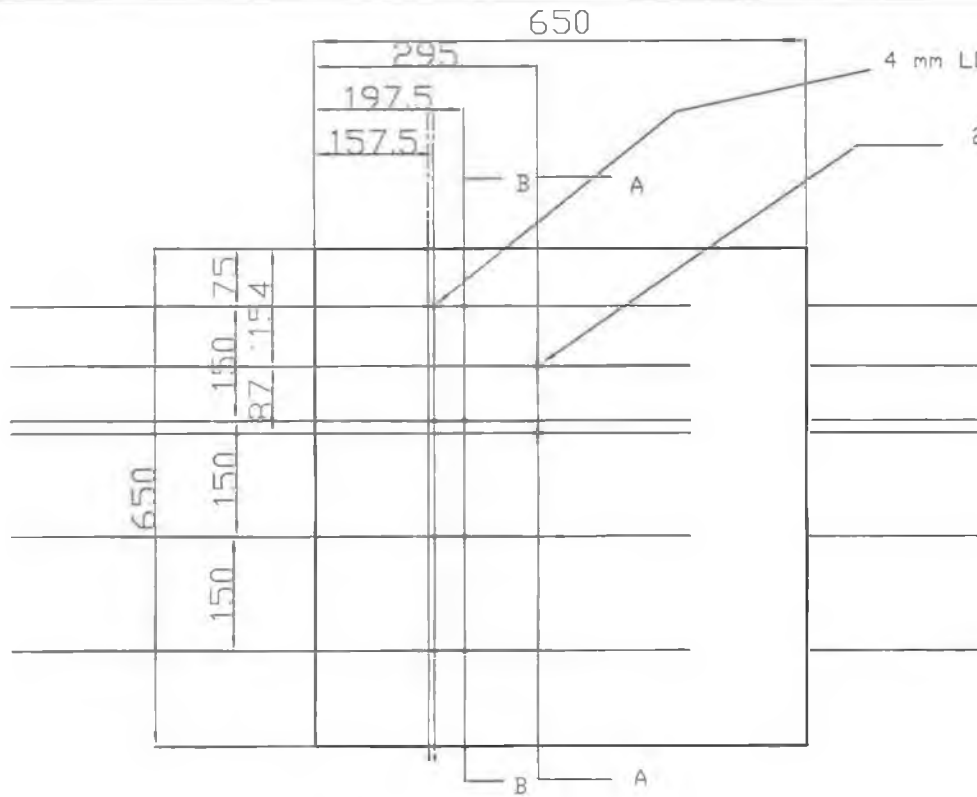
SECTION BB



Isometric view



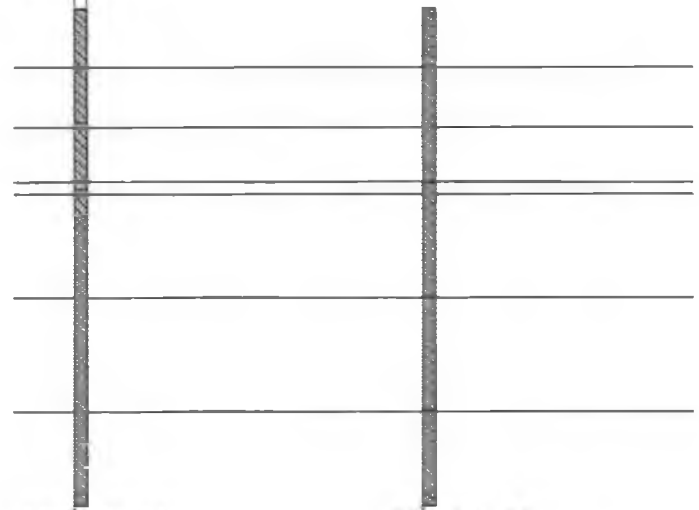
Project	Pressure injection of semi-molten Aluminum into thin walled mold		
Drawing	Appendix		
Material : steel	Date:	Project	Project
Page: 141	Title: PLUNGER ASSEMBLY		
	Quantity 1:		



4 mm LOW PROFILE H CAP SCREW OR COUNTER SINK M4

2 TAPPED HOLES M10

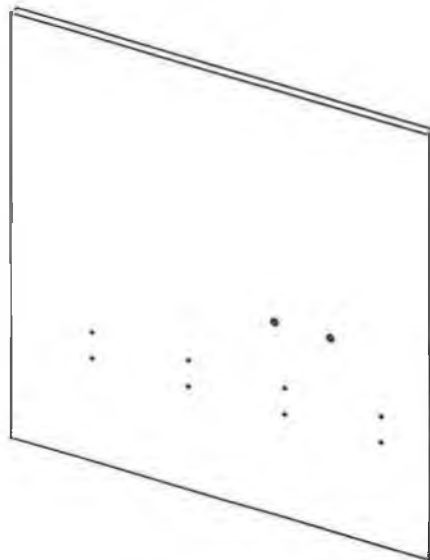
16



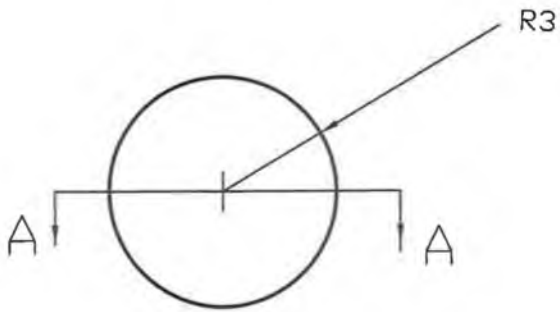
SECTION AA

SECTION BB

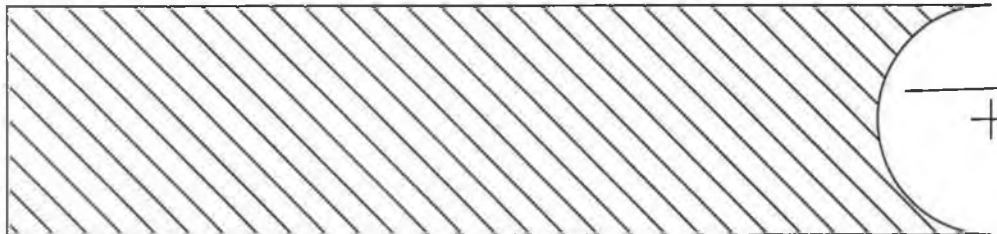
Isometric  
prespective



Project	Pressure injection of semi-molten Aluminum into thin walled mold		
Drawing	Scale : Not to scale		
Material : steel	Date:	Project	Project
Page: 142	Title: Steel plate		Quantity 1:

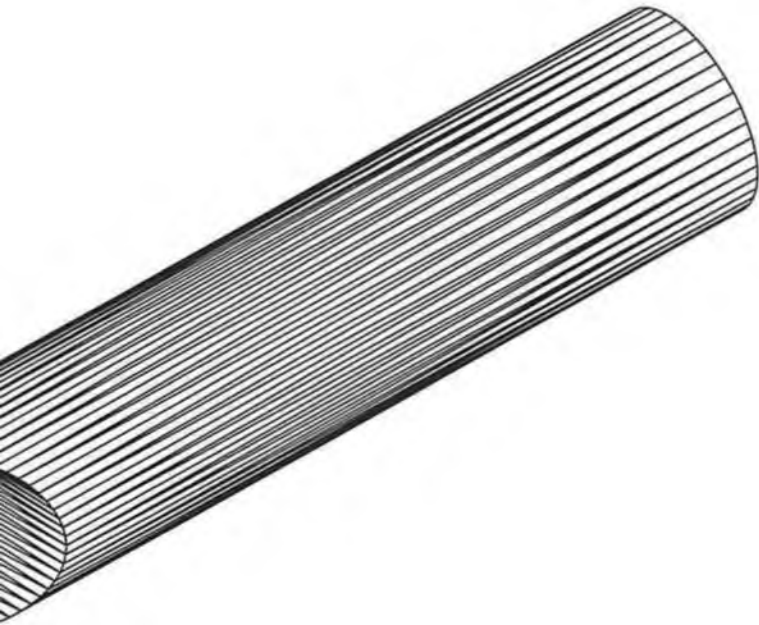


SECTION AA



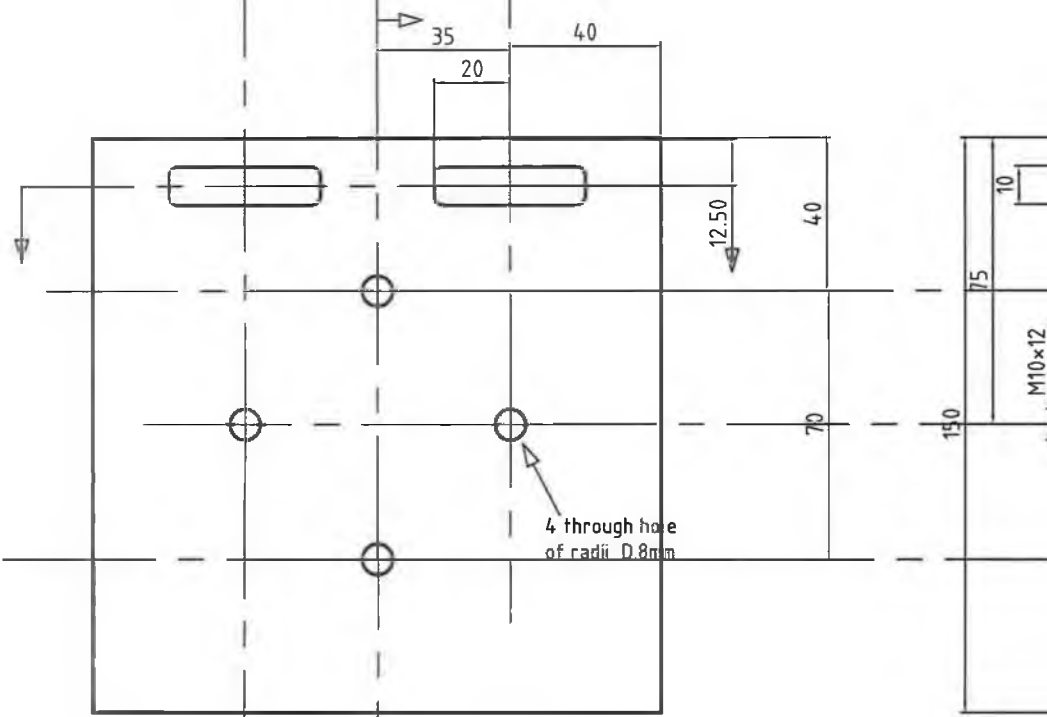
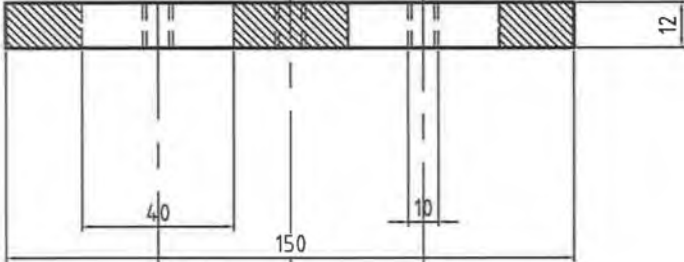
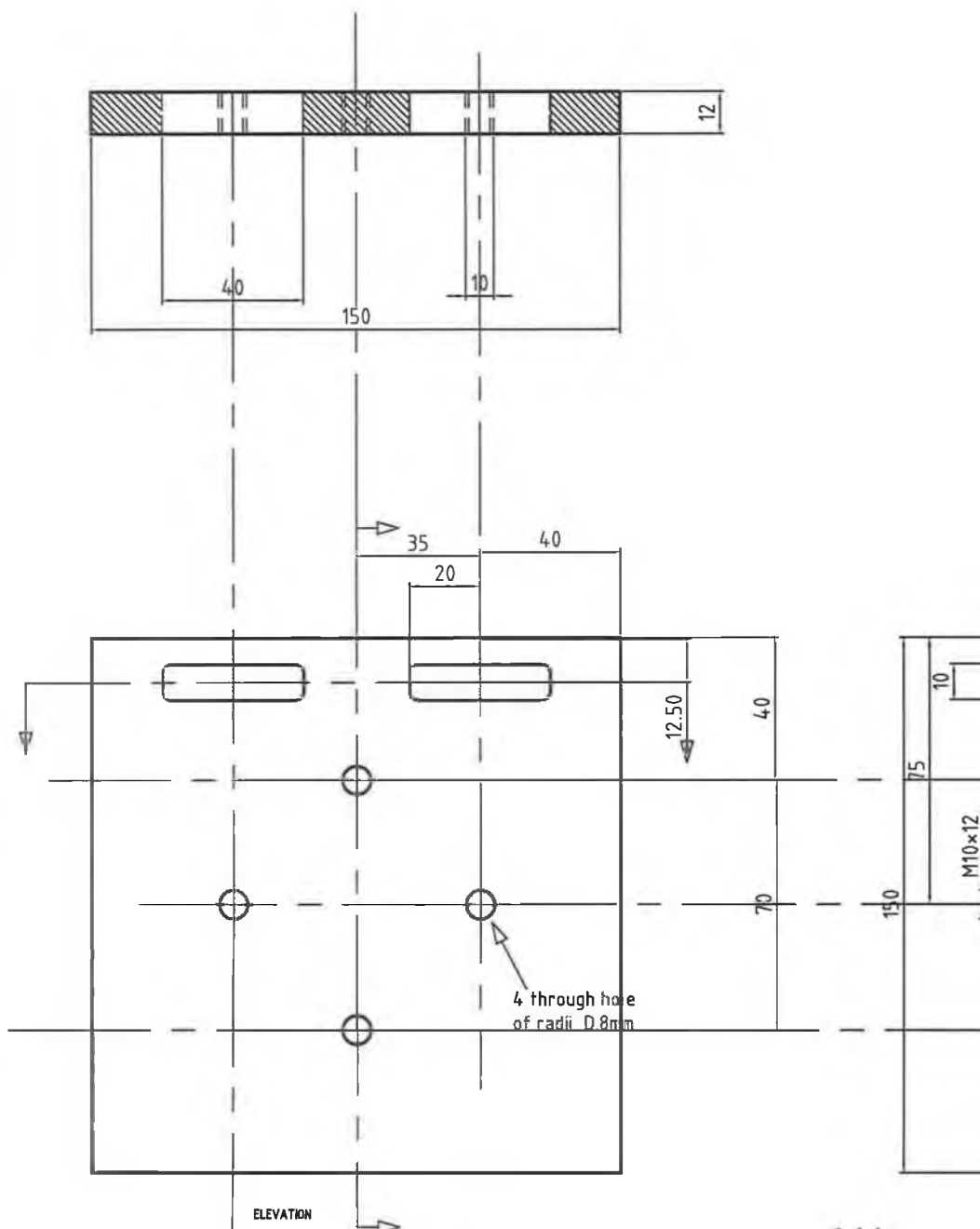
SECTION AA

175



CUT  
WITH  
A  
RADIUS  
OF 3  
MM

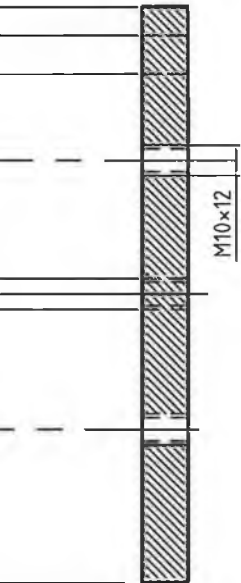
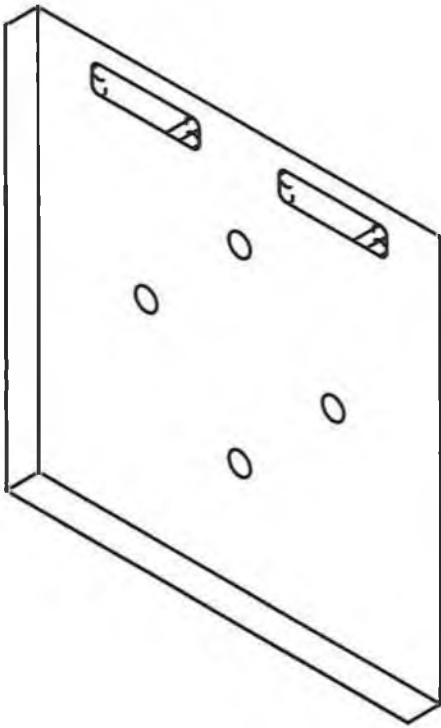
Project	Pressure injection of semi-molten Aluminum into thin walled mold		
Drawing	Appendix		
Material : steel	Date:	Project	Project
Page: 143	Title: steel Rod		



ELEVATION

4 through hole  
of radii D.8mm

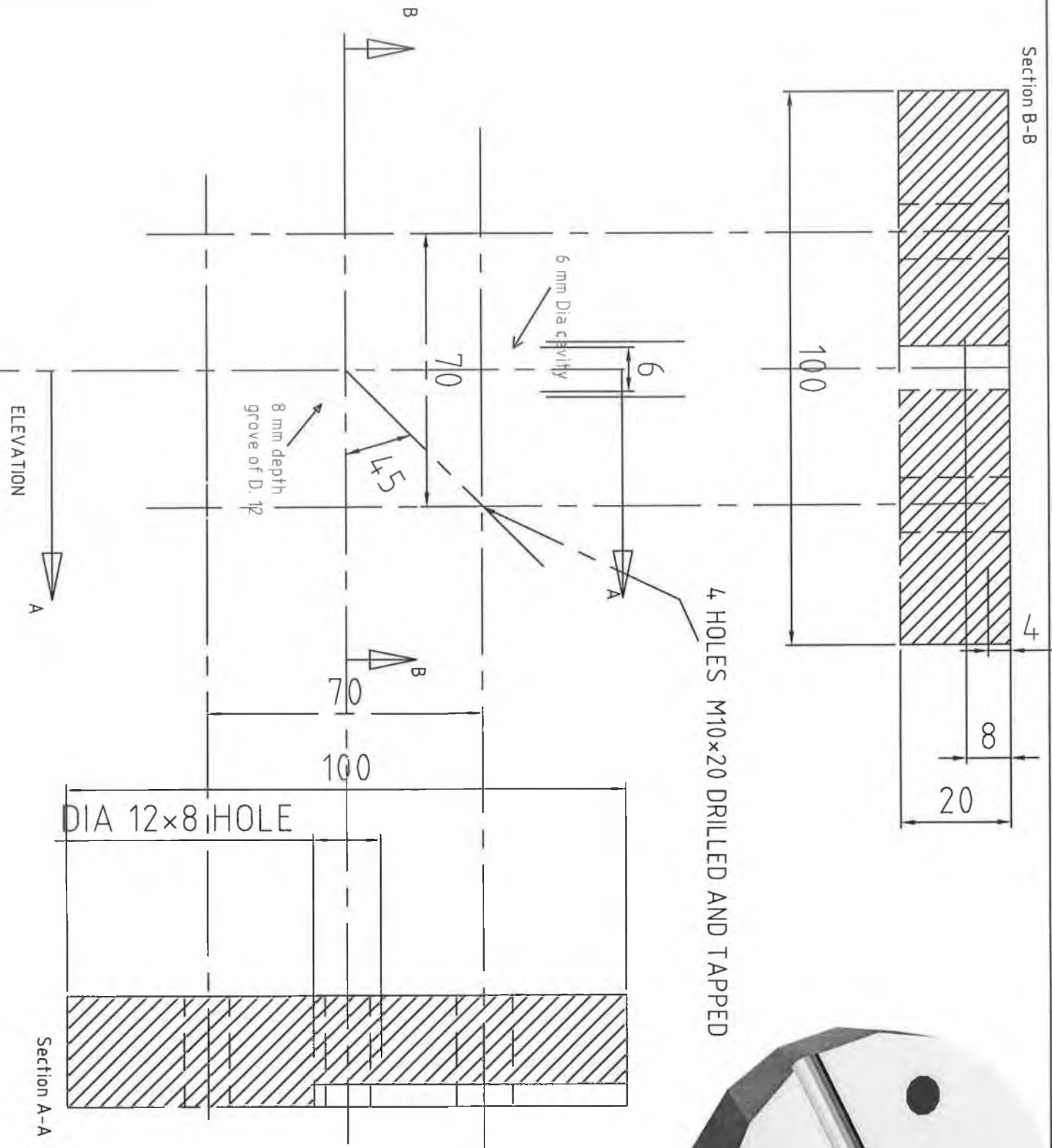
M10x12



END VIEW

Project	Pressure injection of semi-molten Aluminum into thin walled mold		
Drawing	Appendix		
Material : steel	Date:	Project	Project
Page: 144	Title: Rail		





Project	Pressure injection of semi-molten Aluminum into thin walled mold			
Drawing	Appendix			
Material : steel	Date:	Project	Project	
Page: 145		Title: Rail		
		Quantity 1:		

## Appendix: E Pictures of capillary viscometer



Figure E1 Capillary viscometer developed



Figure E2 Plunger-in position

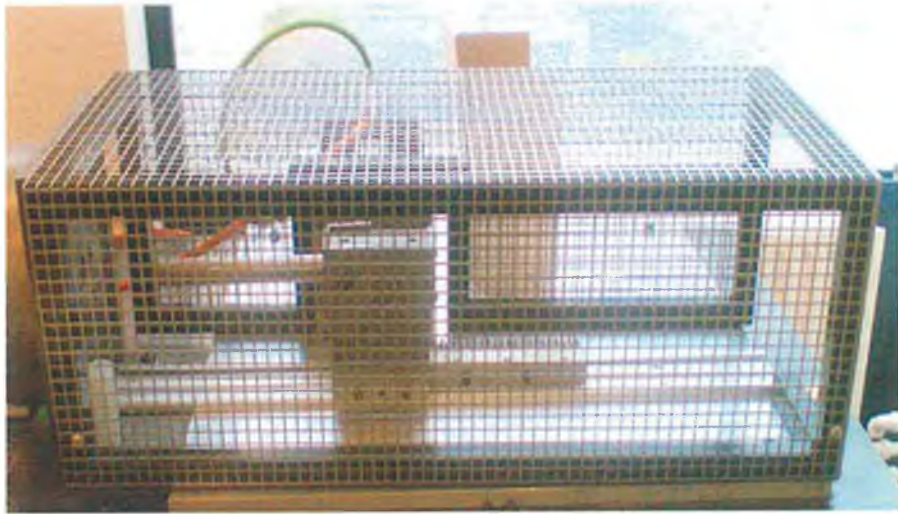


Figure E3 Piston motion mechanism assembly with safety guard



Figure E4 Side view of piston motion mechanism

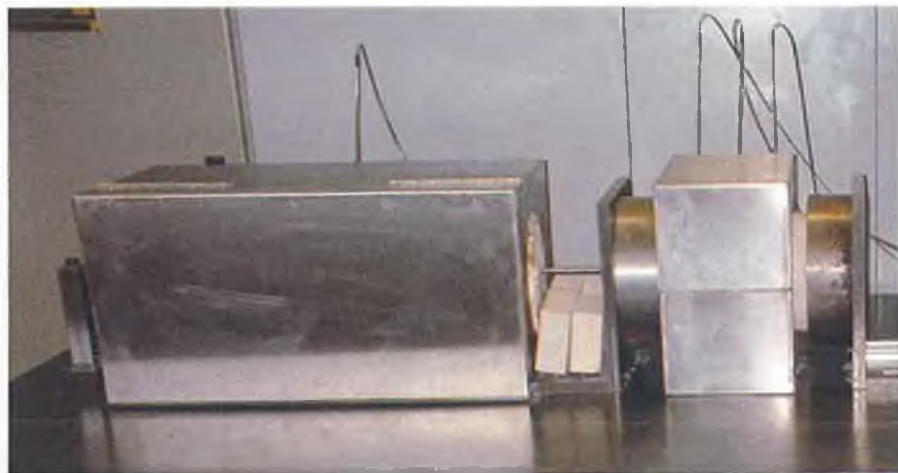


Figure E5 Injection chamber with three thermocouples, injection chamber supports, capillary tube and insulation materials surrounded by steel covers.





Figure E6 Injection chamber, heater bands, steel rod transmitting pressure to load cell, injection chamber supports and insulation material.



Figure E7 Insulating material surrounded by steel plates, capillary tube and end support for the capillary tube.

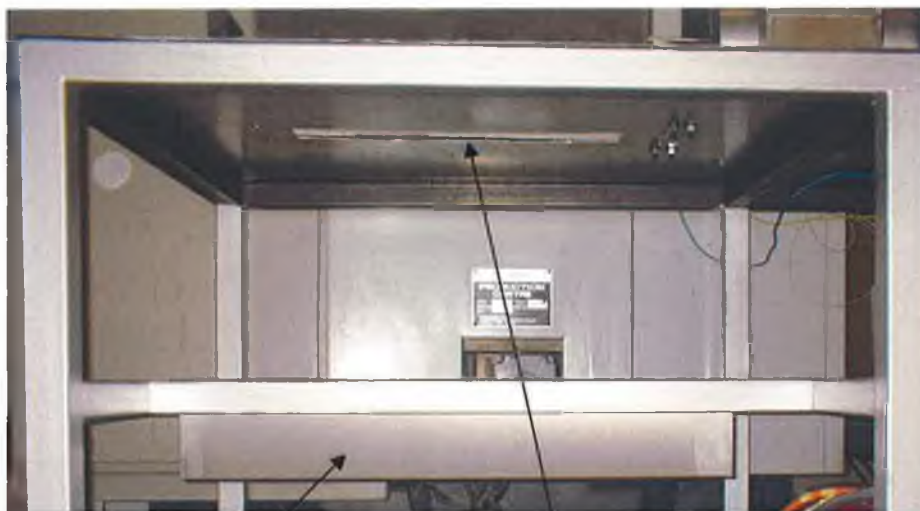


Figure E8 Quenching water tank and rectangular slot underneath the table.



Figure E9 Steel rod transmitting pressure to load cell, load cell holding assembly underneath table.



Figure E10 Temperature controller and motor controller with National Instrument data acquisition box



Figure E11 Safety guard over controllers and data acquisition box.

**Appendix: F Preparation methods, images and microstructure of feedstock for viscometry tests**

<b>Group</b>	<b>Sample Number</b>	<b>Pouring Temperature (°C)</b>	<b>Pseudo-isothermal hold (sec)</b>
1	7, 15, 28 & 30	680	45
2	25, 26 & 27	650	45
3	14, 18 & 24	665	45 and allowed to solidify without quenching
4	19, 20 & 23	630	45
5	8, 9, & 10	680	60
6	16, 21, & 22	650	60
7	11, 12, 13 & 17	630	60
8	29	640	120

Table F.1 Parameters for preparation of feedstock for viscometry tests.



Figure F.1 Images of feedstock billets after finish machining, sample numbers 14, 18, 14, 16, and 21.



Figure F.2 Images of feedstock billets after finish machining, sample numbers 15, 28, 30 & 13, 17 & 20, 19 & 29.



Figure F.3 Images of feedstock billets after finish machining, sample numbers 25, 26, 27 & 8, 9, 10.



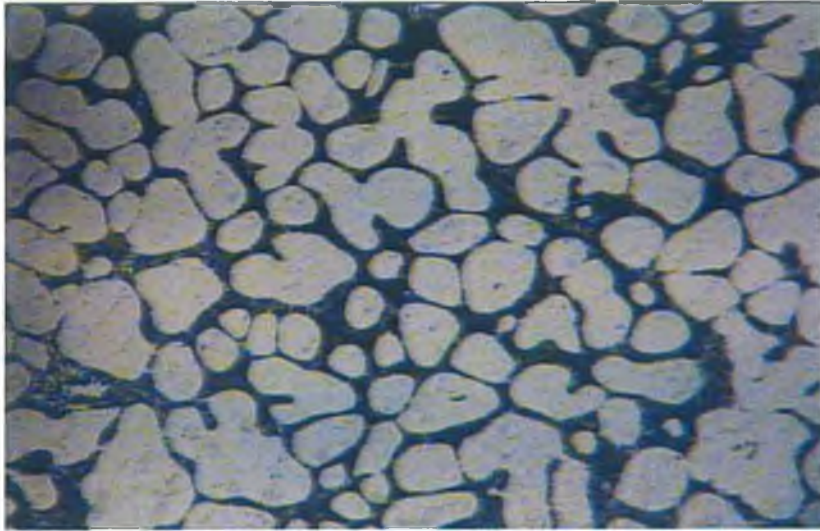


Figure F.4 Microstructure of billet isothermally held for 45 sec and pouring temperature of 630 °C before quenching, , from group 4 in table I.1 above.

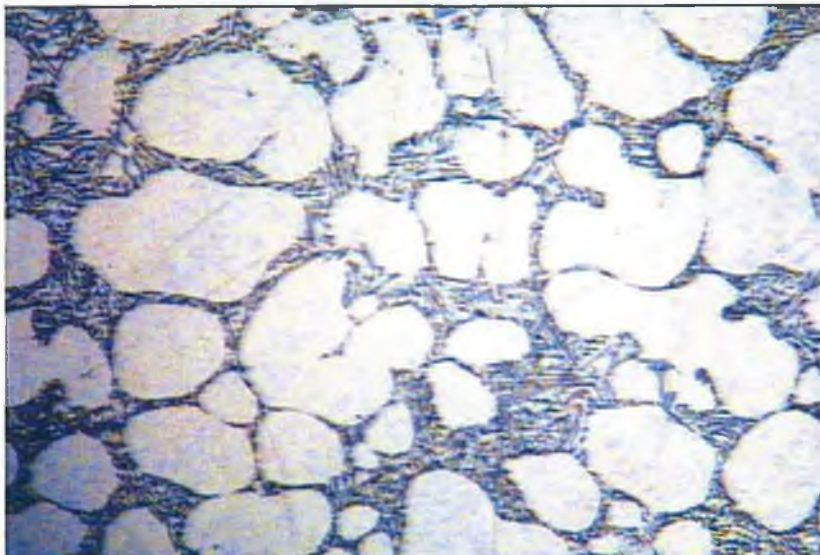


Figure F.5 Microstructure of billet isothermally held for 120 sec and poured at a temperature of 640 °C before quenching, from group 8, sample 29 in table I.1 above.



## **Appendix G: Background to Fluent operation**

### **Mesh**

A collection of point representing the flow field, where the equations of fluid motion are calculated.

### **Model**

Numerical algorithms that appropriate physical phenomenon, like turbulence.

### **Nodes**

The distinct point on the mesh where equation of fluid motion are solved.

### **Finite element analysis**

Engineering problems are often solved with mathematical models using derived differential equations (mass, force and energy) with boundary conditions and initialization. Finite element analysis is used to solve engineering problems like linear, transient, or non-linear problems in stress analysis, heat transfer and fluid flows. Engineering problems are generally composed of Natural behaviour (thermal conductivity, elasticity, viscosity) and Disturbance (temperature, pressure, force and moments of the system). The Finite element method is used to solve large complex geometric problems where the complex equations solve for their simple shape. Finite element method uses the integral formulations to create a system of algebraic equation and a complete solution is obtained by assembling or combining the results for all the individual equations for all the elements. Solving any kind or problem with finite element analysis involves the creation of geometry, meshing geometry, modelling and material properties, initial and boundary condition and initialization.

### **Introduction to Gambit**

There are various methods like CAD, CAM used to create the geometry of the part. GAMBIT is the package use to create and modify geometry. There are many ways to create the geometry for meshing in Gambit. Point, lines and curves can be used to model the geometry. Gambit allows us to create an entity with a label name.. Point or vertices can be created in the coordinates in their required position either by taking the reference point or taking the distance from the relative point in the XY co-ordinate system. In the vertex option of the Gambit, files can be moved, copy, delete,

rotate, translate or reflect any entity according to the system specification. Join together the vertices either by connecting vertices command by picking the required vertices that need to be joined together or by line command by joining together the vertices to make a line. Faces and volumes can be created and given different name for calculation purposes later on by joining together the line or vertices for the specified face by lines or curves and then later, all the lines and curves are grouped in a single geometry to react like a single geometry.

### Methods for Meshing Geometry

For complex geometry, the function are sometime varies and change with time in every domain and element, solving the problem for each cell and solution for all the element will be a solution of the domain. Different techniques can be used to mesh the geometry depending upon the creation of the geometry. We can mesh all the line separately with different number of elements by specifying different interval size and spacing of nodes, we can also mesh faces and volume by taking all into account at the same time and specified the meshing type. If we want to create a mesh on faces, we can mesh each face separately according to the need and calculations at that face. Or can simply use the whole volumes to create the geometry by selecting the volume and mesh typing from the available options. Different kind of mesh generation can be used i.e. triangular element, rectangular, hybrid, tetrahedral and quadrilateral meshes. Triangular element formulation is used for 2D solids. It is simple and less accurate and can be used for complex geometries with acute corners. Rectangular elements have more accurate results as compared to the triangular elements. Equation formulation is for simple than triangular element. Strain matrix is not a constant giving more realistic stress distribution in the structure. Although it is very accurate, but its practical application is limited as it cannot be used with geometries other than rectangles. Quadrilateral element can be used for unparallel, curve and all type of irregular shapes. It is more accurate and gives us good results. Fine meshing can result the accuracy with more element. However, more the element more will be the required computational time and memory. Due to constraining memory and time, it is necessary to limit the number of elements.

## Fluent

Fluent is written in C computer language and an art computer program to model the heat transfer and fluid flow in complex geometries. In a similar manner to typical finite element simulations Fluent uses the finite-volume method to solve the governing equations for a fluid. Fluent provides flexibility and solving problems with unstructured mesh generation around the complex geometries with ease to reduce time we spend on generating meshes. Fluent can support both 2D (triangular or quadrilateral) and 3D (tetrahedral, hexahedral, pyramid, or wedge cells) meshes that allow us to pick the best topologies that are the best suited for a certain application. Fluent includes

- Fluent, solver
- PrePDF, pre-processor for modelling non-premixed combustion in fluent.
- GAMBIT, pre-processor for geometry modelling and mesh generation.
- T-Grid, an additional pre-processor that can generate volume mesh from an existence boundary mesh.

By creating and meshing our geometry in Gambit. Once a mesh has been read into solver (Fluent), rest of the operations like modelling, material properties selection, execution, refining the mesh, operation and boundary condition can be performed within the Fluent.

## Fluent Capabilities

Modelling the flow in 2D and 3D unstructured meshes, compressible and incompressible flow, inviscid laminar and turbulent flow, Newtonian and Non-Newtonian flow, steady and transient flow, conduction, convection and radiation heat transfer, phase change, single and multi-phase modelling, moving and stationary boundary modelling, aerospace, automobile and turbo machinery applications, Material processing application, heat exchanger applications, electronics appliances and in architecture design and fire research.

## Solver Formulation

The solver panel allows selecting the solution method for the calculations. We have a choice to select two numerical methods in fluent i.e.

- Segregated

- Coupled Solution

Law of conservation of mass and momentum will be the governing equations and whenever necessary for energy and scalar quantities like velocity, turbulence and chemical species for both solvers. Control volume techniques could be applied using computational grids, algebraic equations based on individual control volume. Both follow the similar discretization process but follow different approaches to linearize and solve the discretize equations.

For modelling the problem, both the segregated and coupled solver provides accurate results for a broad range of flow and control volume technique is used in both cases. In segregated solver, the governing equations (momentum, continuity, mass flow rate, energy, species, and turbulence and scalar equations) are solved sequentially. Segregated solver solve for a single variable like pressure, velocity and temperature by considering all cells at the same time. Segregated solver is more appropriate for the incompressible, low velocities flow, and it requires low memory spaces as compared to the coupled solver. Segregated solver provide us more physical models which are not available with coupled solvers like volume of fluid model, multiphase model, and Eulerian multiphase model. Several iterations of the solution loops need to be performed before a converged solution is obtained because the segregated solver uses the equations which are non linear and coupled. The steps need to be performed for each iteration. In segregated solution the properties are updated based on initialize solution. Current value of pressure and mass fluxes are used in each turn to solve the  $u$ ,  $v$ , and  $w$  momentum equations for velocity updates. If the velocity doesn't satisfy the continuity equation, pressure correction equation is then added to solve and correct pressure and velocity fields. The equations for scalar are solved whenever needed and a check of convergence set of equation is made. Formulation allows to specify implicit or explicit formulation. In both segregated and coupled solution methods, set of linearize equations for all the dependent variable in each cell are produced, solved and updated from the discrete, nonlinear governing equation. Depending upon the variable and interest, governing equation may take an implicit or explicit form to linearize the governing equations.

Implicit formulation means that for the given variable, unknown value in each cell is computed using a relation that include both existing and unknown values, each unknown values then appears in each equation in the system and must be solved simultaneously to give the unknown value.

Explicit formulation for an unknown variable will only be appearing once in the equation for each cell can be solved one at the time. This type of formulation is only used with the coupled solver and cannot be used for segregated solver.

There are more than one unknown values, like pressure, viscosity, velocity and temperature, and appears in all equation, and only available option with segregated solver, therefore the implicit formulation is selected.

When the domain is axisymmetric about the x-axis, then use the axisymmetric option. Axisymmetric swirl option is used when we are taking into account the axisymmetric flows and three dimensional flows with rotation, flows requiring sliding meshes, rotating or multi rotating reference frames. The velocity and pressure will change as the process will go on, especially when the fluid reaches the conical section, with the decrease of section area, acceleration increases while the pressure decreases, for the variation in pressure and velocity, flow is time dependent as it changes with time, select the time dependent flow. Selecting absolute velocity with first order unsteady state formulation enable the first order accurate dual time stepping, we cannot use the explicit as it is only available with the explicit formulation.

### Volume of fraction model

Volume of fraction model is appropriate for free surface liquid-liquid flow where the dispersed phase volume is less than 10 % and the two phases are not interpenetrating. Volume fraction of all the phases equal to unity. Phases and fluids are not interpenetrating. Variable is introduced for each additional phase and the variable and properties are representation of one phase or mixture or phases depending on volume fraction values in each cell. One set of momentum equation are shared by all phases and in each computational cell, the volume of each phase is tracked throughout the domain. Application of VOF model is in free surface flow, filling, and bubble flow in fluid, liquid motion after dam break, liquid-gas steady of transient flow. The regimes which can best describe the flow of semi-solid material are

1. Mixture model.
2. Eulerian model.

## Eulerian Model

It is more complex model than mixture model. For each phase, it solves the continuity and momentum equations. In Eulerian model, single pressure is shared by all phases. It is used for modelling multiphase flow with interacting phases with liquid, gas or solid or any combination. It can model any number of secondary phases if enough memory is available. Complex multiphase flow modelling with Eulerian model solution is limited by converging behaviour. For complex problem, the problem is first solved with mixture model and then solve for Eulerian model by completing the set up and carry on the calculation taking the mixture model as starting point. Another way of solving complex problem is to solve it first for primary phase keeping volume fraction off for the calculation and after solving turn on the volume fraction with certain value and solve it for all phases.

### Limitation

- $k-\epsilon$ , can be used for turbulence modelling.
- Density variation flow, melting and solidification, inviscid flow, heat transfer, cannot be modelled.
- Mass transfer other than cavitation, evaporation and condensation is not allowed.

### Comparison between mixture model and Eulerian model

The mixture model is used for a wide range of dispersed particles while Eulerian model is used when dispersed phase is concentrated in a portion of domain. If the interphase drag laws are unknown and the applicability to our system is not that important, mixture model can be used instead of Eulerian model. More computational effort and expenses with complexity is involved in Eulerian model as compared to mixture model. Little option doesn't work with Eulerian model. Slip velocity option is associated with slip velocity of the secondary phase. We are not considering any slip velocity between the particles, solving problem for a homogenous multi-phase flow, keeping slip velocity option off, considering all the phases move at the same velocity.

## Appendix: H Fluent simulation results

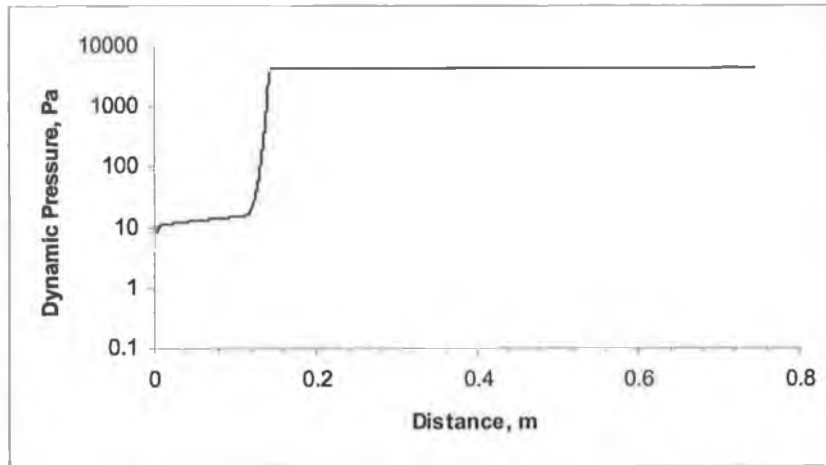


Figure: H.1 Transient state dynamic pressure at  $0.25 f_s$ , 878 K and 0.075 m/s plunger velocity

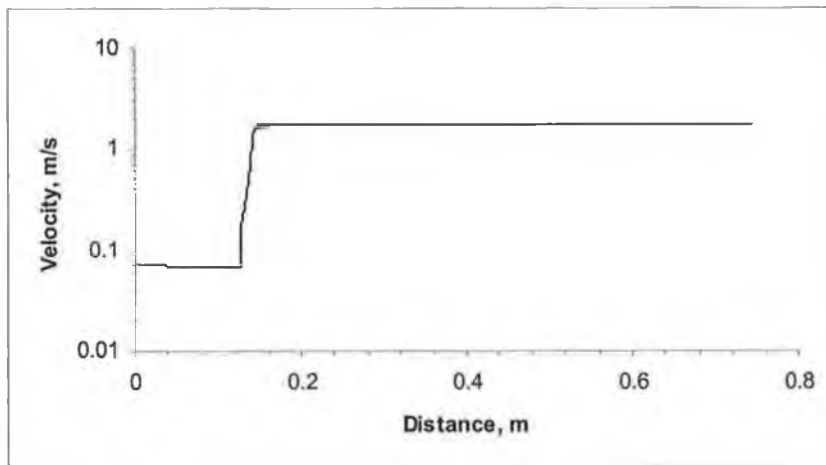


Figure: H.2 Transient state velocity at  $0.25 f_s$ , 878 K and 0.075 m/s plunger velocity

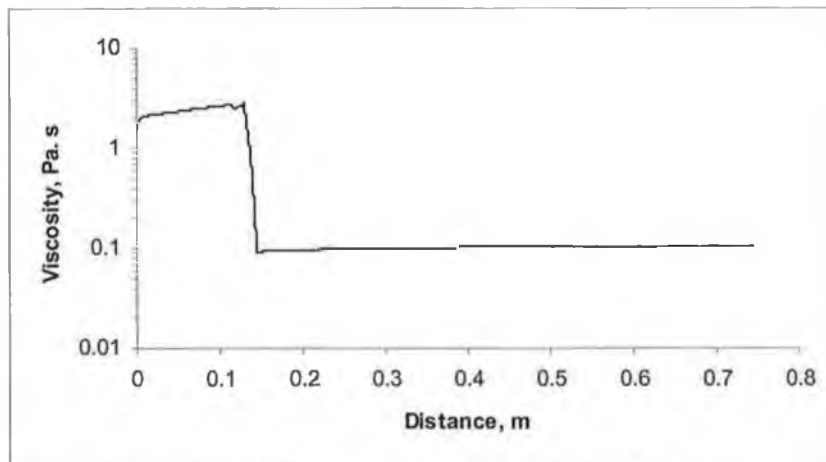


Figure: H.3 Transient state viscosity at  $0.25 f_s$ , 878 K and 0.075 m/s plunger velocity

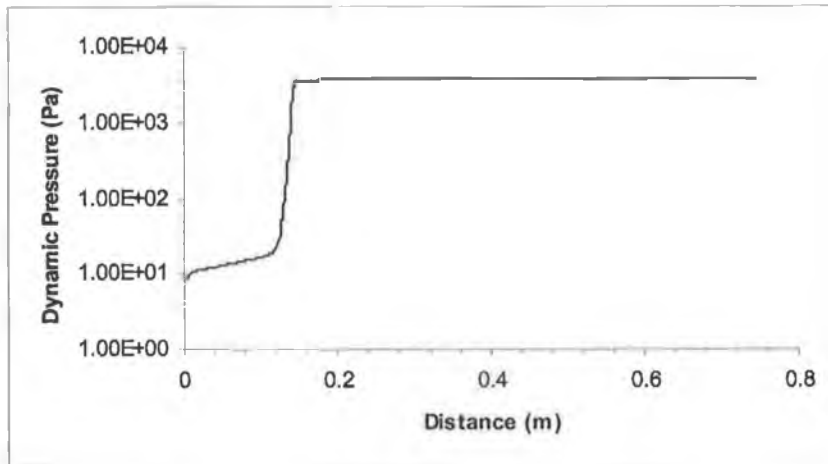


Figure: H.4 Transient state dynamic pressure at  $0.30 f_s$ , 874 K and 0.075 m/s plunger velocity

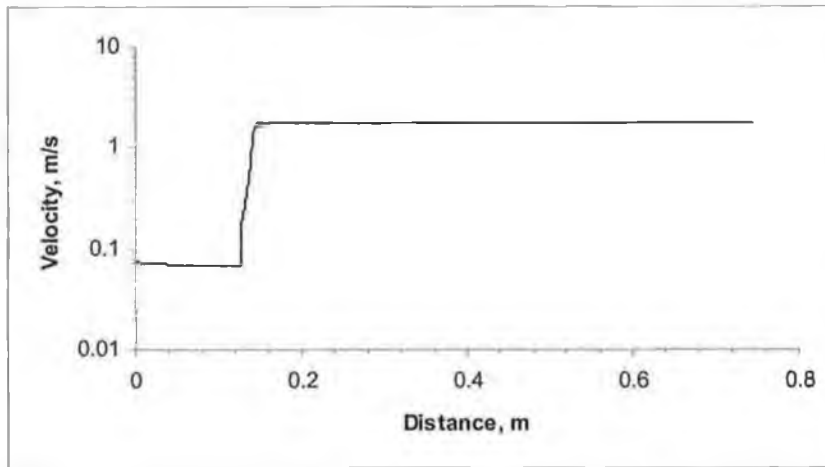


Figure: H.5 Transient state velocity at  $0.30 f_s$ , 874 K and 0.075 m/s plunger velocity

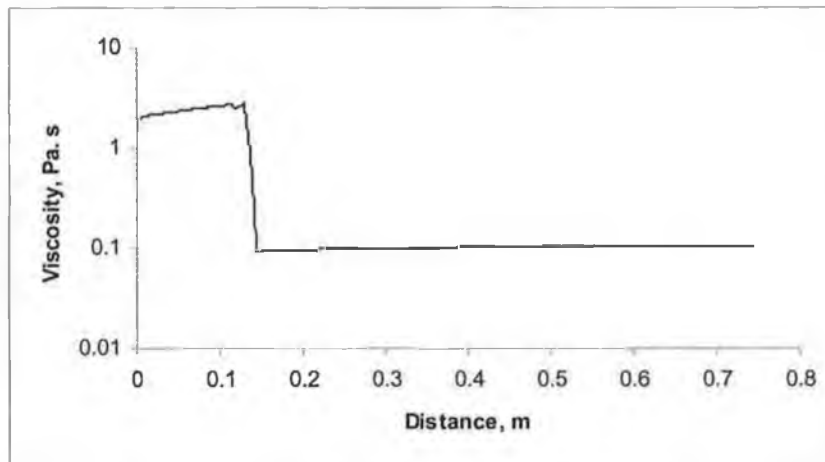


Figure: H.6 Transient state viscosity semi-solid at  $0.30 f_s$ , 874 K and 0.075 m/s plunger velocity



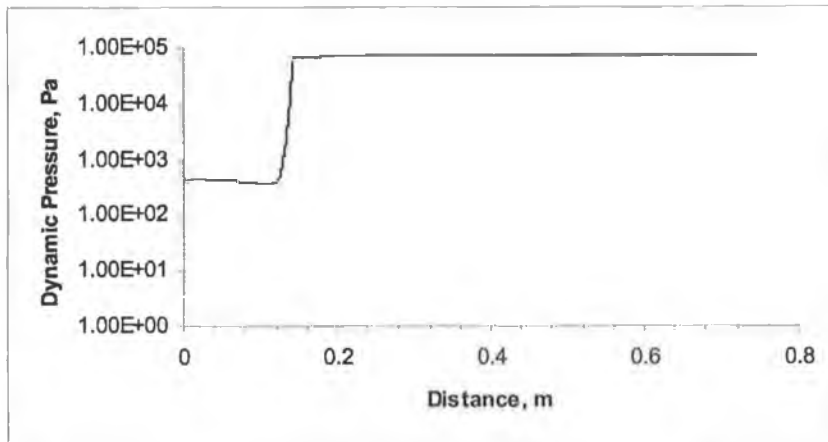


Figure: H.7 Transient state dynamic pressure of A356 at  $0.25 f_s$ , 878 K and 0.5 m/s plunger velocity

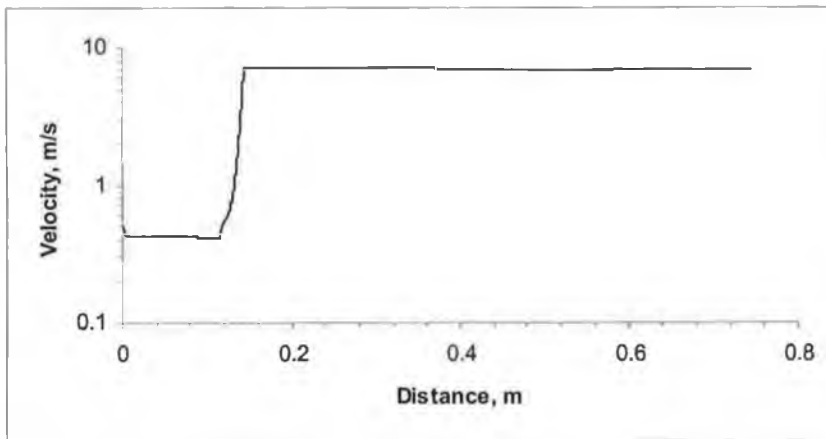


Figure: H.8 Transient state velocity of A356 at  $0.25 f_s$ , 878 K and 0.5 m/s plunger velocity

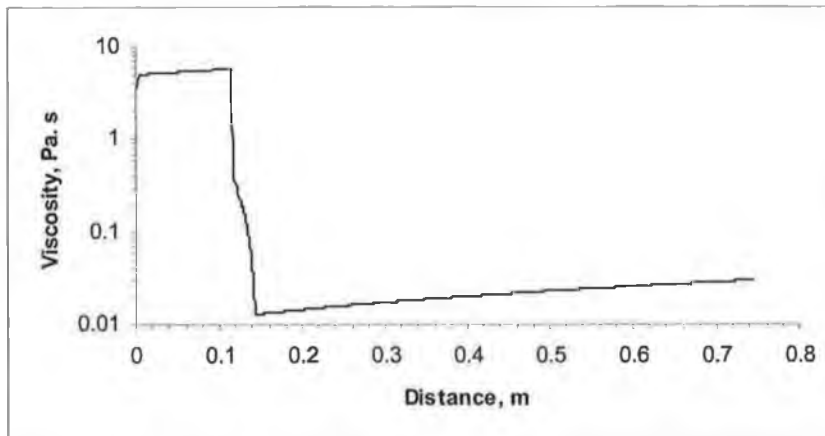


Figure: H.9 Transient state viscosity of A356 at  $0.25 f_s$ , 878 K and 0.5 m/s plunger velocity

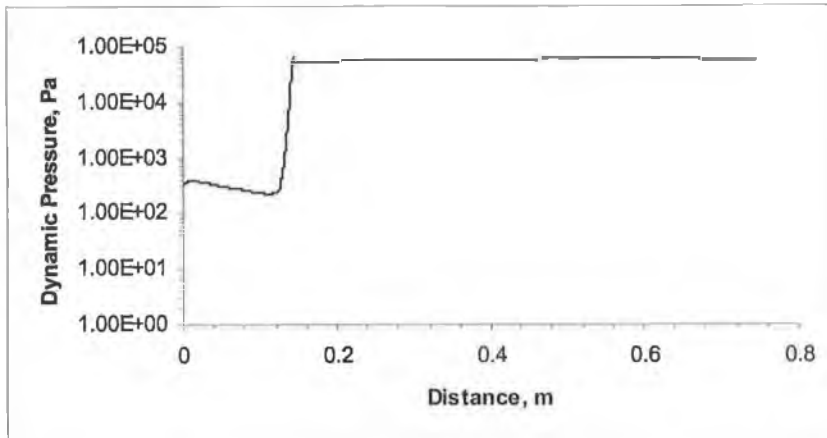


Figure: H.10 Transient state dynamic pressure of A356 at  $0.30 f_s$ , 874 K and 0.5 m/s plunger velocity

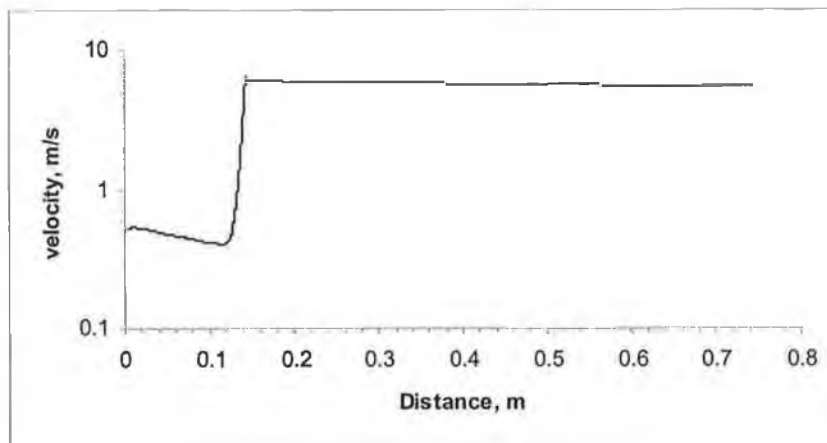


Figure: H.11 Transient state viscosity of A356 at  $0.30 f_s$ , 874 K and 0.5 m/s plunger velocity

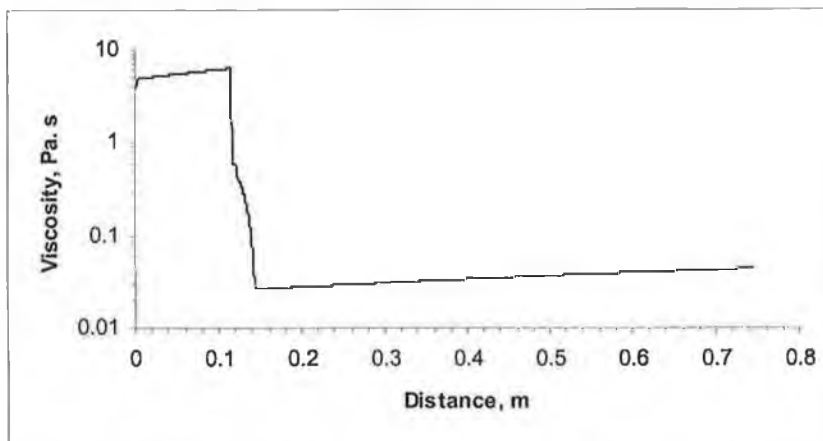


Figure: H.12 Transient state viscosity of A356 at  $0.30 f_s$ , 878 K and 0.075 m/s plunger velocity

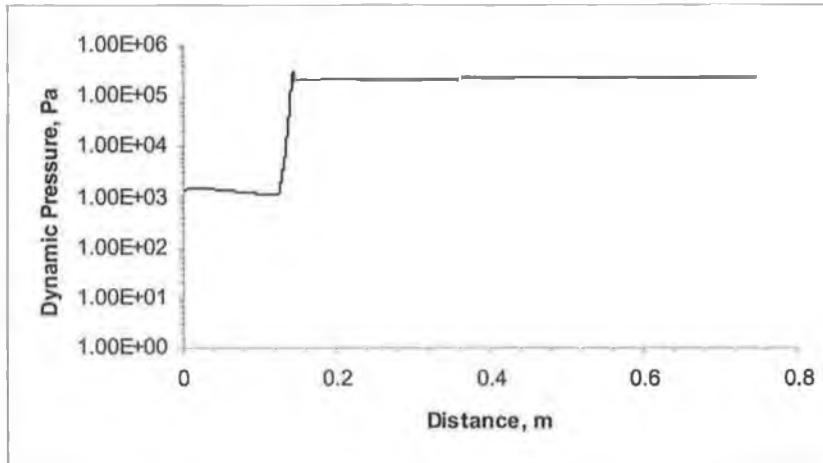


Figure: H.13 Transient state dynamic pressure of A356 at  $0.25 f_s$ , 878 K and 1 m/s plunger velocity

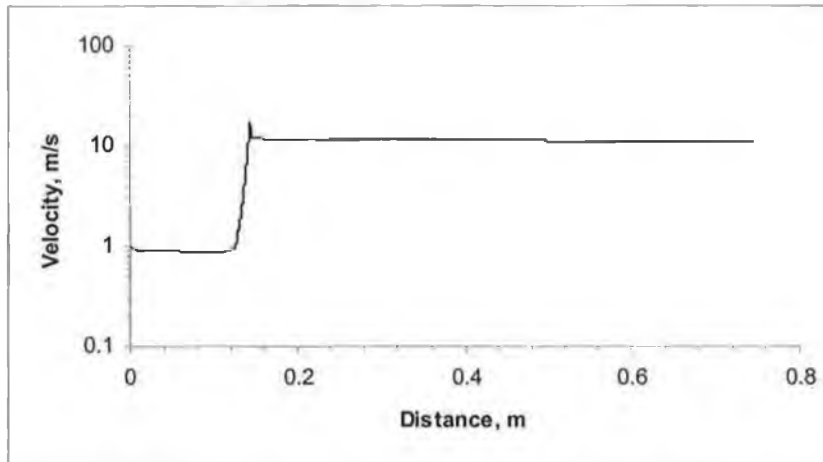


Figure: H.14 Transient state velocity of A356 at  $0.25 f_s$ , 878 K and 1 m/s plunger velocity

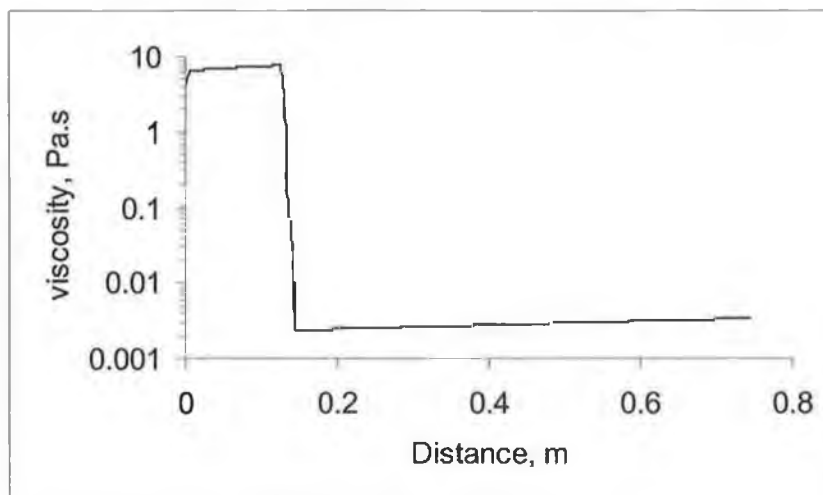


Figure: H.15 Transient state viscosity of A356 at  $0.25 f_s$ , 878 K and 1 m/s plunger velocity

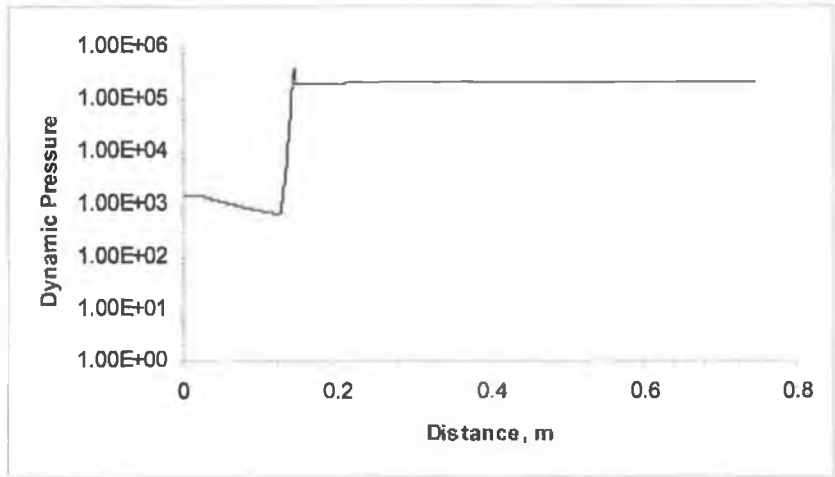


Figure: H.16 Transient state dynamic pressure of A356 at  $0.3 f_s$ , 874 K and 1 m/s plunger velocity

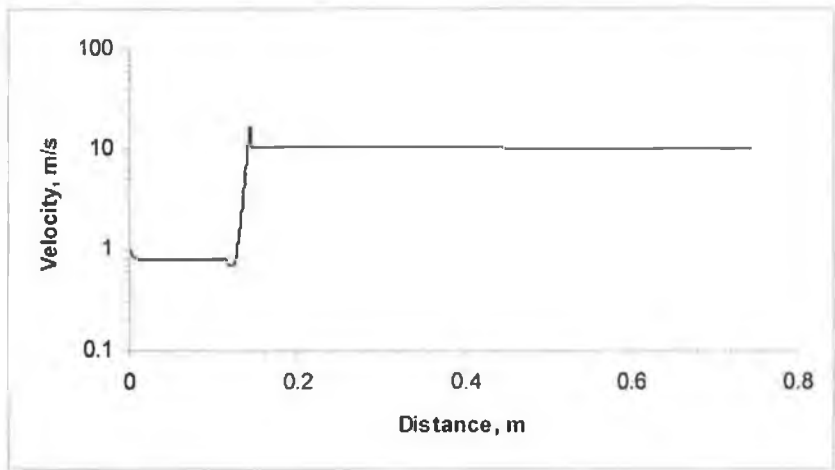


Figure: H.17 Transient state velocity of A356 at  $0.3 f_s$ , 874 K and 1 m/s plunger velocity

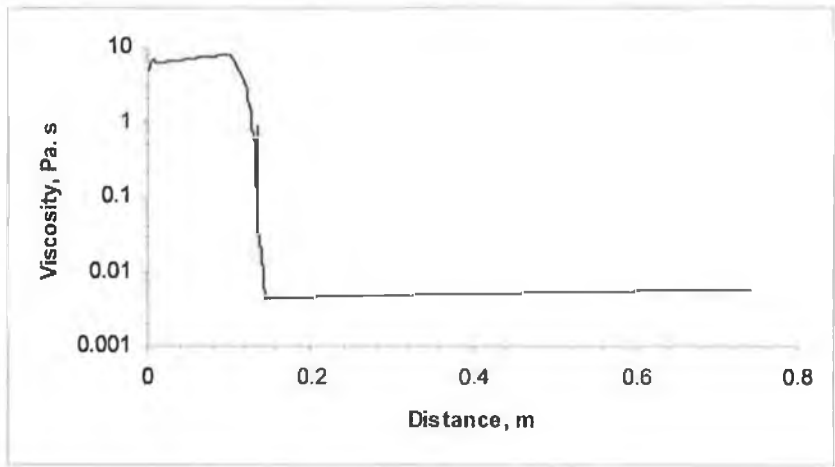


Figure: H.18 Transient state viscosity of A356 at  $0.3 f_s$ , 874 K and 1 m/s plunger velocity

**Appendix: I Velocity, shear rate, rotational speed as well as pressure and viscosity relations for the capillary viscometer**

(Note for graphs below: points 1 to 9 represent increasing shear rate or speed.)

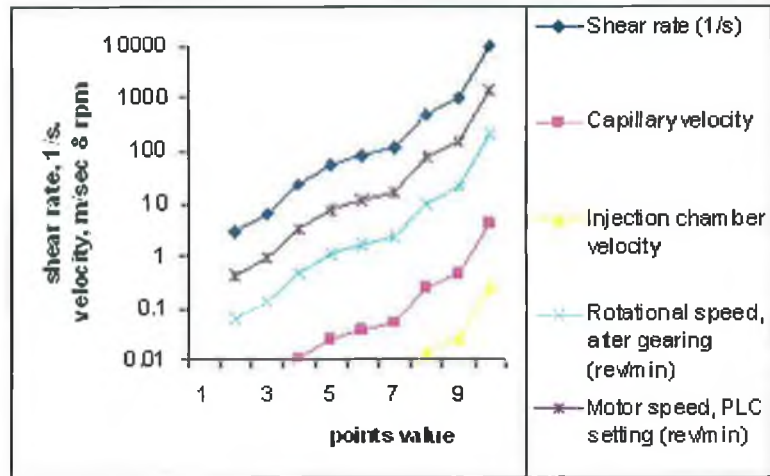


Figure I.1 Velocity values for different shear rates with a flow index of  $n = 0.3$

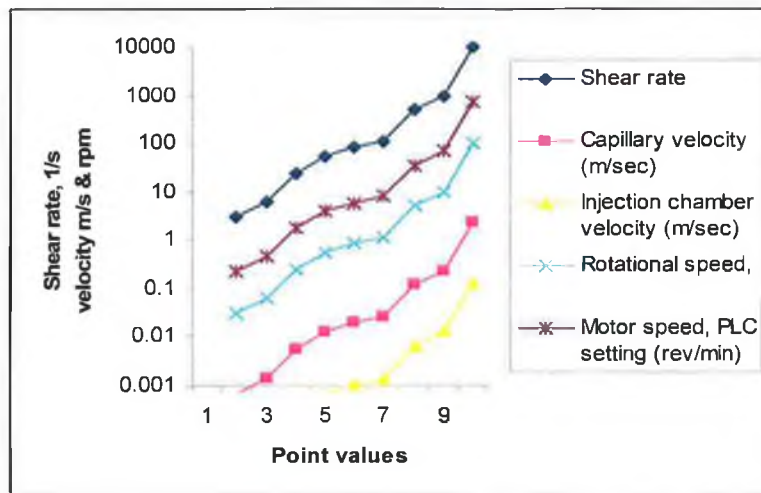


Figure I.2 Velocity values for different shear rates with a flow index of  $n = 0.1$

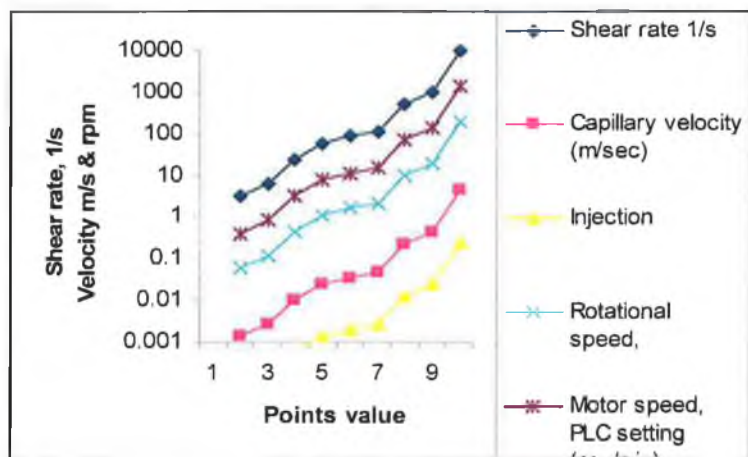


Figure I.3 Velocity values for different shear rates with a flow index of  $n = -0.1$

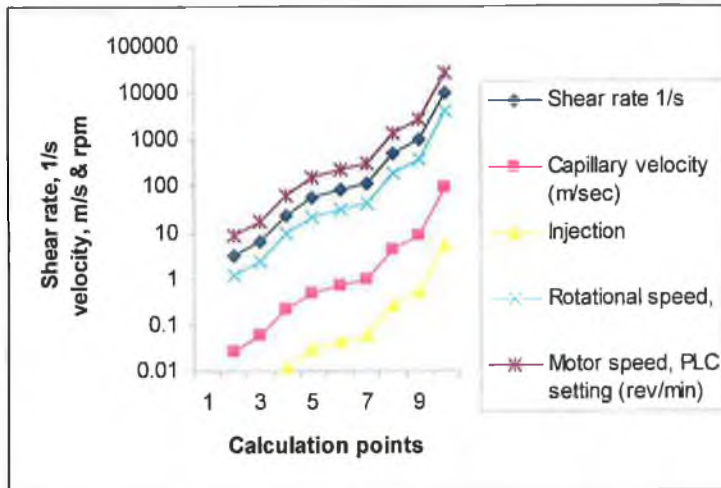


Figure I.4 Velocity values for different shear rates with a flow index of  $n = -0.3$

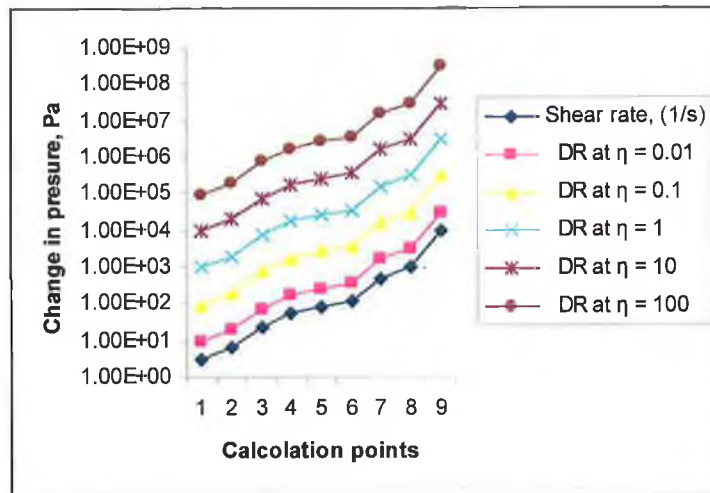


Figure I.5  $\Delta P$  at specified shear rates, viscosities of the semi-solid and  $n = 0.3$

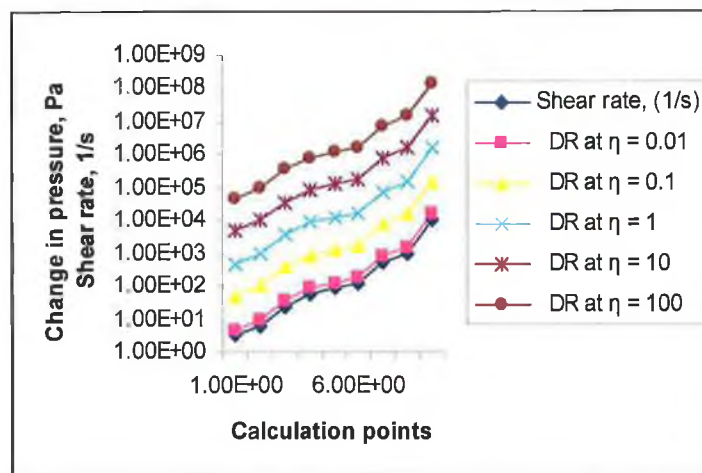


Figure I.6  $\Delta P$  at specified shear rates, viscosities of the semi-solid and  $n = 0.1$

Note: DR represents the change in pressure  $\Delta P$ .

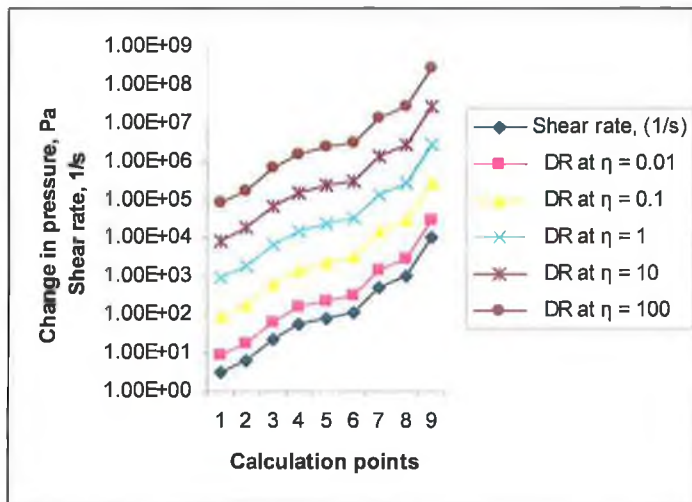


Figure I.7  $\Delta P$  at specified shear rates, viscosities of the semi-solid and  $n = -0.1$

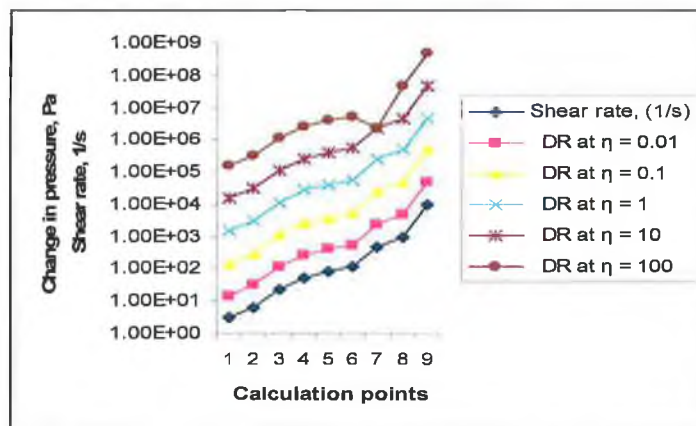


Figure I.8  $\Delta P$  at specified shear rates, viscosities of the semi-solid and  $n = -0.3$

Note: DR represents the change in pressure  $\Delta P$ .

## Appendix J Viscosity result for polypropylene

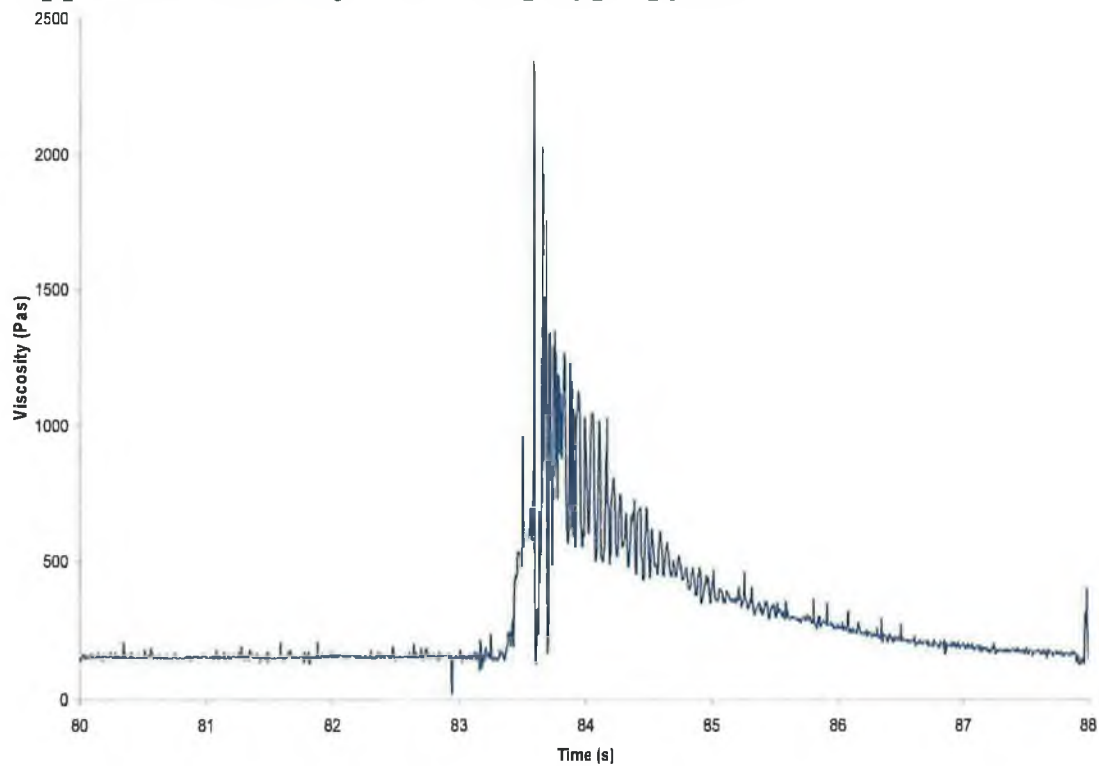


Figure J.2 Calculated viscosity using equation 4.6 vs. time in experimental testing of polypropylene with the capillary viscometer.

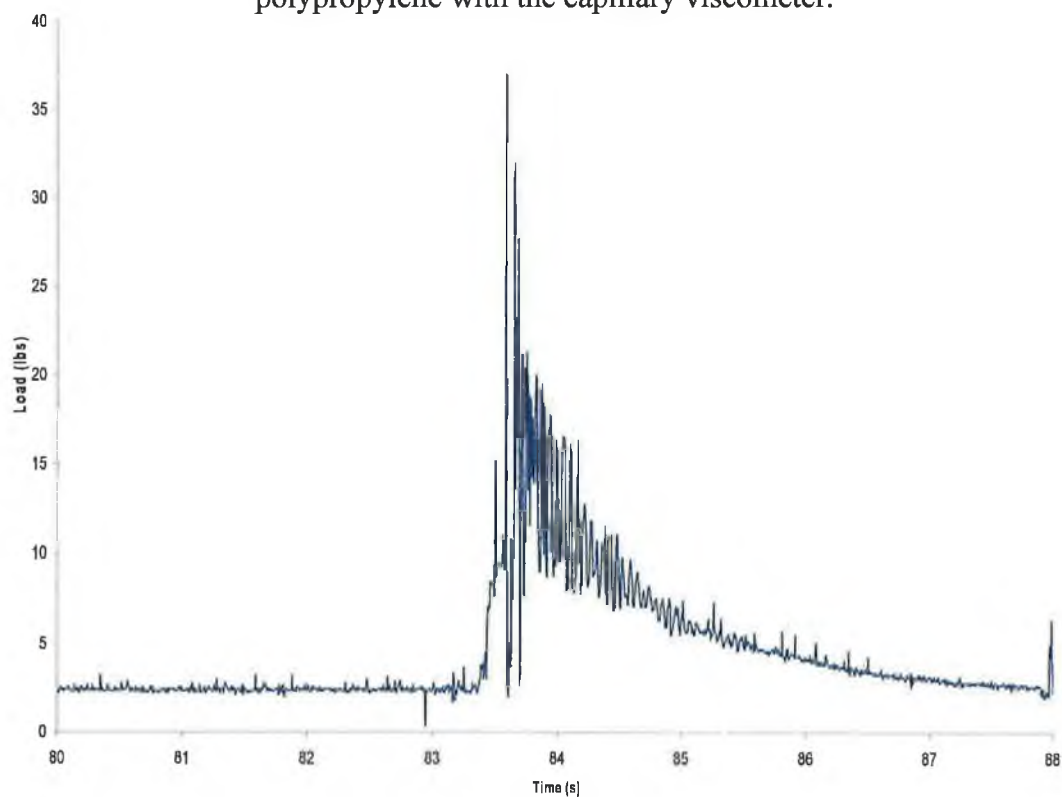


Figure J.1 Load readings vs. time in experimental testing of polypropylene with the capillary viscometer. Length of capillary was 80 mm for this test.